AN INVESTIGATION INTO THE VASCULAR PHENOTYPES OF BREAST PATIENT-DERIVED XENOGRAFTS

Emma Louise Brown

Wolfson College

Cancer Research UK Cambridge Institute

University of Cambridge

This dissertation is submitted for the degree of Doctor of Philosophy

October 2021

This thesis is dedicated to my late grandparents, Bill and Joan.

DECLARATION

This thesis is the result of my own work and includes nothing which is the outcome of work done in collaboration except as declared in the preface and specified in the text It isnot substantially the same as any work that has already been submitted before for any degree or other qualification except as declared in the preface and specified in the text.

It does not exceed the prescribed word limit for the Clinical Medicine and Clinical Veterinary Medicine Degree Committee of 60,000 words.

Signed:_____[Signature redacted]_____

Date: 28th October 2021

Emma Brown BSc.

ABSTRACT

TITLE: An Investigation into the Vascular Phenotypes of Breast Patient-Derived Xenografts

AUTHOR: Emma Brown

Blood vessel networks in tumours are often chaotic, dense and immature resulting in reduced blood perfusion and oxygen delivery, leading to hypoxia (low oxygen levels). Hypoxic tumours are more aggressive, therapy resistant and likely to metastasise, particularly in breast cancer. Equally, hypoxic tumours encourage the growth of new blood vessels from existing vasculature, termed angiogenesis, and high rates of angiogenesis result in immature and chaotic vessels forming, creating a feed-forward loop of poor perfusion and oxygenation. Photoacoustic imaging (PAI) can visualise vascular features in the tumour microenvironment at multiple scales, building a complete picture of the vascular phenotype in a single tumour, which can be monitored longitudinally over time and non-invasively *in vivo*. It's high spatiotemporal resolution, low cost, use of nonionizing radiation and non-invasive properties make PAI an attractive option for monitoring dynamic vascular features not only in a preclinical setting but also throughout a patient's treatment regime, particularly in breast cancer management. Thus far there has been a reliance on cell-line mouse models to provide insight into tumour vascular phenotypes captured with PAI. As a result, several questions remain regarding the sensitivity of PAI to discriminate between patient vascular phenotypes, and which vascular features are important to monitor in patients. In order to translate PAI into the clinic, the field must begin to use more clinically-relevant preclinical models and assess their ability to recapitulate the phenotypes seen in patients. This thesis proposes the use of breast cancer patient-derived xenografts (PDXs) in PAI, to begin to answer the aforementioned questions in clinically-relevant models. However, whether PDXs are good vascular models themselves remains unknown. This thesis conducts a careful evaluation of whether vascular phenotypes differ between 4 breast PDX models and how they evolve over time using PAI with corresponding *ex vivo* immunohistochemistry, used to biologically validate the phenotypes seen *in vivo* and provide additional molecular information. The work assessed how vascular phenotypes change across PDX passages and briefly compared them to originating patient tissue sections. Finally, the origin of these vascular phenotypes is investigated by measuring the underlying hypoxic gene expression of the cancer cells, assuming that the cancer cells shape the mouse host vasculature. The 4 breast PDXs studied displayed different vascular features on *ex vivo* IHC, which PAI was sensitive to *in vivo*. Overall, the PDXs were robust and reliable vascular models, with little inter-passage variability and similarity to patient

vascular phenotypes shown on IHC. Demand and supply of oxygen through the blood vessel network appears to influence the extent of hypoxia in the tumour tissue. Inherent hypoxic phenotypes were measured using PAI, IHC and RNA-seq, which could drive formation of immature vascular networks in some PDX models. This thesis is the first multiparametric investigation into breast PDX vasculature across scales using PAI, IHC and RNA-seq.

ACKNOWLEDGEMENTS

First of all, I would like to thank my supervisor Professor Sarah Bohndiek for allowing me to conduct such an interesting and engaging research project in your lab. You are an incredible scientist and inspire me in my work. You have supported me through the good, the bad and the ugly parts of research and I have grown as a person and as a scientist in your lab.

During the course of my PhD, I have had the privilege to work with the outstanding core facilities at CRUK CI, who have contributed a huge amount to the work presented here. In particular, I would like to thank Cara Brodie, Jodi Miller, Gemma Cronshaw and Dominique Laurent-Couturier. Your expertise has been invaluable to this project and your passion has made you all a joy to work with.

I would like to thank past and present members of the VISIONLab particularly: Isa, Michal, Paul, Janek, Calum, Thierry, Tom and Lina. Thank you for all the guidance and support over the years. Particularly to those of you that worked through this pandemic alongside me, thank you for the 'low-key' happy hours and cold winter walks that kept me going through the second (or was it the third?) lockdown. You are all incredible scientists and more importantly, incredible friends.

I have many friends both inside and outside of Cambridge who I would like to thank for helping me escape from the lab once in a while. A particular thanks to the Wolfson Choir girls Andrea, Carla and Emily, who I have enjoyed many whiskeys and pálinkas with over the past years. I'd like to thank my housemate Angus, who has put up with my many expletives shouted whilst formatting this thesis and my Brindle lab buddy Rike, who I have shared many imaging related woes and successes with. Finally, to my three greatest friends in the world, my RVC girls: Georgie, Liv and Jess. Thank you for always being by my side and ready with a cup of tea, or several glasses of wine, depending on the severity of the situation. I am privileged to call you my friends.

One of the biggest thank yous in these acknowledgements must go to my boyfriend Danis. You are my personal cheerleader and your love and support has motivated me through

writing this thesis, I hope I can do the same for you. Your cheerful and happy nature inspires me every day and I look forward to a wonderful future with you.

CONTENTS

LIST OF TABLES

LIST OF FIGURES

LIST OF COMMON ABBREVIATIONS AND ACRONYMS

ASMA: Alpha smooth muscle actinAT:

Auto-thresholding

CAIX: Carbonic anhydrase IXCLR:

Chord-to-length ratio

Hb: Deoxygenated haemoglobinHbO_2:

Oxygenated haemoglobinHIF:

Hypoxia-inducible factor IHC:

Immunohistochemistry

MSOT: Multispectral optoacoustic tomographyPAI:

Photoacoustic imaging

PDX: Patient-derived xenograftsRF:

Random forest

RSOM: Raster-scanning optoacoustic mesoscopySO_2:

Blood oxygen saturation

SOAM: Size-of-Angle MeasureSNR:

Signal-to-noise ratio TDA: Topological

data analysis

TME: Tumour microenvironmentTHb:

Total Haemoglobin

VEGF: Vascular endothelial growth factor

VF: Vesselness filtering

1 INTRODUCTION

1.1. Introduction

The focus of cancer research has moved from treating the tumour as a homogenous mass of cancer cells to considering the heterogeneity associated with this disease and the dysregulated and dynamic interactions within the wider tumour microenvironment (TME)[1]. The infrastructure of a growing solid tumour is a heterogeneous mixture of cancer and stromal cells, including a milieu of immune cells, adipocytes and fibroblasts. In addition to this complex cellular picture, chemical signals such as hypoxia and physical signals arising from fibrosis, among others (**Figure 1.1**), are linked to poor patient prognosis[2]. This thesis focuses primarily on the role of the immature vascular network and the accompanying hypoxic environment present in manysolid tumours, particularly in breast cancer[3]. Importantly, features of the TME interact with and regulate one another[4–6], and such dynamic relationships influence tumour growth and heterogeneity. Improving our understanding of the role of the vasculature in the TME and cancer progression would strongly benefit from non-invasive visualisationof the tumour as a whole organ *in vivo*, both preclinically in mouse models of the disease,as well as in patients.

Unfortunately, vascular features remain challenging to resolve with non- invasive imaging. As a result, many studies still rely on excised tissues *ex vivo*, which only interrogate a small portion of the tumour at a fixed time point, and are not able to

capture its full spatial and temporal heterogeneity. Visualising vascular features *in vivo* would allow researchers to investigate key questions such as: how the vasculature evolves during tumour development; the interplay between cancer cells and tumour vasculature; and how vascular phenotypes differ between different tumour subtypes. The biomarkers resulting from these studies could then be applied clinically to predict tumour aggressiveness, stratify patients and monitor treatment response. Ultimately, this would transform patient care and improve survival by helping to guide therapeutic strategies, in combination with other informative biomarkers[7,8].
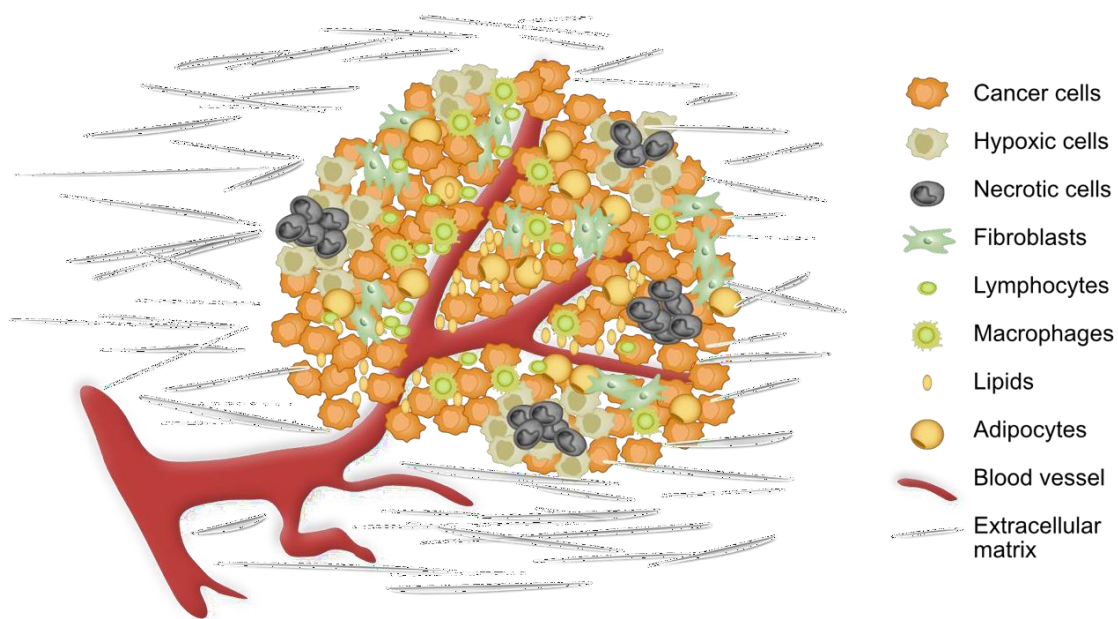
Figure.1.1. The tumour microenvironment (TME). Schematic diagram illustrating the involvement of multiple cell types in a tumour, including endothelial cells and pericytes that make up blood vessels, as well as immune cells, fibroblasts and adipocytes, alongside the cancer cells. Lipids are synthesised by adipocytes and cancer cells. Hypoxia arises as the tumour grows beyond the limit of oxygen diffusion from the surrounding vessels. Fibrosis arises from excessive deposition of extracellular matrix (ECM) components without concurrent degradation. A supportive environmental niche of these chemical and physical signals evolves with the cancer cells to promote tumour development and progression.

A range of existing *in vivo* imaging techniques can be used to visualise different facets of the vascular microenvironment and have already provided valuable insight. Unfortunately, they come with limitations that include limited spatial resolution, extended scan times and poor

specificity from confounding signals. Photoacoustic (PAI, also referred to as optoacoustic) imaging is a promising new modality with potential to overcome these limitations for imaging vascular features in vivo. As PAI advances towards the clinic, it is vital that clinically-relevant biological models are assessed for their ability to recapitulate the vascular phenotypes seen in patients and to test the sensitivity of PAI to resolve these different vascular phenotypes. Currently, most preclinical studies in PAI to date used subcutaneous cell-line models, which poorly recapitulate the microenvironment seen in patients[9]. This thesis investigates the use of patient-derived xenografts (PDXs) of breast cancer, examining their potential to provide more clinically-relevant preclinical models10.

This chapter will first focus on tumour vasculature and hypoxia and their dynamic interactions with other stromal and cellular compartments in the TME that shape the vascular microenvironment. Then, the advantages and disadvantages of current techniques for imaging vascular features ex vivo and in vivo will be discussed, specifically focussing on the potential of PAI. This chapter concludes by outlining the potential of breast PDXs as preclinical cancer models and discusses the opportunity to characterise the vascular microenvironment of breast PDXs with PAI.

1.2. Features of the vascular microenvironment

1.2.1. Tumour vasculature and hypoxia

A growing tumour mass requires a vascular network to supply cancer cells withnutrients and remove metabolic waste products, which then permits cancer cells to extravasate and metastasise. Development of a vascular network typically begins in response to diffusion-limited, or chronic hypoxia, which arises when the diffusion of oxygen from surrounding blood vessels is insufficient to meet the demand of the proliferating cancer cells[3,4]. Activation of hypoxia inducible factors (HIFs, notablyHIF1α) drives the transcription of genes involved in a wide range of cellular functions[3,4], including the production of pro-angiogenic factors, such as vascular endothelial growth factor (VEGF), that stimulate endothelial cells to proliferate, sprout and form new bloodvessels [11,12]. Notably, HIF1α can also be stabilised by the release of reactive oxygen species (ROS) or oncogenic signalling pathways meaning the initiation and acceleration of tumour angiogenesis via the HIF1α-VEGF axis can be hypoxia-independent[13]. With overexpression of VEGF, often an imbalance of pro- and anti-angiogenic factors then occurs, which results in a chaotic and heterogeneous network of blood vessels, includingmany immature vessels with poor pericyte coverage[14], irregular branching and a tortuousmorphology[15–18].

VEGF is a central growth factor in the regulation of blood vessel formation[12]. In pathological angiogenesis, such as in tumours, VEGF has also been found to have multiple roles in regulating pericyte/smooth muscle cell coverage. VEGF signalling was found to inhibit platelet-derived growth factor receptor beta signalling in pericytes/smooth muscle cells resulting in detachment of pericytes which contributed to vessel destabilisation in a fibrosarcoma mouse model[19]. VEGF-mediated vessel permeability is also driven by focal-adhesion kinase (FAK) and Src signalling in endothelial cells, where VEGF induced activation of FAK results in autophosphorylationof FAK, recruitment of Src and further downstream signalling which targets VE-Cadherinat endothelial cell junctions and results in dysregulation of the these junctions and vascular permeability[20,21]. Endothelial cell FAK pathways, under the influence of VEGF,also drive angiogenesis and other cellular processes, through Erk and Akt signalling[22,23]. Other angiogenic signalling pathways are also of note, for example the roles of

angiopoietin (ANG) ligands and their TIE tyrosine kinase receptors in angiogenesis and vessel maturity. ANG2-TIE2 is most often discussed in the context of cancer, with ANG2expression upregulated in many solid tumours, notably breast cancer. ANG2 expression is upregulated by VEGF signalling as well as hypoxia and inflammatory cytokines, all ofwhich can be in abundance in solid tumours[24]. Neutralising ANG-TIE2 interactions is thought to decrease angiogenesis, while blockage of ANG2 with peptibodies was shownto normalise tumour bloods vessels, with increased pericyte coverage, which will strengthen vessels, and increased VE-Cadherin expression at endothelial cell junctions incolorectal cancer cell-line xenografts[25]. Therefore, dual blockage of ANG2 and VEGF has been proposed as a dual anti-angiogenic therapeutic strategy in solid tumours[24].

Tumour vasculature does not follow a hierarchy of well-differentiated arteries, arterioles, capillaries, venules and veins as seen in normal tissue. In addition to this irregular architecture, tumour blood vessels themselves are also structurally distinct fromnormal vessels. Nagy et al. describe 'mother vessels' as the first vessels to develop in tumours under VEGF secretion (**Figure 1.2**). These are highly permeable enlarged sinusoids with loose basement membrane integrity and pericyte attachment. Internal bridging of endothelial cells inside the lumen of mother vessels can create capillaries or glomeruloid microvascular proliferations (GMPs). GMPs are tangled structures with irregularly ordered pericytes and redundant basement membrane. If mother vessels acquire smooth muscle cell coating they can evolve into vascular malformations, which are inappropriately large vessels although not as hyperpermeable as GMPs. Finally, tumours are also supplied by feeding arteries and drained by draining veins, however, even these structures are often abnormal and tortuous[17,26].
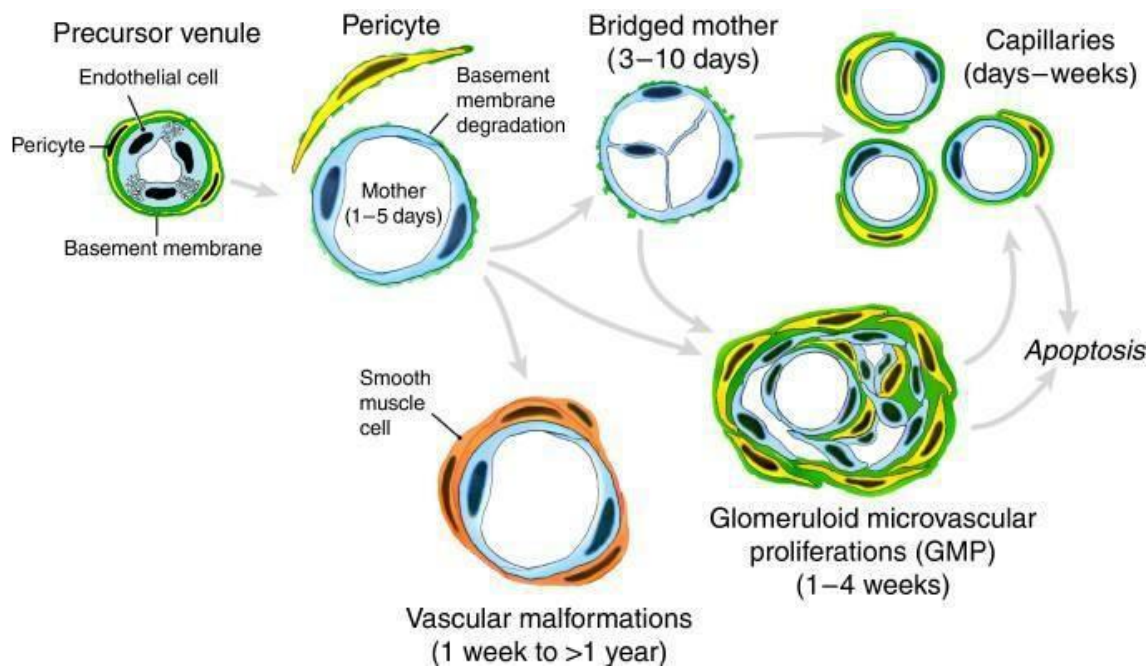
Figure. 1.2. Vessel development in tumours. Schematic taken from Nagy et al. 2009 demonstrating how tumour vessels have a unique structure and evolve from existing venules. Mother vessels (MVs) form first and are hyperpermeable vessels with basement membrane degradation and loose pericyte attachment. From MVs capillaries, glomeruloid microvascular proliferations and vascular malformations can evolve. They are all dysfunctional structures.

Several important prognostic consequences arise from these features of the tumour vasculature. First, repeated dynamic cycles of ischaemia and reperfusion occur due to inefficient orientation of the vessels. Arterio-venous shunting of red blood cells occurs, causing variation in red blood cell flux. Blood flow does not travel in one unidirectional path and the flow rate decreases when the red blood cells travel far from an artery and become hypoxic. Immature vessels which lack pericyte/ smooth vessel coverage are often leaky, causing further issues with blood pooling and a lack of flow and these vessels can collapse, starving nearby cancer and stromal cells of oxygen and nutrients[13,26]. This variation in perfusion causes perfusion-limited, or cycling, hypoxia in cancer and stromal cells generating oxidative stress, which leads to increased stem-cell- like properties of cancer cells and resistance to therapy[27]. Second, heterogeneity of vessel perfusion leads to unequal access of systemic therapeutic agents within the tumour. Although some areas of the tumour – those that are well perfused – will likely receive the expected therapeutic dose, other poorly perfused areas may receive a lower dose, meaning that they can survive the treatment[28]. Any hypoxic tumour areas will also be resistant to

6

traditional chemo- and radiotherapies[4], because many of these therapies mediate their effects via the generation of ROS[29]. Finally, as tumours shift to a predominantly glycolytic metabolism via the expression of HIF target genes, poor perfusion allows lacticacid (from anaerobic glycolysis) and protons (from the conversion of CO_2 produced from the pentose phosphate pathway) to accumulate in the TME, giving rise to acidosis[30,31]. Acidosis can increase cancer cell invasion[32] and metastatic potential[33], and decrease drugefficacy[34]. HIF1α, VEGF and associated pathways are linked to poor prognosis in a rangeof solid tumours[3,35,36], demonstrating the consequences of tumour hypoxia on patient outcome.

In more recent years, there has been debate around whether all tumours are dependent on angiogenesis for growth. Hypoxia is thought to drive other forms of vesselformation in tumours, which are less studied than the traditional 'angiogenic' model but may present explanations for resistance to anti-angiogenic therapies[37]. Cancer cells can co-opt existing vasculature, promote vasculogenesis (formation of new vessels from endothelial cell progenitors) or perform 'vasculogenic mimicry' (VM). VM is describedas the ability of cancer cells to form vessel-like structures themselves, capable of carryingblood[37,38]. It was first observed in uveal melanoma[39] and has since been observed in many solid tumours including breast, lung and glioblastoma[37,40–43]. EMT pathways, under hypoxia, are thought to drive VM but angiogenic pathways are also involved [38,44–46]. Mimicked vessels are leaky and immature and tumours with high-levels of VM are moreaggressive, invasive and poorly prognostic[39,40,43,47,48]. Under hypoxic conditions, it is stillunclear why cancer cells would choose one vessel forming method over another.

1.2.2. Dynamic interactions between features of the TME

It is increasingly evident that features of the TME regulate each other. Hypoxiaplays a central role in these interactions. For example, increased deposition of extracellular matrix proteins in tumours and recruitment of stromal cells leads to fibroticcontraction of the interstitial tissue space, which is associated with: increased interstitialfluid pressure[49]; the collapse of immature blood vessels; and restricted oxygen diffusion,which causes hypoxia[50]. Conversely, at the molecular level, HIF1α directly activates transcription of genes required for collagen synthesis and crosslinking, such as procollagen lysyl hydroxylase 2[51,52], which increases angiogenic signalling and vessel

permeability[53,54]. This could actually result in decreased oxygen delivery to the tumour and thus further hypoxia.

Pro-angiogenic signalling of many stromal cell types is also hypoxia-mediated. Hypoxia drives macrophage polarisation towards an M2 phenotype, which is anti-inflammatory and pro-angiogenic[55]. Many M2 macrophages are TIE2$^+$ and cluster around existing blood vessels, promoting angiogenesis[56–59] and vessel permeability[60]. The milieu of cytokines and growth factors secreted by cancer-associated fibroblasts (CAFs) contain further pro-angiogenic factors[5], while hypoxia upregulates the production of sphingosine lipids[61,62] that are also likely to drive angiogenesis[63,64]. Importantly, endothelial cells should not be considered passive responders to the pro-angiogenic environment surrounding them. Rather they are active players, stimulated by pro-inflammatory cytokines and consequently display a dysfunctional phenotype of increased proliferation, permeability, upregulation of inflammatory cytokines such as IL-6 and upregulation of adhesion molecules. Tumour endothelial cells contribute to an enhanced inflammatory microenvironment, similar to the wound healing response in normal tissue gone awry to promote cancer cell proliferation, survival and extravasation[65]. HIF1α signalling in endothelial cells disrupts barrier function to allow increased intravasation of tumour cells into blood vessels and increase metastases[66]. Additionally, hypoxia and acidosis modulate the function of all immune cell types, meaning that hypoxic niches spatially fine-tune the TME[4,67].

Finally, many therapies modulate the evolution of the TME and the dynamic relationships within. Anti-angiogenic treatments, which often target the VEGF pathway, have been shown to 'normalise' tumour vasculature by increasing vessel maturity, leading to re-oxygenation of the tumour and decreased hypoxia in mouse models[68,69].

These dynamic relationships paint a complicated picture of the TME that will be explored for many years to come. The evidence presented thus far demonstrates that the vascular component of the TME is dynamic and evolves with many other chemical, physical and cellular components. The vasculature is not just growing and branching in tumour development due to an increase in VEGF production, but the resultant phenotype is regulated by hypoxia and hypoxia-driven signalling pathways as well as cell-cell contact and paracrine signalling from nearby stromal cells. These factors in turn regulate hypoxia, infiltration of immune cells and extravasation of tumour cells themselves,

ultimately shaping tumour biology. This thesis will now focus on the vascular component of the TME, named the vascular microenvironment. Being able to monitor the dynamics of the vascular microenvironment *in vivo* is essential to improve our understanding of tumour biology and ultimately improve treatments for patients.

1.3.   Visualising the vascular microenvironment

1.3.1. *Ex vivo* methodology for visualising the TME

Many *ex vivo* imaging methodologies can be used to visualise the TME within tissue sections. Using these methods, one can investigate the morphology, composition, dynamic cell interactions, and molecular expression of biomarkers in the tumour at a single-cell level; they also provide a cornerstone of clinical analyses and are widely used in biological research. Immunohistochemistry (IHC) is a low-cost and easy-to-use method for staining tissue sections that is regularly used in clinic to characterise biomarkers for diagnosis, prognosis and to guide treatment options[70]. Angiogenic markers such as the expression of VEGF have been shown to have higher expression in malignant vs. benign disease, as well as correlate with certain subtypes of breast cancer[71]. These IHC methods are typically interpreted by a pathologist, which can lead to variability in interpretation and lack of reproducibility, highlighting a need for more quantitative methods[70]. Furthermore, typically IHC practices examine only one marker per tissue section, limiting our ability to study the interplay between different factors, although multiplexed methods are starting to emerge through exciting new tools, for example, Imaging Mass Cytometry (IMC)[72], which once combined can be correlated with different cancer subtypes and prognosis[73]. Alternative multiplexing methods include optical microscopy techniques such as second harmonic generation microscopy, which can visualise collagen deposition in addition to the traditional microscopy data[74]. Furthermore, matrix-assisted laser desorption/ionization (MALDI) imaging can image thousands of analytes such as lipids and proteins in tissue, but not cellular structures[75].

Nonetheless, common to these methods is the disadvantage of excising the tissue, which means only a small portion of the tumour is interrogated at a fixed time point, ignoring the full spatial and temporal heterogeneity of the TME. Non-invasive *in*

vivo imaging methods allow true longitudinal imaging of tumours, whereby the same mouse or patient is imaged at multiple time-points to monitor tumour evolution and/or therapy response. Many *in vivo* imaging methods capture the whole tumour volume, or atleast a larger volume than possible with *ex vivo* methods, gaining improved spatial and temporal information on the dynamics of the TME.

1.3.2. Existing *in vivo* imaging modalities of the vascular microenvironment

Several preclinical and clinical imaging techniques are already available to probe the vascular microenvironment (**Table 1.1**). Vascular perfusion can be visualised using intravenous administration of a contrast agent through 'dynamic contrast-enhanced' approaches[76–78] which, despite being widely used, do have some associated toxicity concerns[79,80]. Hypoxia represents a challenge for imaging in medical diagnostics, as the method must generate a positive signal for the absence of oxygen. Preclinical studies using intravital imaging have revealed blood flow fluctuations and perivascular changes in hypoxia [27], though these approaches are invasive (**Table 1.1**). Magnetic resonance imaging (MRI)-based approaches such as blood-oxygen-level-dependent (BOLD) MRI[81]and oxygen-enhanced (OE) MRI [82] correlate with tissue oxygenation and histological markers of hypoxia [81,82]. However, they suffer from intrinsically low sensitivity [83,84]. Positron emission tomography (PET) agents for hypoxia visualisation, including those derived from nitroimidazole, are also available [85,86], but application to studying the TMEis limited by the inherently low spatial resolution of PET and the requirement to administer a radiopharmaceutical. Diffuse optical spectroscopic imaging (DOSI) is a low-cost and readily accessible approach that measures local optical absorption coefficient. DOSI can measure concentrations of oxy- and deoxy-haemoglobin (HbO_2 and Hb, respectively) as surrogate markers of hypoxia [87–89] but has poor resolution at depths beyond ~1 mm due to light scattering in tissue[95].

Table 1.1. Current imaging techniques for visualising different features of the vascular microenvironment *in vivo*

Technique	Principle	Advantages	Disadvantages	References
DCE-CT	Iodinated contrast agents are injected to measure vascular per-fusion.	- Well established CT technique. - Low cost - Widely available.	- Contrast agent can cause toxicity. - Ionizing radiation. - Lack of standardized protocols.	77,79
DCE-MRI	Paramagnetic contrast agents are injected to measure vascular perfusion.	- Well established MRI technique. - Widely available. - Many gadolini-um chelates are approved clinically.	- Contrast agent can cause toxicity. - High cost of MRI.	76,77,80
BOLD MRI	Measures blood oxygenation using the paramagnetic property of deoxyhaemoglobin.	- Well established MRI technique. - Utilises endogenous contrast. - Measurements correlate with tissue oxygenation.	- Signals can be confounded by changes in blood volume and flow. - Intrinsically low signal. - High cost of MRI.	81,83,84

OE MRI	T1 relaxation time is inversely proportional to plasma dissolved oxygen. ΔT1 is measured following a breathing gas challenge to measure areas of low and high blood oxygenation.	• Oxygen contrast is more rapidly reversible than injectable contrast. • Measurements correlate with tissue oxygenation.	• Intrinsically low signal. • High cost of MRI.	82,83,84
FMISO-PET	An injected radiolabelled nitroimidazole derivative accumulates in hypoxic areas.	• FMISO has the potential to give a direct quantification of tissue hypoxia. • Can be used to trace metabolic processes.	• Long uptake time of tracers such as FMISO leads to poor signal-to-noise ratio intumour. • Radioactive isotope administration. • Intrinsically low resolution of PET (~5 mm).	86
EF5-PET	An injected radiolabelled nitroimidazole derivative accumulates in hypoxic areas.	• More stable than FMISO. • Possible correlation to outcome.	• Limited experimental evidence compared to FMISO. • More complicated labelling chemistry compared to FMISO. • Radioactive isotope administration.	85,86

			• Intrinsically low resolution of PET (~5 mm).	
$H_2{}^{15}O$- PET	Radioactive water is injected to measure vascular perfusion.	• Short half-life of ^{15}O enables serial measurement-s in a single scan.	• Short half-life of ^{15}O limits application to sites with an on-site cyclotron. • Radioactive isotope administration. • Intrinsically low resolution of PET (~5 mm).	90
DCE- ultrasound	Microbubbles are injected to generate differences in acoustic impedence with the surrounding tissue, to measure perfusion.	• Low cost. • High resolution (~100 μm-1 mm). • Increased signal-to-noise ratio (SNR) compare-d to conventional ultrasound.	• Contrast agent can cause toxicity. • Ultrasound limited to localised imaging.	78,79
Doppler ultrasound	Utilises the Doppler effect to image the movement of fluids (e.g. blood) and measure their direction and velocity.	• Low cost and widely available. • Allows for serial measurements of	• Challenging to detect motion in small, deep vessels.	91,92,93

		blood flow and perfusion without a contrast agent. ● Easy to combine with other ultrasound techniques.	● Cannot distinguish signal arising from individual or aggregated erythrocytes. ● Ultrasound limited to localised imaging.	
DOSI	Utilises the distinct spectra of deoxy- and oxyhaemoglobinto visualise blood haemoglobin concentration and oxygenation.	● Utilises endogenous contrast. ● Fast acquisition. ● Allows visualisation of multiple TME features through spectral separation.	● Low resolution (~1 cm) at depths at or above 1 cm due to strong attenuation and scattering of diffuse light in tissue.	87,88,89
Intravital microscopy	An intravascular fluorescent contrast agent is injectedto enable optical microscopy of tumour vasculature in a living animal through surgical proced-ures.	● Micron resolution visualisation of capillary networks.	● Invasive. ● Challenging to apply clinically. ● Small field-of-view. ● Depth-limit of ~1 mm due to strong attenuation and scattering of diffuse light in tissue.	94
PAI	Utilises the distinct spectra of deoxy- and oxy-haemoglobin to visualise blood	● Higher penetration depth compared to other optical techniques.	● Depth limit of ~7 cm due to strong attenuation and	95, 98, 99, 104

	haemoglobin concentration and oxygenation.	- Utilises endogenous contrast. - Fast acquisition. - Good technical and biological validationof haemoglobin measurements. - Low cost. - Easy to implement into existing ultrasound systems. - Allows visualisation of multiple TME features through spectral separation. - Has multi-scale capabilities.	scattering of diffuse light in tissue. Difficult to quantify and resolve chromophores with current reconstruction and processing algorithms.

Notably, many of the techniques described suffer from limited spatial resolution, poor specificity from confounding signals and the need to administer contrast agents (**Table 1.1**). Additionally, none of the techniques mentioned are capable of imaging across scales. Modalities such as MRI and PET are capable of capturing the whole tumour volume, but the spatial resolution is low. While intravital imaging gives high resolution, capable of monitoring single-cell dynamics, it can only image a small field-of-view and is an invasive technique. Ultimately there is a trade-off between resolution and field-of-view. Hence, there remains an unmet need for validated imaging biomarkers of the vascular microenvironment that can be measured cost-effectively at high spatial and temporal resolution with a large field-of-view, which could be applied in biological research and in a clinical setting. PAI could offer the flexibility to monitor the vascular microenvironment *in vivo* across scales, without the need to administer contrast agents, providing a more complete picture of the TME.

1.3.3. The principle of photoacoustic imaging

PAI is an emerging imaging modality, currently in clinical trials [96,97], that could improve our visualisation of the TME. To create an image, the tissue of interest is illuminated with pulses of light, which cause a pressure change when absorbed and generate ultrasound waves through the photoacoustic effect (**Figure 1.3A**). The ultrasound waves are detected at the tissue surface using one or more detectors [98–100]. A major advantage of PAI is its scalability: by selecting different light sources, ultrasound detectors and scanning methods, it is possible to tune the spatial resolution, temporal resolution, imaging depth and image contrast. Both image spatial resolution and tissue attenuation scale with increasing ultrasound frequency: low frequency ultrasound detection at a few MHz enables deep-tissue imaging with centimetre penetration and submillimetre resolution, whereas increasing the detection frequency pushes towards micron resolution but compromises the penetration depth. Technical developments in data acquisition and processing speeds will lead to improvements in the temporal resolution, but current state-of-the-art technology can achieve sub-second two- dimensional imaging, and three-dimensional images in seconds to minutes [98–100]. To forman image, ultrasound signals must be acquired from different locations, either by scanninga single detector over the region of interest or by employing a detector array, and then

these signals can be naively backprojected (beamformed) or subjected to more complex reconstruction algorithms to improve image quality [98].
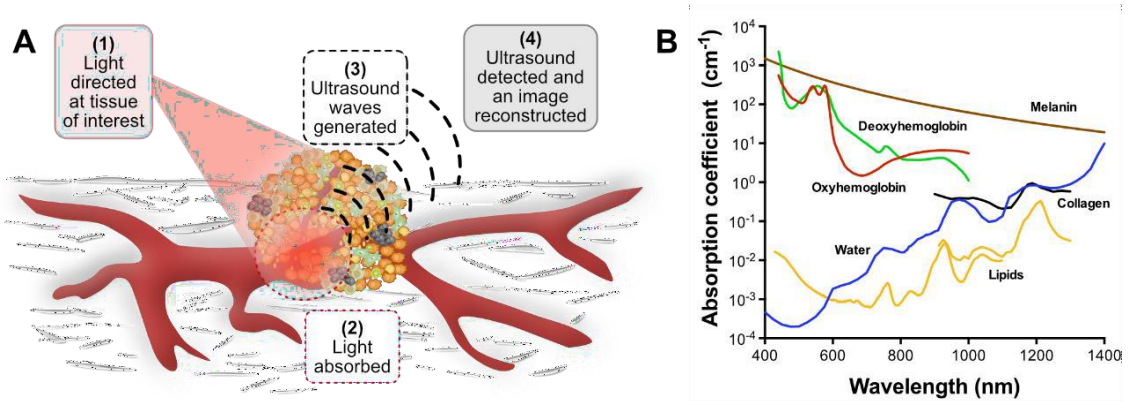
Figure.1.3. Principles of photoacoustic imaging (PAI). (A) During PAI, pulses of light illuminate the tissue (1). When light is absorbed (2), a transient heating gives rise to ultrasound waves (3). The ultrasound waves are then detected and used to reconstruct an image of the optical absorption in tissue (4). (B) Absorption spectra of endogenous molecules that absorb light pulses and can provide insight into the tumour microenvironment (TME). Adapted from Brown et al. (2019) Hb, deoxyhaemoglobin; HbO2, oxyhaemoglobin.

Photoacoustic image contrast arises due to optical absorption, which results in ultrasound generation. When using near-infrared wavelengths of light (620-950 nm) for illumination, several vital endogenous molecules for the TME strongly absorb light (**Figure. 1.3B**). Using only endogenous contrast and acquiring data at multiple wavelengths, PAI can therefore non-invasively visualise vascular morphology, blood oxygenation, fibrosis and lipid content simultaneously with a single technique. Other features, such as cell infiltration, can be imaged by introducing targeted exogenous contrast agents or *in-vitro*-labelled cells, allowing a complete picture of the dynamic relationships in the TME to be revealed with a single technique. Such contrast agents, either injected externally, taken up by cells[101] or expressed in genetically modified cells[102] work by providing additional sources of optical absorption with distinct spectra; the contrast agent is typically bound to, or expressed by, a targeting component in order to highlight specific structural or functional tissue features. PAI with exogenous contrast agents remains subject to the same spatial resolution and penetration depth trade-off as imaging of endogenous molecules; in addition, it is important to select a signalling compound with distinct absorption peaks and strong optical absorption above 600 nm,

thus avoiding signal corruption by endogenous molecules (**Figure. 1.3B**). Compared to existing optical techniques such as DOSI and intravital microscopy, PAI maintains high spatial resolution to a greater imaging depth due to the detection of ultrasound waves, which scatter less than light in tissue. By utilising optical absorption and contrast, PAI maintains high molecular specificity[98–100] compared to standard ultrasound techniques (**Table 1.1**). Additionally, many TME features can be detected simultaneously with PAI due to the multiwavelength data acquisition, without administration of a contrast agent or radioactive agent.

Despite the ability of PAI to image beyond the optical diffusion limit, it has limited penetration depth compared to clinical whole-body modalities such as MRI, PET and CT. Preclinically, PAI is frequently used as a whole-body imaging modality, but this is not possible clinically, where the depth limits of PAI are approached. Introducing PAI through endoscopes can lift this limitation to some extent, but PAI would not compete with whole-body modalities such as PET for disease staging in patients (**Table 1.1**). Nonetheless, in tumours growing within the depth-detection limits of PAI, such as in the breast, PAI could follow initial conventional diagnostic imaging with MRI or ultrasound to provide additional insight into the TME. It is worth noting that combining imaging in a multi-modal approach would allow the limitations of one technique to be compensated for by another, and it is likely that PAI will be used in this way, for example by combining PAI with ultrasound to obtain an anatomical reference for the PAI data[103–105].

Although there are many endogenous molecules in the TME that absorb light in the visible to near-infra red wavelength range to give a photoacoustic signal, the dominant endogenous absorbers are deoxygenated and oxygenated haemoglobin (**Figure 1.3B**). A large volume of preclinical and clinical research to date has focussed on visualisation of tumour vasculature with PAI. The next section of this thesis will discuss how PAI has been used so far to image the vascular microenvironment, across different resolutions and penetration depths along with some of the challenges currently faced, and its potential for preclinical and clinical application in oncology.

1.4. Photoacoustic imaging of the vascular microenvironment

1.4.1. PAI of vasculature and oxygenation

Preclinical PAI in small animal cell-line models allows detailed tumour vascular architecture and morphology to be visualised non-invasively over time at sub-100 μm resolution using just a single wavelength of light, commonly selected as an approximate isobestic point of Hb and HbO_2 (e.g. 532 nm). This method has been used to monitor the developing vasculature in early tumours, showing changes in structure such as increased tortuosity (**Figure 1.4A**)[106,107], diameter and density[108], as well as the recruitment of existing vessels to feed the tumour mass[106,109]. One study demonstrated a decrease in blood vessel density as the tumour developed[110], showing that this parameter may be context-dependent and that PAI can sensitively resolve such differences. Raster-scanning optoacoustic mesoscopy (RSOM) systems aim to bridge the gap between macroscopy and microscopy, achieving ~20 μm resolution at several millimetre depths[111,112]. Preclinically, RSOM has monitored the development of vasculature in several tumour xenograft models[107,109,113], including breast[111] and was sensitive to aggressive vs. slow-growing vascular phenotypes[113]. Overall, these studies show how PAI can provide high-resolution visualisation of the development of tumour vasculature at depths of several milli-or centimetres in pre-clinical cell line xenograft models.

To quantify vascular networks, vessels must be segmented from the background signal. Segmentation of blood vessel networks from images is a developing and expanding field, with many possible approaches taken. These include thresholding images based on signal intensity[107,113–115] and vessel enhancement filtering [116–119], which have been occasionally used in PAI, although the latter is often used only for visual enhancement[117,118]. More advanced methods involving convolutional neural networks and deep learning approaches have been applied in optical microscopy images[120] but are yet to be applied in PAI. It is particularly difficult to segment pathological networks, such as tumour vessels, which do not have an organised linear hierarchy[121]. Additionally, haemoglobin contrast will only show perfused vessels so one must be careful to draw conclusions when the networks will be incomplete[121]. Once segmented, imaging biomarkers such as blood volume could be extracted from these images, but the majority of PAI studies to date did not include quantification or robust statistical analyses. Other

network analyses include algorithms to quantify tortuosity and connectivity[121,122]. These current analyses have yet to be used regularly or be validated and standardised for use in PAI. Often the quantification conducted is manual, basic, poorly described and ad-hoc, with 2D measurements taken even with 3D PAI data107,108,110,113, leading to decreased repeatability and comparability121. With a lack of quantification, a large amount of information is lost from these images that could be exploited in studies of tumour vascular microenvironment biology, particularly as the resolution and quality of images improves.
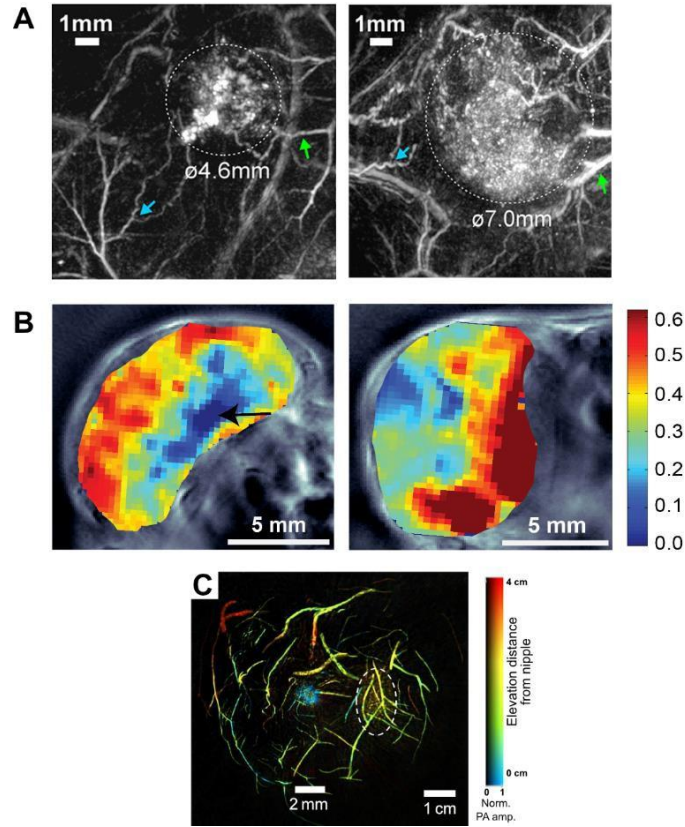
Figure. 1.4. Example photoacoustic images of the vasculature. (A) Shown are x-y maximum intensity projections of a human colorectal tumour (SW1222) and the surrounding vasculature between day 7 and day 8 post-inoculation. Dashed white lines indicate tumour margins. Green arrows show common vascular features between images. Increasing tortuosity of normal blood vessels between day 7 and 8 is indicated by blue arrows. (B) Representative images of PC3 (left) and LNCaP (right) tumours showing the spatial distribution of ΔSO_2 measured using PAI at multiple wavelengths. PC3 tumours displayed lower ΔSO_2 compared to LNCaP tumours and had a core with low ΔSO_2 (black arrow). (C) Depth-encoded PAI images of the breast acquired while the patient, a 49-year-old woman with a stromal fibrosis or fibroadenoma, held her breath. Dashed white lines indicate tumour margin. Figure adapted from Brown et al. (2019).

In addition to high-resolution imaging of vascular networks, utilising the differential absorption spectra of Hb and HbO_2 (**Figure 1.4B**), PAI data can be recorded at multiple wavelengths and subjected to spectral unmixing algorithms to calculate imaging biomarkers related to total haemoglobin concentration ($THb=Hb+HbO_2$) and blood oxygen saturation ($SO_2=HbO_2/THb$). Many studies using multiple wavelength PAI do so using tomographic systems to capture whole tumour volumes preclinically, due to the time limitations associated with raster scanning at multiple wavelengths. Such methodology is termed Multispectral Optoacoustic Tomography (MSOT)[48,123–126]. These

images are captured at a lower resolution but with a higher field-of-view compared to the studies described above.

These functional parameters can provide further insight into the TME. PAI THb tends to be higher in tumours compared to normal tissue[123,124] because of increased angiogenesis and blood vessel density. Vessels also tend to be concentrated around the periphery as the tumour models used, such as melanoma cell-line derived xenografts[127], which tend to be less vascularised in their core. PAI generally measures lower SO_2 values in tumours compared to normal tissue[110,123,124,127,128], consistent with poor perfusion and/or high consumption of O_2 from the blood due to tumour hypoxia. A recent study in breast cancer models demonstrated that SO_2 measurements correlated with vascular maturity, measured by pericyte coverage of vessels *ex vivo*[48]. Altering the gas delivered to the mouse from air to 100% oxygen and measuring the change in SO_2 can distinguish between well-perfused (with high ΔSO_2) and poorly perfused (with low ΔSO_2) regions, as demonstrated in prostate cancer models (**Figure 1.4B**)[125,129]. Importantly, low SO_2 and ΔSO_2 spatially correlate with regions of tissue hypoxia and necrosis[126,130].

PAI biomarkers relating to vascular form and function have also been used to predict and monitor treatment response in preclinical cancer models. Response to anti-angiogenic therapy has been shown across scales, with a decrease in THb and a corresponding increase in HbO_2 in ovarian mouse tumour models[131], and a decrease in tortuosity and vessel diameter in prostate tumour models[132]. These markers indicated vessel normalisation, which was shown *ex vivo* by an increase in pericyte coverage of vessels. RSOM has monitored destruction of the vasculature in response to vascular-targeted therapies, with a corresponding decrease in CD31-labelled vasculature *ex vivo*[107]. High tumour SO_2 was demonstrated to be an early biomarker of radiotherapy response[133] and could predict which tumours would respond to radiotherapy in mouse models of head and neck cancer[134]. These studies demonstrate the potential of PAI in predicting and monitoring tumour response, which could assist with patient stratification and inform therapeutic strategies.

In a clinical context, application of PAI to monitor vascular features of the TME have focussed on breast cancer, where PAI can be combined with existing ultrasound imaging approaches. Handheld PAI probes, similar to existing ultrasound probes, have been used in clinical trials to demonstrate higher THb in tumours compared to normal

tissue[104,135] and an increase in abnormal features such as vessels radiating from the tumour mass[105]. The use of these probes to distinguish breast cancer molecular subtypes is being investigated in clinical trials[136,137], hypothesising that PAI could reduce biopsy errors. However there is some evidence that vascular phenotypes will not be dependent on breast cancer molecular subtypes, which must be carefully considered[138]. Similar to standard X-ray mammography, the Twente photoacoustic mammoscope compresses the breast between a glass window and one flat ultrasound transducer matrix[139]. This system identified malignant lesions that displayed high PA contrast independent of breastdensity, but the penetration depth is limited to 3.2 cm[140]. To increase the penetration depth, and allow the visualisation of vessels in the whole breast, a Dual-Scan mammoscope has been designed, with 2 linear array transducers either side of the compressed breast allowing vessels at 7 cm to be visualised[141142]. Bespoke hemisphericaltransducer arrays, which form a cup that surrounds the whole human breast, have also been developed. These systems have become highly sophisticated in recent years, revealing the detailed vessel networks in the breast[143–146]. Cylindrical systems are similar, compressing the breast into a cylindrical shape, which can achieve 0.5 mm resolution andgain functional parameters with multiple wavelengths[147]. A pivotal study using a cylindrical system recently demonstrated that, when the patient holds their breath duringa very fast 15s scan, thereby decreasing motion artefacts, detailed vascular features can be resolved to a depth of up to 4 cm (**Figure. 1.4C**)[148].

These studies demonstrate how PAI could be utilised to diagnose and stage breast cancers based on vascular features. Despite these engineering advances, little is known about the significance of vascular phenotypes detected with PAI in human breast. Which key features will give insight into patient subtype, stage and/or treatment response and what drives the formation of these features? Many features can be monitored and manipulated easily with preclinical models, however, in the studies described above, all but one used cell-line derived xenografts. These often do not accurately recapitulate the vascular microenvironment seen in patients[9] and more clinically relevant models should be considered as PAI advances towards clinical use.

One of the biggest advantages of PAI, which merits further discussion, is its multi-scale capabilities for visualising vascular features. By scaling the resolution linearly with penetration depth, PAI offers a flexible approach to imaging vascular features *in*

vivo. In preclinical studies, the systems described above were either capable of capturing sub-100 µm resolution of individual blood vessels at superficial depths[106,108,109], or could capture Hb and HbO$_2$ content in whole tumours at cm depths[48,125]. By combining systems with different resolutions and penetration depths, one can capture complementary information on the vascular microenvironment and maximise the information obtained from one tumour arising from the same biological source of contrast.

1.4.2. Current challenges and clinical potential

There is growing evidence that PAI can inform on vascular features in preclinical models and holds promise for clinical translation. Currently, further technical and biological validation of PAI biomarkers is needed to increase uptake of the modality in studies of the vascular microenvironment or clinical evaluation of vascular features[149]. In terms of technical validation, some studies have reported on standardisation of data acquisition and analysis[150–155]. Establishing precise and accurate PAI biomarker measurements will provide confidence, while development of standardised stable test objects, or 'phantoms', that can be applied in a multi-centre setting is vital for routine quality assurance and control[156,157]. Additionally, correcting for spectral distortions of illumination light as it passes through tissue would allow absolute quantification of optically absorbing molecules, but remains a significant challenge to apply *in vivo* and hence is an active area of research in the field[158–160].

In terms of biological validation, the extensive use of cell-line derived cancer models in PAI studies limits the clinical applicability of the work due to the stark genomic and phenotypic differences between clonal cell lines and patient samples[9]. Furtherinsights can be obtained by correlating *in vivo* PAI data with other well-validated *in vivo*imaging methods as well as *ex vivo* analyses such as immunohistochemistry and biochemical assays. In the few studies where this has been achieved preclinically, PAI provided *in vivo* biomarkers of vascular maturity and function that correlate with hypoxia[48,125,130]. Additionally, validation of photoacoustic mammography in patients showed an *in vivo* distribution of haemoglobin signal that had good colocalisation with DCE-MRI and correspondence with vascular patterns measured *ex vivo*[161].

Most clinical studies discussed here are observational and/or conducted in a limited number of patients[104,143–145,148,161]. Their purpose was to investigate how PAI biomarkers

could be used in disease diagnosis or assessment of disease severity, for example in differentiation between benign and malignant disease. The best-developed application in this regard, including multi-centre studies, is in breast cancer. PAI could be easily combined with ultrasound imaging, which is conventionally used in breast cancer patient management. PAI has been demonstrated to accurately downgrade benign masses[105,162] with higher specificity than ultrasound imaging[105], which could reduce unnecessary biopsies and follow-up appointments, reducing patient distress and healthcare costs. PAI is low cost, making it a favourable candidate for screening programmes, and it performs independent of breast density, unlike X-ray mammography[163]. As yet, PAI has not been used in clinical decision-making and the results of these studies did not affect the diagnostic pathways of the patients involved; radiologists interpreting the photoacoustic images were blinded to the rest of the diagnostic work-up. Most of the clinical studies present qualitative results, and more quantitative outputs with more complex and clinically relevant study designs need to be explored[138]. Other superficial malignancies could also be monitored with PAI. For example, high-resolution PAI is capable of visualising microvasculature in human skin and could be applied to monitor the pathological neovascularisation of melanoma[109,164]. Photoacoustic endoscopy is expanding, bypassing limitations in the penetration depth, so could be used to monitor angiogenesis in gastrointestinal tract cancers, cervical and ovarian cancer with further technological advances[165–168]. Large-scale clinical trials are also being planned for inflammatory conditions[96].

To conclude, PAI: can visualise the vascular microenvironment across multiple length and time scales; has high spatiotemporal resolution; is low cost; uses non-ionising radiation; and is non-invasive, with potentially easy integration into existing ultrasound systems. PAI is an attractive option for monitoring the dynamic vascular microenvironment not only in a preclinical setting but also throughout a patient's treatment regime, from diagnosis and staging to monitoring treatment response.

1.5. Patient-derived xenograft models of breast cancer

1.5.1. Current preclinical cancer models

Many of the preclinical studies in PAI described above, use cell-line derived xenografts (CDXs), where cancer cell lines are implanted into mice, subcutaneously or orthotopically, to generate a tumour. These models are useful for studying mechanistic pathways of cancer development and progression[9,169] and in addition are relatively simple to use, with time to engraftment being predictable and consistent in an established model. CDXs are used widely in cancer research and for PAI to study many different aspects of disease such as angiogenesis and vascular dynamics and response to therapy [48,106,107,110,125]. However, because cell lines are derived from a single clone these models do not represent the heterogeneity seen in patient samples and therefore cannot accurately represent tumour evolution or therapy response[9,169].

PAI is currently being evaluated clinically in breast cancer patient management[163]. To facilitate clinical translation, it is vital that the preclinical models used to validate systems and investigate biomarkers of tumour progression and therapy response are representative of patients. Breast cancer in particular is a very heterogeneous disease; there are at least 10 subtypes of breast cancer, or integrative clusters, with each cluster displaying specific genetic characteristics that allow tumours from different patients to be grouped[170,171]. Breast cancer tumours are highly heterogeneous, even within these subtypes, and accurately modelling this heterogeneity in preclinical models is a challenge. Ultimately, this forms a barrier towards clinical translation of PAI to monitor breast cancer, as the diversity of vascular phenotypes that can be studied in the preclinical setting is relatively limited. This thesis aims to evaluate the application of PAI in breast cancer patient-derived xenograft models, which may present a more clinically relevant model[10].

1.5.2. Introducing PDX models

The use of patient-derived xenograft (PDX) models has expanded in recent years[172], as they are thought to capture the heterogeneity seen in patients[10,172]. PDXs are generated by taking a fragment of tumour from a patient and passaging the tumour in immunodeficient mice[173]. The best implantation site for breast PDXs is heavily debated,

with subcutaneous engraftment often chosen[10]. Although this removes the proper anatomical niche seen in orthotopic fat pad models[174] and therefore decreases metastatic potential, these models still capture the tumour architecture seen in patients and the clonal diversity[172]. They can also be used in imaging studies, being placed at an easily accessible, superficial, location. PDX models have been shown to preserve morphology, biomarker expression, genomics, transcriptomics and metastatic potential across serial passages[10,172] making them good models to answer clinically relevant questions relating to new treatments and biomarkers[175–177]. Breast cancer PDXs are being heavily utilised to study how the heterogeneity of tumours affects therapy response[178–182], mechanisms of resistance[183] to therapy and how these can be overcome[184,185].

1.5.3. Utilising PDXs as vascular models

The most well-described and investigated use for breast PDXs is in drug studies. The therapies investigated are most commonly targeted at cancer-driver genes and biomarkers reported to monitor mutations in these genes/ copy number alterations/epigenetic changes[180,183]. There has been little focus on how the TME in PDXs affects their evolution and subsequent therapy response. This is particularly important as the stroma in PDXs will be derived from the mouse host[10] and there has been little to no investigation into how the PDX stroma influences the utility of this model and whether the TME phenotype is representative of the patient. When many breast PDXs are implanted subcutaneously, lacking a traditional environmental niche for the tumour to grow, this could have marked implications on the clonal dynamics, phenotype and therapy response of the PDX[186].

Some studies have begun to investigate the TME of PDXs with imaging techniques. Hyperpolarised 13C MRI imaging has been shown to monitor metabolic changes in response to therapy[187–189], while *ex vivo* mass spectrometry imaging can spatially map fatty acid metabolites in tumours[190]. Insight into hypoxia dynamics following irradiation has been studied with PET and DCE-MRI in pancreatic cancer PDXs[191] and imaging biomarkers of response to anti-angiogenic drugs have been monitored in cervical and colorectal PDXs, with *ex vivo* histology validation[192,193]. In head and neck cancer PDXs, varied vascular phenotypes have been reported and those with higher vascular density were shown to be more sensitive to vascular targeting

agents[194], giving insight into the vascular microenvironment of these PDXs and how it can be targeted. These models have been imaged with PAI, showing changes in blood oxygen saturation that were detectable 24hr after radiotherapy and could predict the change in tumour volume seen 2 weeks later[133]. Although not studied in detail, investigations into how well PDXs recapitulate the TME have shown mixed results so far, with some brain tumour PDXs showing similar radiological and histological features to the patients[195] and others that showed decreased enhancement upon DCE-MRI, and corresponding decrease in expression of angiogenesis-related genes compared to the patient[196]. To our knowledge, similar studies in breast PDXs have not yet been completed, and there is no comprehensive knowledge of how the vascular microenvironment in breast PDXs evolves. Given the dynamic nature of the vascular microenvironment and how it shapes tumour development and therapy response, characterisation of the vascular microenvironment in breast PDXs is needed, to gain further insight into tumour-host interactions in PDXs and assess the utility of the model.

1.5.4. Limitations

Although there is much excitement surrounding PDXs, it must be remembered that there are some limitations to the model. Limitations include high cost[9,186] and a lack of robust standards surrounding the generation and quality assurance of PDX models[197]. In addition, engraftment rates for non-aggressive subtypes (e.g. ER+ breast PDXs) are often low but have been improved with better protocols and decreased time from surgery to mouse[173]. Clonal dynamics can shift in PDXs, and the effect of this is largely unknown so they must be carefully monitored[10,186,198]. The most documented limitation is the need to passage the PDXs in immunodeficient mice, in order for tumours to become established and not be rejected[9,173]. This limits studies of the immune infiltrate in the TME and of the regulation of angiogenesis by immune cells[5]. Humanising the immune system of immunocompromised mice is underway in many laboratories and has the potential to overcome this limitation and advance the use of PDXs[172].

1.6. Project Aims

PAI represents an exciting tool to monitor the chaotic, dense and immature vascular networks in tumours. Engineering advances are enabling breast PAI to enter the clinic, with increasing depth of imaging, however, with a reliance thus far on the use of CDXs for insight into tumour vascular phenotypes captured with PAI, several questions remain:

1) Which vascular features are important to monitor when examining breast tumours? Which provide the greatest insight into the underlying tumour biology, tumour grade and predicting response to the therapy?

2) Is PAI sensitive to different vascular phenotypes in different patients? Mann et al. have already commented that PAI biomarkers of breast molecular subtypes overlap significantly and CDXs used previously in PAI will likely present extreme examples. For the majority of patients, will PAI be useful in stratifying patients beyond the classification of benign vs. malignant disease?

3) Can using PAI on multiple scales provide complementary information about the same tissue? Despite its scalability, the use of multiple PAI systems, with different resolutions and penetration depths, in one study has not been reported.

This thesis proposes the use of PDXs in PAI, to begin to answer the aforementioned questions in clinically-relevant models of breast cancer. However, to answer these questions, PAI along with *ex vivo* methods such as IHC must be used to answer questions surrounding the utility of the model itself:

1) Do PDXs present with different vascular phenotypes and if so, what drives these differences? Does it depend on subtype or other genetic markers?

2) Do PDXs recapitulate the vascular microenvironment seen in patients?

3) Are the vascular phenotypes seen in PDXs robust and repeatable?

In order to answer these questions surrounding the use of PAI in clinical breast cancer management and the utility of PDXs as vascular models of the disease, the following project aims have been defined:

Aim 1: To characterise the vascular phenotypes in breast cancer PDXs using a combination of high-resolution and tomographic PAI and IHC.

Aim 2: To determine whether PAI is sensitive to different vascular phenotypes in PDXs.

Aim 3: To determine whether PDXs are robust and reliable vascular models that represent the patients from which they are derived..

Aim 4: To question the origin of vascular phenotypes in PDXs and gain insight on which features may be the most significant to monitor in clinic.

1.7. Summary

Cancer cells live within their environmental niche known as the TME, where dynamic interactions between cancer and stromal cells as well as chemical and physical signals, shape tumour biology and evolution. The vasculature is a key component of the TME and is often dysfunctional and immature leading to areas of chronic and dynamic hypoxia which further spatially fine-tunes the TME. PAI can visualise vascular features in the TME at multiple scales, building a complete picture of the vascular phenotype in a single tumour, which can be monitored longitudinally over time. It's high spatiotemporal resolution, low cost, use of nonionizing radiation and non-invasive properties with potentially easy integration into existing ultrasound systems make PAI an attractive option for monitoring dynamic vascular features not only in a preclinical setting but also throughout a patient's treatment regime, from diagnosis and staging to monitoring treatment response. In order to translate PAI into the clinic, the field must begin to use more clinically relevant preclinical models and assess their ability to recapitulate the phenotypes seen in patients.

Breast cancer PDXs offer an attractive model for PAI. Implanted subcutaneously on the flank, they sit within the limits of detection for most PAI imaging systems. They have been shown to maintain the genetic properties of the patients from which they were derived, across several passages. However, whether they are good vascular models remains unknown. Here, a careful evaluation of whether vascular phenotypes differ between PDX models and how they evolve over time is conducted using PAI with corresponding *ex vivo* IHC, used to biologically validate the phenotypes seen *in vivo*. The work assesses how vascular phenotypes change across passages and how similar they are to the originating patient. Finally, the question of how these phenotypes form begins to be answered by correlating these phenotypes with the underlying gene expression of the

cancer cells, assuming that the cancer cells shape the mouse host vasculature in their TME.

Chapter 2 presents IHC analyses, investigating the expression of various vascular markers in *ex vivo* tissue from PDXs at early and late-stages of development. Intra-tumour, inter-model and inter-passage heterogeneity are assessed and a preliminary comparison to patient tumours is presented, to evaluate whether PDXs form distinct vascular phenotypes and how variable these phenotypes are across individual tumours and across passages as well as starting to assess the feasibility of these models as representativevascular models of patient tumours. Chapter 3 presents the optimisation of image acquisition, using a novel mesoscopic PAI system and the development and validation ofa new image analysis pipeline to quantify blood volume and topology metrics from the vessel networks captured with mesoscopic PAI. Next, Chapter 4 presents tomographic PAI data, taken with an established system, evaluating blood content and oxygenation inwhole tumours and mesoscopic PAI data is evaluated longitudinally across the PDXs, tomonitor the evolution of the blood vessel networks. Chapter 5 begins to question the origin of the vascular phenotypes captured thus far by examining the hypoxic gene expression of the cancer cells, showing that the cancer cells instruct the mouse host vasculature to form distinct vascular phenotypes. Finally, the oxygen consumption and metabolic requirements of the PDXs are briefly considered, focussing on their differential latency periods.

2 IMMUNOHISTOCHEMISTRY CHARACTERISATION OF VASCULAR PHENOTYPES

I selected 4 breast-patient derived xenografts for in vivo experiments from the biobank generated by the Caldas laboratory and excised and preserved tumour tissue. The pre-clinical genome editing core at the CRUK CI implanted the PDX tissue with my assistance. I analysed all QC IHC samples and compared PDX tissue to patient tissue under the guidance of breast pathologist Dr Elena Provanzano. I manually segmented tumour tissue on IHC sections and conducted all statistical analyses described herein and interpreted all results. The histopathology core at CRUK CI ran all IHC experiments and created algorithms for analysis under my supervision. I would like to thank Alejandra Bruna and Wendy Greenwood from the Caldas laboratory who helped logistically to set-up my own PDX sub-biobank from their own.

2.1. Introduction

2.1.1. Monitoring the vascular microenvironment with IHC

As introduced in detail in Chapter 1, cancer cells live within their environmental niche known as the tumour microenvironment (TME), where dynamic interactions between cancer and stromal cells, as well as chemical and physical signals, shape tumour biology and evolution[1,2]. The vasculature is a key component of the TME and is often dysfunctional and immature leading to areas of chronic and dynamic hypoxia that further spatially fine-tune the TME[3,26,27]. Hypoxic tumours encourage the growth of new blood vessels from existing vasculature, termed angiogenesis, and high rates of angiogenesis result in immature and chaotic vessels forming, creating a feed-forward loop of poor perfusion and oxygenation[2].

Cellular, chemical and physical components of the TME can be labelled by their molecular expression using immunohistochemistry (IHC), a low-cost and easy-to-use method for staining *ex vivo* tissue sections that is regularly used in clinic to characterise biomarkers for diagnosis, prognosis and to guide treatment options[70]. Importantly, IHC provides spatial information unlike other antibody-based labelling techniques that involve dissociation of the tumour, such as western blot, meaning one can visualise which cell types or components of the TME colocalise. For example, when considering the vasculature, colocalisation of vessels and pericytes/smooth muscle indicates vessel maturity and good vessel function, whereas vessels with a lack-of or disconnected pericytes are known to be immature and poorly perfuse the tumour mass[48,199].

In breast clinics, IHC is often used to help subtype patients by providing molecular information such as how many tumour cells express the estrogen receptor (ER) and the proliferation marker Ki67, and to what degree of intensity[70]. Although vascular IHC markers such as CD31 microvessel density, CAIX and VEGF have been demonstrated to be highly prognostic in breast cancer in numerous studies[3,35,36,200], vascular markers are not routinely used in clinic. Equally, before this thesis, little to no investigation of vascular marker expression in breast PDXs had been conducted.

Here, a thorough characterisation of the vascular microenvironment in 4 breast

cancer PDXs was undertaken at the cellular level using IHC, which interrogated changes as the PDXs grow, and also examined their behaviour across passages and in relation to the patient of origin for the PDX. To address Aim 1 of the project, the vascular phenotypes of 4 breast PDX models representing two breast cancer subtypes (basal: STG139 and STG321 and luminal B: AB580 and STG143) were characterised using a panel of IHC stains. Once the tumours had reached ~1 cm in diameter, following *in vivo* imaging that will be reported in subsequent chapters, they were excised for *ex vivo* IHC. The chosen panel of markers relevant to vascular phenotype selected were: CAIX (to mark hypoxic regions), VEGF-A (a potent angiogenic factor), CD31 (to mark endothelial cells and measure vessel area), CD31/ASMA colocalisation (to determine how many CD31^{+} vessels are lined with ASMA^{+} pericytes/smooth muscle cells), and H & E (to measure necrosis and haemorrhage). The variation of IHC metrics across the same tumour in all 4 PDXs was interrogated by comparing 2 IHC sections per tumour, one taken from the centre and the other from an outer portion of the tumour. The variation across tumour passages in STG139 and AB580 was also investigated using 3 passages per model to meet Aim 3 of the project and assess PDX robustness and reliability. Contributing to this, an initial qualitative evaluation of how PDX vascular IHC markers compare to patient tissue is conducted. Finally, an investigation into how marker expression evolves with tumour growth is conducted, to understand whether expression of certain markers is inherent or develops over time and begins to contribute to Aim 4 of the thesis, regarding the origins of PDX vasculature.

2.2. Methods

2.2.1. PDX model establishment and passaging

4 breast PDX models (basal: STG139 and STG321 and luminal B: AB580 and STG143) were chosen for evaluation of their vascular phenotypes. **Table 2.1** outlines the clinical information of the original patient tissue obtained from Bruna et al.[10] These models were chosen for several reasons. First, they represented primary ductal breast tumours of two common subtypes (basal and luminal B). Second, tumour tissue was available in an early passage (P) from the originating patient (<P5) and the tumours engrafted successfully *in vivo*. It is worth noting that two additional models (one for each subtype) were chosen for testing but did not engraft successfully *in vivo* after 12 months, which was the maximum engraftment waiting period as our animal project license allowed the mice to be aged for a maximum of 14 months as the mice implanted begin to suffer age-related pathologies at this age[201]. Finally, initial IHC assessment using FFPE tissue from one PDX tumour per model, (kindly donated by the Caldas lab and processed as described in section 2.2.2.), revealed variation in ASMA vessel coverage (STG139: 15.62%, STG321: 32.53%, AB580: 35.87%, STG143: 21.39%) and CAIX expression (STG139: 84.18%, STG321: 11.35%, AB580: 17.74%, STG143: 0.65%), suggesting that the models may show diverse vascular phenotypes *in vivo*, which could be further evaluated and compared.

Table 2.1. Clinical information of the originating patient tissue that formed the PDXs described in this thesis

Model	Patient pathology diagnosis	Patient PAM50	Integrative Cluster [171]	Patient ER status	Patient PR status	Patient HER2 status	Patient Ki67 status
STG139	Ductal (NST)	Basal	10	Neg	Neg	Neg	High
STG321	Ductal (NST)	Basal	10	Neg	Not known	Neg	High
AB580	Ductal (NST)	Luminal B	8	Pos	Not known	Neg	High
STG143	Ductal (NST)	Luminal B	8	Pos	Neg	Neg	High

All animal procedures were conducted in accordance with project (Bohndiek PE12C2B96) and personal licenses (Emma Brown- I544913B4), issued under the United Kingdom Animals (Scientific Procedures) Act, 1986 and approved locally under compliance forms CFSB1361, CFSB1567, CFSB1745 and CFSB1979. For all models and studies described in this thesis, cryopreserved breast patient-derived xenograft tumour fragments (~2 mm^3) in freezing media (foetal bovine serum, heat-activated ThermoFisherScientific 10500064 +10% dimethyl sulfoxide Sigma D2650) were defrosted at 37°C, washed with Dulbecco's modified eagle's medium (Gibco 41966) and mixed with matrigel (Corning 354262) before surgical implantation. Tumours were implanted subcutaneously into the flank of 6-9 week-old NOD SCID gamma (NSG) mice (Jax Stock #005557) as per standard protocols[10].

Tumour growth was monitored with callipers measuring the diameter along the short and long axes and a mean diameter calculated. Mice were euthanised once the tumour mean diameter reached ~1 cm, which equated to a volume ~0.4 cm^3, unless the tumour was being preserved at an earlier time point for intermediate analysis, in which case mice were euthanised once the tumour mean diameter reached ~0.5 cm, which equated to a volume ~0.1 cm^3. The tumour size limits were determined by the resolution of the photoacoustic imaging systems and within the ethical limits defined by the project

license. Mice were killed by cardiac puncture to collect blood and plasma samples. The right half of each tumour sphere was preserved in formalin (CellPath BAF-6000-08A, 10% formalin for 24hr) and the left half cut into fragments to provide tissue for cryopreservation in liquid nitrogen or freezing media (**Figure 2.1A**). For STG139 P3 and AB580 P2 only 2 mm^3 fragments were taken instead of the semi-sphere in subsequent passages, to provide more tissue for passaging and growing my biobank. To continue to expand and propagate PDX samples for evaluation, passaging was necessary. This was conducted by implanting one fragment from one mouse into another (**Figure 2.1B**). The number of passages, the tumours per passage and the relationship between different tumours is listed in **Table 2.2**.
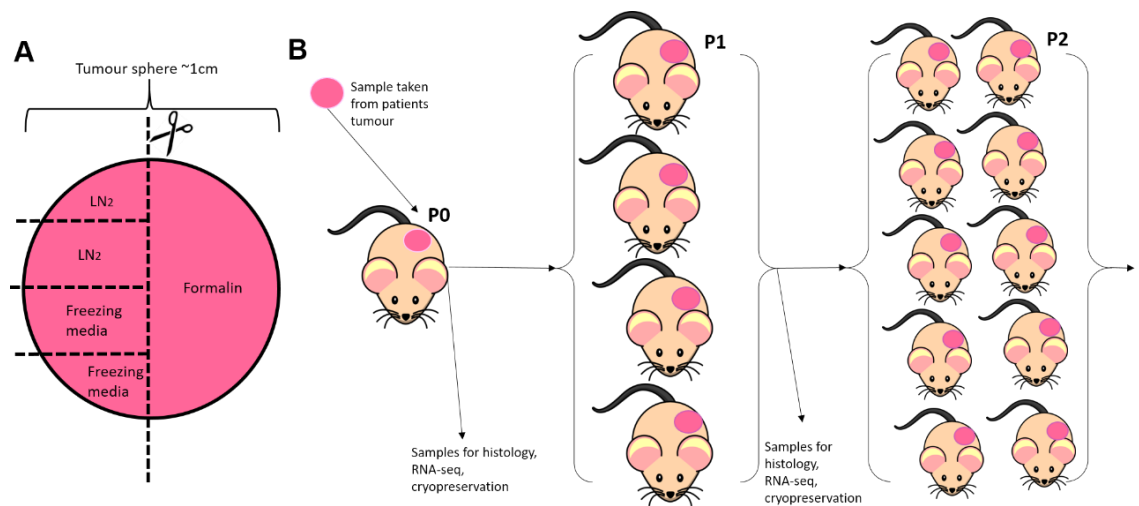
Figure 2.1. PDX tumour preservation and passaging. A) PDX tumours (pink sphere) normally present as spheres that are excised at ~1cm diameter, and cut (dashed line) to preserve one half in formalin, and further fragments are cryopreserved in liquid nitrogen or freezing media. B) PDXs described in this thesis were established by taking a fragment of a patient's tumour and implanting it into an immunocompromised mouse (P0) by the Caldas lab[10]. Subsequent passages were generated by defrosting fragments preserved in freezing media and re-implanting these fragments into subsequent batches of mice (Pn, where n is the passage number, passages are numbered consecutively), to exponentially increase the number of samples available.

Table 2.2. PDX tumour sample names, models, passages and relationship between different tumours.
Tumours originating from Caldas laboratory highlighted in yellow.

Tumour Name	PDX model	Passage Number	Tumour originated from	Tumour volume at excision (cm³)
PEN2	STG139	3	STG139-X2_23785	0.53
PEN3	STG139	3	STG139-X2_23785	0.55
PEN4	STG139	3	STG139-X2_23785	0.7
PEN5	STG139	3	STG139-X2_23785	0.71
PEN6	STG139	3	STG139-X2_23785	0.6
PEN7	STG139	4	PEN6	0.37
PEN8	STG139	4	PEN6	0.37
PEN14	STG139	4	PEN6	0.50
PEN15	STG139	4	PEN6	0.45
PEN18	STG139	4	PEN6	0.75
PEN21	STG139	4	PEN4	0.73

PEN22	STG139	4	PEN4	0.34
PEN23	STG139	4	PEN4	0.41
PEN25	STG139	4	PEN4	0.43
PEN26	STG139	4	PEN4	0.43
PEN28	STG139	4	PEN4	0.43
PEN29	STG139	4	PEN4	0.75
PEN30	STG139	4	PEN4	0.36
PEN31	STG139	4 (repeat)	PEN3	0.41
PEN34	STG139	4 (repeat)	PEN3	0.52
PEN38	STG139	4 (repeat)	PEN5	0.47
PEN40	STG139	4 (repeat)	PEN5	0.45
PEN43	STG139	4 (repeat)	PEN6	0.40
PEN46	STG139	5	PEN18	0.48

PEN47	STG139	5	PEN18	0.51
PEN48	STG139	5	PEN18	0.42
PEN49	STG139	5	PEN18	0.51
PEN56	STG139	5	PEN26	0.38
PEN57	STG139	5	PEN26	0.38
PEN58	STG139	5	PEN26	0.54
PEN59	STG139	5	PEN26	0.43
PEN60	STG139	5	PEN26	0.46
PEN39	STG139	4 (repeat)	PEN5	0.14 (for intermediate analysis)
PEN37	STG139	4 (repeat)	PEN5	0.21(for intermediate analysis)
PEN36	STG139	4 (repeat)	PEN5	0.15 (for intermediate analysis)
PEN32	STG139	4 (repeat)	PEN3	0.19 (for intermediate analysis)

PEN35	STG139	4 (repeat)	PEN3	0.11 (for intermediate analysis)
PEN42	STG139	4 (repeat)	PEN6	0.14 (for intermediate analysis)
PDP1	AB580	2	AB580-X1_23191	0.32
PDP2	AB580	2	AB580-X1_23191	0.75
PDP3	AB580	2	AB580-X1_23191	0.57
PDP7	AB580	3	PDP3	0.37
PDP8	AB580	3	PDP3	0.33
PDP9	AB580	3	PDP3	0.36
PDP11	AB580	3	PDP3	0.32
PDP14	AB580	3	PDP3	0.31
PDP16	AB580	3	PDP3	0.33
PDP17	AB580	3	PDP3	0.31

PDP18	AB580	3	PDP3	0.29

PDP25	AB580	3 (repeat)	PDP2	0.46
PDP27	AB580	3(repeat)	PDP3	0.58
PDP32	AB580	4	PDP9	0.48
PDP35	AB580	4	PDP9	0.45
PDP24	AB580	3 (repeat)	PDP2	0.16 (for intermediate analysis)
PDP28	AB580	3 (repeat)	PDP3	0.11 (for intermediate analysis)
PDP29	AB580	3 (repeat)	PDP3	0.2 (for intermediate analysis)
STP3	STG143	3	STG143-X2 AN17CUK036905	0.31
STP5	STG143	3	STG143-X2 AN17CUK036905	0.39
STP7	STG143	3	STG143-X2 AN17CUK036905	0.34

STP8	STG143	3	<mark>STG143-X2 AN17CUK036905</mark>	0.38
STP9	STG143	3	<mark>STG143-X2 AN17CUK036905</mark>	0.32
STP13	STG143	4	STP3	0.38
STP15	STG143	4	STP3	0.38
STP16	STG143	4	STP3	0.50
STP18	STG143	4	STP7	0.43
STN1	STG321	2	<mark>STG321-X1 13914</mark>	0.28
STN2	STG321	2	<mark>STG321-X1 13914</mark>	0.37
STN3	STG321	2	<mark>STG321-X1 13914</mark>	0.39
STN4	STG321	2	<mark>STG321-X1 13914</mark>	0.38
STN5	STG321	2	<mark>STG321-X1 13914</mark>	0.47
STN6	STG321	2	<mark>STG321-X1 13914</mark>	0.43

STN8	STG321	2	STG321-X1 13914	0.45
STN11	STG321	3	STN4	0.44
STN12	STG321	3	STN4	0.37
STN13	STG321	3	STN4	0.59
STN14	STG321	3	STN4	0.36
STN15	STG321	3	STN5	0.42
STN17	STG321	3	STN5	0.46
STN18	STG321	3	STN5	0.38
STN19	STG321	3	STN5	0.45
STN20	STG321	3	STN5	0.49

2.2.2. Histopathological analysis

All IHC and histology stains were conducted by the CRUK CI Histopathology core facility unless otherwise stated. Formalin-fixed paraffin embedded (FFPE) PDX tumour tissues were cut into 3-4 μm sections. For each marker, two tumour sections were cut if

possible, one from the core of the tumour and the second from an outer portion, approximately 3 mm from the core, to assess intra-tumoural heterogeneity of the markers. Following deparaffinising and rehydration, IHC was performed using a BOND automated stainer with a bond polymer refine detection kit (Leica Biosystems) and 3,3'-diaminobenzadine as a substrate. The markers chosen, working dilutions, antigen retrieval methods and reasons to support the use of this marker are detailed in **Table 2.3**.Adjacent serial sections were used for CD31 and ASMA staining. Haematoxylin and Eosin (H&E) staining was performed using an automated system (ST5020 Leica,Biosystems).

Additionally the PDX tumour blocks underwent a quality control (QC) IHC analysis to ensure that the resultant PDX had not changed significantly in phenotype or undergone neoplastic transformation of human or murine lymphocytes in the immunocompromised mice, which has been reported anecdotally (Caldas laboratory) and in several publications[186,197]. Information and reasoning on the choice of markers can be found in **Table 2.4**. Dr Elena Provanzano provided training and guidance such that I was then able to personally assess the QC markers.

All PDXs described in this thesis underwent the QC IHC analysis and passed (for thresholds see **Table 2.4**), maintaining their original ER and Ki67 status and contained low numbers of lymphocytes. Nearly all PDXs were epithelial, confirmed by breast pathologist Dr Elena Provanzano using H&E, pan-cytokeratin and E-cadherin stained sections. STG139 occasionally presented with a high percentage of mesenchymal tumour cells (above 50%), which were identified as cells with a spindle-like appearance by Dr Elena Provanzano. This has previously been reported anecdotally (Caldas laboratory) and expected in this model. Example QC IHC is shown in **Figure 2.2.**

Table 2.3. Antibodies used for histopathological assessment of PDX vascular phenotypes

Marker	Supplier & Catalogue number	Working dilution & Antibody retrieval method	Reasons to support use of this marker	References
Anti-mouse CD31	Cell signalling 77699	1:100, Tris-EDTA HIER 20min	Stable and highly expressed endothelial cell marker. Microvessel density correlates with prognosis, tumour size, grade and VEGF expression in breast cancer.	202 203,204,205
Anti-mouse ASMA	Abcam ab5694	1:500, Tris-EDTA HIER* 10min	CD31/ASMA co-localisation considered marker of vessel maturity. ASMA widely used marker of smooth muscle cells and pericytes in tumours. Most abundant protein in smooth muscle cells and required for full differentiation. Abnormal expression in tumoural pericytes widely reported.	48,199,126,206
Anti-human CAIX	Bioscience Slovakia AB1001	1:1000, Sodium Citrate HIER 20min	A stable marker of chronic hypoxia. Often correlates with exogenous pimonidazole staining. Downstream of HIF, with longer half-life of 2-3 days. Expression predictive and prognostic in breast cancer.	3,207
Anti-human VEGF	Thermo Scientific RB-9031	1:250, Sodium Citrate HIER 20min	Most prominent pro-angiogenic factor. Expression prognostic in many solid tumours.	2,3,18
Haematoxylin and Eosin (H&E)	Leica Microsystems Eosin 1%-3801590 Haem.-3801560E		General tissue architecture. Can easily visualise cell shape, stromal content, necrosis and haemorrhage.	

Table 2.4. Antibodies used for quality control IHC assessment of PDXs

Marker	Supplier & Catalogue number	Working dilution & Antibody retrieval method	Reasons to support use	Threshold to pass QC
Anti-human ER	Novocastra NCL-ER-6F11/2	1.071 µg/ml, Sodium Citrate, HIER 30 min	Surrogate for intrinsic subtype (PAM50) analysis. Check if PDX has maintained ER status in patient.	>1% tumour cells staining =positive <1% tumour cells staining =negative. Must remain same as patient. [10]
Anti-human Ki67	Dako M7240	1:400 (if xenograft) 1:200 (if primary human) Tris EDTA, HIER 30 min	Marker of proliferation. Surrogate for intrinsic subtype (PAM50) analysis. Check if PDX has high or low proliferation.	Must remain same as patient- high (>20%) or low (<20%) positivity. Both lumB and basal models have high proliferation. [10]
Anti-mouse Ki67	Bethyl Laboratories IHC-00375	1:1000, Sodium Citrate, HIER 20 min	Marker of proliferation. Positive tumour cells would indicate spontaneous murine transformation	Only murine stromal cells can be positive.
Anti-human CD45	Dako M0701	1.5 µg/ml, Tris EDTA, HIER 20 min	Pan-lymphocyte marker. Positivity in malignant cells would indicate human lymphoid origin.	Must be negative
Anti-mouse CD45	Abcam ab25386	5 µg/ml, Sodium Citrate, HIER 20 min	Pan-lymphocyte marker. Positivity in malignant cells would indicate murine lymphoid origin.	Murine lymphocytes in stroma will be positive.

Anti-mouse CD45 (B220 isoform)	R&D Systems MAB1217	0.67 µg/ml, Sodium Citrate, HIER 10 min	Identifies a select subset of B-cells. Positivity would indicate murine B-cell lymphoma formation	Murine B-lymphocytes in stroma will be positive.
Anti-human CD3	Thermo Scientific RM-9107-S0	1:300, Sodium Citrate, HIER 20 min	Identifies human T cells. Positivity would indicate human T-cell lymphoma formation.	Must be negative
Anti-human CD20	Novocastra NCL-L-CD20-L26	0.95 µg/ml, Tris EDTA, HIER 20 min	Identifies human B cells. Positivity would indicate human B-cell lymphoma formation.	Must be negative
Anti-human pan-cytokeratin	Dako M3515	1:200, Sodium Citrate, HIER 20 min	Used to stain normal and neoplastic cells of epithelial origin.	Must be some positivity, even if focal.
Anti-human E-cadherin	Dako M3612	1:25, Sodium Citrate HIER 30 min	Used to stain normal and neoplastic cells of epithelial origin. Lobular carcinomas will be E-cadherin negative.	Must be some positivity, even if focal.
Haematoxylin and Eosin (H&E)	Leica Microsystems Eosin 1%- 3801590 Haem.- 3801560E	N/A	General tissue architecture. Can easily visualise cell shape, stromal content, necrosis and haemorrhage.	Cell morphology should be similar to original patients/previous passages
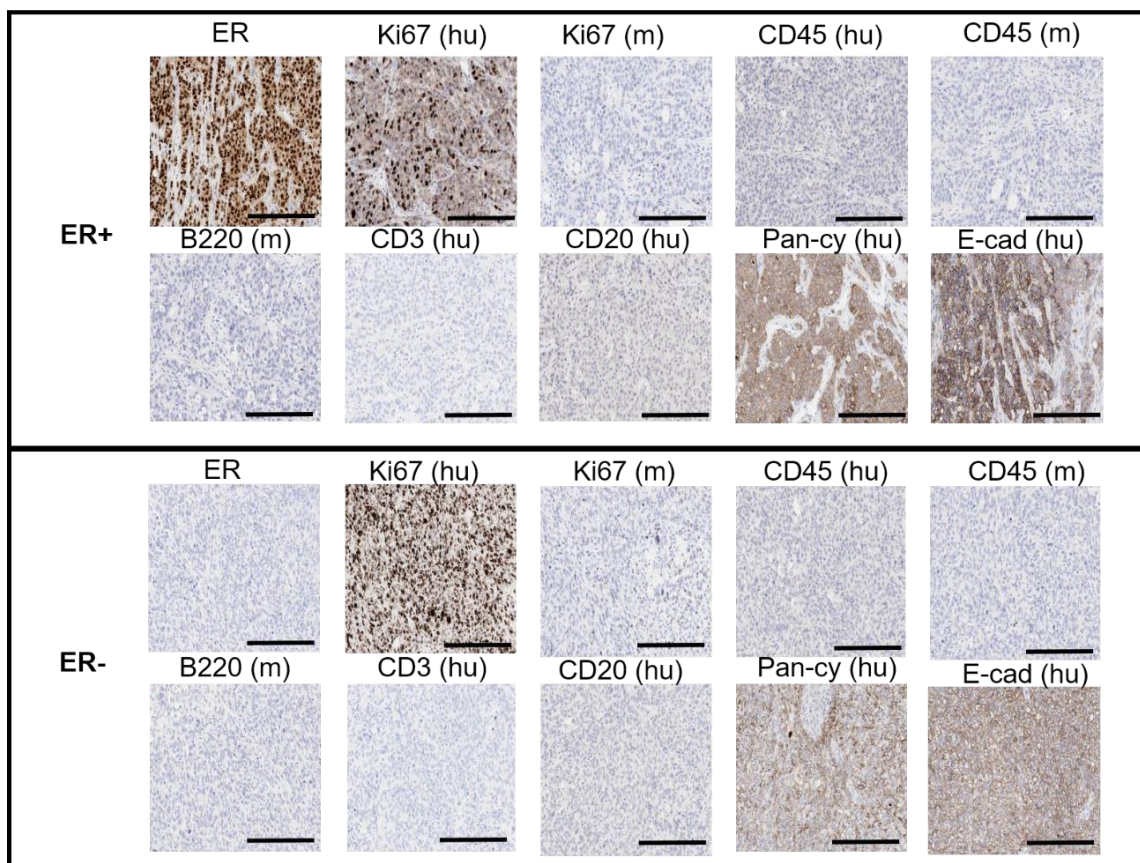
Figure 2.2 Example results of quality-control IHC panel in the PDXs. Scale bar = 200 µm. Top panel example images of an ER+ PDX and bottom panel example images of an ER- PDX. The following IHC staining's are shown (from left to right): anti-human estrogen receptor (ER), anti-human Ki67 (proliferation marker), anti-mouse Ki67 (proliferation marker), anti-human CD45 (lymphocyte marker), anti-mouse CD45 (lymphocyte marker), anti-mouse CD45 (B220) (B-cell subset marker), anti-human CD3 (T-lymphocyte marker), anti-human CD20 (B-lymphocyte marker), anti-human pan-cytokeratin, anti-human E-cadherin.

2.2.3. Patient samples and Tissue Microarray

A tissue microarray (TMA) was prepared by the CRUK CI histopathology core using duplicate 0.6 mm cores extracted from FFPE blocks containing material from patient tumours STG321, AB580 and STG143[10]. The FFPE STG139 patient tumour blockwas not included in the TMA. 3-4 µm sections were processed as described above in section 2.2.1 using Leica's Polymer Refine Kit on their automated BOND platform. For the TMA cores, IHC was performed for the following antibodies: CD31 (anti-human Dako M0823), α-smooth muscle actin (ASMA) (anti-human Sigma A2547) at 1:100 and 1:1000 respectively. Adjacent serial sections were used for CD31 and ASMA staining. For all patient samples, H&E staining was performed using an automated system (ST5020Leica, Biosystems).

2.2.4. Image analysis

Stained FFPE sections were scanned at 20x magnification using an Aperio ScanScope (Leica Biosystems) and analysed using HALO (v3.2) (Indica Labs) or ImageScope (v12.3.2) (Leica Biosystems) softwares. Regions of interest (ROIs) were drawn over the whole viable tumour area, excluding skin and necrotic regions. All analyses were conducted within the defined ROIs.

Using HALO, a random-forest tissue classifier was trained by Cara Brodie from the CRUK CI Histopathology core under my guidance to classify viable tissue, necrosis, haemorrhagic and glass regions in H&E sections. A new classifier for each PDX model was used, due to vast differences in the H&E colour and texture for each model. On average, the classifier was trained using 4 annotations per class per image on a training set of ~7 images. The number of images used for training was determined by the robustness needed for the classifier to cope with changes in colour and texture across thedataset. Quality of the classifier output was assessed by eye by myself and Cara Brodie and example images can be found in **Figure 2.3**. Necrosis area (μm^2) and haemorrhage area (μm^2) were quantified as a percentage of the total classified area (μm^2).

Further using HALO, a random-forest tissue classifier was trained by Dr Julia Jones from the CRUK CI Histopathology core under my guidance to classify CD31 area, viable tissue, and glass regions. The same classifier was used across all datasets, owing to the high consistency of colour and texture in the CD31 staining. On average, the classifier was trained using 6 annotations per class per image on a training set of ~3 images. The low number of images used for training was determined by the lowrobustness needed for the classifier to cope with changes in colour and texture across thedataset. Quality of the classifier output was assessed by eye by myself, Dr Julia Jones andCara Brodie and example images can be found in **Figure 2.7**. The area of CD31 (mm^2) within the ROI was quantified and normalised to the ROI (mm^2), as a surrogate for vesseldensity. Subsequently, an Area Quantification algorithm was applied to the serial ASMAstained section by Dr Julia Jones under my guidance. The same algorithm was used acrossall datasets, owing to the high consistency of colour and intensity in the ASMA staining.The user defined the colour of the ASMA staining and set an intensity threshold to defineweak and strong pixel colour intensity. Here, strong positive pixels were defined as those

with ASMA staining (strong brown colour) and all other pixels were defined as weak positive. Then, the classifier run on the CD31 section was overlaid onto the ASMA section, and the Area Quantification algorithm run only in CD31 areas defined by the classifier. The algorithm mark-up displayed CD31 and ASMA colocalised pixels in red and CD31 only pixels in yellow (Fig. 2.5). The area of colocalised pixels (μm^2) / CD31 classified area (μm^2) was defined as the ASMA vessel coverage (%).

Using ImageScope, two Positive Pixel Count algorithms were applied to CAIX and VEGF sections by Cara Brodie and Monika Golinska under my guidance. The same algorithm for either CAIX or VEGF analysis was used across all datasets, owing to the high consistency of colour and intensity in the CAIX and VEGF stainings. The user defined the colour of the CAIX or VEGF staining and set an intensity threshold to define weak, moderate and strong positive pixel colour intensity, similar to the Area Quantification algorithm described above. Any pixels with colour intensity below the weak threshold were classed as negative. The number of positive pixels/ total number of pixels in the ROI was defined as the positivity of CAIX (%) or VEGF (%).

2.2.5. Statistical analysis

Statistical analysis was performed using GraphPad Prism v.9. Each tumour was considered as an independent biological replicate. To compare the means of STG139, STG321, AB580 and STG143 a one-way ANOVA was performed with Tukey's multiple comparison correction, unless the data violated the assumptions of a Gaussian distribution or equal variances, in which case Kruskal-Wallis test with Dunn's multiplicity correction and Welch's ANOVA with Dunnett's T3 multiplicity correction were conducted respectively. The same tests were performed to compare means across 3 passages. To compare means across passage repeats within STG139 and AB580 an unpaired student's t-test was performed unless the data violated the assumption of a Gaussian distribution, in which case a Mann-Whitney test was conducted. To compare core and outer section means a paired student's t-test was performed unless the data violated the assumption of a Gaussian distribution, in which case a Wilcoxon test was performed. IHC vascular markers were correlated to tumour volume and correlation assessed by Pearson's or Spearman's correlation coefficient, depending on data distribution. Significance is assigned for p-

values <0.05.

2.3. Results

2.3.1. Investigating the hypoxic and necrotic microenvironment of the PDX tumours

Initially, a visual inspection of H&E sections was performed that demonstrated vast differences in tissue morphology between the PDX models (**Figure 2.3**). STG139 tumours displayed large areas of necrosis and haemorrhage (**Figure 2.3A**) along with a mixture of epithelial and mesenchymal-like tumour cells. STG321 tumour cells form 'islands' of epithelial cells with necrotic centres and stroma surrounding (**Figure 2.3B**). AB580 tumours form a necrotic core (**Figure 2.3C**), while STG143 tumours display little necrosis and are the most glandular of the 4 PDXs (**Figure 2.3D**), with large tubular formation and mucus production, as confirmed by breast pathologist Dr Elena Provanzano.

Upon quantification using a random forest classification mask, STG139 tumours were the most necrotic of the PDXs investigated, both in the core (**Figure 2.4A**) and outer (**Figure 2.4B**) tumour sections, while STG321 and STG143 were the least necrotic throughout the tumour volume (**Figure 2.4A,B**). Necrosis displayed little intra-tumoural heterogeneity in STG139, which was highly necrotic throughout the tumour volume (**Figure 2.4C**) while necrosis increased in the outer section of STG321 tumours compared to the core, which could be due to tissue preparation of the outer sections (**Figure 2.4D**). The outer sections were prepared by cutting the preserved tumour semi-sphere in two along this central axis. In STG321, this caused many of the cellular 'islands' around the rim of the tumour to fray or become damaged in this outer section. AB580 PDXs were also highly necrotic in the core section (**Figure 2.4A**) but necrosis decreased significantly in this model in the outer section (**Figure 2.4B,E**), demonstrating the central necrotic core present in this model. The other luminal B model STG143 had low levels of necrosis throughout the tumour volume (**Figure 2.4F**).

Finally, haemorrhage was detectable only in the basal models, more often in STG139 (**Figure 2.4G**). Note that in all quantifications for the remainder of this chapter and throughout this thesis, basal models (STG139 and STG321) are presented in shades of blue contained in circles, while luminal models (AB580 and STG143) are presented in

burgundy and orange contained in squares. Overall, STG139 was found to be a highly necrotic and haemorrhagic model, while STG321 and STG143 are mostly viable and AB580 tumours form a necrotic core, with viable tissue surrounding.
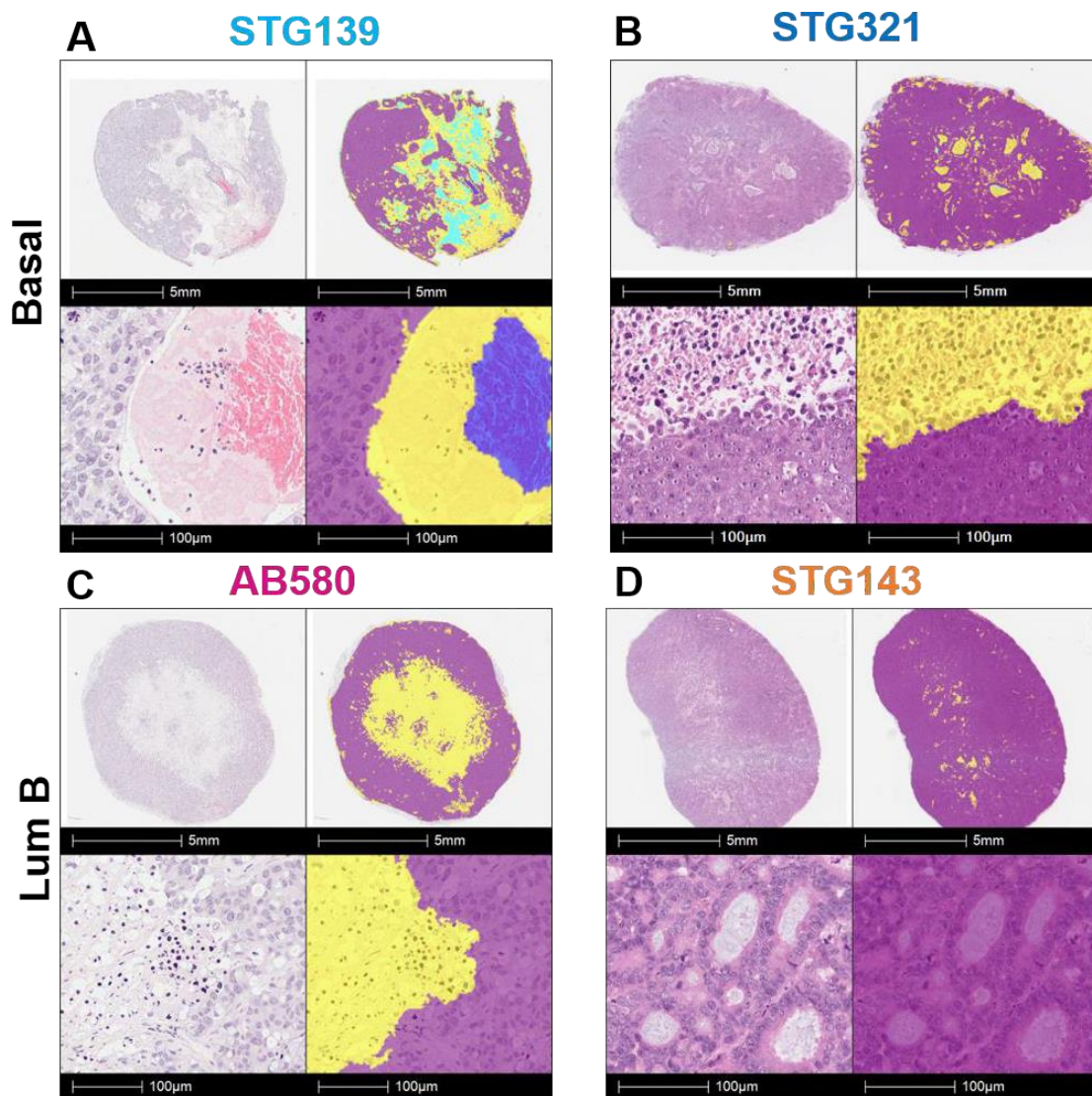
Figure 2.3. Tissue morphology, necrosis and haemorrhage differ between the PDXs. In all subfigures top left= whole H and E section, top right= whole H and E section with mask, bottom left= H and E section at 20X magnification, bottom right= H and E section at 20X magnification with mask. Mask colours: purple= viable tissue, yellow= necrosis, dark blue= haemorrhage, light blue= glass. A) STG139 with large areas of necrosis and haemorrhage, B) STG321, forming islands with necrotic centres, C) AB580 with a necrotic core, D) STG143, with less necrosis and multiple tubule formation and mucin production.
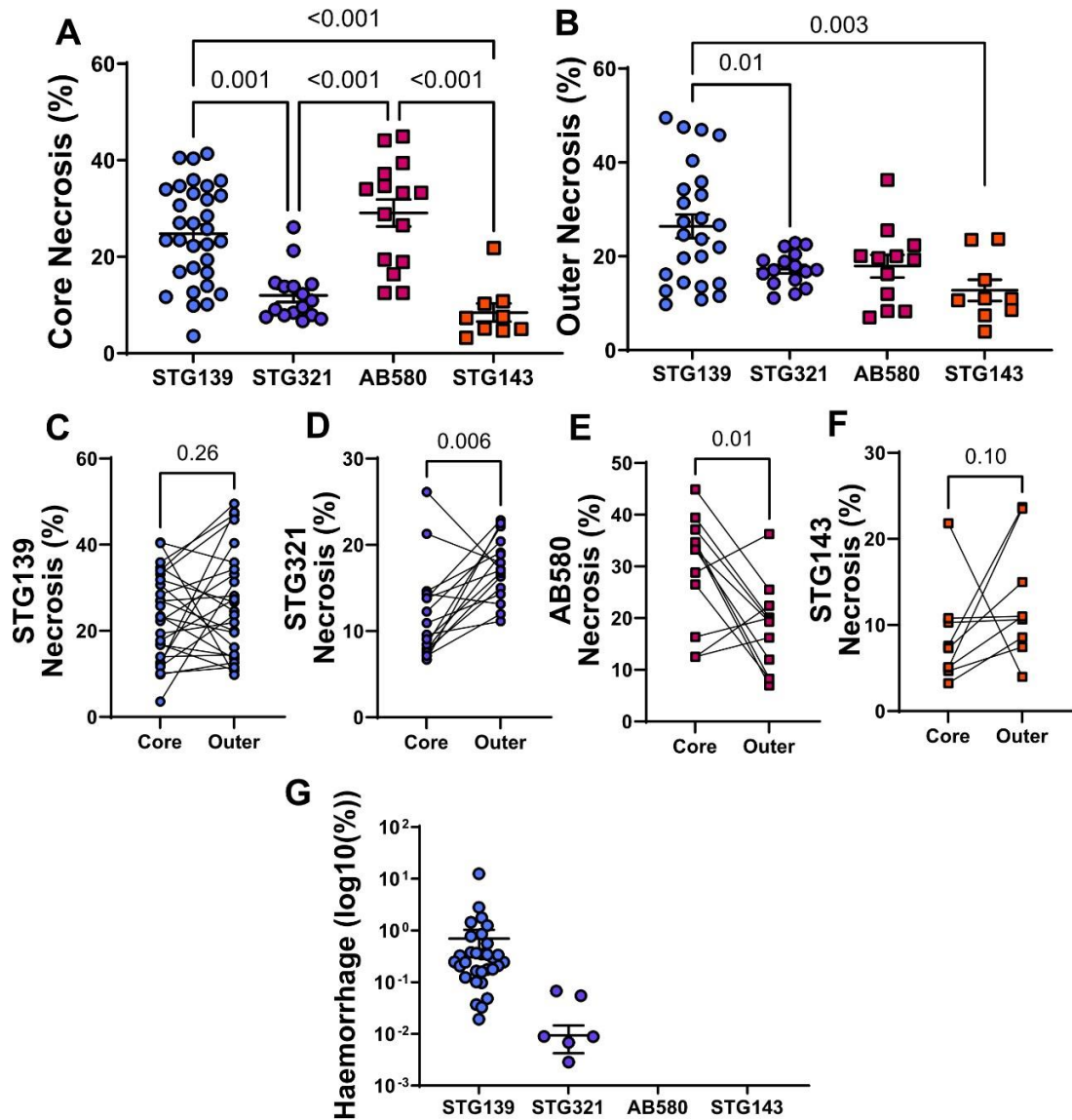
Figure 2.4. STG139 displays a necrotic and haemorrhagic phenotype throughout the tumour volume.
Necrosis as a percentage of the tumour area on H and E sections taken from the core of tumour (A) and from an outer portion of the tumour (B). Comparison of necrosis (%) in core vs. outer H and E sections forSTG139 (C), STG321 (D), AB580 (E) and STG143 (F). Haemorrhage as a percentage of the tumour area on H and E sections taken from the core of tumour (G) on a log scale to show presence of haemorrhage inbasal models only. In A, B and G, data presented as a scatter dot plot with mean ±SEM. In C-F matched data from the same tumour are joined by a straight line. In all subfigures, each data point represents data from one section of one tumour (biological replicate). In A) and B) p-values for significant (p<0.05) pairwise comparisons are shown calculated by Kruskal-Wallis test with Dunn's multiplicity correction andWelch's ANOVA with Dunnett's T3 multiplicity correction respectively. In C-F all p-values are shown calculated by paired t-test (C and E) or Wilcoxon test (D and F). p-values <0.05 considered significant. The following n numbers refer to the number of tumours per PDX model in each sub-figure: for(A, G) $n^{STG139}=32$, $n^{STG321}=16$, $n^{AB580}=15$, $n^{STG143}=9$ (in G only values for STG139 and STG321 displayed in log scale). For (B-F) $n^{STG139}=25$, $n^{STG321}=16$, $n^{AB580}=12$, $n^{STG143}=9$.

Next, I sought to evaluate whether the necrotic PDXs were also hypoxic, using CAIX IHC. As expected, STG139 was observed to have very high CAIX expression in most tumour cells (**Figure 2.5**). Upon quantification using an intensity-based threshold, STG139 had significantly higher CAIX positivity than all other models in the core (**Figure 2.6A**) and outer (**Figure 2.6B**) sections, with no intra-tumoural heterogeneity (**Figure 2.6C**). CAIX positivity was consistently lower in the other basal model STG321(**Figure 2.6A, B**) although expression was heterogeneous across the tumour volume, with significantly lower CAIX positivity in the outer tumour sections compared to the core (**Figure 2.6D**). Relatively speaking, AB580 tumours were also highly hypoxic with ~30-40% CAIX positivity in both core and outer sections (**Figure 2.6A, B, E**), although CAIX positivity was only significantly higher than STG321 and STG143 in the outer sections (**Figure 2.6B**). Expression was consistently low in STG143, however just like STG321 expression was heterogeneous across the tumour volume (**Figure 2.6F**). Overall, hypoxic levels were highest in the two necrotic PDXs, STG139 and AB580, and hypoxia did not associate with PDX subtype.
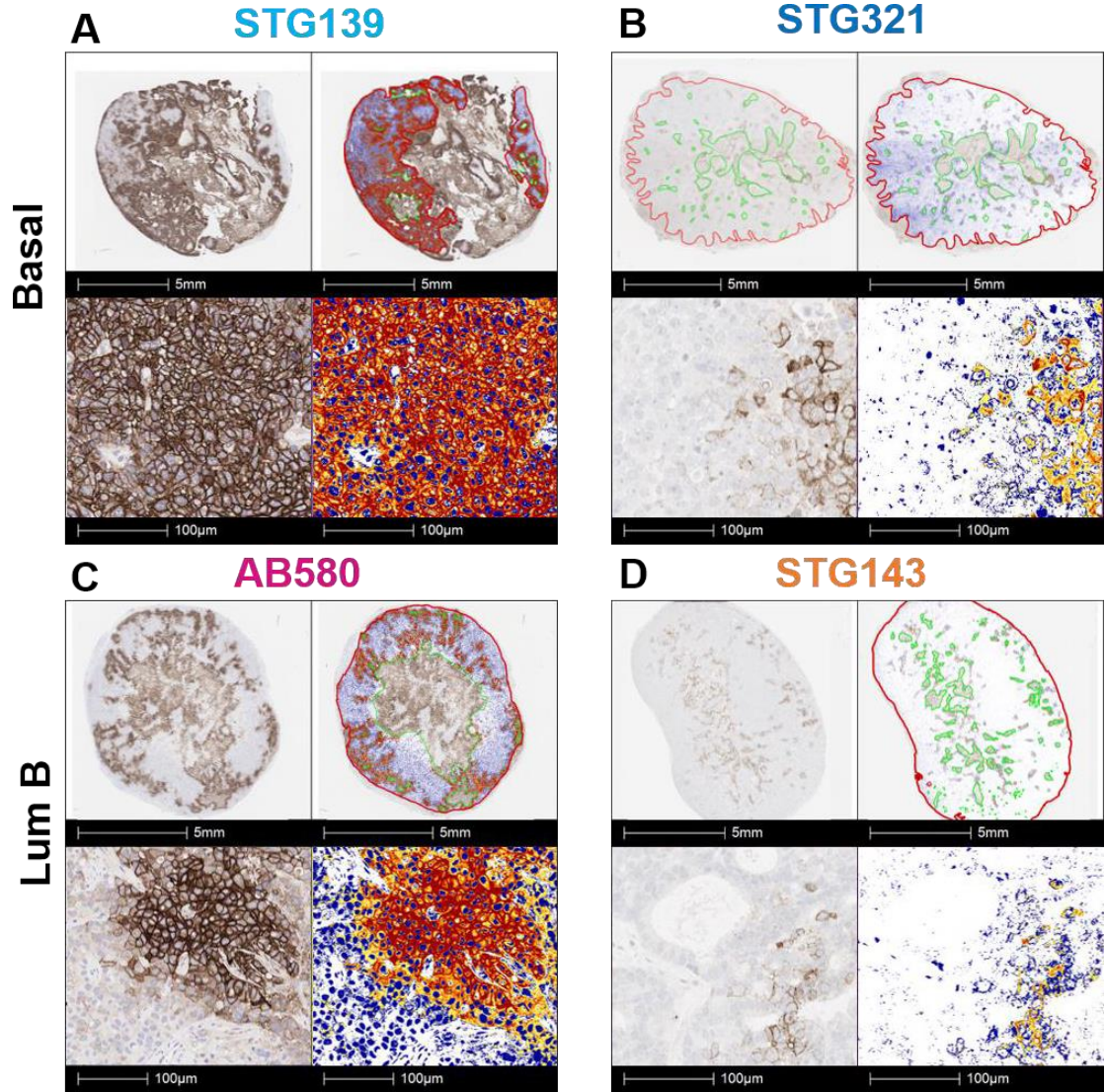
Figure 2.5. Necrotic PDXs STG139 and AB580 express high CAIX levels. In all subfigures top left= whole CAIX IHC section, top right= whole CAIX IHC section with intensity-based threshold mark-up, bottom left= CAIX IHC section at 20X magnification, bottom right= CAIX IHC section at 20X magnification with intensity-based threshold mark-up. Mark-up colours: red= strong CAIX expression, orange = medium CAIX expression, yellow= weak CAIX expression, blue= nuclei (note weak haematoxylin (nuclei) staining in STG321 and STG143). A) STG139, B) STG321, C) AB580, D) STG143.
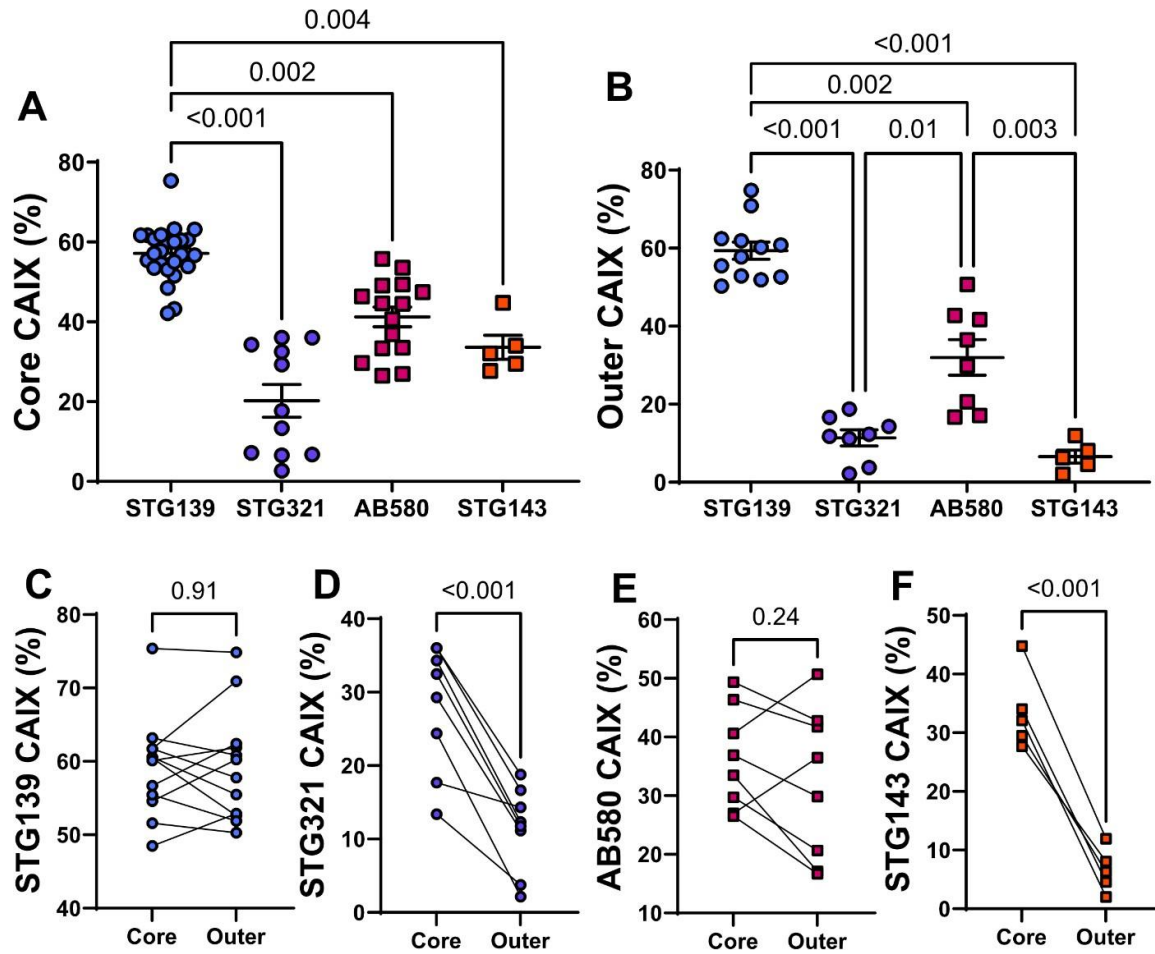
Figure 2.6. STG139 and AB580 are highly hypoxic tumours throughout the tumour volume. CAIX total positive pixels as a percentage of the total tumour area pixels on CAIX IHC sections taken from the core of tumour (A) and from an outer portion of the tumour (B). Comparison of CAIX (%) in core vs. outer sections for STG139 (C), STG321 (D), AB580 (E) and STG143 (F). In A and B, data presented as scatter dot plot with mean ±SEM. In C-F matched data from same tumour are joined by straight line. In all subfigures, each data point represents data from one section of one tumour (biological replicate). In A) and B) p-values for significant (p<0.05) pairwise comparisons are shown calculated by Kruskal-Wallis test with Dunn's multiplicity correction and Welch's ANOVA with Dunnett's T3 multiplicity correction respectively. In C-F all p-values are shown calculated by paired t-test. p-values <0.05 considered significant. The following n numbers refer to the number of tumours per PDX model in each sub-figure: for (A) $n^{STG139}=25$, $n^{STG321}=15$, $n^{AB580}=11$, $n^{STG143}=5$. For (B-F) $n^{STG139}=12$, $n^{STG321}=8$, $n^{AB580}=8$, $n^{STG143}=5$.

Knowing the strong links between necrosis and hypoxia with vascular form and function[2,5], I next sought to evaluate the vessel area and pericyte/smooth muscle vessel coverage in the IHC sections as a proxy for vessel density and vessel maturity respectively. Visual inspection of serial CD31 and ASMA sections, which label endothelial cells and pericytes/ smooth muscle respectively, showed STG139 to have a high density of vessels that were not covered by ASMA$^+$ pericytes/smooth muscle (**Figure 2.7A**), which are considered immature. In contrast, the other basal modelSTG321 was found to also have many vessels, particularly in the stroma surrounding thecellular 'islands', yet these were consistently covered by ASMA$^+$ pericytes/smooth muscle and could be considered relatively mature (**Figure 2.7B**). Both luminal B models,AB580 and STG143, displayed low vessel density with partial ASMA coverage on visualinspection (**Figure 2.7C, D**).

Quantitative results using a CD31 mask overlaid onto an ASMA section, to identify CD31$^+$ASMA$^+$ pixels and CD31$^+$ASMA$^-$ pixels, support the qualitative inspections. First, CD31 vessel area was consistently highest in STG139 compared to both luminal B models, and in outer sections it was also higher than STG321 (**Figure 2.8A, B**). STG321 CD31 vessel area was relatively high compared to both luminal B models, which displayed low CD31 area, as seen visually (**Figure 2.8A, B**). CD31 vesselarea was fairly heterogeneous across the tumour volume; overall CD31 vessel area increased in STG139 and decreased in STG321 (**Figure 2.8C, D**). Despite 2 outliers, CD31 vessel area was stable across AB580 sections (**Figure 2.8E**) and decreased in the outer section of STG143 (**Figure 2.8F**).

When assessing vessel maturity, ASMA vessel coverage was consistently highest in the basal model STG321 compared to the other PDXs, in both core and outer sections, and was particularly low in the other basal model STG139 (**Figure 2.9A, B**). AB580 and STG143 ASMA vessel coverage was in-between the two extremes presented by the basal models. Although not significant, AB580 presented with ~1.15-fold higher ASMA vessel coverage than STG143. ASMA vessel coverage showed little intra-tumouralheterogeneity apart from a slight decrease in STG321 from core to outer sections (**Figure2.9C-F**), but it should be noted that tissue preparation of the outer section may have increased necrosis and decreased vessel density and maturity in this model.

Despite both basal models having considerably more vessels than the luminal B models, STG321 presents with a more mature vessel phenotype and less hypoxia and necrosis, whereas STG139 has an immature vessel phenotype and is more hypoxic, necrotic and haemorrhagic in comparison.
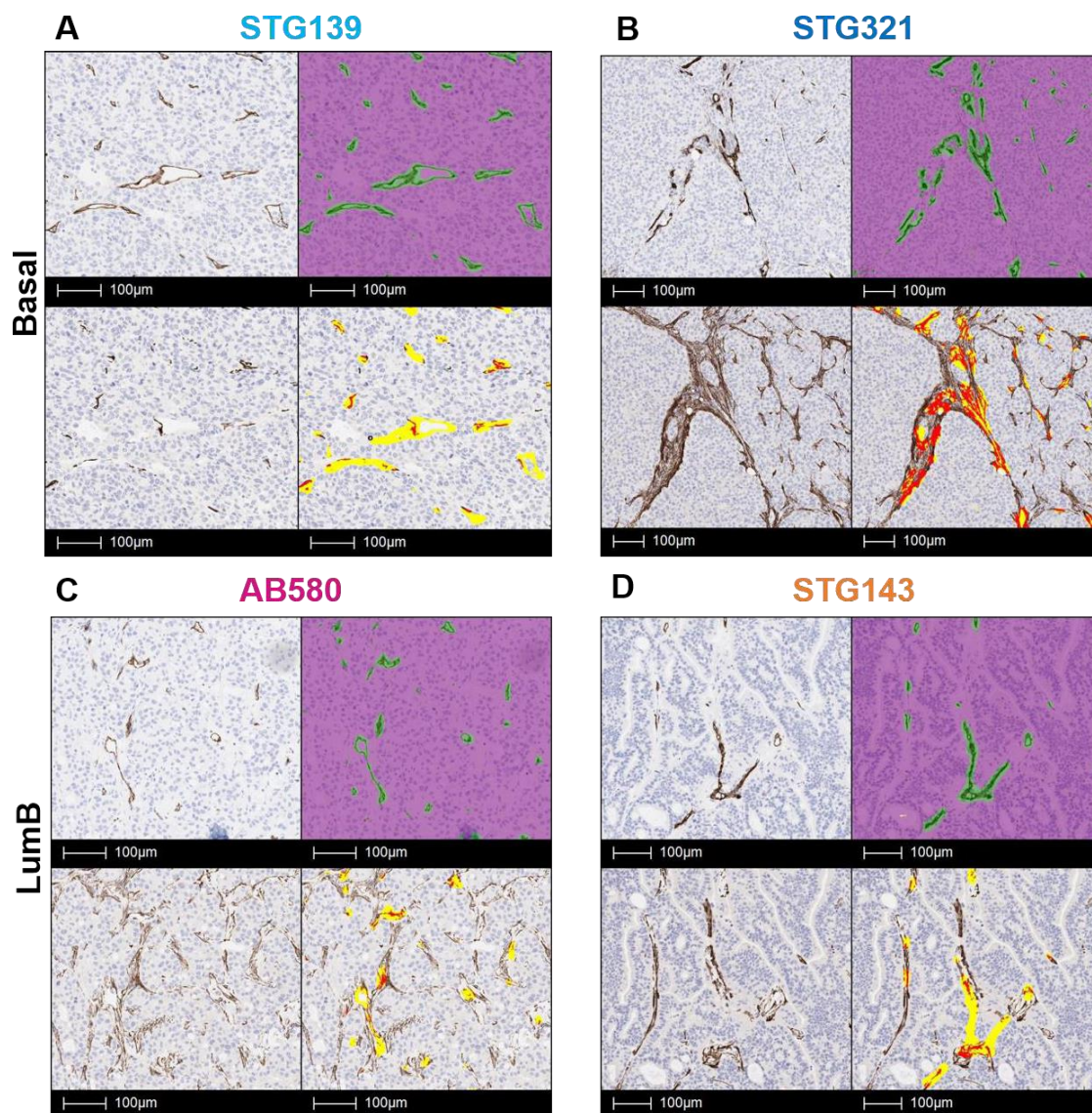
Figure 2.7. PDXs display differences in ASMA vessel coverage. In all subfigures top left= CD31 IHC section at 10X magnification, top right= CD31 IHC section at 10X magnification with mask, bottom left= serial ASMA IHC section at 10X magnification, bottom right= serial ASMA IHC section at 10X magnification with mask. CD31 mask colours: purple= tissue, green= CD31 positive vessel. ASMA mask colours: red= colocalisation with CD31+ vessel, yellow= CD31+ vessel alone. A) STG139, B) STG321, C) AB580, D) STG143.
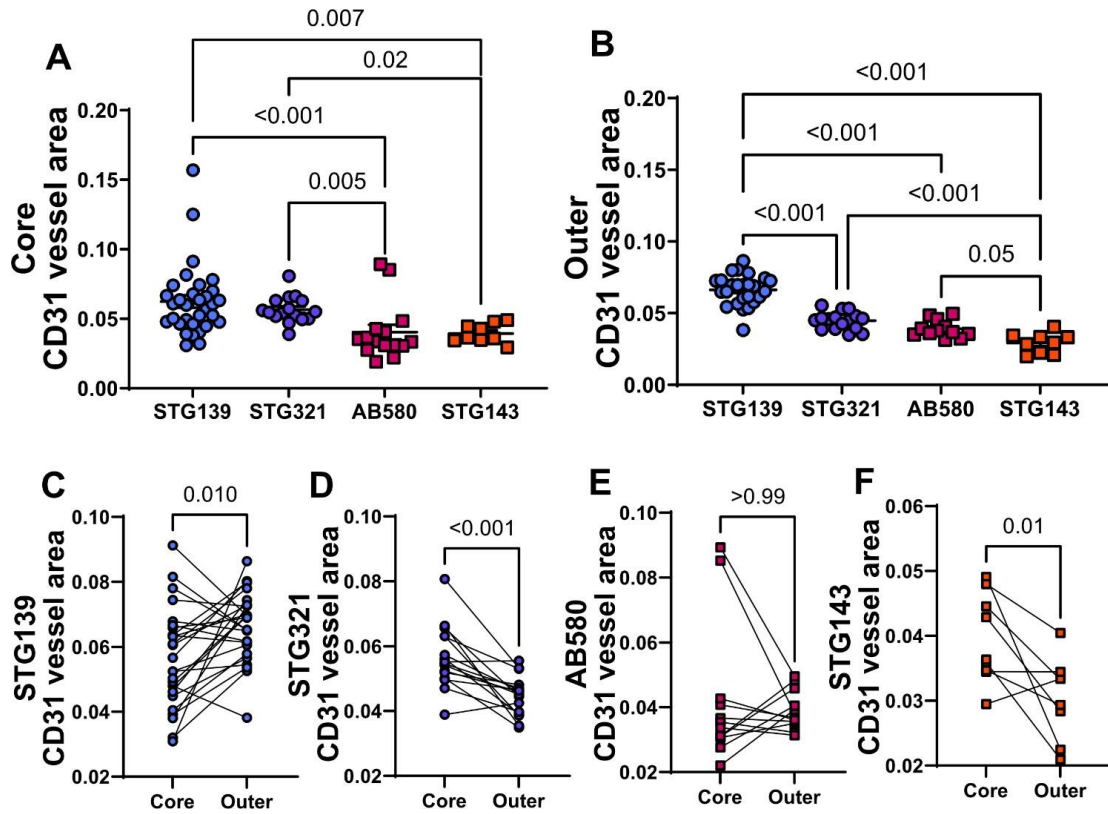
Figure 2.8. STG139 tumours have the highest vessel density. CD31 vessel area (green mask area normalised to total tumour area) on CD31 IHC sections taken from the core of tumour (A) and from an outer portion of the tumour (B). Comparison of CD31 vessel area in core vs. outer sections for STG139 (C), STG321 (D), AB580 (E) and STG143 (F). In A and B, data presented as scatter dot plot with mean ±SEM. In C-F matched data from same tumour are joined by straight line. In all subfigures, each data point represents data from one section of one tumour (biological replicate). In A) and B) p-values for significant (p<0.05) pairwise comparisons are shown calculated by Kruskal-Wallis test with Dunn's multiplicity correction and One-way ANOVA with Tukey's multiplicity correction respectively. In C-F all p-values are shown calculated by paired t-test (C, D, F) or Wilcoxon test (E). p-values <0.05 considered significant. The following n numbers refer to the number of tumours per PDX model in each sub-figure: for(A) n^{STG139}=32, n^{STG321}=16, n^{AB580}=15, n^{STG143}=9. For (B-F) n^{STG139}=25, n^{STG321}=16, n^{AB580}=12, n^{STG143}=9.
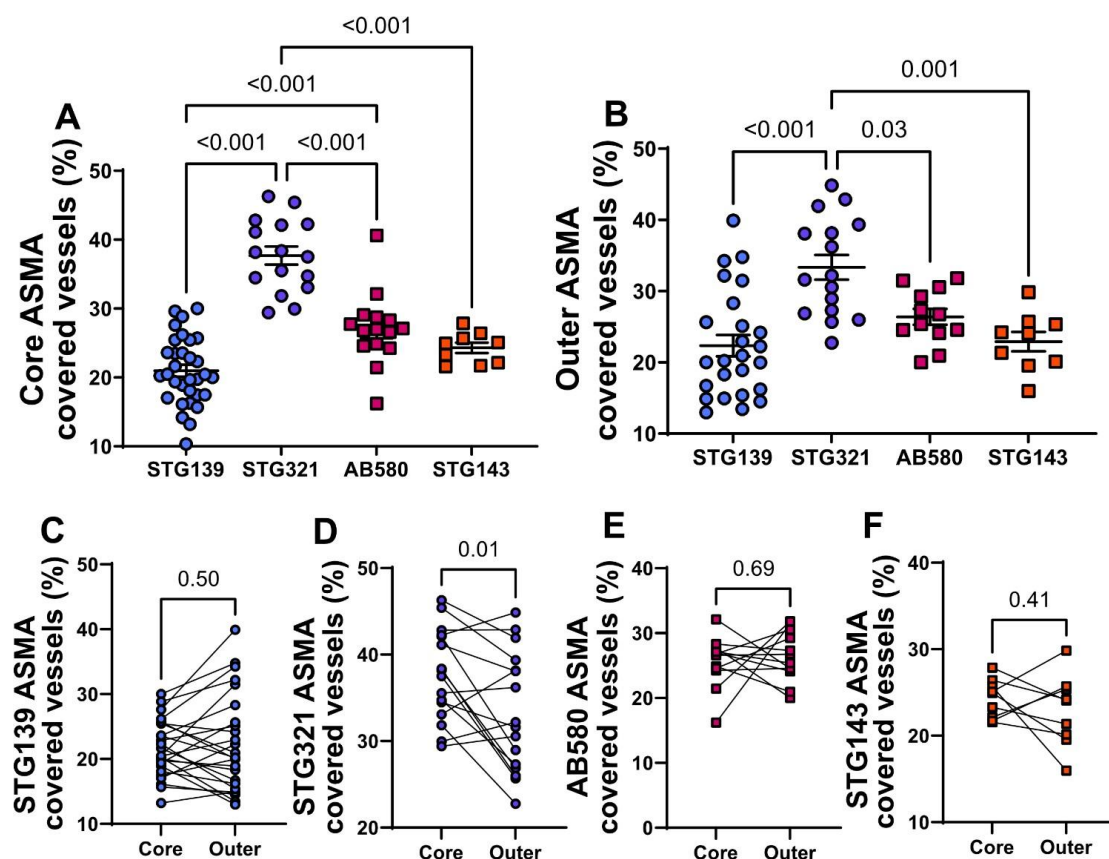
Figure 2.9. STG139 has immature vessels, with low ASMA vessel coverage. ASMA vessel coverage of CD31+ vessels (number of red pixels/number of red+yellow pixels, expressed as a percentage) on ASMA IHC sections taken from the core of tumour (A) and from an outer portion of the tumour (B). Comparison of ASMA vessel coverage (%) in core vs. outer sections for STG139 (C), STG321 (D), AB580 (E) and STG143 (F). In A and B, data presented as scatter dot plot with mean ±SEM. In C-F matched data from same tumour are joined by straight line. In all subfigures, each data point represents data from one section of one tumour (biological replicate). In A) and B) p-values for significant (p<0.05) pairwise comparisons are shown calculated by One-way ANOVA with Tukey's multiplicity correction respectively. In C-F all p-values are shown calculated by paired t-test. p-values <0.05 considered significant. The following n numbers refer to the number of tumours per PDX model in each sub-figure: for (A) n^{STG139}=32, n^{STG321}=16, n^{AB580}=15, n^{STG143}=9. For (B-F) n^{STG139}=25, n^{STG321}=16, n^{AB580}=12, n^{STG143}=9.

Finally, I sought to investigate the angiogenic potential of the 4 PDXs by assessing the protein level of VEGF, the most potent pro-angiogenic factor. IHC was conducted to target VEGF-A on sections taken from the core of each tumour. It was not possible to assess the level of VEGF expression in outer tumour sections, due to discontinuation of the VEGF antibody by the supplier and no suitable replacement could be found within the time constraints of the project. VEGF expression was present in most tumour cells in STG139, AB580 and STG143 but expression was variable in STG321 and often lower in this model (**Figure 2.10A-D**). Interestingly, expression was of a higher intensity in STG139 (**Figure 2.10A**, red colour) and although positive expression was detected in AB580 and STG143 this was of medium intensity (**Figure 2.10C,D,** orange colour). Overall, VEGF expression was lowest in STG321 (**Figure 2.10B,E**) demonstrating that this model is less angiogenic compared to the other PDXs, and presents with a more mature vessel phenotype.
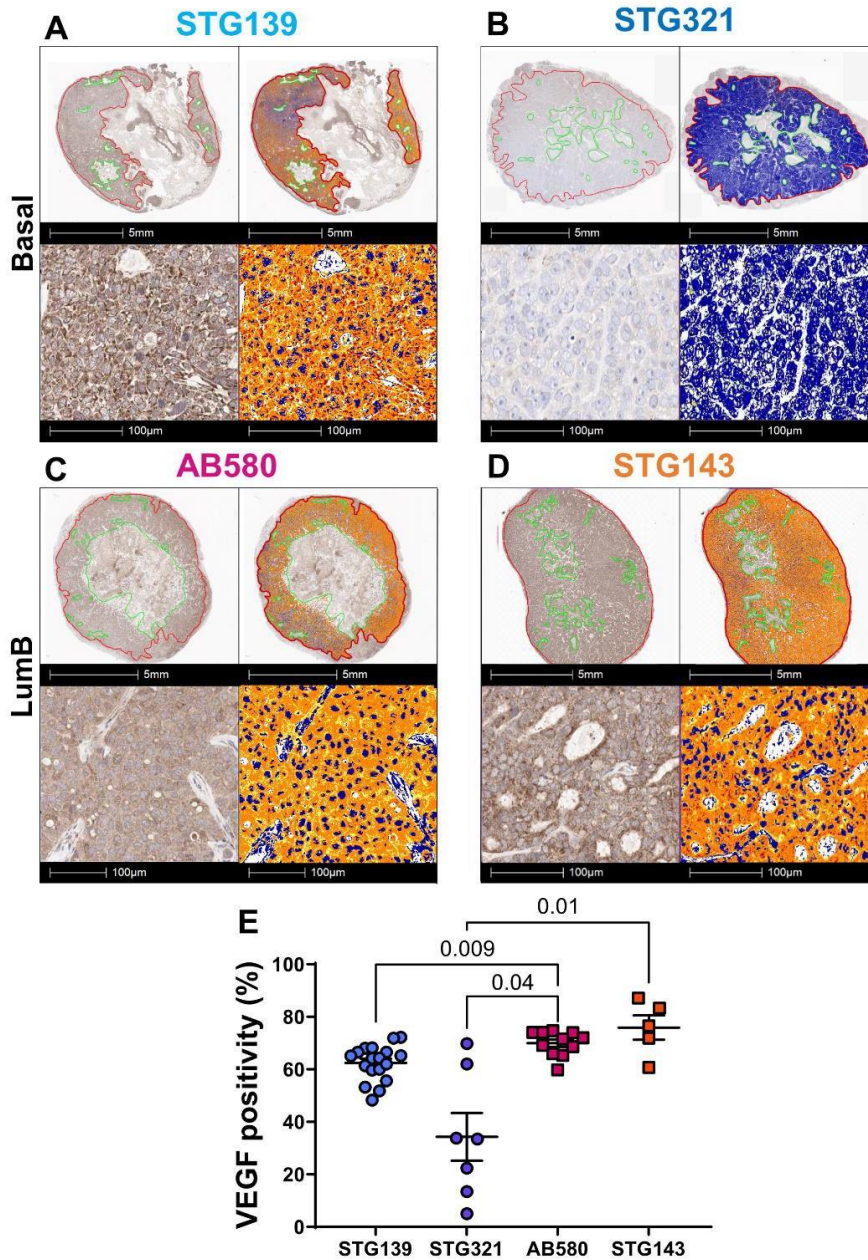
Figure 2.10. STG321 is less angiogenic with lower VEGF expression. In all subfigures top left= whole VEGF IHC section, top right= whole VEGF IHC section with mask, bottom left= VEGF IHC section at 20X magnification, bottom right= VEGF IHC section at 20X magnification with mask. Mask colours: red= strong VEGF expression, orange = medium VEGF expression, yellow= weak VEGF expression, blue= nuclei (note weak haematoxylin (nuclei) staining in STG321 and STG143). A) STG139, B) STG321, C) AB580, D) STG143. E) VEGF total positive pixels as a percentage of the total tumour area pixels on VEGF IHC sections taken from the core of tumour. In E, data presented as scatter dot plot with mean ±SEM, each data point represents data from one section of one tumour (biological replicate). p-values for significant (p<0.05) pairwise comparisons are shown calculated by Welch's ANOVA with Dunnett's T3 multiplicity correction respectively. The following n numbers refer to the number of tumours per PDX model for (E) $n^{STG139}=18$, $n^{STG321}=7$, $n^{AB580}=11$, $n^{STG143}=5$.

2.3.2. PDXs have low inter-passage heterogeneity showing repeatable and robust vascular phenotypes

To continue to expand and propagate PDX samples for evaluation, it is necessary to passage them. This means to take tumour fragments from one mouse and implant them into another mouse. Bruna et al.[10] have previously shown that these PDXs are genetically stable and represent the patient from which they were derived across several passages (i.e. up to 15 passages after sample collection from the patient). However, little is known regarding the mouse stromal compartment and whether the vascular phenotypes identified in Section 2.3.1 are stable across passages, or whether they suffer from passage-dependence.

To meet Aim 3 of this thesis and assess inter-passage heterogeneity of the vascular phenotypes, I evaluated expression of the same IHC vascular markers from 2.3.1 (except VEGF due to antibody shortage), in the core sections across 3 early passages of STG139 and AB580 tumours, assessing one basal and one luminal B PDX. Additionally, one passage per model was repeated, where the implantation of tumour fragments from the previous passage was repeated in new mice, to assess how repeating a passage could also introduce heterogeneity in phenotype.

Overall, vascular phenotypes were stable across the 3 passages in both STG139 and AB580 (**Figure 2.11**). For STG139, levels of necrosis, CD31 vessel area and ASMA vessel coverage remained consistent. Interestingly, CAIX positivity increased slightly across passages such that passage 5 (P5) was almost significantly higher than P3(p=0.06), suggesting some selectivity for the most aggressive, hypoxic cells (**Figure 2.11A-D**). There was a significant decrease in necrosis from P3 to P4 in AB580 tumours(**Figure 2.11E**), however it should be noted there are only 2 tumours that successfully engrafted and grew in this passage so there is limited information available for statisticaltesting. Despite an apparent decrease in necrosis, these same tumours appeared to have slightly higher hypoxia (**Figure. 2.11F**) than the previous passage, however, this is not quite significant (p=0.06). CD31 vessel area and ASMA vessel coverage remained consistent across AB580 passages (**Figure 2.11G, H**).

When comparing the repeated passages, some differences in vascular phenotype

were seen. From P4 to the repeat (P4r) in STG139, we see a significant drop in necrosis (**Figure 2.11A**) concurrent with a significant increase in CD31 vessel area (**Figure 2.11C**). From P3 to P3r in AB580, CD31 vessel area increases (**Figure 2.11G**) concurrentwith a decrease in ASMA vessel coverage (**Figure 2.11H**). However, it should be noted that the outer section of both P3r tumours had a CD31 vessel area that is very similar to the original P3 tumours (**Figure 2.8E**, 0.05 and 0.038), suggesting that the result in **Figure 2.11G** may be an outlier and CD31 vessel area quantification is influenced by thesectioning. Despite some variation in the passage repeat, PDXs appear to show little inter-passage heterogeneity displaying repeatable and robust vascular phenotypes across several passages.
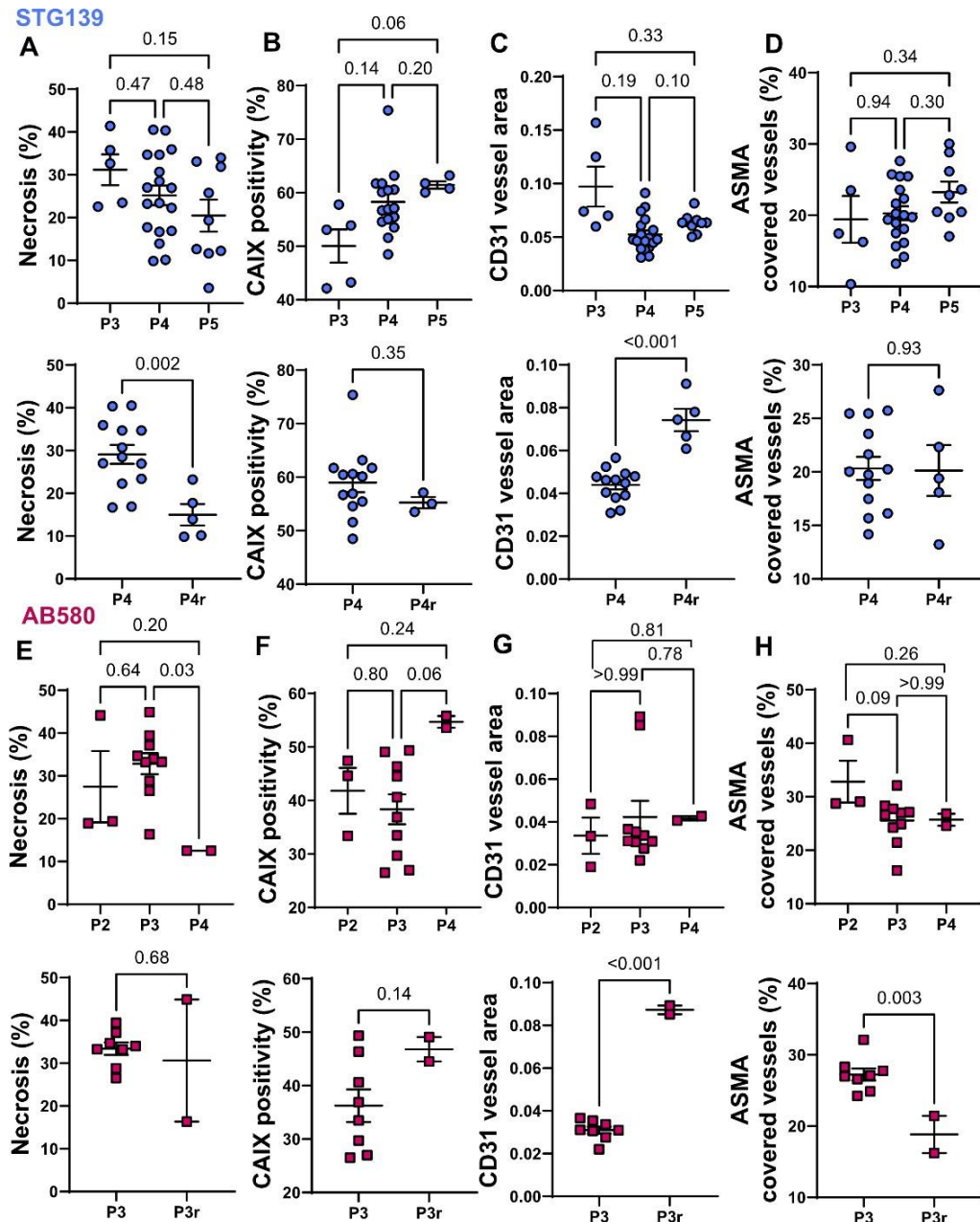
Figure 2.11. Vessel phenotypes are mostly stable between successive PDX passages though show some variation in replicate passages. In all subfigures: top= expression of marker across 3 consecutive passages (P) and bottom= expression of marker across one passage vs. a repeat of the same passage (r). A and E: Necrosis as a percentage of the tumour area on H and E sections taken from the core of tumour in STG139 and AB580 respectively. B and F: CAIX total positive pixels as a percentage of the total tumour area pixels on CAIX IHC sections taken from the core of tumour in STG139 and AB580 respectively. C and G: CD31 vessel area (green mask area normalised to total tumour area) on CD31 IHC sections taken from the core of tumour in STG139 and AB580 respectively. D and H: ASMA vessel coverage of CD31+ vessels (numberof red pixels/number of red+yellow pixels, expressed as a percentage) on ASMA IHC sections taken fromthe core of tumour in STG139 and AB580 respectively. In all subfigures, data presented as scatter dot plot

with mean ±SEM, each data point represents data from one section of one tumour (biological replicate). In top subfigures p-values for all comparisons across passages shown calculated by One-way ANOVA with Tukey's multiplicity correction (A,D,E,F,H), Welch's ANOVA with Dunnett's T3 multiplicity correction (B,C) or Kruskal-Wallis test with Dunn's multiplicity correction (G). In bottom subfigures p-values for all comparisons across repeat shown calculated by unpaired t-test. For all, $p<0.05$ considered significant. The following n numbers refer to the number of tumours per PDX passage in each sub-figure. For top subfigures: (A, C, D) P3 n=5, P4 n=18, P5 n=9. (B) P3 n=5, P4 n=16, P5 n=4. (E-H) P2 n=3, P3 n=10, P4 n=2. For bottom subfigures: (A, C, D) P4 n=13, P4r n=5. (B) P4 n=13 P4r n=3. (E-H) P3 n=8, P3r n=2.

2.3.3. An initial comparison to patient tumour vasculature was conducted

In addition to assessing the repeatability and robustness of the breast PDXs, Aim 3 of the thesis was to identify whether PDXs represent the diversity of vascular phenotypes in patients. To this end, I compared PDX IHC and histology to that arising from the original patient, using the limited patient tissue available. This included H&E and CD31 and ASMA serial tissue microarray (TMA) sections for STG321, AB580 and STG143 and an H&E tissue section for STG139.

With an initial analysis by visual inspection, under the guidance of breast pathologist Dr Elena Provanzano, I found the PDX phenotypes to be similar to the patient from which they were derived. In STG139, the tumour cell morphology was consistent across patient to PDX, with a large number of mesenchymal-like tumour cells, with a spindle-like appearance on H&E and vacuolated nuclei (**Figure 2.12A**), typical of an aggressive breast tumour. Interestingly, there was no necrosis detectable in the patient H&E unlike in the PDX tissue (**Figure 2.3**), although this may be due to the limited tissue sample collected. With only the H&E section available for this model, the CD31 and ASMA serial sections are shown for the PDXs only, which showed a large number of CD31$^+$ vessels that were without ASMA vessel coverage (**Figure 2.12A**, coloured arrows), but unfortunately the comparison to patient tumour vessels was not possible due to the lack of available clinical material.

In STG321 H&E, I found the presence of stroma and the formation of cellular 'islands' (**Figure 2.12B**, black arrows) in both patient and PDX tissue. There were many CD31$^+$

vessels, which were consistently covered by $ASMA^+$ pericytes/ smooth muscle in both the patient and PDX tissue (**Figure 2.12B**, coloured arrows), suggesting that the dense and mature vascular phenotype of STG321 is preserved from patient to PDX. It should be noted that the $ASMA^+$ pericytes/ smooth muscle in patient and PDX tissue had differential formation, with the PDX tissue forming much thicker fibrous strands, despite a similar vascular phenotype overall.

In AB580 the H&E showed similar tissue morphology between patient and PDX, with stroma and tubule formation (**Figure 2.12C**, black arrows). Interestingly the vascular phenotypes were again similar between patient and PDX on the tissue available, with low $CD31^+$ vessel density and at least partial but not complete ASMA vessel coverage in both patient and PDX tissue (**Figure 2.12C**, burgundy arrow- complete coverage, orange arrow- partial/no coverage).

A similar result was found in STG143, with tubule formation found on H and E for both patient and PDX tissue, demonstrating that the PDXs retained the glandular morphology of this tumour (**Figure 2.12D**). Additionally, both PDX and patient tissue displayed few $CD31^+$ vessels in comparison to STG321, and at least partial but not complete ASMA vessel coverage in both patient and PDX tissue (**Figure 2.12D**, burgundy arrow- complete coverage, orange arrow- partial/no coverage). It should be noted that the $ASMA^+$ pericytes/ smooth muscle in both AB580 and STG143 patient tumours is similar in morphology of the PDX stroma. These results appear to show that both AB580 and STG143 patient tumours have a low density and partially mature vascular phenotype that is preserved in the PDX tumours. However, with a lack of clinical material available for this thesis, a quantitative comparison could not be made. Although the TMA data provided an interesting indication for further investigation with larger clinical samples, it is not yet clear whether the PDXs truly represent the vasculature seen in patients' tumours.
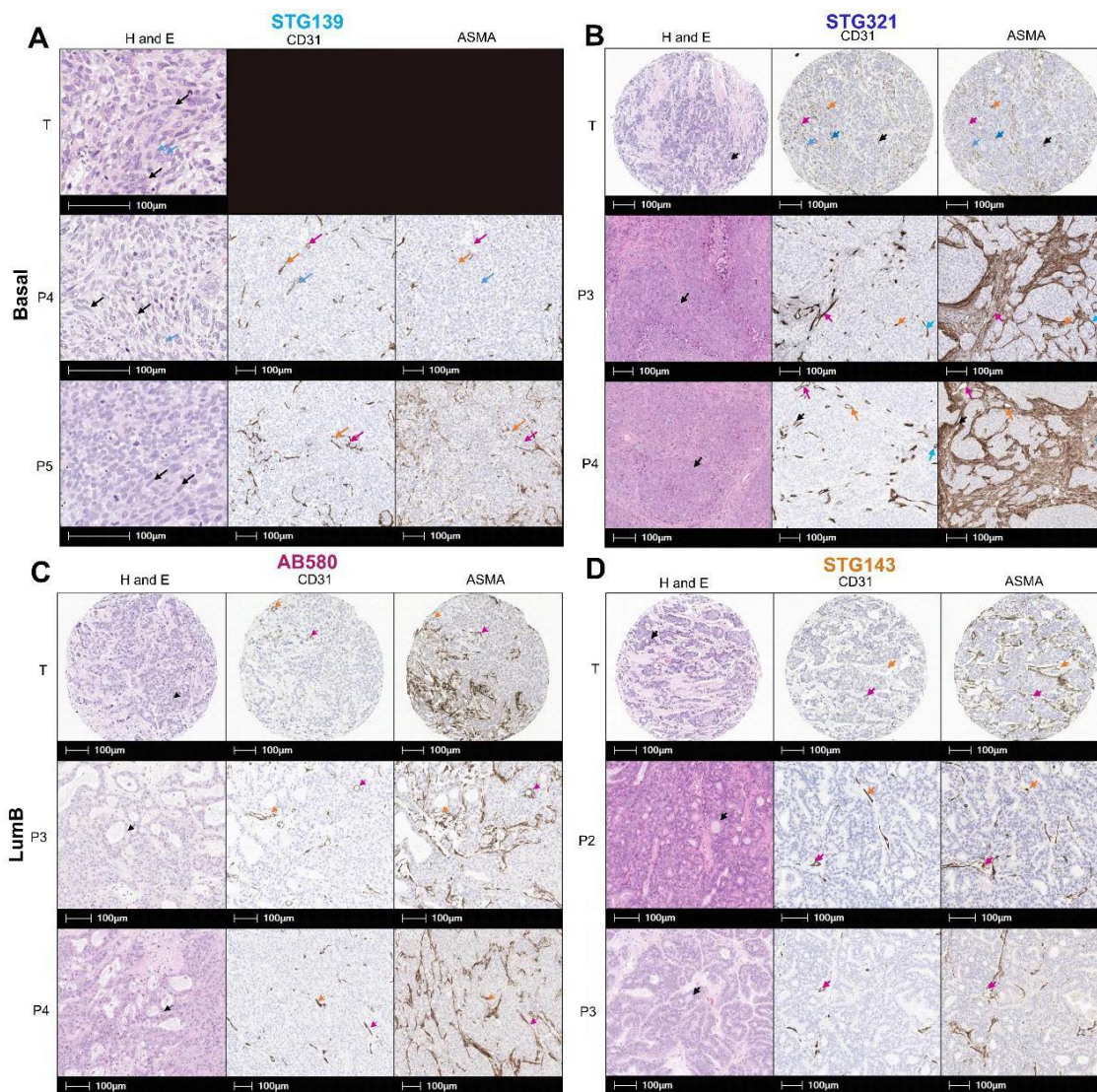
Figure 2.12. Comparing PDX to patient vessel phenotypes. In all subfigures H and E, CD31 and ASMA sections are compared (where available) across patient tumour (T), and two consecutive PDX passages (P). A) STG139 First column: Patient tumour H and E whole tissue section at 20X magnification showing presence of mesenchymal-like tumour cells (black arrows) and vacuolated nuclei (blue arrows) also presentin subsequent PDX passages. Second column: PDX CD31 IHC at 5X magnification. Third column: corresponding serial ASMA IHC at 5X magnification. B) STG321: First column: Patient tumour H and E 0.6 mm TMA core and subsequent PDX passages at 5X magnification, formation of 'islands' shown by black arrows. Second column: CD31 IHC on either patient 0.6 mm TMA core or whole PDX section at 5X magnification. Third column: corresponding serial ASMA IHC at same magnification. C) AB580 and D) STG143: First column: Patient tumour H and E 0.6 mm TMA core and subsequent PDX passages at 5X magnification, tubule formation shown by black arrows. Second column: CD31 IHC on either patient 0.6 mm TMA core or whole PDX section at 5X magnification. Third column: corresponding serial ASMA IHCat same magnification. For all CD31 and ASMA columns: Burgundy, orange, blue and black arrows show CD31 vessels with corresponding area on ASMA IHC.

70

2.3.4. Vascular markers do not appear to evolve as PDXs grow

Towards Aim 4 of the thesis, I investigated whether the vascular phenotypes found using IHC evolved as tumours grew. This would provide some insight as to whether the PDX vascular phenotypes are inherent, or whether they develop over time. Core sections were taken from a range of STG139 and AB580 tumour volumes and expression of the IHC vascular markers were correlated to tumour volume (**Figure 2.13**).

Unsurprisingly, necrosis increased significantly by ~2-fold as tumours grew in STG139 and necrosis also increased in AB580, albeit not significantly (p=0.15) (**Figure 2.13A, B**). This is a common observation in developing tumours, due to the increasing distance of cells from surrounding vasculature as tumours grow[48]. Interestingly, CAIX positivity remained stable as tumours grew in STG139 but increased by ~1.7-fold in AB580 tumours (**Figure 2.13C, D**), suggesting that the levels of hypoxia are inherent to STG139 but develop in AB580. CD31 vessel area and ASMA vessel coverage were stable across tumour growth in both models (**Figure 2.13E-H**). Overall, there was no significant evolution of vessel area or vessel maturity in the PDXs investigated.
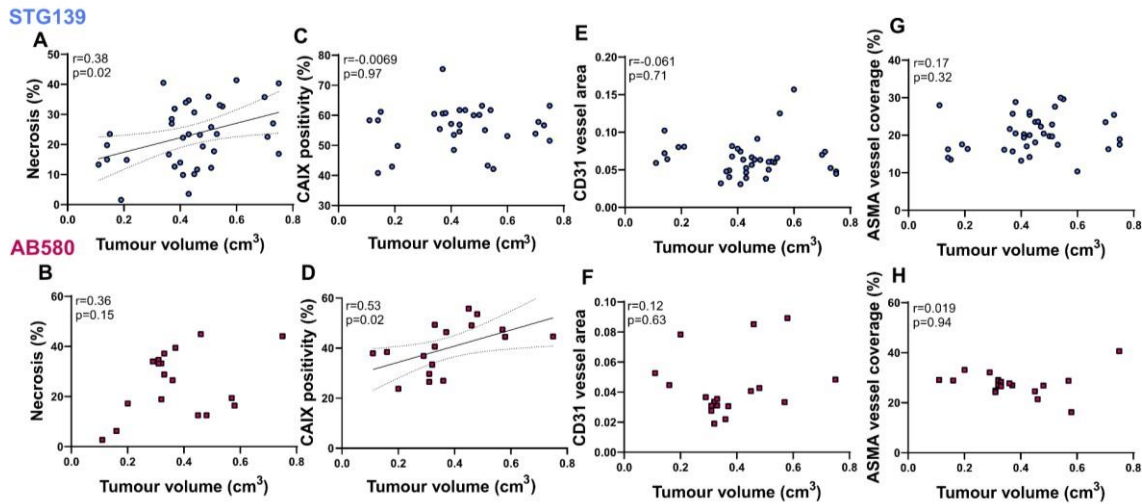
Figure 2.13. Hypoxia increases with tumour growth in AB580 but is stable in STG139. Expression of marker across tumour volumes in STG139 (A-D) and AB580 (E-H) tumours. A and B: Necrosis as a percentage of the tumour area on H&E sections taken from the core of tumour. C and D: CAIX total positive pixels as a percentage of the total tumour area pixels on CAIX IHC sections taken from the core of tumour.E and F: CD31 vessel area (green mask area normalised to total tumour area) on CD31 IHC sections takenfrom the core of tumour. G and H: ASMA vessel coverage of CD31+ vessels (number of red pixels/numberof red+yellow pixels, expressed as a percentage) on ASMA IHC sections taken from the core of tumour. Inall subfigures data shown as scatter plots where each data point is one tumour (biological replicate). Least square's regression line shown in black with 95% confidence intervals denoted by dotted line in (A) and (C). Pearson's or spearman's correlation coefficient shown with all p-values, p<0.05 considered significant.The following n numbers refer to the number of tumours represented in each sub-figure: for (A, E, G) n=38. For (B-H) n=18. For (C) n=31.

2.4. Discussion

2.4.1. PDXs display distinct vascular phenotypes on IHC that are model-dependent

The vascular phenotypes, assessed by measuring necrosis, hypoxia, vessel area and vessel maturity markers, of the chosen PDX models are highly diverse. The basal STG139 PDX model displayed a hypoxic and necrotic microenvironment, filled with a high density of immature vessels that are unlikely to be capable of properly delivering oxygen to the tumour mass, perpetuating the hypoxic microenvironment. In stark contrast, the other basal model STG321 lacks angiogenic ability, and presents with a mature vessel phenotype, with vessels present in the stroma surrounding cellular 'island' structures. These vessels are likely more mature and less leaky than vessels in STG139, hence are able to properly perfuse the tumour mass and deliver oxygen, resulting in less hypoxia and necrosis in STG321. On average the two basal models had a 2.8-fold difference in hypoxia levels measured by CAIX IHC and a 1.8-fold difference in ASMA covered vessels. The luminal B models also present with distinct vascular phenotypes, AB580 with a highly necrotic core and high hypoxia, and STG143 being viable and normoxic in comparison. On average, necrosis in the core of AB580 tumours was 3.4-fold higher than the core of STG143 tumours. Vessel area was low in both luminal B models, particularly in AB580, with STG139 having a 1.7-fold higher vessel area than AB580. Interestingly, the two luminal B models had similar vessel densities and vessel maturity, with AB580 even having slightly higher ASMA vessel coverage than STG143, raising questions regarding the origin of the hypoxic vs. normoxic phenotypes present in these two models respectively, which will be discussed further in Chapter 5 in relation to their growth patterns.

Using two sections from the core and outer portions of the tumour, it was apparent that some intra-tumoural heterogeneity in vascular phenotypes exists. The most stable marker was ASMA vessel coverage, which remained stable across the tumour volume in all PDXs except in STG321. Interestingly, CD31 vessel area was the least stable marker and was heterogeneous across all PDXs except AB580, however, as vessel area mostly captures the number of vessels and ASMA vessel coverage captures the functionality of

the vessels, then CD31 vessel area will be more influenced the location of the section cut compared to ASMA vessel coverage.

Other intra-tumoural heterogeneity included the presence of a necrotic core in AB580, increased necrosis from the core to outer section in STG321 and decreased hypoxia from core to outer sections in STG321 and STG143. In STG321, the preparation of the outer tumour section, which included cutting the existing FFPE block into two halves, disrupted cellular 'islands' around the tumour rim and increased necrosis here. The tissue appears to have been frayed and broken around the edge during the processing, which will result in increased necrosis upon analysis. This could explain the increased necrosis and decreased CD31 vessel area and ASMA vessel coverage seen in the outer sections of this model. The reason for the decreased CAIX expression in the outer sections of STG321 and STG143 is unclear, but could be due to differences in CAIX signalling pathways across the tumour volume[208]. Other hypoxia markers such as pimonidazole exogenous staining would be useful to colocalise with CAIX expression in the future and validate that the CAIX expression is truly indicative of hypoxia and not confounded by expression arising from other pathways[207]. Importantly, despite some intra-tumoural heterogeneity when comparing the core and outer sections, the same overall conclusions remain the same for each marker: STG139 was the most necrotic and hypoxic PDX of the models investigated, with the highest vessel density while STG321 had the highest vessel maturity and was the least angiogenic PDX.

A major finding of this chapter is that the vascular phenotypes formed are model-dependent, not subtype-dependent. Although only 2 models of each subtype have been presented due to the lack of engraftment of additional models, these findings suggest that there may be a huge amount of diversity in vascular phenotypes within molecular subtypes, such that grouping vascular features by molecular subtype may not be useful. Because each PDX forms its own distinct vascular phenotype, the formation of vasculature in PDXs is driven by the cancer cells within the PDX itself, and not by the mouse host. This suggests that the human PDX cancer cells are instructing the mouse stromal cells to form distinct phenotypes. This idea will be further explored in Chapter 5 when interpreting data from RNA-sequencing of the PDX cancer cells.

2.4.2. PDX vascular phenotypes are robust and repeatable

STG139 and AB580 showed little inter-passage heterogeneity. The PDXs show variability in measurements such as necrosis, however this variability does not appear to be introduced by passaging and the overall phenotypes do not change significantly with passaging. Note, however, that all passages are related, ultimately by originating from a single patient tumour, but in this study through the fragments from tumours in the previous passage being re-implanted to create the next passage; these relationships are listed in **Table 2.2**. The nature of passaging may introduce bias, which was not formally assessed in this thesis, but this is also the nature of working with PDX models. One would therefore assume there to be little passage-dependency, unless differences in batches of mice or variables relating to the surgery were to dramatically influence results, which does not seem to be the case in this work. Interestingly, tumour fragments were implanted withoutcontrol on the spatial location that they came from in the tumour, yet this does not appearto have introduced significant heterogeneity in the overall vascular phenotype.

Despite some variability in the passage repeats, it should be noted that the data across three passages includes both original and repeated data and none of the conclusions change as a result of the passage repeats. Therefore, it seems as though the values obtained for the repeats fit within the permissible variability of each model.

Preservation of intra-tumoural heterogeneity and the genetic landscape of the patient, across several passages, is considered one of the biggest advantages to using patient-derived xenografts as an alternative preclinical model to cell-line xenografts[9]. Although there is some debate over the evolution introduced by the mouse host environment on the PDX genetic landscape[198,209], samples from the Caldas lab biobank, which is where the 4 PDXs presented here are sourced from, have been shown to accurately preserve gene expression, DNA methylation, copy number alterations, mutation profiles, morphology and importantly drug treatment response from the patient's from which they were derived[10]. Here, I have shown that this remarkable genetic stability translates into vascular phenotypic stability, with preservation of vascular phenotype across several passages and an indication that this is also preserved from the patient samples.

In stark contrast, the ability of cell-line xenografts (CDXs) to accurately preserve phenotypes of clinical samples is generally poor. As a consequence of culturing conditions, clonal selectivity results in homogenous cell clones and tissue samples, and culturing can also introduce oxidative stress amounting to genetic and phenotypic changes which reflect adaptation to culturing conditions and not clinical samples[9]. One study directly comparing PDX and CDX melanoma models found higher expression of hypoxic genes including *ca9* in the CDXs, supposedly due to adaptation to cell culturing conditions that the PDXs weren't exposed to[210]. Comparing CAIX levels in the breast PDXs here to previous measurements in breast CDXs measured in our laboratory suggests that CAIX levels were similar to those measured in STG139 and AB580 but they were 3-fold higher than those measured in STG321 and STG143. Other studies have also demonstrated a lack of clinical representation by cell lines models such as one study which found drug resistant gene expression to be more similar between cell-lines from different tissue origins than they were to the clinical samples they are supposed to represent[211].

In our laboratory, the ER+ MCF-7 and ER- MDA-MB-321 breast cancer CDXs show stable and distinct vascular phenotypes[48]. CD31 vessel area was higher in the ER- tumours than the ER+ tumours, which is similar to the results presented in the 4 PDX models here. However, it should be noted that the CD31 vessel area measured in the ER- CDX was up to 4-fold higher than in the highest scoring PDX STG139 measured here, while all other PDXs had similar CD31 vessel area to the ER+ MCF-7 model, showing a larger effect size in the CDXs. Additionally, ER- tumour hypoxia, measured by CAIX, was higher while VEGF expression and ASMA vessel coverage were lower compared to the ER+ tumour. Here, there were marked differences in hypoxia, VEGF expression and ASMA vessel coverage between PDXs of the same subtype. In our previous work, the CDX phenotypes were considered to represent differences in breast cancer subtypes[48], however the results from the PDXs presented in this chapter show that there is a high degree of diversity in vascular phenotype between PDXs of the same subtype, necessitating further investigation into which vascular features (if any) are subtype-dependent.

Having shown that the vascular phenotypes appear to be preserved across several passages, I hypothesise that the 'instructions' received by the mouse host from the cancer

cells determines the vascular phenotype that forms *in vivo* and hence must originate from and be driven by the cancer cells themselves. The vascularphenotypes are inherent to the PDX, and perpetuate across several passages of the model.Therefore, I propose these breast PDXs to be robust and repeatable models of the disease vasculature.

2.4.3. Vascular markers generally do not evolve with increasing tumour size

To further investigate the inheritability of vascular phenotypes, I investigated whether these phenotypes evolve over time, and may therefore be driven by a more dynamic interaction that is heavily influenced by the mouse host, or whether the same phenotype is observed regardless of tumour size. Overall the latter was true, except for necrosis, which nearly always increases as tumours grow[48,212]. Vessel areaand ASMA vessel coverage were remarkably consistent across tumour sizes in STG139 and AB580, indicating that these phenotypes are inherent to the PDX. It should be notedthat the CD31 vessel area is normalised to the tumour area, and therefore this result indicates that the density of vessels is stable, despite the absolute CD31 vessel area increasing as tumours grew in both STG139 and AB580. This is common in tumours as they often outgrow their vessel supply and ultimately develop areas of ischaemia and increased necrosis[26], which was observed in these PDXs.

Interestingly, hypoxia levels, measured by CAIX IHC, were constitutively high in STG139 but increased with tumour size in AB580. In STG139, this constitutive hypoxia could also be associated with the passaging element of PDXpropagation. When a new tumour is implanted, this is actually a fragment of a much largertumour, and so perhaps hypoxic pathways already 'turned on' in this fragment continue to be expressed in the new smaller tumour, and drive the formation of immature vascularnetworks in STG139. Ultimately these immature vascular networks are not able to properly perfuse the tumour, perpetuating and perhaps even exaggerating the hypoxic phenotype. In AB580, although CAIX levels begin at a high level of 30% they rise to ~50% as tumour volume increases, suggesting that the sparse vessel network in AB580 cannot deliver adequate oxygen to the growing tumour, resulting in increased hypoxia as tumours grow.

2.4.4. Future work

There are several advancements to this investigation of IHC vascular markers in PDXs that should be conducted in the future.

The addition of further markers to more broadly characterise themicroenvironment would help with interpretation of the findings in this chapter. Such a study could be enabled through multiplexed IHC in the same section, or through a technology such as imaging mass cytometry (IMC)[73], to gain increased spatial information on the co-localisation of vascular elements with hypoxia and fibrosis or immune cell components. This would provide more information on how the different TME elements interact and could indicate which TME elements are important forremodelling the vasculature. It would also be possible in future to use emerging technologies for spatial transcriptomics to link the vascular phenotype to the underlying genotype in a spatially resolved manner. These new technologies provide an exciting route to better understand the nature of the instructions given by the cancer cells in forming new vessels within PDX tumours. Additionally, the use of TUNEL staining should be conducted to mark areas of cell death and confirm the findings on H&E, particularly as the levels of necrosis measured on H&E were found to be very variable within STG139 and AB580.

One element of the vascular microenvironment that was not considered during the preparation of this thesis was vascular mimicry (VM), as an alternative vessel forming mechanism in tumours. VM is defined as the ability of cancer cells to form vessel-like structures themselves, which are capable of carrying blood[39,44,48]. Hypoxia is thought to regulate VM and therefore, analysing stainings such as CD31/periodic-acid Schiff dual staining will be conducted in the future to give an indication on which vessels are lined with endothelial cells and which are lined with tumour cells, and whether the more hypoxic PDXs are also more VM prone.

2.4.5. Limitations

Despite the knowledge gained by conducting vascular IHC on the four different breast PDXs, there are several limitations of this work to consider. First, the use of only 2 sections decreases the spatial heterogeneity captured, although intra-tumoural heterogeneity appears limited in the present PDXs (**Figure 2.4-10**). To increase the volume

captured and gain spatial information of the IHC markers, 3D IHC could be conducted and algorithms to enhance section co-registration between 100s of sections are being investigated[213]. Nonetheless this method is very laboursome and destroys the tissuesample for future use.

Second, I have attempted to describe inter-passage heterogeneity of markers, but I could only do so with 2 models over 3 passages in the time allocated for preparation of this thesis. Looking at IHC markers across several passages would of course provide a trajectory for analysis, particularly on interesting observations such as a trend for increased CAIX expression in STG139 across passages, which could indicate selectivity for a hypoxic phenotype in this model. Additionally, the engraftment rate of AB580 across passages and repeats was very variable, such that in one passage and one repeat only 2 mice grew tumours, limiting the interpretation of the results. In general, luminal B PDXs had a much lower engraftment rate than the basal PDXs, likely due to differences in the aggressiveness of the tumours. The lower engraftment rate in itself could lead to selection effects in the emerging tumours of later passages.

Finally, the comparison to patient tissue is limited due to clinical restrictions on the tissue blocks. Currently, only previously stained TMA sections were available for STG321, AB580 and STG143 and only one H&E sample for STG139. In future, whole sections from the original blocks should be taken and stained with the presented vascular IHC panel, quantified and scored blindly by a pathologist. It should be noted that comparison to other clinical breast IHC is also limited, due to the semi-quantitative nature of most studies, which only score sections and the limited sample size of clinical tissue[214–216]. Nevertheless, the staining intensity and distribution of necrosis, CAIX and CD31 vessel area in clinical breast samples is similar to that observed in this work[200,214]. Interestingly,the association of vascular phenotypes with molecular subtypes is debated, and perhaps the PDXs can provide more insight into the diversity of vascular phenotypes in breast cancer.

2.4.6. Summary

This chapter has presented quantitative IHC evaluation of the vascular phenotypes formed in 4 breast PDXs. The PDXs displayed distinct vascular phenotypes on IHC, with differences in necrosis, hypoxia, vessel area and vessel maturity. This work shows that

vascular phenotypes are important when selecting PDXs for specific biological assays and the diversity observed suggests that these are potential models to be used in imagingand therapeutic studies, where some models may be resistant to therapy and others more responsive as a result of these different vascular phenotypes. The panel of IHC markers presented here could be used routinely when selecting PDXs and other models for imaging and drug studies and perhaps for stratifying patients for therapies in future. ThesePDXs appear to be robust and reliable vascular models of the disease, with little inter- passage heterogeneity observed and initial comparisons to patient vasculature were made. Finally, little evolution in vessel density or maturity was seen as tumour size increased.

IHC has provided a comprehensive molecular and cellular overview of thevascular phenotypes present in these breast PDXs. Nonetheless, to conduct IHC it is necessary to excise the tissue at a fixed time point, and by analysing just a few sections, the temporal and spatial dynamics of the TME are not captured by this method. Despite attempts to monitor evolution of the vascular markers presented here, IHC cannotaccomplish truly longitudinal imaging as the same mice are not monitored over time. In subsequent chapters, the knowledge gained by IHC will be combined with non-invasive PAI conducted in the same mice during tumour evolution. High-resolution PAI has been applied to monitor the same mouse at multiple time-points to visualise vascular evolution of the PDXs in a volumetric mode that is not possible with IHC, while tomographic PAI has captured tumour vascular dynamics across an imaging session, gaining improved spatial and temporal information on the dynamics of the TME than with IHC alone. In turn, IHC is used to validate our *in vivo* imaging biomarkers as a gold-standard method, which has previously been conducted occasionally in PAI preclinical studies using cell-line xenografts[48,107,126], and here conducted for the first time in breast PDXs.

3 OPTIMISING MESOSCOPIC PAI ACQUISITION AND ANALYSIS FOR VISUALISATION AND QUANTIFICATION OF TUMOUR VASCULATURE

The work presented in this chapter is the result of a close collaboration across a large team, bringing together a broad range of expertise. I optimised the mesoscopic PAI imaging methodology for data acquisition from in vivo tumour models in the laboratory.I subsequently conceived the work described herein and supervised the development and validation of the entire analysis pipeline by: directing the work, collating and interpreting the results, performing all in vivo imaging and analysing the correlations between in vivo data and IHC.

Contributions from others in the team are as follows: Dr Paul Sweeney developed the in silico vascular networks, the 3D ROI CNN (using in vivo data collected by myself), calculated blood volume and ran network structural and topological data analysis throughout this chapter; Dr Bernadette Stolz developed the structural and topological

data analysis code supervised by Professor Heather Harrington and Professor Helen Byrne; Dr Janek Gröhl and Thierry Lefebvre ran the photoacoustic imaging simulation on the in silico vascular networks; Thierry Lefebvre developed the ilastik random forest pipeline and optimised vesselness filtering, both under my supervision, and calculated SNR for in silico and phantom datasets; Dr Ziqiang Huang developed the pre-processing, auto-thresholding, vesselness filtering and median filtering elements of the pipeline using my in vivo data and under my supervision; Lina Hacker created and imaged the string phantom; and Dr Dominique Laurent-Couturier calculated mean-squared error and R-squared values for the in silico data and analysed pairwise comparisons for the in vivo data. The histopathology core at CRUK CI ran the IHC and created algorithms for analysis under my guidance.

Parts of this chapter have been submitted for publication as Brown, Sweeney and Lefebvre et al. Quantifying Vascular Networks in Photoacoustic Mesoscopy.

3.1. Introduction

3.1.1. The potential of mesoscopic PAI

Tumour blood vessel networks are often chaotic and immature[15–17,121,217], with inadequate oxygen perfusion and therapeutic delivery[27,28]. The association of tumour vascular phenotypes with poor prognosis across many solid cancers[217] has generated substantial interest in non-invasive imaging of the structure and function of tumour vasculature, particularly longitudinally during tumour development. Imaging methods that have been tested to visualise the vasculature include whole-body macroscopicmethods, such as computed tomography and magnetic resonance imaging, as well as localised methods such as ultrasound and photoacoustic imaging[217]. Microscopy methods can achieve much higher spatial resolution but are typically depth limited at up to ~1 mmdepth and frequently applied *ex vivo*[217–221].

Of the available tumour vascular imaging methods described in Chapter 1 (**Table 1.1**), photoacoustic imaging (PAI) is highly scalable, being applicable for studies from

the microscopic to macroscopic regimes. By measuring ultrasound waves emitted from endogenous molecules, including haemoglobin, following the absorption of light, PAI can reconstruct images of vasculature at depths beyond the optical diffraction limit of ~1 mm[98–100,221]. State-of-the-art mesoscopic systems now bridge the gap between macroscopy and microscopy, achieving ~20 μm resolution at up to 3 mm in depth[111,112]. Due to this penetration depth limitation, label-free mesoscopic PAI has been mostly considered for dermatological imaging in the clinic, with many advances made in imaging vascular structures associated with psoriasis and other skin conditions[111,222]. Pre- clinically, label-free mesoscopic PAI can provide insight into several inflammatory conditions involving vascular network abnormalities, as well as oncology[223]. MesoscopicPAI has been used to monitor the development of vasculature in several tumour xenograftmodels[107,109,113] and can differentiate aggressive from slow-growing vascular phenotypes[113]. Studies to date, however, have been largely restricted to qualitative analyses due to the challenges of accurate 3D vessel segmentation, quantification and robust statistical analyses [107,109–111,113,224]. Instead, PAI quantification is typically manual and ad-hoc, with 2D measurements often extracted from 3D PAI data[107,108,110,113,115], reducing repeatability and comparability across datasets.

3.1.2. Segmenting and analysing vascular networks

To assess the performance and accuracy of such vessel analyses, ground truth datasets are needed with *a priori* known features[225]. Creating full-network ground truth reference annotations could be achieved through comprehensive manual labelling of PAI data, but this is difficult due to: the lack of available experts to perform annotation witha new imaging modality; the time taken to label images; and the inherent noise and artefacts present in PAI data. Despite the numerous software packages available to analyse vascular networks[121], their performance in mesoscopic PAI has yet to be evaluated, hence there is an unmet need to improve the quantification of vessel networksin PAI, particularly given the increasing application of PAI in the study of tumour biology[107,111,113].

To quantify PAI vascular images and yield further insights into the role of vessel networks in tumour development and therapy response, accurate segmentation of the

vessels must be performed[121]. A plethora of segmentation methods exist and can be broadly split into two categories: rule-based and machine learning-based methods. Rule-based segmentation methods encompass techniques that automatically delineate the vessels from the background based on a custom set of rules[226]. These methods are limited in flexibility and tend to consider only a few features of the image, such as voxel intensity[107,113–115] but are easy-to-use with no training dataset requirements. On the other hand, machine learning-based methods, such as random forest classifiers, delineate vessels based on self-learned features[226,227]. Nonetheless, learning-based methods are data-driven, requiring large and high quality annotated datasets for training and can have limited generalisability to new datasets. To tackle some of these issues, several software packages have been developed in recent years, which have become increasingly popular in life science research[121,228,229]. Prior to segmentation, denoising and feature enhancement methods, such as Hessian-matrix based filtering, can also be applied to overcome the negative impact of noise and/or to enhance certain vessel structures within an image[117,119,118].

3.1.3. Summary

This chapter will explore the capabilities of a new commercial mesoscopic PAI system, raster-scanning optoacoustic mesoscopy (RSOM), to image breast PDXs. In order to visualise vascular networks at high-resolution *in vivo*, optimisation of image acquisition was necessary, as the system had never been used in breast PDX imaging previously, and has only been reportedly used twice before on tumour cell-line xenograft models[107,109]. Once image acquisition was optimised, segmentation and analysis of the vascular networks captured was validated. Chapter 4 will subsequently describe how the RSOM image acquisition and analysis pipeline established in this chapter was applied to the characterisation of breast PDX vascular networks longitudinally.

Segmentation and analysis optimisation was conducted in collaboration with other lab members. Ground truth PAI data was generated using simulations of synthetic vascular architectures generated *in silico* and in addition, using a string phantom as a real-life imaging object of known proportions. The performance of two common vessel segmentation methods was compared and validated, with or without the application of

vesselness filtering, against these ground truths. Following skeletonisation of the segmentation masks, structural and topological data analyses were performed to establish how segmentation influences the shape and structure of a vascular network acquired using PAI. Finally, the segmentation and analysis pipeline was applied to two breast PDXs (STG139 and AB580) and undertook a biological validation of the segmentation and subsequent structural and topological metrics using the *ex vivo* IHC vascular panel described in Chapter 2.

3.2. Methods

3.2.1. Mesoscopic photoacoustic imaging

3.2.1.1. Animals

Breast PDXs were established as described in 2.2.1 and tumours collected for IHC as described in 2.2.2. For this work, 5 STG139 passage 3 tumours and 3 AB580 passage 2 tumours were utilised specifically for RSOM image acquisition. One image of 6 STG139 passage 4 and 8 AB580 passage 3 tumours captured when tumours were ~1 cm in diameter at end-point were used as a subset to test the segmentation pipelines. Details of RSOM PDX images used for analysis training are detailed in **Table 3.1**.

3.2.1.2. String phantom

A string phantom was used as a ground truth structure. The agar phantom was prepared as described previously[152] including intralipid (Merck, I141-100ML) to mimic tissue-like scattering conditions. The string phantom was prepared according to a previously characterised recipe[152] by mixing 1.5 g agarose (Fluka Analytical, 05039-500G) in 97.3 mL deionised water in a glass media bottle and heated in a microwave until the solution turned clear. After cooling down the solution to 60°C, 2.08 mL of pre-warmed intralipid (Merck, I141-100ML) was added to generate a reduced scattering coefficient of 5.0 cm^{-1}, which mimics tissue-like scattering conditions. The mixture was poured into a 3D-printed phantom mould, which was designed in Autodesk Fusion 360 (San Rafael, CA, USA) and printed using an Anet A6 Printer with polylactic acid (PLA PRO 1.75 mm Fluorescent Yellow PLA 3D Printer Filament, 832-0254, RS Components, UK) as a base material. **Figure 3.1** shows the phantom mould with and without agar. Red-coloured synthetic fibres (Smilco) were embedded at three different depths defined by the frame of the phantom to provide imaging targets with a known diameter of 126 μm. The top string was positioned at 0.5 mm from the agar surface, the middle one at 1 mm, and the bottom one at 2 mm (**Figure 3.1**).
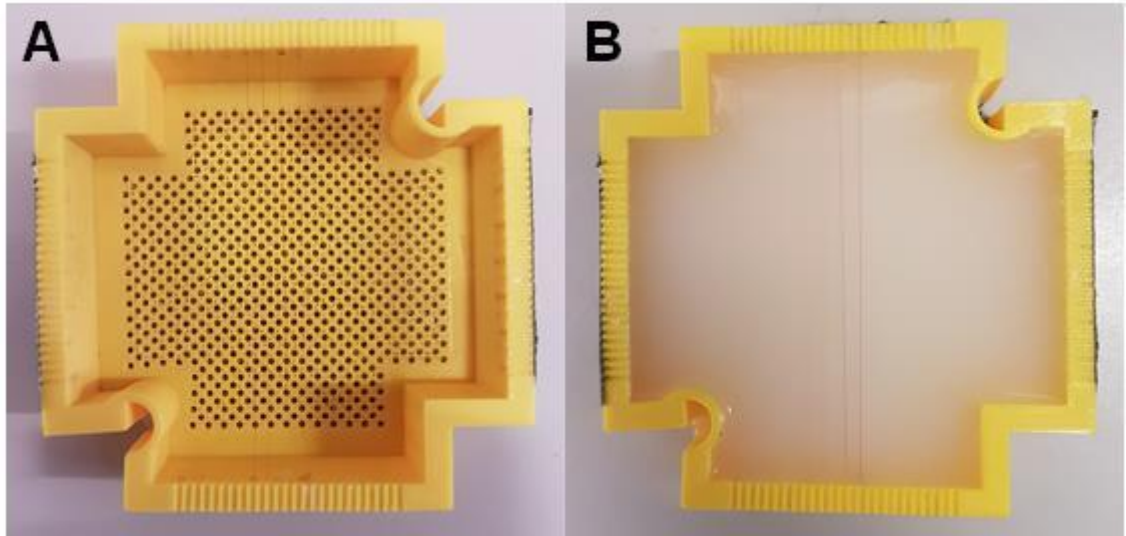
Figure 3.1. Photographs of the string phantom. (A) 3D-printed mould with the embedded strings and (B) with the agar gel. The top string was positioned at 0.5 mm from the agar surface, the middle one at 1 mm, and the bottom one at 2 mm depth.

3.2.1.3.   RSOM imaging

Mesoscopic PAI was performed using the raster-scan optoacoustic mesoscopy (RSOM) Explorer P50 (iThera Medical GmbH, **Figure 3.2**). The system uses a 532 nm laser for excitation. Two optical fibre bundles are arranged either side of a transducer, which provide an elliptical illumination beam of approximately 4 mm x 2 mm in size. The transducer and lasers collectively raster-scan across the field-of-view, which has a maximum size of 12x12 mm, with step sizes of 20 μm in the x- and y- axes. A high-frequency single-element transducer with a centre frequency of 50 MHz (>90% bandwidth) detects ultrasound. The system achieves a lateral resolution of 40 μm, an axial resolution of 10 μm and a penetration depth of up to ~3 mm[230].

For image acquisition of both phantoms and mice, degassed commercial ultrasound gel (AquaSonics Parker Lab) was applied to the surface of the imaging target for coupling to the scan interface. Images were acquired at either 100% (phantom) or 85% (mice) laser energy and a laser pulse repetition rate of 2 kHz (phantom) or 1 kHz (mice). Lower energies were recommended for mice imaging by the manufacturer, so as not to risk burning the skin. Image acquisition took approximately 7 min. Animals were anaesthetised using 3-5% isoflurane in 50% oxygen and 50% medical air. Mice were shaved and depilatory cream applied to remove hair that could generate image artefacts;

single mice were placed into the PAI system, on a heat-pad maintained at 37°C. Respiratory rate was maintained between 70-80 bpm using isoflurane (~1-2% concentration) throughout image acquisition.

Optimisation of RSOM *in vivo* tumour image acquisition was performed. Several mechanisms were explored to delineate the tumour including the use of marker pens, parafilm, ultrasound gel quantity and compression. Two different mouse body positions were explored: dorsal and lateral. The positions are illustrated in **Figure 3.3**. In this chapter, only images from the dorsal position are considered in the *in vivo* subset for simplicity, as these were of better visual quality in both STG139 and AB580 tumours.
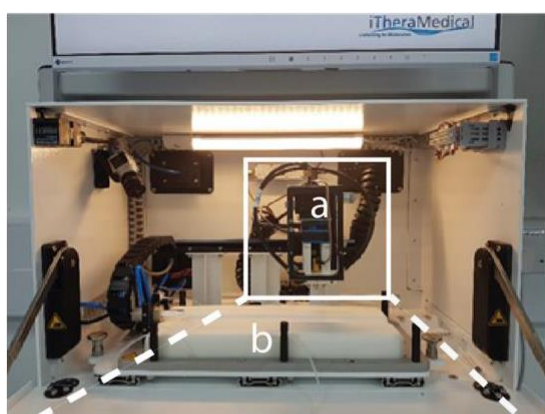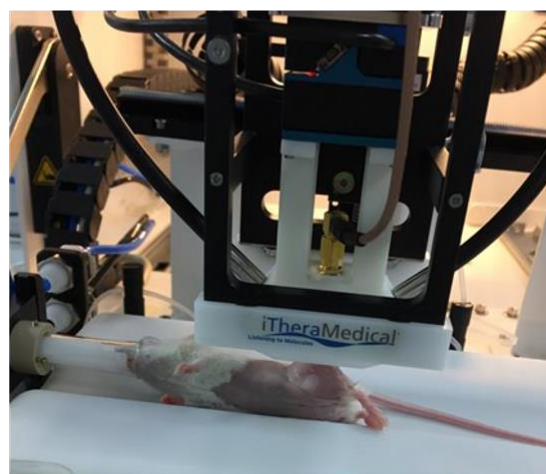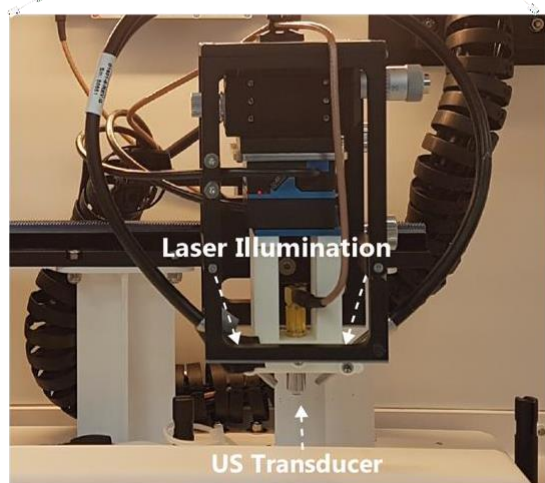
Figure 3.2. RSOM system design. A) RSOM imaging chamber laser illumination delivered by 2 optical fibres which sit either side of a single-element ultrasound transducer. A heat-pad is present for small animal imaging. B) Anaesthetised mouse on the heat pad, shaved and prepared for imaging, with ultrasound gel over the tumour region on the mouse flank, and a water bath covering the transducers and optical fibres, for ultrasound coupling.
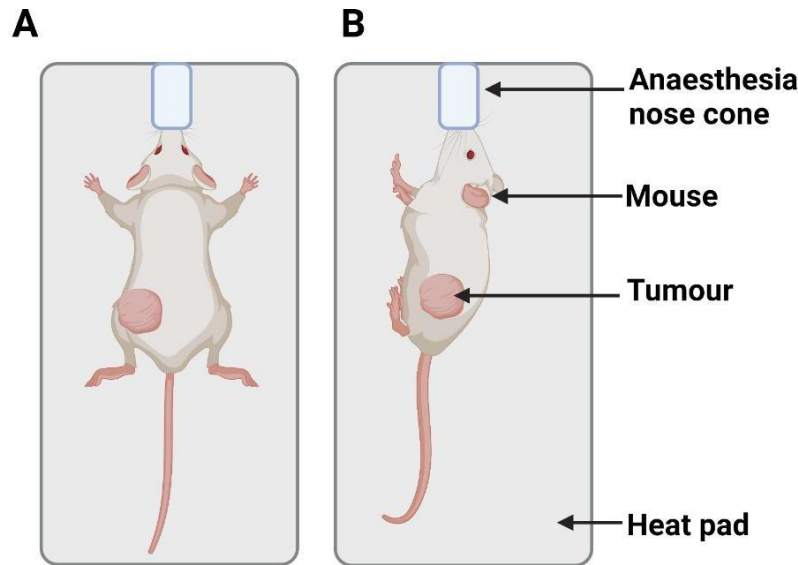
Figure 3.3. RSOM mouse positions. Illustration demonstrating the two mouse body positions explored when optimising RSOM image acquisition in vivo. Images show mouse with one tumour on the flank lying on heat pad under anaesthesia delivered via a nose cone in A) Dorsal or B) Lateral position. Image created using BioRender.com.

3.2.2. *In silico* experiments

3.2.2.1. Generating ground truth vascular architectures

To generate an *in silico* ground truth vascular network, Lindenmayer systems[231] were used. These are language-theoretic models that were originally developed to model cellular interactions but have been extended to model numerous developmental processes in biology[232]. Here, Lindenmayer systems were applied to generate realistic, 3D vascular architectures[233,234] (referred to as L-nets) and corresponding binary image volumes. A stochastic grammar was used[234] to create a string that was evaluated using a lexical and syntactic analyser to build a graphical representation of each L-net. To transfer the L-net to a discretised binary image volume, a modified Bresenham's algorithm[235] was used in 3D to create a vessel skeleton. Voxels within a vessel volume were then identified using the associated vessel diameter for each centreline.

3.2.2.2.Photoacoustic image simulation of synthetic ground truths

To test the accuracy of the segmentation pipelines, the L-nets were then used to simulate *in vivo* photoacoustic vascular networks embedded in muscle tissue using the Simulation and Image Processing for Photoacoustic Imaging (SIMPA) python package (SIMPA v0.1.1, https://github.com/CAMI-DKFZ/simpa)[236] and the k-Wave MATLAB toolbox (k-Wave v1.3, MATLAB v2020b)[237]. Planar illumination of the L-nets on the XY plane was achieved using Monte-Carlo eXtreme (MCX v2020, 1.8) simulation on theL-net computational grid of size 10.24 x 10.24 x 2.80 mm^3 with 20 μm isotropic resolution. The optical forward modelling was conducted at 532 nm using the optical absorption spectrum of 50% oxygenated haemoglobin for vessels (an approximation of tumour vessel oxygenation based on previously collected photoacoustic data[48]) and of water for the background. Next, the 3D acoustic forward modelling was then performed on the illuminated L-nets assuming a speed of sound of 1500 ms-1 in k-Wave. The photoacoustic response of the illuminated L-nets was measured with a planar array of sensors positioned on the surface of the XY plane with transducer elements of bandwidthcentral frequency of 50 MHz (100% bandwidth) and using a 1,504 time steps, where a time step is 5x10-8 Hz$^-$^{1}. Finally, the 3D initial PA wave-field was reconstructed using fast Fourier transform-based reconstruction[237], after adding uniform Gaussian noise on the collected wave-field.

3.2.3. Segmentation and network analysis

All acquired data were subjected to pre-processing prior to segmentation, skeletonisation, structural and topological data analysis (TDA), with an optional step of vesselness filtering also tested (**Figure 3.4**). Prior to segmentation, data were filtered in the Fourier domain in XY plane to remove reflection lines, before being reconstructed using a backprojection algorithm in viewRSOM software with motion correction for *in vivo* images (v2.3.5.2 iThera Medical GmbH) with a voxel size of 20 x 20 x 4 μm^3 (X,Y,Z). Raw data was stored as MATLAB data (*.mat) file format with a unique identifier for tracing in subsequent downstream segmentation and analyses. To reduce background noise and artefacts from the data acquisition process, reconstructed images were subjected to a high-pass filter, to remove echo noise, followed by a Wiener filter inMATLAB (v2020b, Mathworks) to remove stochastic noise which potentially originates

during image acquisition. Then a built-in slice-wise background correction[238] was performed in Fiji (v2.1.0)45 to achieve a homogenous background intensity (**Figure 3.5**).
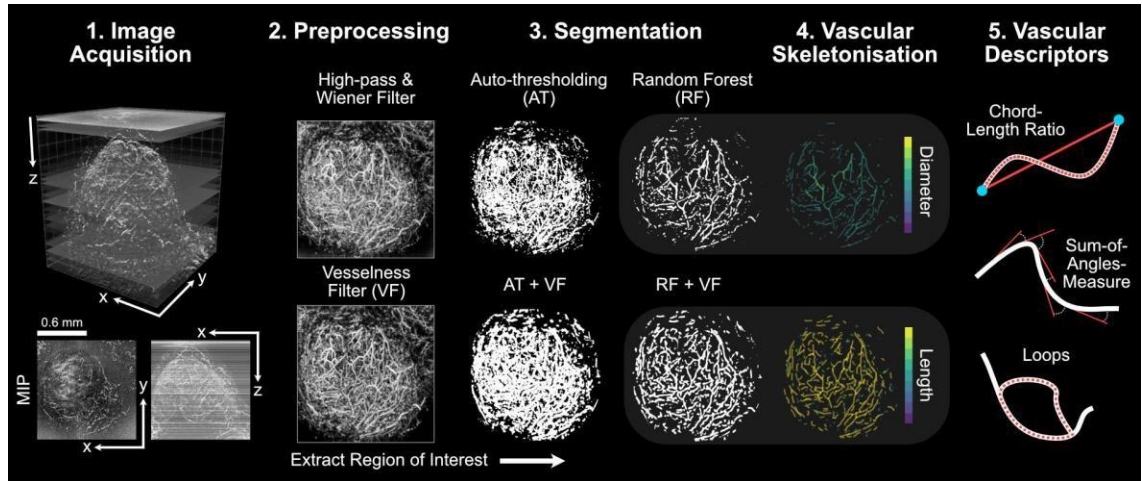
Figure 3.4. The RSOM image analysis pipeline. 1) Images are acquired and reconstructed at a resolution of 20 x 20 x 4 μm^3 (tumour example shown with axial and lateral maximum intensity projections – MIPs). 2) Image volumes are pre-processed to remove noise and homogenise the background signal (high-pass and Wiener filtering followed by slice-wise background correction). Vesselness filtering (VF) is an optional and additional feature enhancement method. 3) Regions of interest (ROIs) are extracted and segmentationis performed on standard and VF images using auto-thresholding (AT or AT + VF, respectively) or random forest-based segmentation with ilastik (RF or RF + VF, respectively). 4) Each segmented image volumes are skeletonised (skeletons with diameter and length distributions shown for RF and RF + VF, respectively). 5) Vascular descriptors including structural and topological metrics are calculated from each skeleton to quantity vascular network geometry.
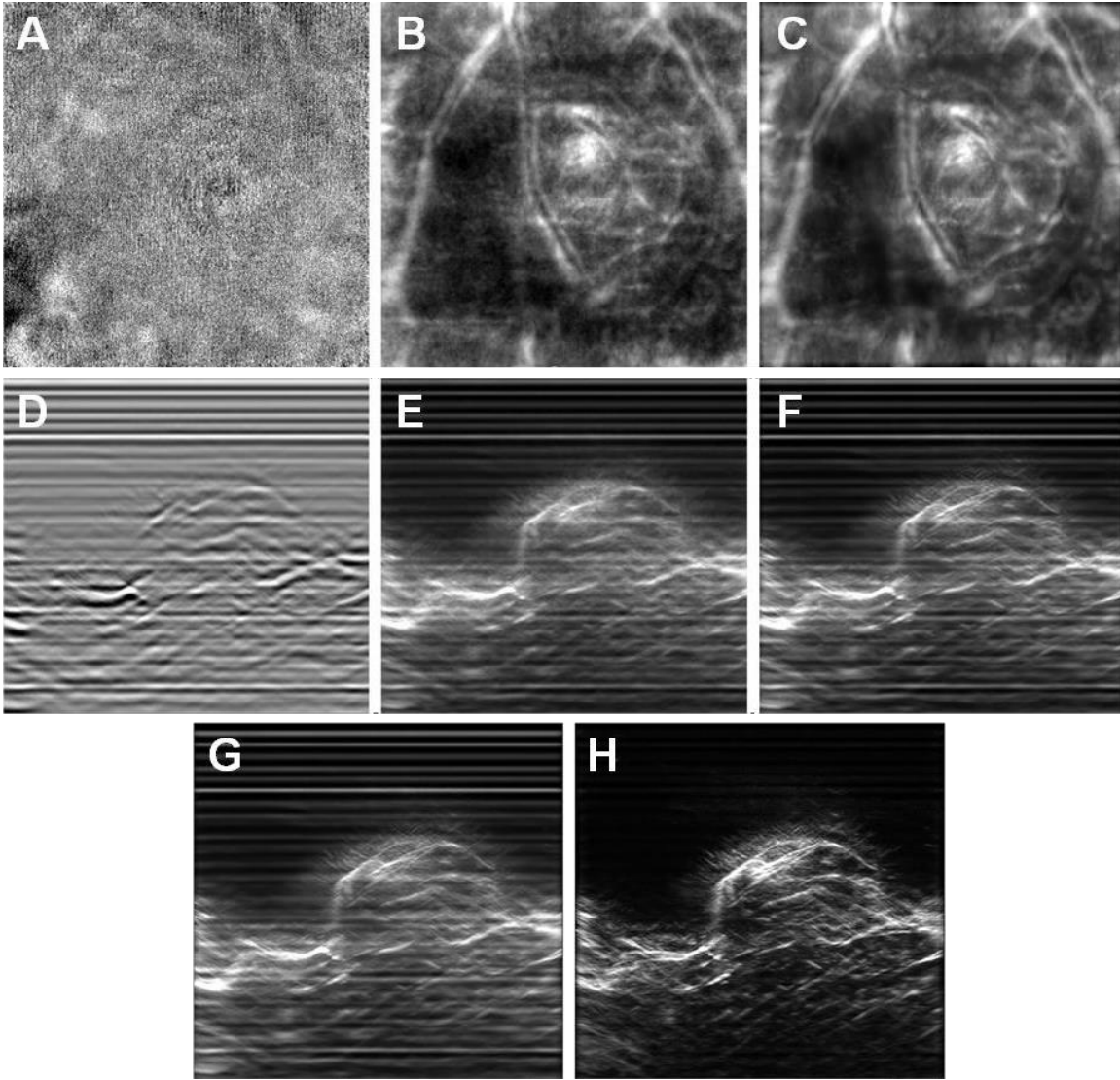
Figure 3.5. RSOM data pre-processing in MATLAB and Fiji. Mean Intensity Projection (MIP) 2D view of an example RSOM tumour dataset along Z axis (A-C) and Y axis (D-F) axis. Images measure 6 x 6 mm. From left to right: raw data (A, D), high-pass filtered data (B, E), Wiener filtered data (C, F). The images are processed sequentially through this pipeline, using high-pass filtering to remove echo noises and low-pass adaptive Wiener filtering to further remove stochastic noise in the datasets. (G) MIP Y-axis image after MATLAB pre-processing. (H) MIP Y-axis image after background correction with rolling ball subtraction in Fiji. The periodical horizontal line artefacts are mostly removed after background correction.

3.2.3.1. Image segmentation using auto-thresholding or a random forest classifier

Using two common tools adopted in the life sciences, both a rule-based moment preserving thresholding method (included in Fiji v2.1.0) and a learning-based segmentation method based on random forest classifiers (with ilastik v1.3.325) were tested (**Figure 3.4**). These popular packages were chosen to enable widespread use of theresults. Moment preserving thresholding, referred to as auto-thresholding (AT) for the remainder of this chapter, computes the intensity moments of an image and segments theimage while preserving these moments[239]. Training of the random forest (RF) backend was performed on 3D voxel features in manually labelled regions, including intensity features, as with the AT method, combined with edge filters, to account for the intensitygradient between vessels and background, and texture descriptors, to discern artefacts inthe background from the brighter and more uniform vessel features, each evaluated at different scales (up to a sigma of 5.0).

A key consideration in the machine learning-based segmentation is the preparation of training and testing data (**Table 3.1**). For the *in silico* ground truth L-net data, all voxel labels are known. All vessel labels were used for training, however, only partial background labels were supplied to minimise computational expense by labellingthe 10 voxel radius surrounding all vessels as well as 3 planes parallel to the Z-axis (edgesand middle) as background. For the phantom data, manual segmentation of the strings from background was performed to provide ground truth. Strings were segmented in all slices on which they appeared and background was segmented tightly around the string. For the *in vivo* tumour data, manual segmentation of vessels was made by a junior user (Thierry Lefebvre) supervised by an experienced user (Emma Brown), including imagesof varying signal-to-noise ratio (SNR) to increase the robustness of the algorithm for application in a range of unseen data. Up to 10 XY slices per image stack in the trainingdataset were segmented at different depths to account for depth-dependent SNR differences.

Table 3.1: Training and testing dataset split for random forest-based segmentation in ilastik.

Data	Ground truth labels	Training	Testing
In silico	Original binary labels of L-net branches and surrounding background	30 L-nets	30 L-nets
Phantom	Manual labelling of all X,Y slices containing strings and of surrounding background	2 string phantom scans	5 string phantom scans
In vivo	Manual labelling of 10 X,Y slices per image at distributed depths and of surrounding background	20 PDX tumour scans	14 PDX tumour scans

Between pre-processing and segmentation, feature enhancement was tested as a variable in the segmentation pipeline (**Figure 3.4**). In Fiji, a modified version of the original Sato filtering (α=0.25)[240] was adapted to calculate vesselness from Hessian matrix eigenvalues[241] across multiple scales. Five scales in a linear Gaussian normalizedscale space were used, from which the maximal response was measured to produce the final vesselness filtered images (20, 40, 60, 80, and 100 μm)[240].

Finally, all segmented images (either from Fiji or ilastik) were passed through a built-in 3D median filter in Fiji, to remove impulse noises (**Figure 3.6**). To summarise the pipeline (**Figure 3.4**), the methods under test for all datasets were:

1.   Auto-thresholding using a moment preserving method (AT);

2.   Auto-thresholding using a moment preserving method with vesselness filtering pre-segmentation (AT+VF);

3.   Random forest classifier (RF);

4.   Random forest classifier with vesselness filtering pre-segmentation (RF+VF).
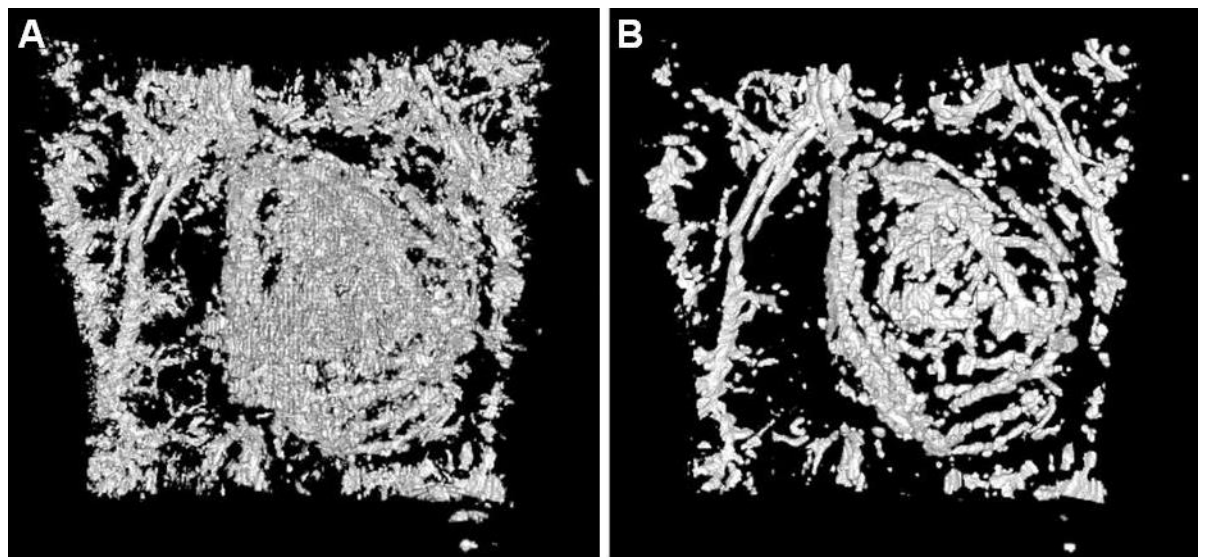
Figure 3.6. Median filtering of segmented RSOM images. A 3D rendering of the exemplar RSOM dataset used in Figure 3.5 is shown. (A) Auto-thresholded dataset. (B) Auto-thresholded dataset after 3D Median filtering, to remove impulse noise. Images field-of-view measures 6 x 6 mm.

3.2.3.2. Extracting tumour ROIs using a 3D CNN

To analyse the tumour data in isolation from the surrounding tissue required delineation of tumour regions of interest (ROIs). To achieve this, a 3D convolutional neural network (CNN) was trained to fully automate extraction of tumour ROIs from PAI volumes. The 3D CNN is based on the U-Net architecture[242] extended for volumetric delineation[243]. Details on the CNN architecture and training are provided in **Appendix 1**.

3.2.3.3. Structural and Topological Data Analysis

Following segmentation of the vascular networks, the networks were skeletonised and their shape and structure analysed using a combination of standard structural metrics (vessel diameters, lengths etc.) and topological data analysis (TDA), to evaluate the performance of the different segmentation methods in respect of the biological characterisation of the tumour networks. TDA can analyse geometric features of spatial networks and is beginning to be applied in biomedical fields, to monitor networks such as bronchial trees[244], and tumour vasculature in response to therapy[245]. Prior to TDA, segmented image volumes were skeletonised using the open-source package Russ-learn[246,247]. This package quantifies the following standard structural metrics: vessel diameters and lengths, vessel tortuosity (sum-of-angles measure, SOAM) and curvature (chord-to-length ratio, CLR) and number of edges and nodes. Following development of the package by Dr Bernadette Stolz[245], topological features were quantified: the number of connected components (CCs, Betti number $\beta0$) and looping structures (Loops, Betti number $\beta1$). **Table 3.2.** provides descriptions of vessel tortuosity, curvature and topology metrics.

Table 3.2. Structural and topological metric descriptions.

Metric	Description
Connected Components, β_0	0-dimensional topological feature i.e., the no. of subgraphs (vascular subnetworks).
Loops, β_1	1-dimensional topological feature i.e., the no. of looping structures in vascular graph.
Sum-of-angles measure (SOAM)	The sum of angles between tangents to the curve taken at regular intervals normalised against vessel length i.e., the average change in angle per unit length. Measures vessel tortuosity.
Chord-to-length ratio (CLR)	The ratio between the Euclidean distance connecting the two ends of a blood vessel and the length of the blood vessel e.g., a straight vessel has a CLR equal to 1. Measures vessel curvature.

3.2.4. Immunohistochemistry

For *ex vivo* validation, IHC was conducted for anti-human CAIX, anti-mouse CD31 and anti-mouse ASMA on core tumour sections as described in 2.2.2.

3.2.5. Statistical analysis

Statistical analyses were conducted using GraphPad Prism v.9 and R v4.0.1. Comparison of blood volume measured between dorsal and lateral mouse positions was calculated using a Spearman's rank correlation coefficient. The mean square error and R-squared statistics were used to quantify the accuracy and strength of the relationship between the segmented networks to the ground truth L-nets. For each outcome of interest,

the ground truth was predicted (on a scale compatible with the normality assumption according to model checks) by means of each method estimates through a linear model. As model performance statistics are typically overestimated when assessing the model fit on the same data used to estimate the model parameters, we used bootstrapping (R = 500) to correct for the optimism bias and obtain unbiased estimates[248]. Bland-Altman plots were produced for each paired comparison of segmented volume to the ground truth volume in L-nets and associated bias and limits of agreement (LOA) are reported. For L-nets, F1 scores were calculated[249]. PAI quality pre-segmentation was quantified by measuring SNR, defined as the mean of signal over the standard deviation of thebackground signal. Comparisons of string volume in top, middle and bottom positions, aswell as SNR, were completed using one-way ANOVA with Tukey multiplicity correction.

For each outcome of interest, *in vivo* data were analysed as follows: A linear mixed effect model was fitted on a response scale (log, square root or cube root) compatible with the normality assumption according to model checks with the segmentation methods as a 4-level fixed predictor and animal as random effect, to take the within mouse dependence into account. Noting that the residual variance was sometimes different for each segmentation group, a heteroscedastic linear mixed effect was fitted allowing the variance to be a function of the segmentation group. The results of the heteroscedastic model were preferred to results of the homoscedastic model when the likelihood ratio test comparing both models led to a p-value <0.05. Two multiplicity corrections were performed to achieve a 5% family-wise error rate for each dataset: For each outcome, a parametric multiplicity correction on the segmentation method parameters was first used[250]. A conservative Bonferroni p-value adjustment was then added to it to account for the number of outcomes in the entire *in vivo* dataset. The following pairwise comparisons were considered: AT vs. AT+VF, AT vs. RF, RF vs. RF+VF and AT+VF vs. RF+VF. Comparisons of blood volume, structural and topology metrics between STG139 and AB580 tumours were completed with an unpaired student's t-test. Comparisons between IHC and blood volume, structural and topology metrics were calculated using Pearson's or Spearman's correlation coefficient, depending on the data distribution. All p-values <0.05 were considered statistically significant.

3.3. Results

3.3.1. Optimisation of RSOM image acquisition enabled high-quality and high-resolution imaging of PDX vasculature

Before RSOM images could be analysed, optimisation of image acquisition was necessary as this was the first study performed with RSOM in breast PDXs. Initially, the SNR was low due to breathing motion (**Figure 3.7A**), the tumour region couldn't be delineated (**Figure 3.7B**), and the tumour was often cut- off in the x-axis due to poor positioning (**Figure 3.7C**). Several mechanisms were explored to delineate the tumour. Marker pens to outline the ROI caused a saturating effect (**Figure 3.7D**). Using parafilm to surround the mouse body with a small hole cut for the tumour, was unsuccessful. In collaboration with the instrument supplier a software update was installed to enable reconstructions to occur during image acquisition, allowing the transducers and optical fibres to be re-positioned and image re-taken if required. Using copious amounts of ultrasound gel improved coupling of the mouse skin to the membrane and increased SNR. Compressing the mouse body with the stage increased SNR, by reducing motion artefacts caused by breathing, which was particularly successful with smaller tumours. However, I had to ensure that excessive compression was not applied, as this could occlude blood vessels at the tumour surface (**Figure 3.8**). Breathing motion occasionally increased in the lateral compared to the dorsal position, as the tumour would lie closer to the ribcage. However, blood volume from RF segmented tumour images captured in dorsal vs. lateral positions is strongly correlated (r=0.77, p<0.001, **Figure 3.9**), so the two can be considered to capture a similar proportion of tumour vasculature. An optimum image is shown in **Figure 3.10** where the whole PDX tumour ROI is visible, the SNR is high and tumour vasculature can be visualised at high resolution with outstanding quality.
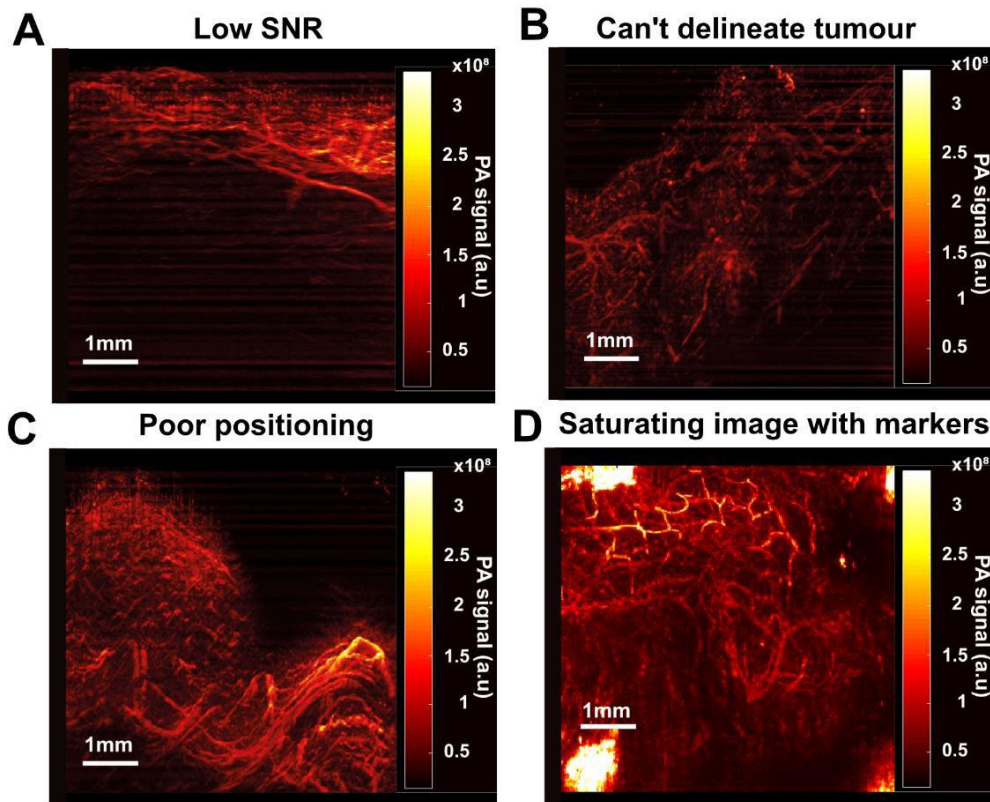
Figure 3.7 Optimisation of RSOM tumour image acquisition was necessary. A) Image shows maximum intensity projection (MIP) in zx plane where SNR is low B) Image shows MIP in zy plane where tumour cannot be delineated C) Image shows MIP in zx plane where the tumour is cut-off in the x axis due to poor positioning. D) Image shows MIP in xy plane where using marker pens saturated the image.
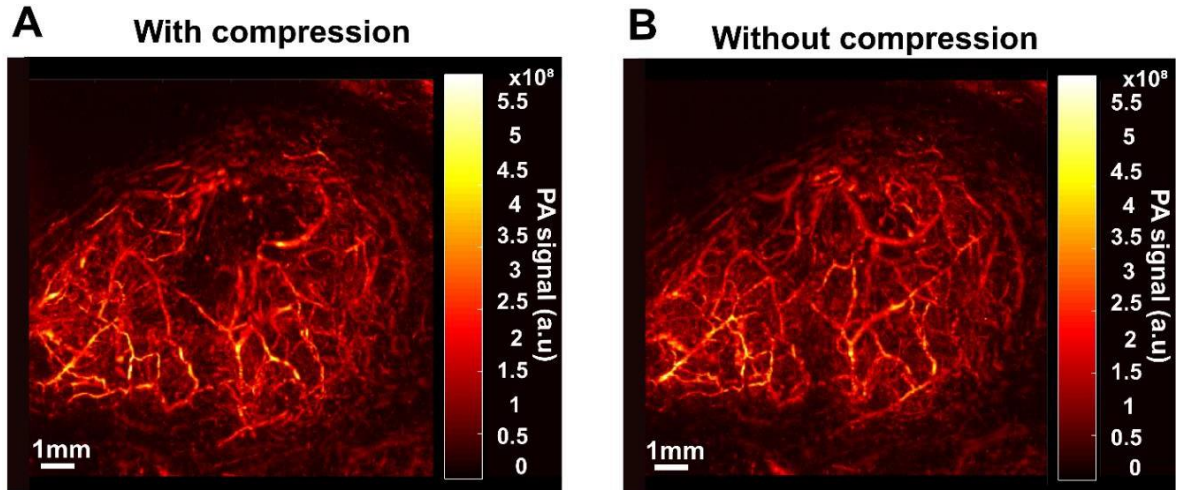
Figure 3.8. Compression of tumour with scan interface must be balanced. Despite the fact that compression was necessary to reduce breathing motion artefacts and increase SNR, the user must be careful to not compress excessively as this causes occlusion of blood vessels at the tumour surface. Images show xy MIPs A) with excessive compression causes a false void and B) without compression, showing vessels that were occluded in A.
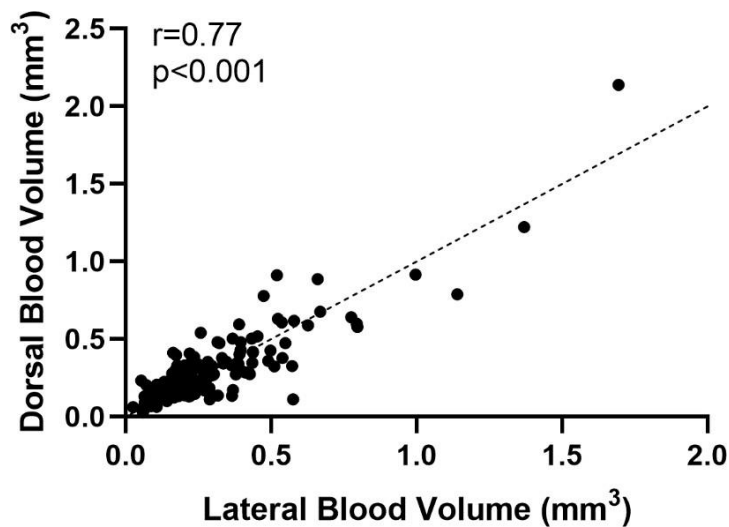
Figure 3.9. Blood volume calculated from segmented RSOM images captured in dorsal and lateral mouse positions is highly correlated. Spearman's rank correlation coefficient=0.77 $p<0.001$. Each data point represents one tumour at one time point. 1:1 dotted line shown. Number of tumour images analysed n=162.
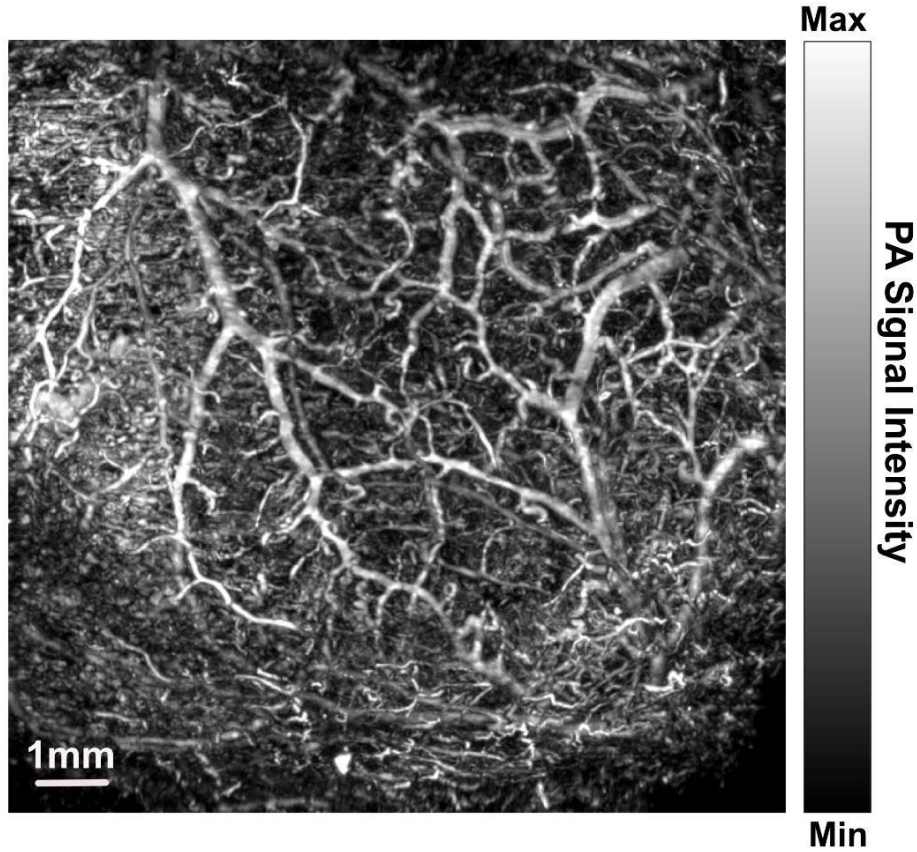
Figure 3.10. Optimal RSOM image of a breast PDX tumour. XY MIP shown.

3.3.2. *In silico* simulations of synthetic vasculature enable segmentation precision to be evaluated against a known ground truth

Having optimised RSOM image acquisition in breast PDXs, an analysis pipeline to extract features such as blood volume, vessel tortuosity and network topology metrics was developed and validated, which would enable characterisation and comparison of *in vivo* vascular networks using mesoscopic PAI. To enable image analysis, vessel segmentation must be performed. However, until this work, ground-truth mesoscopic PA images were not readily available to test the accuracy of segmentation algorithms. Here, *in silico* synthetic vascular networks are presented as a ground-truth solution, and 4 different segmentation pipelines were tested using these ground-truths.

The ground truth consisted of a reference data set of vascular network binary masks (n=30) generated from a Lindenmayer System, referred to as L-nets (**Figure 3.11A**). PAI data was simulated from these L-nets (**Figure 3.11B**), and subsequently

vesselness filtering (VF) was used as an optional and additional feature enhancement method (**Figure 3.11B**). The four segmentation pipelines selected for testing (**Figure 3.4**) were applied to the simulated PAI data (**Figure 3.11C**). Visually, random forest (RF) methods appear to segment a more complete vascular network (**Figure 3.11C**) and they are particularly good at segmenting vessels at depths furthest from the light source (**Figure 3.11D**) where SNR is lower (**Figure 3.12A**).

The segmented and skeletonised vascular volumes from the simulated PAI data were compared to the ground truth known from the L-net. The learning-based RF segmentation outperformed auto-thresholding (AT) in making the segmentation masks, with significantly higher R^2 (segmented BV: AT: 0.68, AT+VF: 0.58, RF: 0.84, RF+VF: 0.89, **Figure 3.12B** skeleton BV: AT: 0.59, AT+VF: 0.73, RF: 0.90, RF+VF: 0.93, **Figure 3.12C**) and lower MSE (**Figure 3.12D**), with respect to the ground truth L-net volumes. Bland-Altman plots, used to illustrate the level of agreement between segmented and ground truth vascular volumes, showed a mean difference compared to the reference volume of 0.61 mm^3 (LOA -0.48 to 1.7 mm^3, **Figure 3.12E**) and F1 score of 0.73 $\pm$ 0.11 (0.49-0.88) for RF segmentation, albeit with a wide variation indicated by the LOA. Vesselness filtering (VF) prior to RF segmentation resulted in a similar mean difference 0.74 mm^3 (LOA -0.50 to 2.0 mm^3, **Figure 3.12F**) and F1 score of 0.66 $\pm$ 0.11 (0.44-0.84). In comparison, the rule-based AT segmentation showed poor performance in segmenting vessels with lower signal intensity at depth (**Figure 3.11C**), yielding a mean difference of 1.1 mm^3 (LOA -0.60 to 2.8 mm^3). VF did not improve AT segmentation, yielding thesame mean difference as AT alone, *i.e.* 1.1 mm^3 (LOA -0.52 to 2.8 mm^3). (**Figure 3.12G,H**). F1 scores were also poor for both at AT methods, with0.39 $\pm$ 0.10 (0.21-0.59)for AT and 0.37 $\pm$ 0.09 (0.16-0.52) for AT+VF.

In all cases, the mean difference shown in Bland-Altman plots increased with ground truth vascular volume, especially in the rule-based AT segmentation. Such behaviour could be due to the fact that more vessel structures lie at a greater distance from the simulated light source, suffering a depth-dependent decrease in SNR (**Figure 3.12A**). RF segmentation was better able to deal with this variation, particularly beyond ~1.5 mm, compared to the AT segmentation, which consistently underestimated the vascularvolume.

Next, each segmentation mask was skeletonised to enable structural and topological data analysis (TDA) to test how each segmentation method quantitatively influences these metrics[245] and performs in respect of the biological characterisation of the tumour networks. In addition to the standard metrics of vessel diameters and lengths, vessel tortuosity (sum-of-angles measure, SOAM) and curvature (chord-to-length ratio, CLR) and number of edges and nodes, topology metrics were quantified: the number of connected components (Betti number β_0) and looping structures (1D holes, Betti number β_1) (see **Table 3.2** for metric descriptions).

Here, the accuracy between the segmented and ground truth was calculated by MSE (see **Figure 3.12D**). Across all skeletons, an increased number of connected components (β_0) and changes to the number of looping structures (β_1) were measured from the simulations compared to the ground truth L-nets, resulting in high MSE for all methods (**Figure 3.12D**), as expected due to depth-dependent SNR and PAI echoartefacts. In all other structural metrics, AT+VF outperformed the other segmentation methods in its ability to accurately preserve the L-nets structure, with the lowest MSE values for vessel lengths, chord-to-length ratio (CLR), size-of-angle measure (SOAM), number of edges and number of nodes (**Figure 3.12D**).

Vessel diameters are accurately preserved by both RF segmentation methods, supporting the observation that these methods perform accurate vascular volume segmentation. The number of edges and nodes were also well preserved by RF and RF+VF (**Figure 3.12D**). This further supports the high accuracy of both RF methods to segment vascular structures.
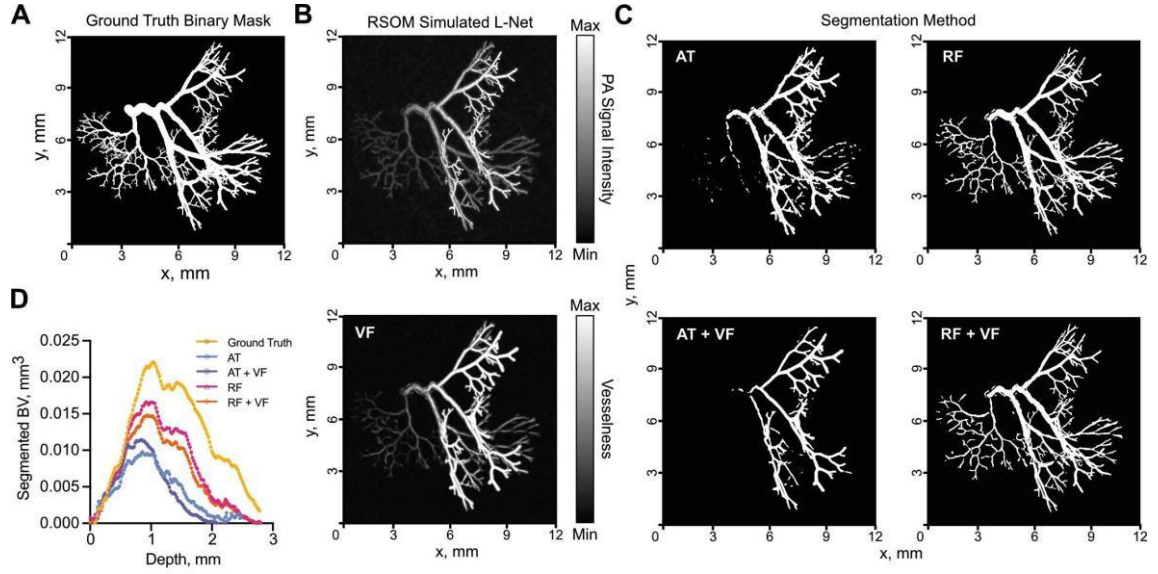
Figure 3.11. Exemplar vascular architectures generated *in silico* and processed through the RSOM image analysis pipeline. (A-C) XY maximum intensity projections of L-net vasculature. (A) Ground truth L-Net binary mask used to simulate PAI image shown in (B, top) and subsequent optional vesselness filtering (VF) (B, bottom). (C) Segmented binary masks generated using either auto-thresholding (AT), auto-thresholding after vesselness filtering (AT + VF), random forest classification (RF); or random forest classification after vesselness filtering (RF+VF). (D) Segmented blood volume (BV) average across L-net image volumes, plotted against image volume depth (mm). For (D) n=30 L-nets analysed.
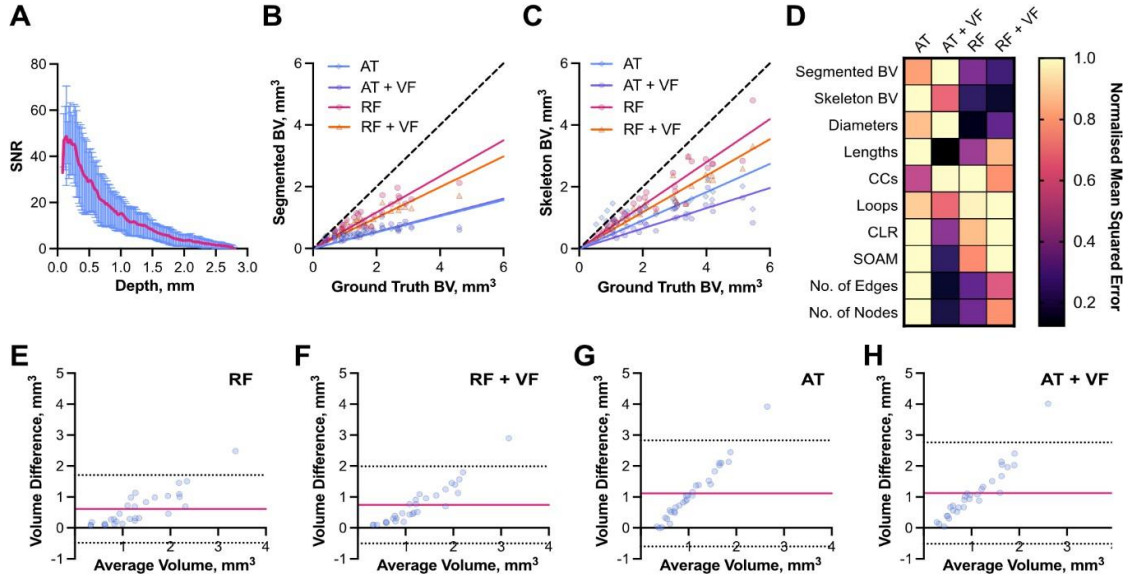
Figure 3.12. Learning-based random forest classifier outperforms rule-based auto-thresholding in segmenting simulated PAI vascular networks. (A) Depth-wise comparison of signal-to-noise ratio (SNR) measured in RSOM-simulated L-nets across depth. (B, C) A comparison between ground truth blood volume (BV) and (B) segmented or (C) skeletonised blood volumes (BV). The dashed line indicates a 1:1 relationship. (D) Heat map displaying normalised (with respect to the maximum of each individual metric) MSE comparing all metrics, calculated from segmented L-nets compared to ground truth L-nets, to each segmentation method. Abbreviations defined: connected components, β0 (CC), chord-to-length ratio (CLR), sum-of-angle measure (SOAM). (E-H) Bland-Altman plots comparing volume measurements from ground truth L-nets with that of each segmentation method: (E) RF, (F) RF+VF, (G) AT, (H) AT+VF. Pink lines indicate mean difference to ground truth, whilst dotted black lines indicate limits of agreement (LOA). For all subfigures n=30 L-nets analysed.

3.3.3. Random forest classifier accurately segments a string phantom

A phantom test object was designed to further compare the performance of the segmentation pipelines in a real-life ground truth scenario. Agar phantom scans (n=7) were acquired through raster-scanning optoacoustic mesoscopy and contained threestrings of the same known diameter (126 μm), length (~8.4 mm) and consequently volume(104.74 μm^3), positioned at 3 different depths, 0.5 mm, 1 mm, and 2 mm, respectively (**Figures 3.1 and 3.13A**). Image stacks were subsequently processed through the analysispipeline (**Figures 3.4 and 3.13B-C**).

Similar to the findings from *in silico* experiments, skeletonised string volumes decreased as a function of depth in all methods (**Figure 3.13D**), due to the decreased SNR with depth (**Figure 3.13E**). Interestingly, the significance of this decrease was very high for all comparisons (top vs. middle, top vs. bottom and middle vs. bottom) in both AT methods (all p<0.001), but there was an improvement in string volume predictions across depth for both RF methods, such that middle vs. bottom string volumes were not significantly different in RF+VF (p=0.42). For all segmentation methods, the segmented string volumes quantified are inaccurate relative to ground truth (dotted line in **Figure 3.14A**). The lateral diameter of the strings is relatively accurately determined (**Figure 3.14B**), however there is an underestimation of the diameter in the Z-direction arising from the illumination geometry of the PAI system used (**Figure 3.14C**). Only the top halfof the string is illuminated in this system, so only this half produces detectable PA signaland is segmented. Skeletonisation likely provides a more accurate prediction of string volume as it fills in the bottom half of the vessel left incomplete due to this illumination artefact, to provide a more accurate prediction of vessel diameter in the Z-axis (**Figure 3.13D** and **Figure 3.14D**).

In summary, RF methods performed better with depth-dependent decreases in SNR compared to the AT methods, which fail to segment the full extent of the string at depth.
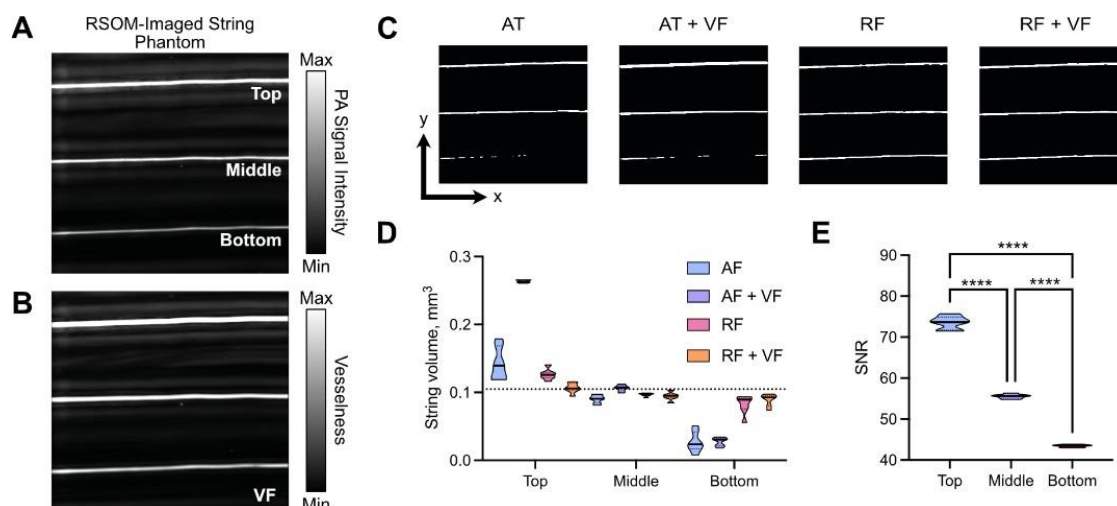
Figure 3.13. Random forest classifier outperforms auto-thresholding in segmenting a string phantom.
XY maximum intensity projections of string phantom imaged with RSOM show that random forest-based segmentation outmatches auto-thresholding when correcting for depth-dependent SNR. (A) RSOM imaged string shows measured string PA signal intensity with top (0.5 mm), middle (1 mm) and bottom (2 mm) strings labelled. (B) VF displays the string RSOM image following vesselness filtering. (C)Binary masks are shown following segmentation using: (AT) auto-thresholding; (RF) Random forest classifier; (AT+VF) vesselness filtered strings with auto-thresholding; and (RF+VF) vesselness filtered strings with random-forest classifier. (D) Skeletonised string volume calculated from segmented images of3 strings placed at increasing depths in an agar phantom. Results from all 4 segmentation pipelines are shown. Dotted line indicates ground truth volume 0.105 mm^3. All volume comparisons (top vs. middle, topvs. bottom, middle vs. bottom) where significant (p<0.05) except middle vs. bottom for RF+VF (p=0.42).
(E) SNR decreases with increasing depth. (D, E) Data represented by truncated violin plots with interquartile range (bold) and median (dotted), ****=p<0.0001. For (D) and (E) n=7 phantom scans analysed.
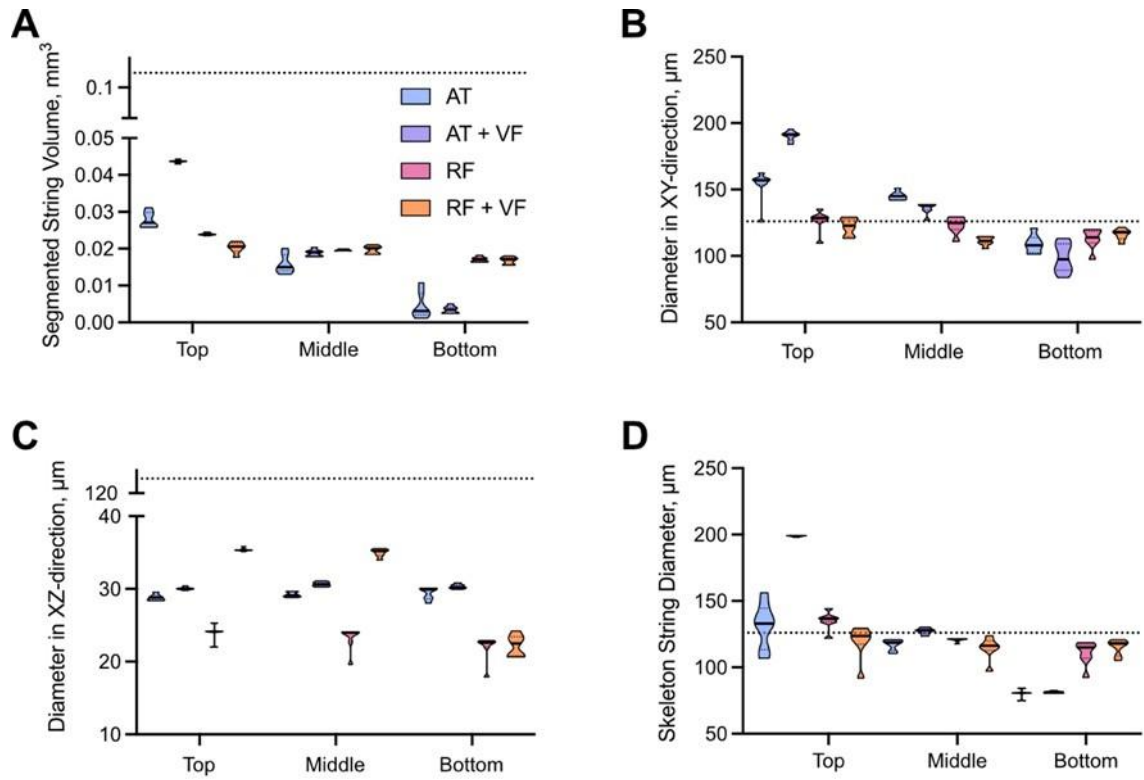
Figure 3.14. Segmented string diameters are not accurate in the Z direction resulting in inaccurate segmented volume relative to ground truth. (A) XY or (B) XZ diameter of each string segmented with the 4 segmentation pipelines. Note the ground truth diameter of 126 µm is shown with a dotted black line across both graphs. The XZ diameter is inaccurate in all methods due to the one-sided single-point illumination of the RSOM. This underestimation of XZ diameter results in an underestimation of segmented string volume (C) dotted line represents ground-truth volume of 0.10473 mm^3. (D) Diameter of string skeleton with ground truth indicated by dotted line. Data represented by truncated violin plots with interquartile range (dotted) and median (solid). For all subfigures n=7 phantom scans analysed.

3.3.4. Vesselness filtering of *in vivo* tumour images impacts computed blood volume

Having established the performance of AT and RF-based segmentation methods *in silico* and in a string phantom, the influence of the chosen method in quantifying tumour vascular networks from size-matched breast PDX tumours of two subtypes (STG139 n=6; AB580 n=8, total n=14) was investigated.

Visual inspection of the tumour networks subjected to the processing pipelines suggests that VF increases vessel diameters *in vivo* (**Figure 3.15A-C**). This could be due to acoustic reverberations observed surrounding vessels *in vivo*, which VF scores with high vesselness, spreading the apparent extent of a given vessel and ultimately increasing volume. The quantitative analysis confirmed this hypothesis, where significantly higher skeletonised blood volumes were calculated in the AT+VF and RF+VF masks compared to AT and RF alone (**Figure 3.15D**).
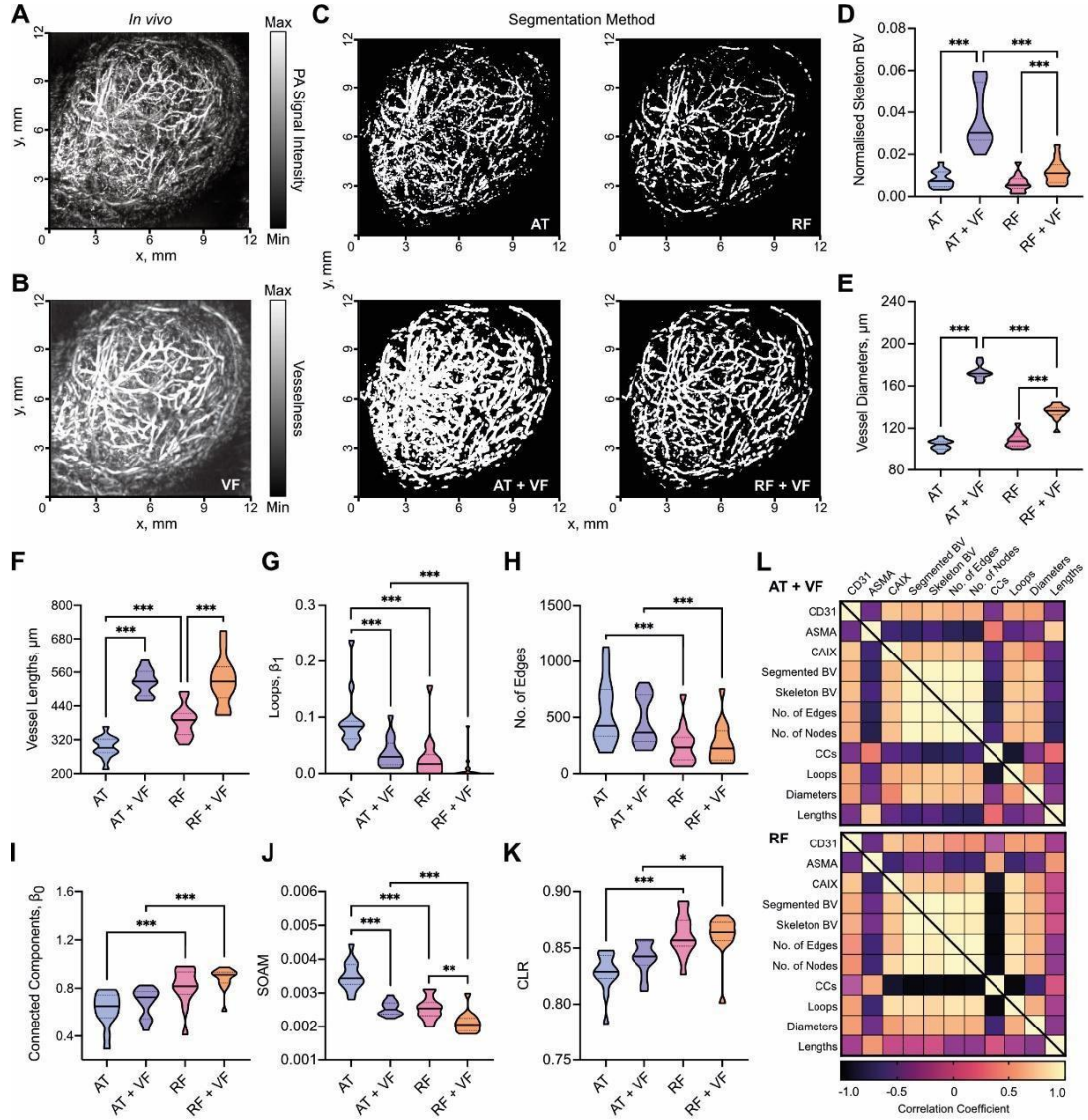
Figure 3.15. Vesselness filtering increases blood volume calculations from in vivo tumour images. XY Maximum intensity projections of breast PDX xenograft tumours imaged with mesoscopic PAI: (A) original image before segmentation; (B) original image with vesselness filtering (VF) applied; (C) a panelshowing segmentation with each method (AT: auto-thresholding, AT+VF: auto-thresholding with VF, RF:random forest classifier, and RF + VF: random forest with VF). (D) Skeletonised tumour blood volume (BV) from all 4 segmentation methods normalised to ROI volume. Structural and Topological data analysis(TDA) was performed on skeletonised tumour vessel vascular networks for the following metrics: (E) Totalnumber of edges; (F) Connected components, β_0; (G) loops, β_1; (H) sum-of-angle measure (SOAM); (I) vessel lengths; (J) vessel diameters; (K) chord-to-length ratio (CLR). In (D-K), data are represented by truncated violin plots with interquartile range (dotted) and median (bold). Pairwise comparisons of AT vs.AT+VF, AT vs. RF, RF vs. RF+VF and AT+VF vs. RF+VF calculated using a linear mixed effects model($*$= $p<0.05$, $**$=$p<0.01$, $***$=$p<0.001$,). L) Matrix of correlation coefficients for comparisons between IHC, BV, structural and TDA metrics for (top) AT+VF and (bottom) RF segmented networks. Pearson or spearman coefficients are used as appropriate, depending on data distribution. The following n numbers

111

refer to the number of tumours represented in each sub-figure: for (D) n=14, (E-K) n=13 due to imaging artefact in one tumour image which will impact network structure and topology and was therefore excluded. For (L)comparisons involving BV n=14, all other metrics n=13.

3.3.5. Topological and structural analyses of *in vivo* tumour vasculature are impacted by the choice of segmentation method

The *in vivo* segmented masks were next subjected to TDA and structural analyses. As expected from the initial *in silico* and string phantom evaluations, VF led to increased vessel diameters and lengths (**Figure 3.15E,F**), and consequently blood volume (**Figure 3.15D**). In comparison to RF methods, the *in silico* analysis indicated that AT performs poorly in differentiating vessels from noise and introduces many vessel discontinuities. This is exacerbated *in vivo* due to more complex vascular networks and real noise, leading to an increase in segmented blood volume (vs. RF p=0.01), smaller vessel lengths (**Figure 3.15F**), increased looping structures (**Figure 3.15G**), and a greater number of edges (**Figure 3.15H**).

The prior *in silico* and phantom experiments indicate that RF-based methods havea greater capacity to segment vessels at depth. Here, there was an increase in connected components for RF-based methods *in vivo* (**Figure 3.15I**). RF methods also show lower SOAM (**Figure 3.15J**) and higher CLR (**Figure 3.15K**), suggesting that RF-segmented vessels have less tortuosity and curvature, respectively, compared to AT+VF segmented vessels. Based on the *in silico* observations, it is possible that RF vessels are less tortuous than in reality, and AT+VF may better preserve this vessel feature.

These findings *in vivo* support the indications from *in silico* and phantom studies where RF-based methods provide the most reliable prediction of vascular volume,whereas AT+VF best preserves vessel structure towards the tissue surface.

Next, the TDA and structural metrics were correlated with the following *ex vivo* IHC metrics: CD31 staining area (to mark vessels), ASMA vessel coverage (as a marker of pericyte/smooth muscle coverage and vessel maturity) and CAIX (as a marker of hypoxia) to provide *ex vivo* biological validation of the *in vivo* metrics. The *in silico,* phantom and *in vivo* analyses indicated that AT+VF and RF were the top performing

segmentation methods and so I focussed on these. Note, none of the metrics derived from AT segmented networked significantly correlated with IHC metrics.

Both AT+VF and RF skeletonised blood volume correlate with CD31 staining area (r=0.54, p=0.05; and r=0.61, p=0.02 respectively; **Figure 3.15L**). This is as expected as elevated CD31 indicates a higher number of blood vessels and consequently vascular volume. The following correlations are observed for ASMA vessel coverage: vessel diameters (r=-0.41, p=0.17; and r=-0.43, p=0.14, respectively); looping structures (r=-0.68, p=0.01; and r=-0.58, p=0.04, respectively); number of edges (r=-0.69, p=0.01; and r=-0.65, p=0.02, respectively); number of nodes (r=-0.70, p=0.01; and r=-0.65, p=0.02, respectively); vessel lengths (r=0.76, p=0.03; and r=0.5, p=0.08, respectively); connected components (r=0.38, p=0.22; and r=0.59, p=0.03, respectively). Considering the strengths of AT+VF and RF, these results are biologically intuitive as tumour vessel maturation may lead to higher pericyte coverage, lower vessel density and the pruning of redundantvessels. Elevated pericyte coverage is known to decrease vessel diameters[251], whereas high vessel density resulting from high angiogenesis rates can result in immature vessel networks[217]. Pruning may lead to a reduction in looping structures and consequently an increase in vessel lengths or vascular subnetworks.

Finally, levels of hypoxia in the tumours, measured by CAIX IHC, positively correlated in both AT+VF and RF methods with skeletonised blood volume (r=0.72, p=0.007; and r=0.72, p=0.004, respectively), number of edges (r=0.59, p=0.04; and r=0.84, p<0.001, respectively), nodes (r=0.72, p=0.007; and r=0.84, p<0.001, respectively) and looping structures (r=0.61, p=0.03; and r=0.85, p<0.001, respectively).In the case of blood volume, edges and nodes, these results are expected as it has been shown that breast cancer tumours with dense but immature and dysfunctional vasculatures exhibit elevated hypoxia[48,217], likely due to poor perfusion. CAIX negatively correlated with connected components for RF networks (r=-0.87, p<0.001) (**Figure 3.15L**), reflecting results for ASMA vessel coverage.

Cross-validation between *ex vivo* IHC and vessel network analyses indicated that RF and AT+VF segmentation methods can reliably capture biological characteristics in tumours.

113

3.3.6. *Ex vivo* immunohistochemistry and network structure analyses highlight distinct vascular networks between STG139 and AB580 breast patient-derived xenografts

Finally, IHC and TDA/structure analyses were compared between the two breast PDXs represented. **Figure 3.16** presents the results of the RF segmentation method as similar trends and significances are observed using AT+VF (**Appendix 2**) unless stated otherwise.

Analysis of IHC images (**Figure 3.16A**) from this data subset showed that STG139 tumours had higher CD31 staining area (**Figure 3.16B**), less ASMA+ pericyte vessel coverage (**Figure 3.16C**) and higher CAIX levels (**Figure 3.16D**) compared to AB580 tumours. AB580 tumours were still hypoxic with CAIX expression, however, the observed level of CAIX staining is significantly lower than in STG139 tumours. The IHC data supports the structural and TDA measurements from both AT+VF and RF segmented networks where STG139 tumours had denser networks, with higher blood volume, diameter, and looping structures (**Figure 3.16E, F, G**). AB580 tumours had a sparse network but structural and TDA analysis showed more subnetworks (**Figure 3.16H**) with longer vessels (**Figure 3.16I**) which was significant in AT+VF segmented networks (**Appendix 2**), which could indicate a more mature vessel network than STG139 tumours based on prior correlative analyses above (**Figure 3.15L**). Interestingly, the differences in network maturity were not driven by differences in vessel tortuosity (**Figure 3.16J, K** and **Appendix 2**). No significant differences between the two models were observed for blood vessel tortuosity or curvature.
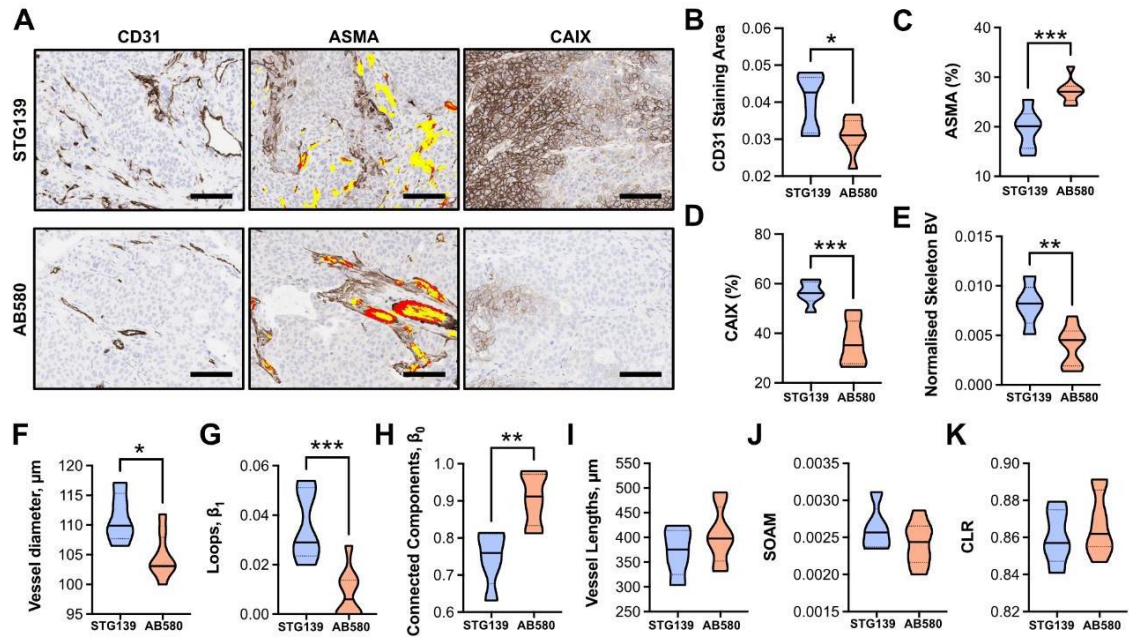
Figure 3.16. STG139 tumours have dense and immature vascular networks which result in hypoxic tumour tissue. (A) Exemplar IHC images of CD31, ASMA and CAIX stained STG139 and AB580 tumours. Scale bar=100 µm. Brown staining indicates positive expression of marker. ASMA sections display CD31 overlay, where red indicates areas where CD31 and ASMA are colocalised (ASMA vessel coverage) and yellow indicates areas where CD31 is alone. (B) CD31 staining area quantified from CD31 IHC sections and normalised to tumour area. (C) ASMA vessel coverage of CD31+ vessels (number of redpixels/number of red+yellow pixels, expressed as a percentage) on ASMA IHC sections. (D) CAIX total positive pixels as a percentage of the total tumour area pixels on CAIX IHC sections. (E-K) Structural andTopological data analyses comparing STG139 and AB580 tumours. Data are represented by truncated violin plots with interquartile range (dotted black) and median (solid black). Comparisons between STG139 and AB580 tumours made with unpaired t-test. *= p<0.05, **=p<0.01, ***=p<0.001. The following n numbers refer to the number of tumours per PDX model in each sub-figure: for (B-E) STG139 n=6, AB580 n=8. For (F-K) STG139 n=5, AB580 n=8, one STG139 tumour image is excluded with artefact that would impact network structure/topology.

3.4. Discussion

3.4.1. Optimising RSOM acquisition as a novel non-invasive method for visualising PDX vasculature *in vivo*

In order to visualise and quantify PDX vascular networks using RSOM, it was necessary to optimise the image acquisition, as this was a new system, not just in this lab but also worldwide, with very few reports of its use in imaging tumour xenograft blood vessels[107,109] and no reports of imaging PDX blood vessels. This was a challenge owing to large amounts of noise introduced by RSOM imaging *in vivo*, particularly the impact of breathing motion on SNR. Breathing motion is inevitable when imaging a live subject,and the extent of the introduced noise in the images depended on: breathing rate, breathing volume, distance from tumour to mouse ribcage, and size of tumour. Breathing rate was kept constant at 70-80 bpm, however, breathing volume was harder to control, with some mice breathing heavier than others under anaesthesia. The distance of the tumour from the ribcage could be extended by using the dorsal instead of the lateral position, which was occasionally necessary. In general, smaller tumours would suffer the effects of breathing motion more than larger tumours, and a minimum diameter of ~0.5 cm was chosen as a threshold for acceptable image quality in future work. Compression of tumours and the mouse body with the scan interface was essential to reduce breathing motion, however, excessive compression occluded vessels and created false vascular voids at the tumour surface. An optimum balance was found where sufficient compression would result in high-resolution and high quality images of tumour vasculature, in dorsal and lateral positions, without creating vascular voids.

3.4.2. Segmentation pipeline for vascular network quantification

Once RSOM image acquisition had been optimised, an image analysis pipeline was created to quantify the images. To quantify the vasculature, PA images need to be accurately segmented. Manual annotation of vasculature in 3D PAI is difficult due to depth-dependent signal-to-noise and imaging artefacts. Whilst a plethora of vascular segmentation techniques are available[121,227], their application in PAI has been limited due to a lack of an available ground truth for training, comparison and validation.

In this study, we first sought to address the need for ground truth data in PAI segmentation. Two ground truth datasets were generated to assess the performance of rule-based and machine learning-based segmentation approaches with or without feature enhancement via vesselness filtering. The first is an *in silico* dataset where PAI was simulated on 3D synthetic vascular architectures; the second is an experimental dataset acquired from a vessel-like string phantoms. These allowed us to evaluate the ability of different segmentation methods to preserve blood volume, vessel network structure and topology.

The first key finding was that machine learning-based segmentation using RF classification provided the most accurate segmentation of vessel volumes across the *in silico*, phantom and *in vivo* datasets, particularly at depths beyond ~1.5 mm, where SNR diminishes due to optical attenuation. Compared to the AT approaches, RF-based segmentation partially overcomes the depth dependence of PAI SNR since it identifies and learns edge and texture features of vessels at different scales and contrasts. Such intrinsic depth-dependent limitations are often ignored in the literature, where analyses are typically performed on 2D maximum intensity projections for simplicity[107–110,113,115], suggesting that a fully 3D machine learning-based segmentation is needed to accurately recapitulate the complexity of *in vivo* vasculatures measured using PAI.

As blood vessel networks can be represented as complex, interconnected graphs, structural and topological data analyses were applied to further assess the strengths and weaknesses of the chosen segmentation methods. This led to three further key findings: 1) for all ground truth datasets, AT underperforms across all metrics; 2) AT+VF outperforms all other methods in preserving vessel lengths, loops, curvature (CLR) and tortuosity (SOAM); 3) RF outperforms RF+VF in preserving topology.

As observed above, AT methods struggle to segment vessels with low SNR. Additionally, where intensity varies across a vessel structure, this results in many disconnected vessels when segmenting with AT alone, as only the highest intensity voxels will pass the threshold. Only when vesselness filtering (VF) is applied does AT do well at preserving network structure. VF alters the intensity values from the PA signal to a prediction of 'vesselness', generating a more homogeneous intensity across the vessel structures and ultimately a more continuous vessel structure is segmented. This likely

explains why AT+VF best preserves vessel length and subsequently vessel tortuosity, curvature and loops, while AT alone performs poorly. For AT, VF improved BV predictions *in silico* via better preservation of lengths but not diameters, as the phantom experiments indicated that AT+VF overestimates diameter. Additionally, because both RF methods preserve a greater number of subnetworks at depth than both AT methods, this likely decreased structure and topology preservation in both of these methods compared to AT+VF, due to some discontinuities in segmented subnetworks compared to the ground-truth *in silico*. This can be explored in future work, for example, by developing string phantoms with more complex topologies.

Owing to the homogenous intensity of vessels introduced by VF, one could therefore assume that RF+VF would be the most accurate method at preserving network structure and topology (by combining the machine-learning accuracy of segmentation with the shape enhancement of VF). However, this is not the case. RF alone is able to account for discontinuities in vessel intensity, unlike AT, meaning it does not rely on VF to enhance structure and topology preservation. In fact, the slight inaccuracy in diameter preservation introduced by VF *in silico* likely decreases structure and topology preservation in RF+VF compared to RF alone. In comparison, RF+VF *in silico* improved on RF BV by reducing connected components as diameter and length accuracy declines, whereas BV improved in a string phantom by more accurate prediction of diameters. All this considered, RF performs feature detection across scales in the manually labelled voxels to learn discriminating characteristics for vessel classification and segmentation. Adding VF before RF segmentation may confound this segmentation framework, because VF systematically smooths images and removes non-cylindrical raw image information, which may have been vital in the RF learning of vascular structures on the training dataset. This may explain why RF+VF was not found to be the best segmentation method, since it can only be as good as the vesselness-filtered image for learning vessel segmentation. Further, the effect of unconscious biases on segmentation performance imposed when manually labelling images with and without VF to train the classifier should be considered. The segmentation accuracy of classifiers trained by multiple users can be explored in future to formally investigate these effects.

Applying structural and TDA analysis to the *in vivo* tumour PDX subset measured

trends consistent with the *in silico* and phantom experiments, such as multiple vessel discontinuities in AT. I therefore chose to focus on the top performing methods, AT+VF and RF. Cross-validating structural and TDA analysis with *ex vivo* IHC confirmed that these two segmentation methods can reliably extract biologically relevant information from mesoscopic PA images. For example, predictions of BV correlated with endothelial cell and hypoxia markers via CD31 and CAIX staining, respectively; and metrics relating to the maturation of vascular structures correlated with ASMA vessel coverage. Applying the segmentation pipeline to compare STG139 and AB580 breast cancer PDX models showed structural and TDA analyses can capture the higher density and immaturity of STG139 vessel networks which result in decreased oxygen delivery and high hypoxia levels in comparison to AB580 tumours, which presented with a sparse but more mature vessel network.

3.4.3. Limitations

Despite the promising findings presented in this chapter, avenues of further development exist to: improve the realism of ground truth data, including advances in simulation complexity, and tissue-specific synthetic and phantom vasculatures. While the *in silico* PAI dataset incorporated the effects of depth-dependent SNR and Gaussian noise found in *in vivo* PAI mesoscopic data, further development of the optical simulations could, for example, recapitulate the raster-scanning motion of illumination optical fibres, instead of approximating a simultaneous illumination plane of single-point sources in this study. The limited aperture of the raster-scanning ultrasound transducer could not be simulated in k-Wave as it is not yet implemented for 3D structures. In terms of vascular complexity, the string phantom represented the simplest vessel networks but future work could introduce more complex and interconnected vessel-like networks in order toreplicate more realistic vascular topologies[252].

3.4.4. Future work

Interestingly, none of the *ex vivo* IHC metrics correlated with chord-length ratios or sum-of-angles-measures. This may be expected as the 2D IHC analysis does not fully encompass the 3D structural characteristics of the vascular network. 3D IHC, micro CT or light sheet fluorescence microscopy may provide improved *ex vivo* validation using

exogenous labelling to identify 3D vascular structures, such as tortuosity, atendpoint[253,254].

The past decade has also seen the rise of a multitude of blood vessel segmentation methods using convolutional neural networks and deep learning[255]. Applying deeplearning to mesoscopic PAI could provide a means to overcome several equipment- related limitations such as: vessel discontinuities induced by breathing motion *in vivo*; vessel orientation relative to the ultrasound transducer; shadow and reflection artefacts; or underestimation of vessel diameter in the z-direction due to surface illumination. Whilst skeletonisation addressed diameter underestimation and observed the influence of discontinuities on the extracted TDA metrics, they were not deeply characterised or corrected. Nonetheless, whilst deep learning may provide superior performance when fine-tuned to specific tasks, the resulting methods may lack generalisability across tissueswith differing SNR and blood structures, requiring large datasets for training. In this studyopen-source and widely accessible software to biologists in the life sciences were chosen.Such a platform shows more potential to be employed widely with limited computationalexpertise.

3.4.5. Summary

In summary, I have optimised RSOM image acquisition, segmentation and analysis with a focus on visualising and quantifying breast PDX vascular networks. Onceimage acquisition was optimised, an *in silico,* phantom*, in vivo*, and *ex vivo*-validated end-to-end framework was developed for the segmentation and quantification of vascularnetworks captured using mesoscopic PAI. *In silico* and phantom ground truth PAI datasets were created to validate segmentation of 3D mesoscopic PA images. A range ofsegmentation methods were applied to these ground-truths and to images of breast PDX tumours obtained *in vivo*, including cross-validation of *in vivo* images with *ex vivo* IHC,to analyse performance of blood vessel segmentation. Learning-based segmentation, viaa random forest classifier, best accounted for the artefacts present in mesoscopic PAI, providing a robust segmentation of vascular volume at depth in 3D and a good approximation of vessel network structure and topology. Despite the promise of the

learning-based approach to account for depth-dependent variation in SNR, auto-thresholding with vesselness filtering more accurately represents structural and topological characteristics in the superficial blood vessels as it better preserves vessel lengths. Therefore, when quantifying PA images, users need to consider relative importance of each metric as the choice of segmentation method can directly impact the

resulting analyses. This work has highlighted the potential of a combination of structural and topological data analysis to provide a detailed parameterisation of tumour vascular networks, from classic metrics such as vessel diameters and lengths to more complex topology metrics characterising vessel connectivity and loops. Our results further underscore the potential of photoacoustic mesoscopy as a tool to provide biological insight into studying vascular network *in vivo* by providing life scientists with readily deployable and cross-validated pipeline for data analysis.

4 PHOTOACOUSTIC IMAGING
OF PDX VASCULATURE

I conducted all in vivo imaging described herein, and worked in collaboration to analyse and interpret the data in relation to the PDX models, conducted statistical analyses of tomographic PAI and mesoscopic topology data and analysed correlations between in vivo data and IHC.

Thierry Lefebvre segmented the mesoscopic PAI networks using the ilastik random forest pipeline described in Chapter 3. Dr Paul Sweeney applied a 3D ROI CNN to the segmented networks to calculate blood volume and ran topological data analysis developed by Dr Bernadette Stolz, as described in Chapter 3. Dr Michal R. Tomaszewskiand Thomas Else authored and ran code to analyse tomographic PAI data. Dr DominiqueLaurent- Couturier analysed the segmented blood volume longitudinally over time usinga linear mixed effects model.

4.1. Introduction

4.1.1. The potential of PAI to visualise breast cancer vasculature

Several preclinical and clinical imaging techniques have emerged to probe the vascular microenvironment in breast cancer. These include dynamic contrast-enhanced (DCE)-MRI or DCE-Ultrasound to measure vascular perfusion[76–78] and positron emission tomography (PET) agents for hypoxia visualisation, including those derived from nitroimidazole[85,86]. Preclinical intravital imaging can monitor blood flow andperivascular changes in hypoxia[27], though this approach is invasive and has a small field-of-view.

Notably, many of the existing techniques suffer from limited spatial resolution, poor specificity from confounding signals or the need to administer contrast agents or radiopharmaceuticals[79,80,86]. Importantly, none of the techniques mentioned are capable of imaging across scales. Hence, there remains an unmet clinical need for validated imaging biomarkers of the vascular microenvironment that can be measured cost- effectively at high spatial and temporal resolution with a large field-of-view, which couldbe applied in biological research and in a clinical setting. Photoacoustic imaging (PAI) could offer the flexibility to monitor the vascular microenvironment *in vivo* across scales,without the need to administer contrast agents, providing a more complete picture of the tumour microenvironment (TME).

The potential of high-resolution, or mesoscopic, PAI to visualise preclinical tumour vasculature was introduced in Chapter 3, where I have developed a pipeline for accurate mesoscopic PA image acquisition and analysis of vascular networks in breast patient-derived xenografts (PDXs). In this chapter, the pipeline will be applied to the 4 breast PDXs introduced in Chapter 2, to monitor development of blood vessel networks in these models longitudinally. This chapter will also introduce the use of tomographic PAI to investigate vascular phenotypes in breast PDXs, utilising multiple wavelengths to visualise both Hb and HbO_2 and calculate imaging biomarkers related to total haemoglobin concentration [$THb=Hb+HbO_2$] and blood oxygen saturation [$SO_2=HbO_2/THb$]. Multi-wavelength tomographic PAI systems can capture whole tumour volumes pre-clinically and is thereby termed Multispectral Optoacoustic

Tomography (MSOT)[48,123–126]. These images are captured at a lower resolution but with a higher field-of-view compared to mesoscopic PAI. Mesoscopic and tomographic PAI have been used jointly here for the first time, to provide complementary information on the vascular microenvironment of the 4 breast PDXs non-invasively *in vivo*.

Imaging biomarkers from both mesoscopic and tomographic PAI can provide further insight into breast vasculature. Mesoscopic PAI captures vascular networks at ~40 µm resolution but at superficial depths of a few mm[109] and has so far been used in murine mammary tumour models to monitor rim-core disparities in vascularisation[123] and to monitor changes in vascular density and diameter as tumours grow[108]. Tomographic PAI achieves a resolution of ~200 µm at cm depths[125], depending on the system geometry used and was recently applied to human breast cell-line xenograft models and demonstrated a correlation between SO_2 measurements and vascular maturity, measured by pericyte/ smooth muscle coverage of vessels *ex vivo*[48]. It is likely tomographic resolutions and depths could be translated to clinic, and high-resolution techniques utilised to gain biological information pre-clinically, due to limits in penetration depth. Gas-challenge biomarkers, measured by altering the gas delivered to the mouse from air to 100% oxygen, have yet to be applied in breast cancer models but have shown promise in providing biomarkers for perfusion and hypoxia in prostate cell-line models[125,129,130].

In a clinical context, PAI has been applied in numerous clinical trials to monitor vascular features of the TME in breast cancer, where PAI can be combined with existing ultrasound imaging approaches for additional anatomical information. Multiple engineering advances have been made in recent years, with promise shown in the use of handheld probes[104,105,135], 'mammoscopes'[139-141] and hemispherical[144,145] and cylindrical[147,148] systems that cup the breast. State-of-the art clinical systems can achieve up to 7 cm penetration depth[141,142] with high resolutions of up to 255 µm reported[148], enabling visualisation of vascular networks at depth in the breast. Despite these engineering advances, little is known about the biological significance of the vascular phenotypes detected with PAI in the human breast. As the use of these systems increases in breast cancer clinical trials[136,137] it is vital that certain questions are answered, such as: which key features will give insight into underlying tumour biology and what drives the formation of these features? It is difficult to answer these questions preclinically,

particularly with the use of cell-line models, as these often do not accurately recapitulate the TME[9] and present extreme phenotypes that may not be seen in patients. In this chapter, for the first time, the use of breast PDXs in PAI is investigated, to gain insight into different elements of the vascular microenvironment of breast cancer in more clinically-relevant models of the disease.

4.1.2. Summary

This chapter will build on the work presented in Chapters 2 and 3. Here, a thorough characterisation of the vascular microenvironment in 4 breast cancer PDXs wasundertaken with 2 PAI systems at different resolutions and depths: mesoscopic PAI and tomographic PAI. This is the first reported combined use of these two modalities, gainingcomplementary information on PDX vasculature from the same biological source of contrast. This work continues to address Aim 1 of the project, and will be combined withand correlated to the molecular information provided by the IHC characterisation conducted in Chapter 2. First, blood content, oxygenation and gas-challenge analyses were conducted with already established methodology for tomographic PAI. This is accompanied by the use of a new mesoscopic PAI system and image analysis pipeline presented in Chapter 3 applied here to the 4 PDXs longitudinally, and blood volume is modelled against tumour volume using a linear mixed effects model. Structural and topological analyses were also applied to the vascular networks and I show how the twosystems provide complementary information of the vascular microenvironment in the PDXs. I show that PAI is sensitive to the different vascular phenotypes present in the 4 PDXs, meeting Aim 2 of the project and that there is little evolution of vascular phenotype, suggesting these are inherent, providing data towards Aim 4 of the project. Finally, inter-passage variability in PAI metrics is assessed, to test not only the robustnessand repeatability of the PDXs (Aim 3), but also the robustness of using the PAI systems over years in the same models, which has not been tested previously.

4.2. Methods

4.2.1. MSOT experimental procedure

MSOT was used to acquire PA images in a manner similar to previously described protocols[48,125,152]. Once tumours had reached 0.5 cm mean diameter, tumours wereimaged with multispectral optoacoustic tomography (MSOT) on several occasions (aiming for fortnightly imaging sessions with flexibility to allow for the rate of tumour volume increase and ensure MSOT images were captured throughout tumour growth). The threshold of 0.5 cm was set based on previous experiments considering feasibility of MSOT imaging and aligned with enrolment for RSOM imagingdescribed in Chapter 3. Once tumours reached ~1 cm mean diameter mice were euthanised after a final MSOT imaging session and samples collected as described in 2.2.1.

Briefly, MSOT was performed in the inVision 256-TF scanner (iThera Medical GmbH)[256]. The system uses a tunable 660-1300 nm laser. Light is delivered through ten fibre bundles to create a near-uniform diffuse illumination beam across the imaging plane. An array of transducers covering an angle of 270° detects ultrasound waves for tomographic reconstruction. The system has a spatial resolution of approximately 190 μm at 3 cm depth[125] (**Figure 4.1**).

Typically, MSOT imaging was conducted immediately after RSOM, so that induction of anaesthesia and hair removal occurred only once at the start of the session. Mice were anaesthetised using 3-5% isoflurane in 50% oxygen and 50% medical air. Mice were shaved and depilatory cream applied to prevent hairs introducing image artefacts. Respiratory rate was maintained between 70-80bpm using isoflurane (~1-2% concentration) throughout image acquisition. As described previously[48,125], a singlemouse was wrapped in a polyethylene membrane, with ultrasound gel to couple the skinto the membrane, placed into the MSOT system and immersed in water inside the imaging chamber (**Figure 4.1**). Water was maintained at 36 °C throughout the procedure. Mice were allowed to stabilise in the water for 15 min before image acquisition. The animal holder was translated along the cranial-caudal axis of the tumour, with images acquired every 1 mm. Images were acquired using 25 wavelengths between 660-1090 nm with an

average of 10 pulses per wavelength. An overall imaging session lasted approximately 10 min.
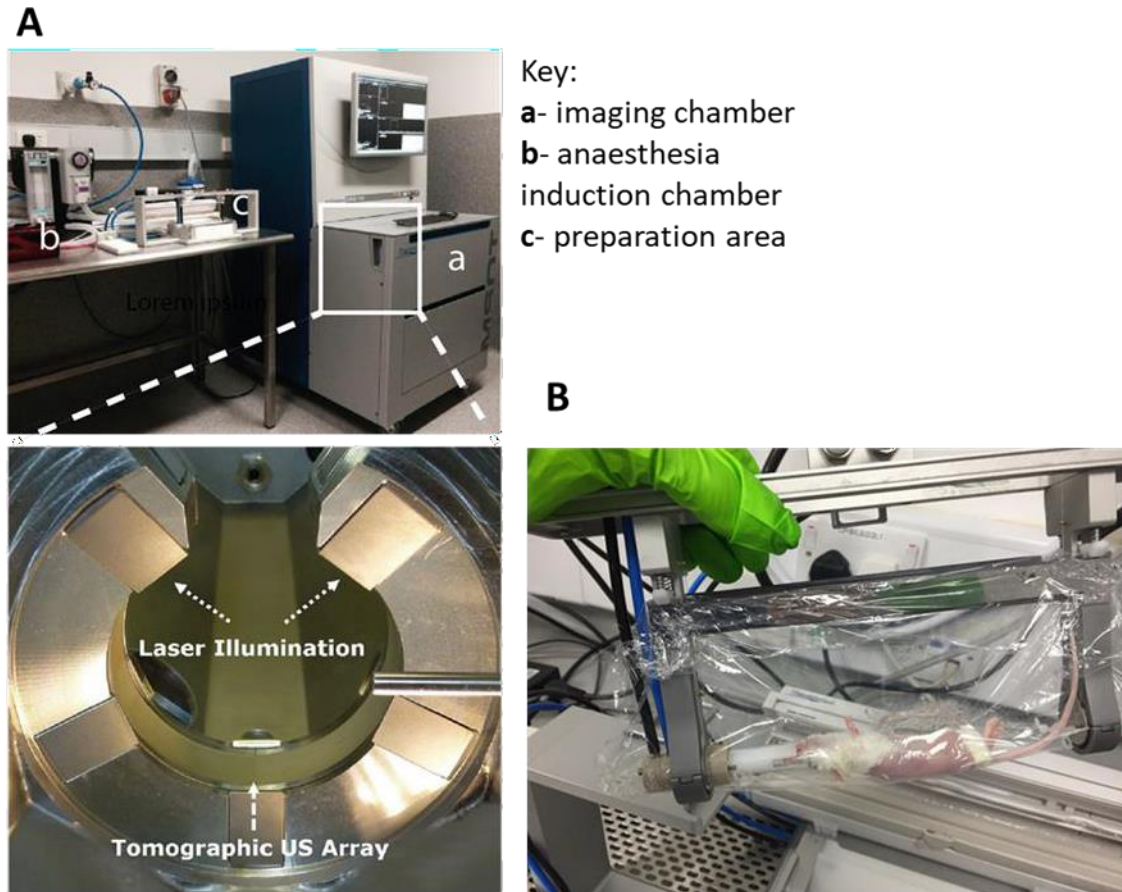
Figure 4.1. MSOT imaging set-up. (A) The ultrasound transducers are arranged in a curved 270° array in the imaging chamber (a) immersed in water. The animal is anaesthetised in the induction chamber (b), before being shaved if necessary and prepared for imaging (c). Part (B) shows the mouse holder with the mouse wrapped in a polyethylene membrane. The holder is placed into the imaging chamber and is translated through the ultrasound transducer array.

4.2.2. OE-OT experimental procedure

A gas challenge was conducted during the MSOT imaging session at the final time point prior to sacrifice, according to procedures described previously[125,126]. Briefly, the breathing gas was changed manually from medical air (21% O_2) to 100% O_2. Animals were stabilised on medical air for 5 min prior to switching. Images of a single slice in the centre of the tumour (which approximately co-localises with the core IHC section) were taken whilst the mouse was kept on medical air for a further 3 min before being switched to 100% O_2 for 5 min. Images were acquired using 15 wavelengths between 700-880 nm with an average of 6 pulses per wavelength. Each slice took 11.5s to acquire.

4.2.3. MSOT image analysis

Longitudinal tomographic photoacoustic data were analysed using custom code written in Python[257] by Thomas Else. Images were reconstructed by filteredbackprojection over wavelengths of 700-850 nm with a band-pass filter applied between 5 kHz and 7 MHz, impulse response correction, and a manually-selected speed of sound. Images were reconstructed with a pixel size of 75 μm x 75 μm, which is approximately equal to half of the in-plane resolution. The photoacoustic spectrum was averaged across all pixels in the ROIs before applying spectral unmixing based on the optical absorption spectra of Hb and HbO_2 using the matrix pseudoinverse function in the Python library NumPy.

Due to a lack of knowledge surrounding the light fluence distribution in the mouse body, MSOT cannot be used to accurately calculate absolute SO_2 and therefore we denote oxygenation within tumours as an apparent SO_2^{MSOT} rather than absolute SO_2, computed as the ratio of oxygenated [HbO_2] to total haemoglobin [$THb^{MSOT}=HbO_2+Hb$]. ROIs were drawn manually around the largest cross section of each tumour at the final time point (which approximately co-localises with the core IHC section), excluding the skin. For earlier time points, ROIs were drawn around the tumour in same section using the aorta/vena cava as reference, to ensure that the same section of tumour is monitored over time. The mean THb^{MSOT} and SO_2^{MSOT} within the tumour ROI were calculated. For visualization of mean THb^{MSOT} and SO_2^{MSOT} spatial maps, images were down sampled to 225 μm x 225 μm pixels to increase the signal to noise ratio, and mean THb^{MSOT} and

$SO_2{}^{MSOT}$ calculated per pixel.

OE-OT image analysis was performed in MATLAB (Mathworks) using custom software written by Dr Michal Tomaszewski. The processing described here is equivalent to the Python processing described above, the only significant difference being the reconstruction method chosen, which was based on speed of reconstruction (model-based methods are considered more quantitative but run 10x slower than backprojection methods in practice). Photoacoustic image reconstruction was performed using a model-based algorithm in ViewMSOT software (version 3.8, iThera Medical GmbH) over wavelengths of 700-850 nm, with impulse response correction using a manually-selected speed of sound. Images were reconstructed with a pixel size of 75 μm x 75 μm. In MATLAB, ROIs were drawn manually around the largest cross section of each tumour (which approximately co-localises with the core IHC section), excluding the skin. The photoacoustic spectrum was averaged across all pixels in the ROIs and a matrix pseudoinverse function (pinv function in MATLAB 2018b) was used for spectral unmixing of the relative weights of oxy- [HbO$_2$] and deoxy-haemoglobin [Hb].

OE-OT metrics were calculated as follows: THb^{MSOT} and $SO_2{}^{MSOT}$ were captured under air [$SO_2{}^{MSOT}$(Air)] prior to gas challenge, and 5 minutes after, under 100% O$_2$ [$SO_2{}^{MSOT}$(O$_2$)], with both values taken as averages of 10 consecutive measurements every ~30s. Average $\Delta SO_2{}^{MSOT}$ ($SO_2{}^{MSOT}$(O$_2$) - $SO_2{}^{MSOT}$(Air)) and 'Responding Fraction' [ratio of responding to total pixels] were calculated in the tumour region of interest (ROI) These metrics were previously established and validated by Dr Michal Tomaszewski [125,126]. Responding fraction was quantified by reconstructing the images on an array of 225 μm x 225 μm pixels. A pixel was classified as responding if the $\Delta SO_2{}^{MSOT}$ increased by more than 2%.

4.2.4. Statistical analyses

4.2.4.1. Longitudinal modelling of mesoscopic blood volume data

Once tumours had reached 0.5 cm mean diameter, tumours were imaged with RSOM (as described in 3.2.1) on several occasions (aiming for weekly imaging sessions with flexibility to allow for the rate of tumour volume increase and ensure RSOM images were captured throughout tumour growth). Here, 2 passages from each model were

analysed. Raw data was segmented using the same ilastik random-forest classifier framework presented in Chapter 3 with an additional 5 images included in the training to analyse the second passage data, to allow for a visible changes in SNR across this dataset. Data from the first passage of STG139 and AB580 was excluded in the analysis, owing to the optimization of image acquisition with these tumours. Tumour ROIs were segmented using a custom made 3D convolutional neural network (CNN) based on my manual annotations of a subset of the data (see Appendix 1).

Blood volume calculated from segmented images was modelled longitudinally as tumour volume increased, using a linear mixed effects (LME) model. When modelling a response variable, such as blood volume, over time, a standard linear regression may suffice to observe how explanatory variables such as PDX model influence the response variable over time. This modelling is valid when observations can be assumed to be independent (different mice), but often lead to incorrect conclusions/inference with more complex data structures, like longitudinal data, for example, as it ignores the dependence between observations of the same mouse. LME models generalise the usual linear model to non-independent data[258]. They incorporate both 'fixed effects' and 'random effects' when explaining the response variable. Fixed effects, as the name suggests, are fixed, and cannot vary, and are associated with an entire population, such as the PDX model. Random effects, typically used to take the within-cluster dependence into account, are associated with individual experimental units drawn at random from a population, such as individual mice[259].

The random effect part of the model can be defined in many ways depending on the clustering pattern/structure. The simplest and most common LME model is the random intercept[258]. This model assumes that each individual within a population has its own unique effect on the overall population intercept, resulting in a different intercept for each individual. This model assumes that for each individual, the effect of the explanatory variable on the response variable is the same, i.e. each individual has the same slope but different intercepts[260]. If this is not the case with the data, and the effect of the explanatory variable on the response variable varies with each individual, then including the random effect of slopes may better fit the data[260]. Other methods to cluster random effects are available, although the two described here are most common and the choice of clustering

method will depend on the data structure[258].

Another advantage of LME models is that they allow partial pooling of the data. Complete pooling occurs in standard linear regression, which ignores the clustering of the data and typically underestimates the standard error of the regression. One could conduct separate regressions per individual (i.e. no pooling) however this will likely lead to overfitting, and it ignores the similarities amongst individuals. Partial pooling in LME models accounts for both similarities and differences amongst individuals in a population. Partial pooling is also important when there are few observations for one individual, or unbalanced datasets, as the partial pooling will produce a group-specific effect closer to the overall population effect for individuals with less observations which would not occur with no pooling[258].

Here, a heteroscedastic random intercept and slope linear mixed effect model was used to analyse the relationship between blood volume (on the cube root scale) and tumour volume (on the linear scale) for the 4 PDX models of interest. Blood volume was transformed using a cubic root to linearise the data and reduce standard error. The chosen model allows to estimate a regression line between blood volume and tumour volume for each model (by considering as fixed effect the regressor volume, the 4-level factor model and the interaction between both) while taking the within-mouse dependence into account by means of random effects and allowing the residual variance to depend on model (heteroscedasticity) and controlling for PDX passage. The final model was selected after a sequence of likelihood ratio tests which suggested that adding random slopes and a modelling of the heteroscedasticity of the residuals improved the adequacy of the model to the data. The likelihood ratio tests also suggested that blood volume was dependent on passage and that the effect of passage can be assumed to be the same for all models (no significant effect of the interaction term between tumour volume, model and passage). Passage was controlled for in an additive way in the final model. The later passage of each model analysed has a blood volume intercept which is on average 0.075 mm (on cube root scale) lower than the first passage analysed. Extensive model checks analysing the relationship of normalised residuals with different variables (group, model, passage, volume) as well as the distribution of the estimated residuals and random effects suggested a good fit of the final model to the data.

Wald Z-tests were used to analyse the contrasts of interest with and without a parametric multiplicity correction. The contrasts of interests were: pairwise comparisons between all 4 PDX models and a comparison between the model slopes and a slope=0, as a measurement of blood volume evolution as tumour volume increased.

In all modelling, images from both the dorsal and lateral mouse positions were considered (**Figure 3.3**). This allowed two images to be included per tumour per time point, which increased the number of observations per tumour as occasionally one position had to be excluded from analysis due to breathing motion or compression artefact. They were considered to capture a similar proportion of tumour vasculature, owing to their highly correlated blood volume values (r=0.77, p<0.001 **Figure 3.9**).

4.2.4.2. Analysis of topology data and tomographic PAI biomarkers

Statistical analysis was performed using GraphPad Prism v.9. Each tumour was considered as an independent biological replicate. To compare the means of STG139, STG321, AB580 and STG143 a one-way ANOVA was performed with Tukey's multiple comparison correction, unless the data violated the assumptions of a Gaussian distribution or equal variances, in which case Kruskal-Wallis test with Dunn's multiplicity correction and Welch's ANOVA with Dunnett's T3 multiplicity correction were conducted respectively. The same tests were performed to compare means across 3 passages. To compare: small (~0.1 cm^3) and large (~0.4 cm^3) tumour means between STG139 and AB580, passage repeats within STG139 and AB580 and across 2 passages an unpaired student's t-test was performed unless the data violated the assumption of a Gaussian distribution, in which case a Mann-Whitney test was conducted. To compare small (~0.1 cm^3) vs. large (~0.4 cm^3) tumour means within STG139 and AB580 a paired student's t-test was performed, unless the data violated the assumption of a Gaussian distribution, in which case a Wilcoxon test was conducted. Comparisons between IHC and PAI metrics were calculated using Spearman's correlation coefficient. All IHC metrics were averaged between the core and outer sections (described in 2.2.2). Significance is assigned for p-values <0.05.

4.3. Results

4.3.1. End-point Tomographic PAI shows differences in blood content and oxygenation between the PDXs

To provide insight into the PDX vascular phenotypes captured with PAI for Aim1 of the thesis, I first measured blood content (THb^{MSOT}) and blood oxygenation ($SO_2{}^{MSOT}$) across the whole tumour area using tomographic PAI from data collected at the final time point (tumour ~1 cm in diameter) in the 4 breast PDX models introduced in Chapter 2 (basal: STG139 and STG321, luminal B: AB580 and STG143). The sensitivityof these metrics to differing vascular phenotypes in the PDXs was considered, as part ofAim 2 of the thesis.

THb^{MSOT} was ~3-fold higher in STG139 than all other PDXs (**Figure 4.2A**), with evidence of haemorrhage present in the images, shown as bright intense spots (**Figure 4.2B**). This observation is supported by the high CD31 vessel area (**Figure 2.8**) and haemorrhage measured *ex vivo* (**Figure 2.4**) in this model. Interestingly, comparing THb^{MSOT} across the 4 PDXs reflects the pattern of CD31 vessel area on the core IHC section (**Figure 2.7A**), not only in relation to STG139, but also with the other models. The basal model STG321 had significantly higher THb^{MSOT} and vessel area than the luminal B model AB580. Here, the other luminal B model STG143 also has higher THb^{MSOT} than AB580, but there is no difference in vessel area, perhaps due to the differentsample sizes measured.

When measurements of $SO_2{}^{MSOT}$ were taken whilst the mouse was breathing air, there were no significant differences between the models (**Figure 4.2C**). When the breathing gas was changed to O_2, differences in $SO_2{}^{MSOT}$ were observed in the basal models (**Figure 4.2D**). Here, STG321 had significantly higher $SO_2{}^{MSOT}(O_2)$ than STG139, despite the wide range of $SO_2{}^{MSOT}(O_2)$ values measured for STG139. This is corroborated by previous IHC measurements that showed the two basal models had significant differences in vessel maturity and hypoxia. THb^{MSOT} and $SO_2{}^{MSOT}(O_2)$ were sensitive to differing vascular phenotypes in the PDXs, towards Aim 2 of the thesis.

Finally, dynamic measurements taken during the gas challenge ($\Delta SO_2{}^{MSOT}$ and

responding fraction, **Figure 4.2E, F**) did not show any overall differences between the 4PDX models measured, likely due to the large variability observed. Further work is needed to understand the origins of this variability, given the otherwise remarkably consistent results from the breast PDX models.
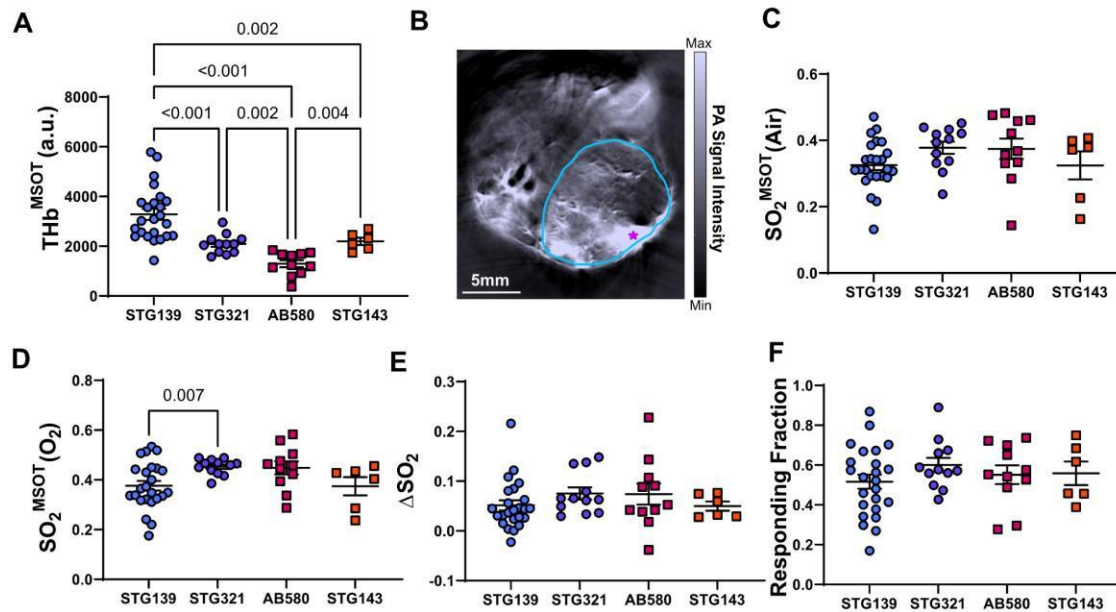
Figure 4.2. Tomographic PAI with a gas challenge at end-point shows differences in blood content and oxygenation between the PDXs. Tomographic PAI metrics measured in the central slice across all 4PDX models, each point representing one tumour. A) Blood content (THb^{MSOT}) B) Exemplar tomographic slice for STG139 with tumour ROI drawn in light blue and haemorrhagic region labelled with purple star.

C) Blood oxygenation whilst mouse is breathing air ($SO_2^{MSOT}(Air)$) D) Blood oxygenation whilst mouse is breathing oxygen ($SO_2^{MSOT}(O_2)$) E) Difference between D and C (ΔSO_2^{MSOT}) and F) Responding Fraction defined as fraction of pixels considered as responding to the gas challenge (a pixel is classed as responding if ΔSO_2^{MSOT} is above 2%). Data presented as a scatter dot plot with mean ±SEM. In all subfigures, each data point represents data from one tumour (biological replicate). In A) and D) p-values for significant ($p<0.05$) pairwise comparisons are shown calculated by Welch's ANOVA with Dunnett's T3 multiplicity correction. In C) and F) pairwise comparisons by One-way ANOVA with Tukey's multiplicity correction were conducted with no significant p-values ($p<0.05$) reported. In E) pairwise comparisons by Kruskal-Wallis test with Dunn's multiplicity correction were conducted with no significant p-values ($p<0.05$) reported. The following n numbers refer to the number of tumours per PDX model in all sub-figures: $n^{STG139}=24$, $n^{STG321}=12$, $n^{AB580}=11$, $n^{STG143}=6$.

4.3.2. Longitudinal Tomographic PAI reveals minimal evolution in vascular function

Towards Aim 4 of the thesis, an initial investigation was conducted into whether the vascular phenotypes found using tomographic PAI evolved as tumours grew. As with the Chapter 2 IHC (**Figure 2.13**), this would provide some insight as to whether the PDX vascular phenotypes are inherent, or whether they develop over time. With PAI this measurement is truly longitudinal unlike in IHC, because the same tumour can be monitored non-invasively over time. Tomographic slices from the centre of small tumours (~0.1 cm^3) and large tumours (~0.4 cm^3) in a subset of the basal model STG139 and luminal B model AB580 were compared (see exemplar images in **Figure 4.3**) and are denoted as small or large respectively in **Figure 4.3-4.**

Interestingly, the SO_2^{MSOT} and mean THb^{MSOT} images clearly show that the metrics did not significantly change as tumours grew and while SO_2^{MSOT} is higher in AB580, model STG139 has more blood content, with higher THb^{MSOT} (**Figure 4.3**).

Upon quantification, SO_2^{MSOT} remained stable as tumours grew in both PDX models (**Figure 4.4A, B**), suggesting that the blood oxygenation does not change with tumour size and is inherent to the PDX. Mean THb^{MSOT} (**Figure 4.4C, D**) decreased by ~1.25-fold in both models but this was not significant. It should be noted that the mean THb^{MSOT} is normalised to the tumour area, and therefore this result indicates that the density of vessels is stable in growing tumours, similar to CD31 vessel area measured on IHC (**Figure 2.13C, D**). Model comparisons between the PDXs showed higher mean THb^{MSOT} and lower SO_2^{MSOT} in STG139 compared to AB580, regardless of whether this was measured in small (**Figure 4.5A,B**) or large (**Figure 4.5C,D**) tumours. Overall, there was minimal vascular phenotype evolution in the PDXs investigated by tomographic PAI, similar to the findings from IHC. Owing to an apparent lack of evolution in either THb^{MSOT} or SO_2^{MSOT} from this initial analysis, further modelling was not conducted on the full longitudinal dataset.
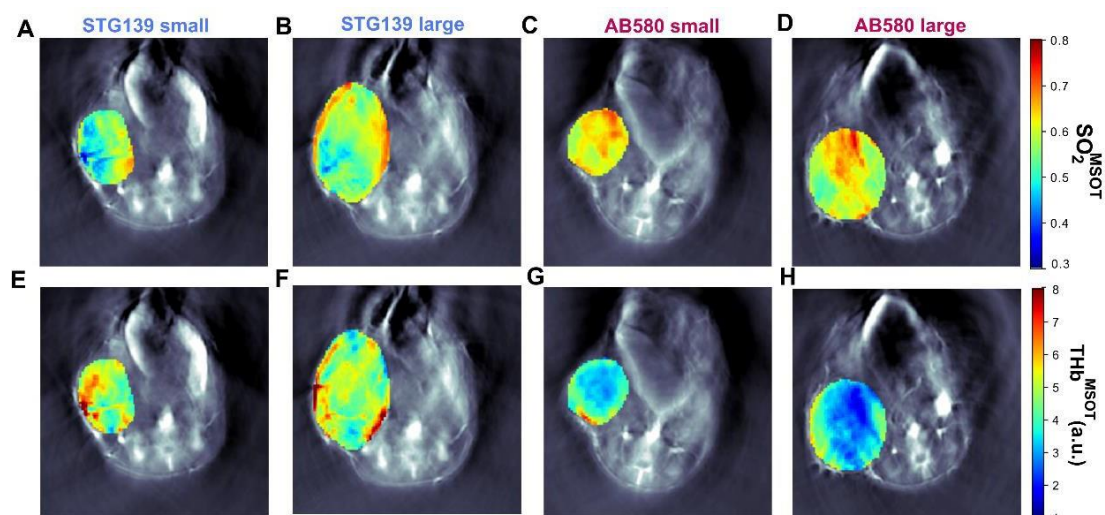
Figure 4.3. Blood oxygenation and total haemoglobin do not evolve as PDXs grow. Images shown as tomographic slices with mouse body in greyscale and tumour ROI in a colour map depicting blood oxygenation (SO^{MSOT}) (top row$_2$) or mean total haemoglobin (THb^{MSOT}) (bottom row). A and E) Example images of a small (~0.1 cm^3) STG139 tumour, B and F) Example images of a large (~0.4 cm^3) STG139 tumour, C and G) Example images of a small (~0.1 cm^3) AB580 tumour, D and H) Example images of a large (~0.4 cm^3) AB580 tumour.
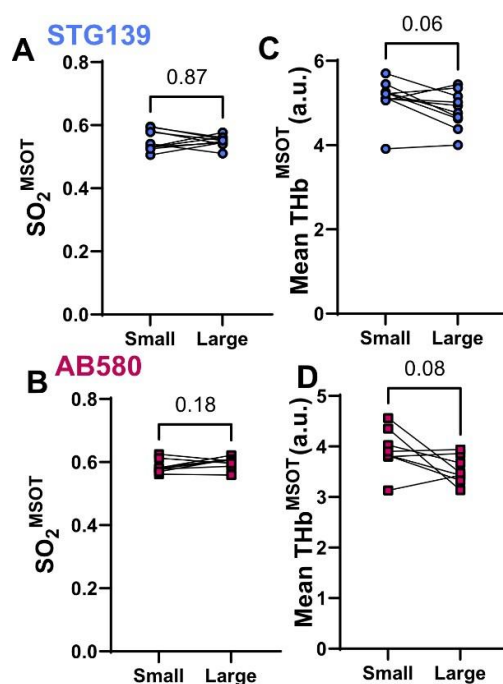
Figure 4.4. PDXs vessel density may decrease during growth but blood oxygenation is stable. Tomographic PAI metrics compared between small (~0.1 cm^3) and large (~0.4 cm^3) PDXs in STG139 (top row) and AB580 (bottom row) models. A and B) Blood oxygenation SO$_2^{MSOT}$, C and D) mean total.

haemoglobin (THb^{MSOT}). In all subfigures, matched data from the same tumour are joined by a straight line In all subfigures, each data point represents data from one tumour (biological replicate). All p-values are shown calculated by paired t-test (A, B, and D) or Wilcoxon test (C). p-values <0.05 considered significant. The following n numbers refer to the number of tumours per PDX model in all sub-figures: n^{STG139}=10, n^{AB580}=8.
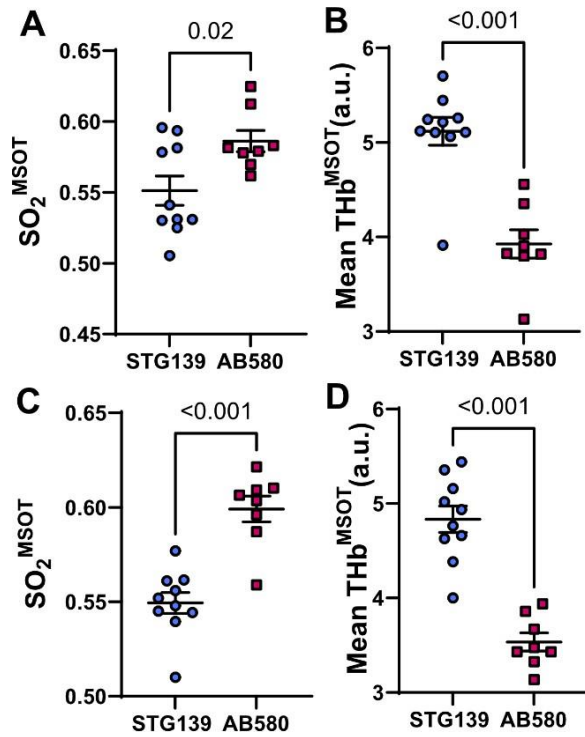
Figure 4.5. Model comparisons are not size-dependent with blood oxygenation higher in AB580 and blood content higher in STG139. Tomographic PAI metrics compared between STG139 and AB580 tumours at small (~0.1 cm^3, top row) and large (~0.4 cm^3, bottom row) sizes. A and D) Blood oxygenation SO_2^{MSOT}, B and E) mean total haemoglobin (THb^{MSOT}), C and F) sum THb^{MSOT}. In all subfigures, data presented as a scatter dot plot with mean ±SEM. In all subfigures, each data point represents data from one tumour (biological replicate). All p-values are shown calculated by unpaired student's t-test (A, C, and D-F) or Mann-Whitney test (B). p<0.05 considered significant. The following n numbers refer to the number of tumours per PDX model in all sub-figures: n^{STG139}=10, n^{AB580}=8.

137

4.3.3. End-point mesoscopic PAI reveals differences in blood volume and network architecture

Mesoscopic PAI was utilised as a technique which could visualise and quantify the PDX vascular networks at a mesoscopic resolution, in-between the microscopic IHCand macroscopic tomographic imaging already conducted, providing complementary information on the vascular phenotypes on a sub-volume of the tumours. As described in Chapter 3, an analysis pipeline which was developed as part of this thesis enables blood volume and topology metrics to be quantified from segmented mesoscopic PA images. Here, this pipeline was applied across all 4 PDX models. An initial analysis of the vascular phenotypes quantified at end-point is now discussed to meet Aim 1 of the thesisand the sensitivity of the mesoscopic metrics to the differing vascular phenotypes is discussed, to meet Aim 2, before the longitudinal imaging was considered.

The blood volume at end-point showed differences between the models that are not subtype-dependent (**Figure 4.6**), alike to the tomographic and IHC measurements. Within this sub-volume, STG139 had ~2-fold higher blood volume than the other PDXs, reflecting THb^{MSOT} data. CD31 vessel area measured on IHC also showed STG139 to have the most vessels (**Figure 2.8**), however STG321 also had high THb^{MSOT} and high vessel area across the core tumour section *ex vivo* but not the outer section. Blood volumemeasured using mesoscopic PAI is able to differentiate between the differing blood content in the PDXs, partially meeting Aim 2 of the thesis.
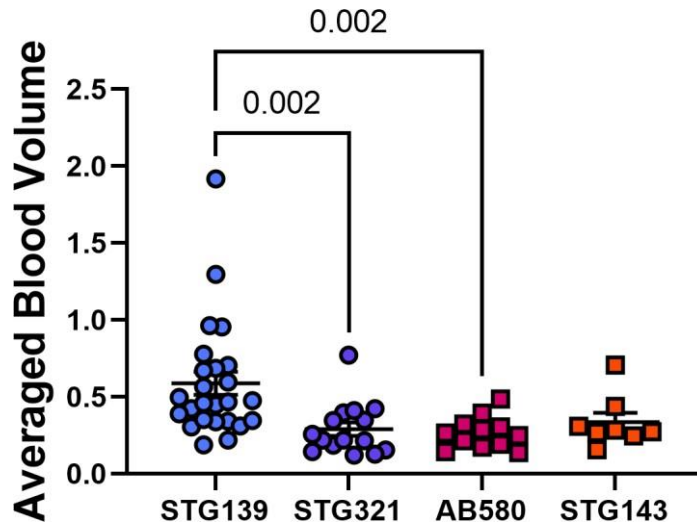
Figure 4.6. Blood volume measured at the final time-point is highest in STG139. Blood volume averaged between dorsal and lateral positions. Pairwise comparisons of the means between the models compared by Kruskal- Wallis test with Dunn's multiplicity correction. Data presented as a scatter dot plotwith mean ±SEM. Each data point represents data from one tumour (biological replicate). p<0.05 considered significant. The following n numbers refer to the number of tumours per PDX model: n^{STG139}=25, n^{STG321}=16, n^{AB580}=12, n^{STG143}=8.

Once images were segmented and blood volume calculated, they were skeletonised and topological data analyses (TDA) conducted as part of the mesoscopic PAI analysis pipeline developed in Chapter 3. Due to time constraints, TDA analyses were conducted solely on networks imaged at end point (tumour volume ~0.4 cm^3).

Structural and TDA metrics do not appear to be subtype dependent as the basal models STG139 and STG321 showed distinct topologies. STG321 networks had significantly more connected components (**Figure 4.7A**, p=0.02), fewer looping structures (**Figure 4.7B**, p=0.02) and smaller diameters (**Figure 4.7C**, p=0.11). Considering previous ASMA (pericyte/smooth muscle) vessel coverage IHC data presented in Chapter 2 (**Figure 2.9**), and the *ex vivo* validation of our analysis pipeline conducted in Chapter 3 (**Figure 3.16**), these TDA metrics appear to reflect network maturity. STG321 vessel networks, present as a more mature network on TDA, which iscorroborated by high ASMA vessel coverage previously measured on IHC (**Figure 2.9**).Conversely, STG139 networks had lower pericyte/smooth muscle coverage (**Figure 2.9**)

and TDA analyses present an interconnected, dense mass of vessels with a high number of edges (**Figure 4.7D**), supported by blood volume data presented in **Figure 4.6** and CD31 vessel area data (**Figure 2.7**). The two luminal B models had no significant differences in ASMA vessel coverage measured on IHC (**Figure 2.9**), which was in-between the two extremes denoted by the basal models. In mesoscopic PAI, the two luminal models had no significant differences in connected components (**Figure 4.7A**), looping structures (**Figure 4.7B**) or diameters measured (**Figure 4.7C**). However, on average AB580 had a network structure more similar to the mature STG321 networks while STG143 had a network structure more similar to the immature STG139 networks on average. TDA metrics quantified from mesoscopic PA images appear to be sensitive to network maturity in the PDXs, partially meeting Aim 2 of thesis.
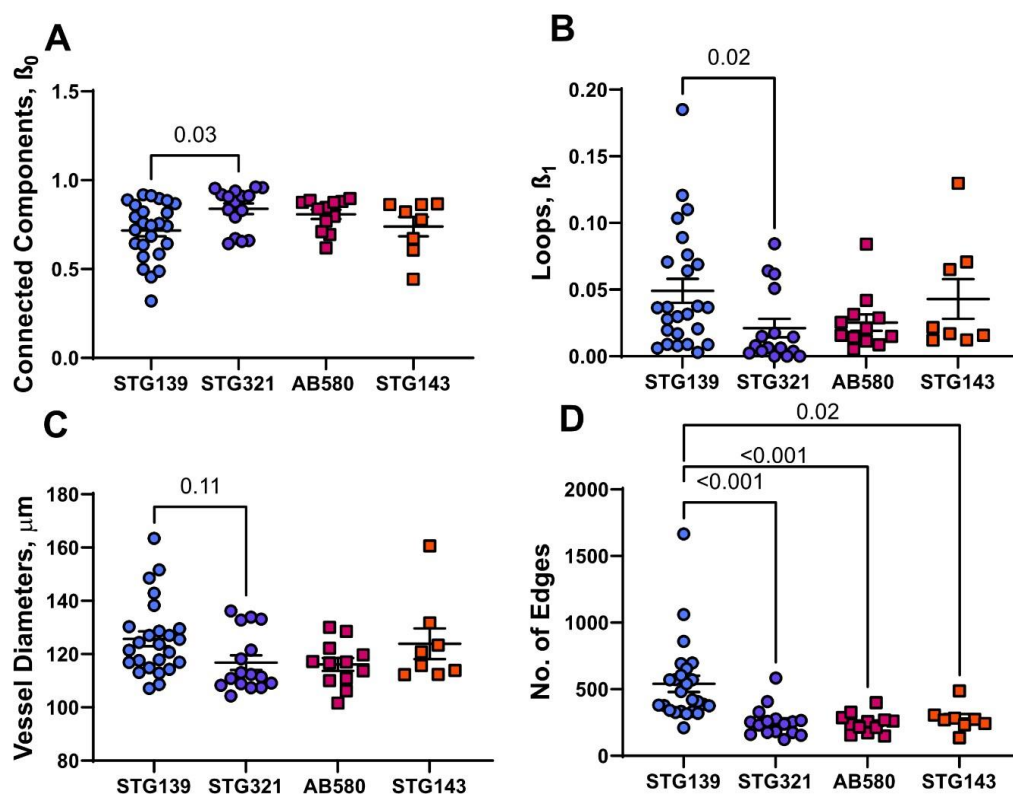
Figure 4.7. Topological data analyses reveal mature vessel networks in STG321. All values averaged between dorsal and lateral positions. A) Connected components (β_0) B) Loops (β_1) C) Vessel diameters (μm) and D) Number of Edges. In all subfigures, data presented as a scatter dot plot with mean $\pm$SEM. In all subfigures, each data point represents data from one tumour (biological replicate). The following n numbers refer to the number of tumours per PDX model in all sub-figures: n^{STG139}=25, n^{STG321}=16, n^{AB580}=12, n^{STG143}=8. p-values for STG139 and STG321 pairwise comparisons areshown calculated by Kruskal-Wallis test with Dunn's multiplicity correction. p-values <0.05 considered significant.

140

4.3.4. Mesoscopic PAI reveals differences in the evolution of PDX blood vessel networks over time

Owing to the fact that photoacoustic imaging (PAI) is non-invasive, true longitudinal imaging of subjects over time is possible. Despite this, modelling the changes in PAI metrics across time is not routine. In fact, studies often comment on changes in metrics such as vessel density as tumours grow[113] but appropriate modelling and statistical analysis is not conducted. I hypothesised that high-resolution mesoscopic PAI could capture changes in blood vessel networks in breast PDXs over time, as the networks developed, which were perhaps not detectable with tomographic PAI of the whole tumour. Towards Aim 4 of the thesis, longitudinal changes in blood volume captured by mesoscopic PAI were monitored in the 4 PDXs.

Visual inspection of example images shows rapid development of vasculature in the basal model STG139, with excessive branching and a haemorrhage developing in only 6 days (**Figure 4.8A**). Note that the tumour volume also increased rapidly in this example, while it took the luminal B STG143 tumour 20 further days, from the first imaging time point, to reach a similar size. Vessel density and morphology appeared to remain stable in the other basal model STG321 (**Figure 4.8B**), while vessel density rapidly increased in the luminal B model AB580 (**Figure 4.8C**) and looping structures visibly increased in the STG143 example (**Figure 4.8D**).
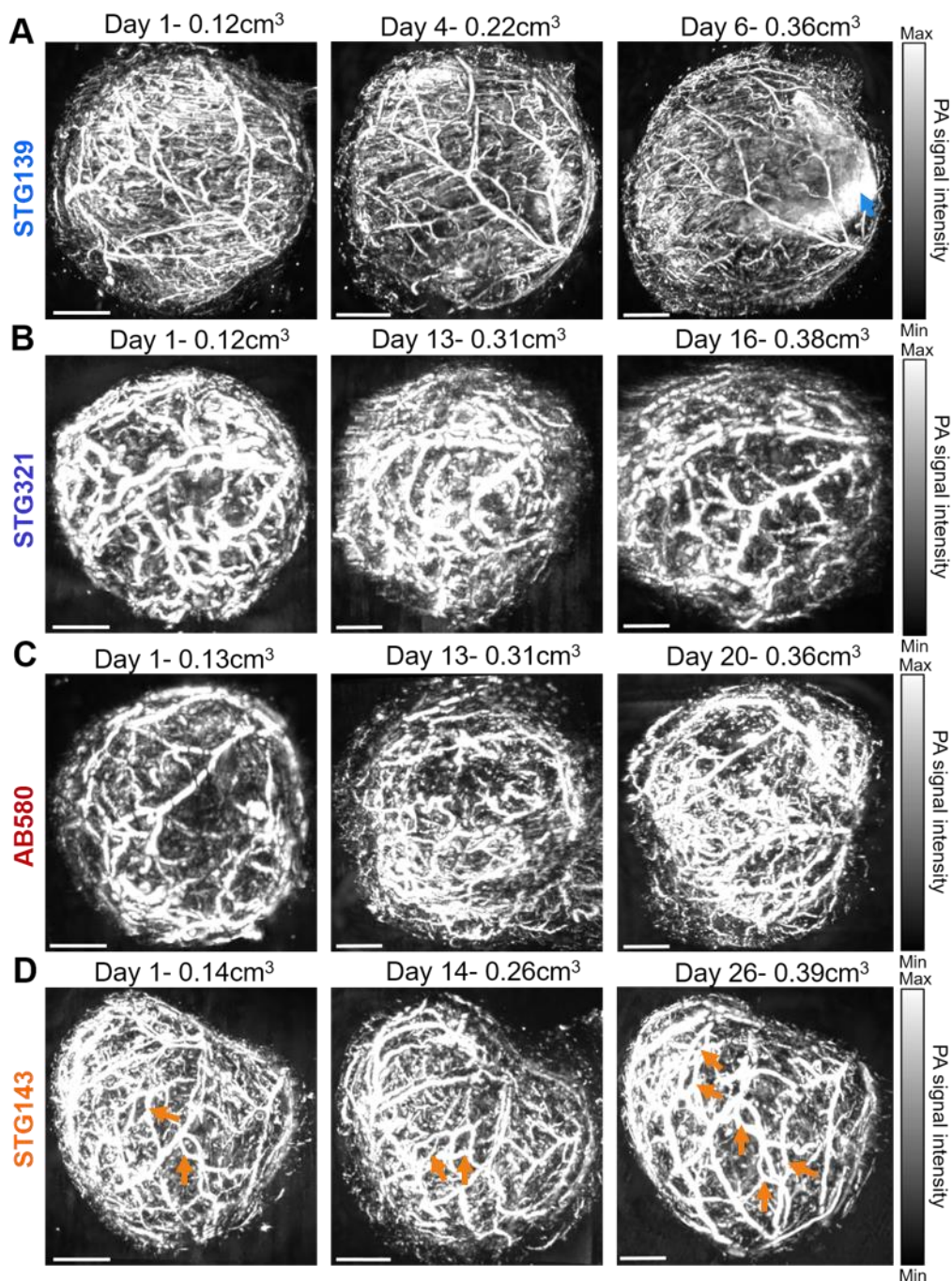
Figure 4.8.

Visual inspection of breast PDX vessel networks captured with longitudinal mesoscopic PAI. All images shown are 2D snapshots of a 3D rendering. Scale bar=2 mm. A) STG139, B) STG321, C)AB580, D) STG143. Blue arrow marks area of haemorrhage in an STG139 tumour. Orange arrows mark looping structures in an STG143 tumour.

To initially explore the potential of mesoscopic PAI to quantify changes in blood vessel networks over time, the blood volume (calculated from segmented mesoscopic images), was measured in small (~0.1 cm^3) and large (~0.4 cm^3) tumours of the basal model STG139 and luminal B model AB580. Blood volume was normalised to ROI volume, in a similar manner to the THb^{MSOT} normalisation to ROI area on tomographic PAI. Interestingly, the normalised blood volume increased significantly between small and large tumours in STG139 (**Figure 4.9A**) but the evolution in AB580 tumours was more variable, with some increase and some decrease in normalised blood volume between small and large tumours (**Figure 4.9B**). This initial evaluation indicated that thedensity or size of blood vessels within the mesoscopic field-of-view was increasing overtime in STG139, and the differences between STG139 and AB580 tumours indicated thatmodel differences in the evolution of blood volume may occur. I therefore performed a longitudinal analysis and modelling of the entire mesoscopic PAI dataset across all 4 PDXs, to understand how blood volumes evolves in the sub-volume captured by mesoscopic PAI.
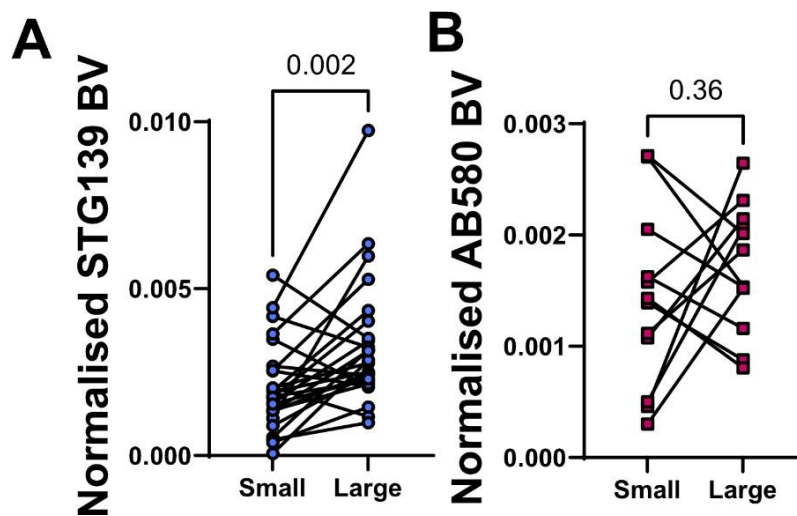
Figure 4.9. Initial analyses indicate changes in blood vessel networks captured with mesoscopic PAI as tumours grow. Blood volume, normalised to ROI volume and averaged between dorsal and lateral positions, compared between small (~0.1 cm^3) and large (~0.4 cm^3) tumours in (A) STG139 and (B) AB580 by Wilcoxon test or Paired t-test respectively. In all subfigures, matched data from the same tumour are joined by a straight line. In all subfigures, each data point represents data from one tumour (biological replicate). The following n numbers refer to the number of tumours per PDX model in all sub-figures: n^{STG139}=25, n^{AB580}=12. $p < 0.05$ considered significant.

Longitudinal analysis across multiple time points of all 4 models showed that blood volume increased with tumour volume in all models except STG321 (**Figure 4.10A**). Blood volume modelled linearly (**Figure 4.10B**) increased at a higher rate in basal model STG139 compared to the other basal model STG321 (p=0.016 without multiplicity correction and p=0.07 with multiplicity correction, **Figure 4.10B**). The two luminal B models also showed increased blood volume as tumours grew (**Figure 4.10**), with slopes in-between the two extremes denoted by the basal models. STG143 had a steeper slope than AB580, but the two were not significantly different. Interestingly, all models had slopes which significantly differed from zero except for STG321 (p<0.001 for STG139, p=0.002 for STG143, p=0.05 for AB580, p=0.19 for STG321), demonstrating the minimal evolution of blood volume in this model. STG321 does not appear to create many new blood vessels as tumour size increases, consistent with thelack of angiogenic potential indicated with IHC. Longitudinal mesoscopic PAI is sensitive to blood vessel network development, partially meeting Aim 2 of the thesis.
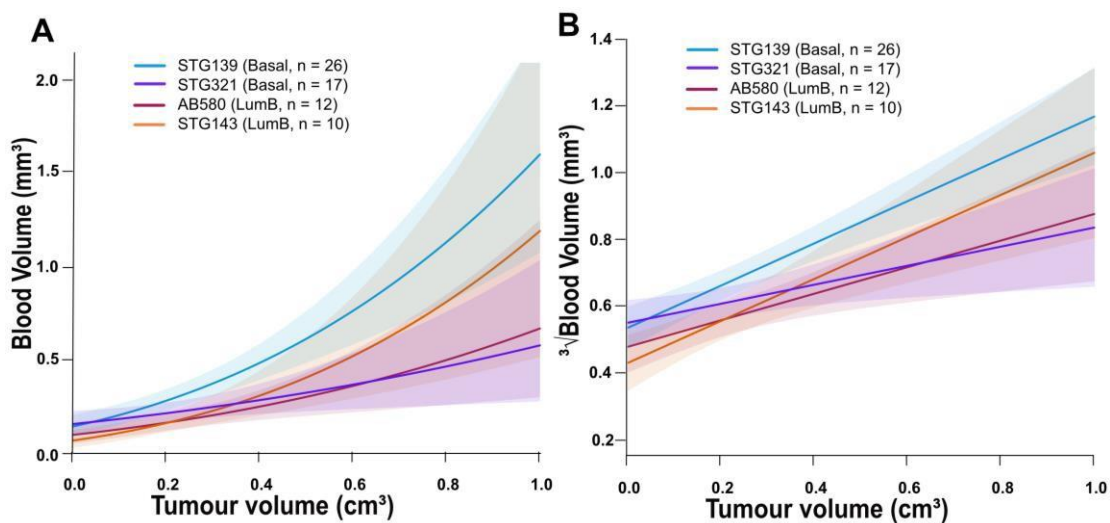
Figure 4.10. Modelling blood volume as tumour volume increases shows the angiogenic potential of the PDXs. A) Increase in blood volume as tumour volume increases for STG139, AB580 and STG143. B) Blood volume on the cubic root scale, modelled linearly as tumour volume increases. Data in shown as lineof best fit in bold with standard error in shaded areas. Light blue= STG139, Dark Blue= STG321, Burgundy= AB580 and Orange= STG143. The n numbers shown in each subfigure refer to the number of tumours per PDX model.

4.3.5. Measurements of blood content show inter-passage variability

To meet Aim 3 of thesis and assess inter-passage heterogeneity of the vascular phenotypes, tomographic PAI metrics taken during end-point imaging (THb^{MSOT}, SO$_2$ ^{MSOT}(Air), SO$_2$^{MSOT}(O$_2$), ΔSO$_2$ ^{MSOT} and responding fraction) across 3 early passages of STG139 tumours was evaluated. The same data was collected in AB580 tumours, but this data is not sufficiently powered to be analysed. Additionally, one passage per STG139 and AB580 model was repeated, where the implantation of tumour fragments from the previous passage was repeated in new mice, to assess how repeating a passage could also introduce heterogeneity in phenotype. Mesoscopic PAI metrics (blood volume, connected components, loops, vessel diameter and number of edges) were assessed across two passages for all 4 models and the repeated passage for STG139 and AB580. However, measuring changes across two passages is not considered as powerful, as trends are not measured. This was also an assessment of the robustness in measurements taken by the tomographic and mesoscopic PAI systems, as these measurements were taken in the same models over a period of ~3 years.

Data from Chapter 2 indicated that the PDXs showed little inter-passage heterogeneity in vascular phenotypes measured with IHC (**Figure 2.11**). Here, SO$_2$^{MSOT}(Air), SO$_2$^{MSOT}(O$_2$), ΔSO$_2$^{MSOT} and responding fraction remained consistent across 3 passages of STG139 (**Figure 4.11A-D**). THb^{MSOT} was higher in P3 compared to P4 and P5 (**Figure 4.11E**), which reflects CD31 vessel area data (**Figure 2.11C**) where a slight decrease in vessel area from the initial passage was seen. These findings show that only THb^{MSOT} varies across the passages from all tomographic PAI metrics measured.

SO$_2$^{MSOT} was consistent across the repeats of the same passage of STG139 (**Figure 4.11F, G**) although there was a slight increase in ΔSO$_2$^{MSOT} (**Figure 4.11H**), which when the data was binarised to the responding fraction was significantly higher (**Figure 4.11I**). THb^{MSOT} was stable across the repeats (**Figure 4.11J**). PAI metrics relating to vascular function/oxygenation were also consistent across the passage repeat for AB580 (data not shown), with no significant differences. Briefly, the same trends were measured across 2 passages of STG321 and STG143, where all metrics were stable except for THb^{MSOT} which decreased in both (p=0.07 and p=0.05) between the initial and later passages (**Figure 4.12**).
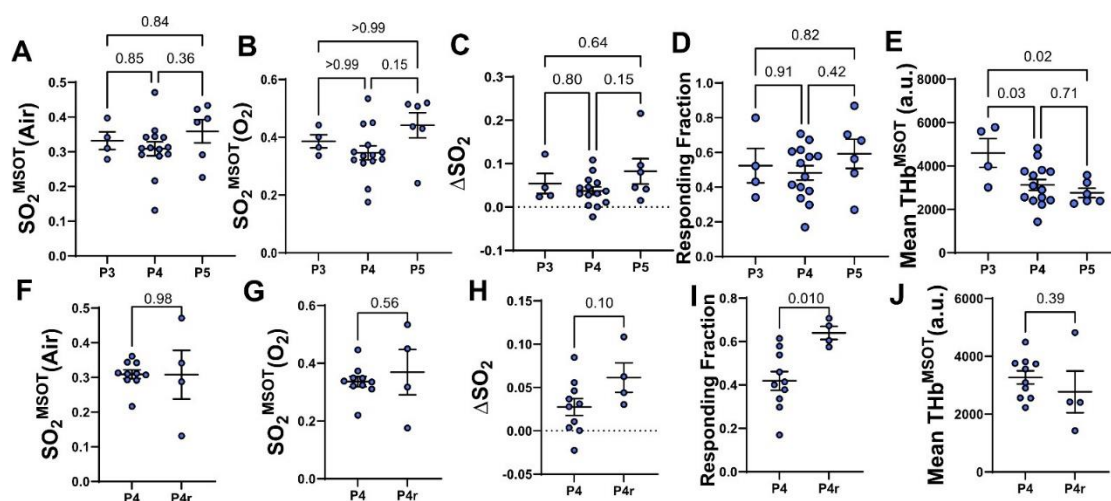
Figure 4.11. Total haemoglobin decreased across PDX passages in STG139. Top row= PAI metric measured across 3 consecutive passages (P) and Bottom row= PAI metric measured across one passage vs. a repeat of the same passage (r). A and F: Blood oxygenation whilst mouse is breathing air (SO_2^{MSOT}(Air)). B and G: Blood oxygenation whilst mouse is breathing oxygen ($SO_2^{MSOT}(O_2)$). C and H: Difference between $SO_2^{MSOT}(O_2)$ and SO_2^{MSOT}(Air) (ΔSO_2^{MSOT}). D and I: Responding Fraction (RF) defined as fraction of pixels considered as responding to the gas challenge (a pixel is classed as responding if ΔSO_2^{MSOT} is above 2%). E and J: Blood content (THb^{MSOT}). All measurements in STG139. In all subfigures, data presented as a scatter dot plot with mean ±SEM. In all subfigures, each data point represents data from one tumour (biological replicate). In top subfigures p-values for all comparisons across passages shown calculated by One-way ANOVA with Tukey's multiplicity correction (A, C, D, E), or Kruskal- Wallis test with Dunn's multiplicity correction (B). In bottom subfigures p-values for all comparisons across passage repeats shown calculated by unpaired t-test. The following n numbers refer to the number of tumours per PDX passage in each sub-figure: for (A-E) P3 n=4, P4 n=14, P5 n=6. For (F-J) P4 n=10, P4r n=4. For all, p<0.05 considered significant.
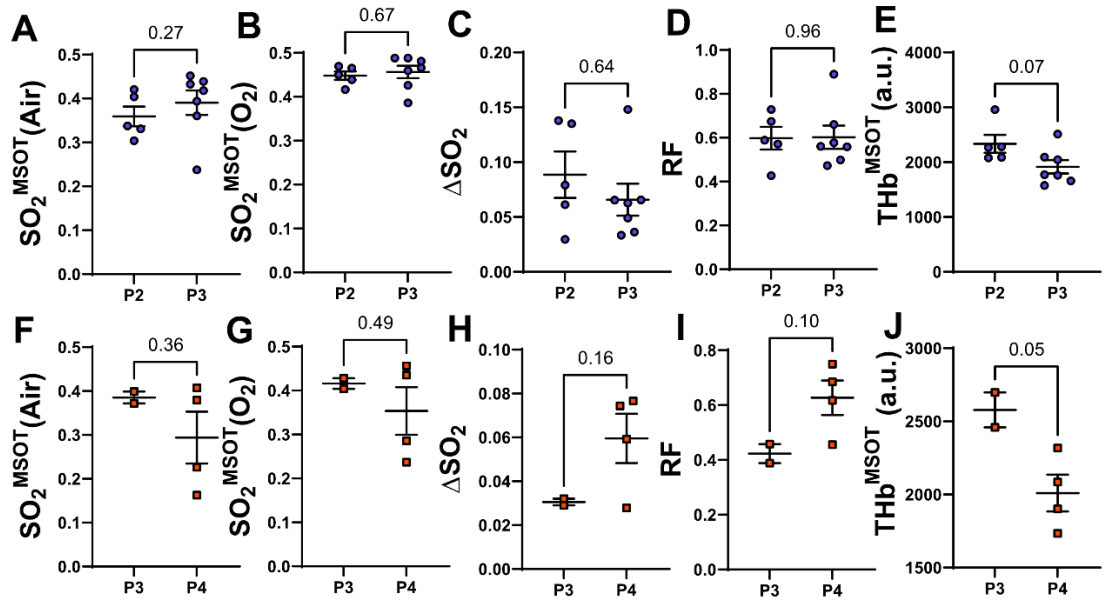
Figure 4.12. Total haemoglobin decreased across passages in STG321 and STG143. PAI metric measured across 2 consecutive passages (P) in STG321 (top row) and STG143 (bottom row) tumours. A and F: Blood oxygenation whilst mouse is breathing air (SO$_2^{MSOT}$(Air)). B and G: Blood oxygenation whilst mouse is breathing oxygen (SO$_2^{MSOT}$(O$_2$)). C and H: Difference between SO$_2^{MSOT}$(O$_2$) and SO$_2^{MSOT}$(Air) (ΔSO$_2$). D and I: Responding Fraction (RF) defined as fraction of pixels considered as responding to the gas challenge (a pixel is classed as responding if ΔSO^{MSOT} is above 2%). E and J: Blood content (THb^{MSOT}). In all subfigures, data presented as a scatter dot plot with mean ±SEM. In all subfigures, each data point represents data from one tumour (biological replicate). p-values for all comparisons across passages calculated by unpaired t-test. The following n numbers refer to the number of tumours per PDX passage in each sub-figure: for (A-E) P2 n=5, P3 n=7. For (F-J) P3 n=2, P4 n=4. For all, p<0.05 considered significant.

Alike to variability in THb^{MSOT}, blood volume measured by mesoscopic PAI was also variable across passages. Blood volume decreased at end-point from the first to second passage in all models except AB580 (although not significant for STG143, p=0.16) (**Figure 4.13A-F**). This supports the decrease in THb^{MSOT} measured in STG321 and STG143 (**Figure 4.12E,J**). THb^{MSOT} did not significantly decrease from P4 to P5 in STG139 (**Figure 4.11E**) but blood volume did (**Figure 4.13A**), suggesting that blood volume measured in mesoscopic PAI is not always representative of blood content across the whole tumour. Blood volume was stable across passage repeats of STG139 and AB580 (**Figure 4.13D, E**).

147
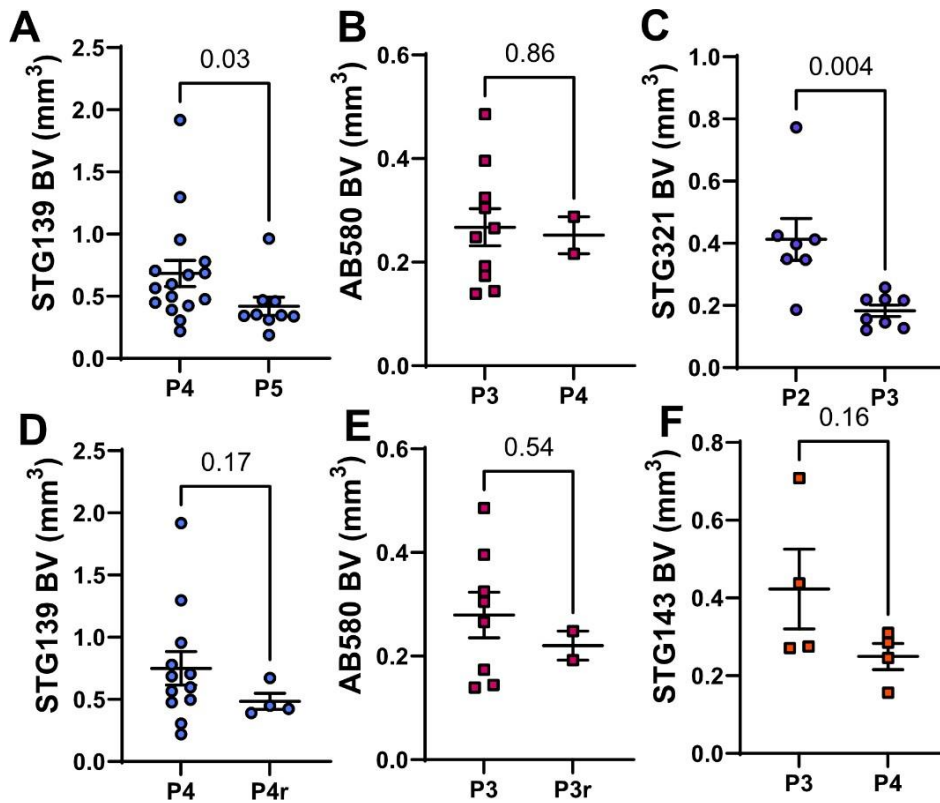
Figure 4.13. Blood volume varies across passages in the PDXs. Blood volume measured in: (A) STG139 across P4 and P5, (B) STG139 across P4 and repeat (P4r), (C) AB580 across P3 and P4, (D) AB580 across P3 and repeat (P3r), (E) STG321 across P2 and P3, (F) STG143 across P3 to P4. In all subfigures, data presented as a scatter dot plot with mean ±SEM. In all subfigures, each data point represents data from one tumour (biological replicate). In all subfigures p-values for all comparisons across passages shown calculated by unpaired t-test except for figures (A, D) where a Mann-Whitney test was used. For all, $p < 0.05$ considered significant. The following n numbers refer to the number of tumours per PDX passage in each sub-figure: For (A) P4 n=16, P5 n=9. For (B) P3 n=10, P4 n=2. For (C) P2 n=7, P3 n=8. For (D) P4 n=12, P4r n=4. For (E) P3 n=8, P3r n=2. For (F) P3 n=4, P4 n=4.

Additionally, I assessed whether the second passage of each model analysed with mesoscopic PAI caused a significant effect on the LME modelling. As noted in the methods describing the model fit I found that passaging decreased the intercept across all models, but did not have a significant effect on slope. Therefore, although the exact blood volume value at the start of tumour growth may shift with passaging, the trend in blood volume evolution is consistent across the 4 PDXs analysed. Assessing any effect of passage repeats was not possible here as this data was not sufficiently powered.

148

Structural and topology metrics were also consistent across the two measured passages and across passage repeats in STG139 and AB580 (**Figure 4.14 subfigures A-D, all boxes**), except for the number of edges in STG139, which decreased significantly from P4 to P5, similarly to blood volume (**Figure 4.13A**). Across the two passages measured for STG321, connected components increased and loops, diameter and edges decreased (**Figure 4.14 subfigure E, all boxes**). The same trend was also seen in STG143, however none of these changes were significant (**Figure 4.14 subfigure F, all boxes**).

Taken together, these data reveal that PAI detects variability in total haemoglobin and blood volume metrics between passages whereas variability in vascular function or oxygenation is not detected.
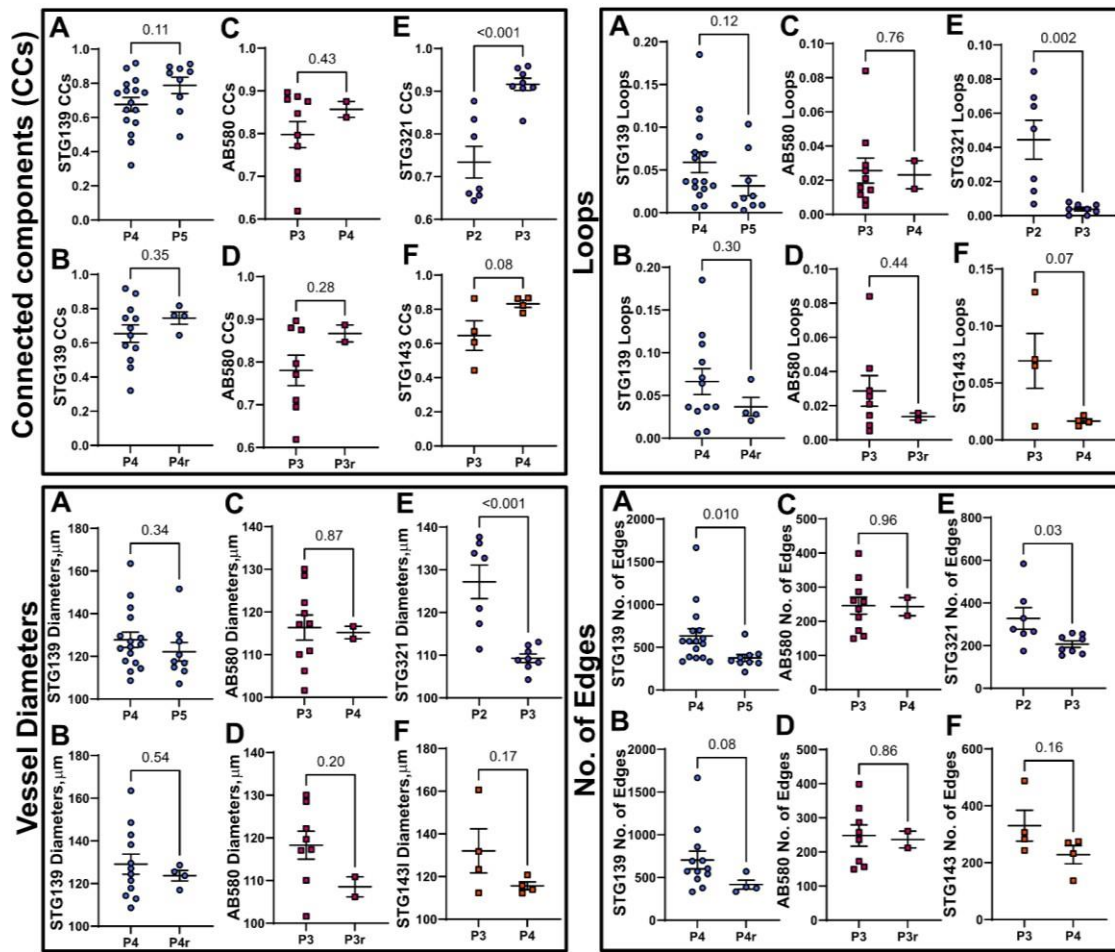
Figure 4.14. Structural and Topology metrics are fairly stable across the two passages measured. 4 boxes of subfigures are presented for each metric examined and they are titled: Connected components (CCs), Loops, Vessel diameters and Number of Edges. In each box, subfigures A-F: (A) STG139 across P4 and P5, (B) STG139 across P4 and repeat (P4r), (C) AB580 across P3 and P4, (D) AB580 across P3 andrepeat (P3r), (E) STG321 across P2 and P3, (F) STG143 across P3 to P4. In all subfigures, data presented as a scatter dot plot with mean ±SEM. In all subfigures, each data point represents data from one tumour (biological replicate). In all subfigures p-values for all comparisons are shown calculated by unpaired t- test except for figure (A) in CCs, Loops and Edges, figure (C) in Loops and figure (B) in Edges where a Mann-Whitney test was used. For all, p<0.05 considered significant. The following n numbers refer to the number of tumours per PDX passage in each sub-figure: for (A) P4 n=16, P5 n=9. For (B) P4n=12, P4r n=4. For (C) P3 n=10, P4 n=2. For (D) P3 n=8, P3r n=2. For (E) P2 n=7, P3 n=8. For (F) P3 n=4,P4 n=4.

4.3.6. PAI metrics are corroborated by underlying *ex vivo* IHC vascular markers

Throughout the chapter, general comparisons to the IHC results presented in Chapter 2 have been made. It is vital that *in vivo* imaging metrics are compared to *ex vivo* IHC, to provide a biological explanation of the *in vivo* imaging signals. To conclude this investigation of vascular phenotypes using PAI, I formally correlated each mesoscopic and tomographic PAI metric measured *in vivo* at end-point to the IHC vascular markers described in Chapter 2.

THb^{MSOT} calculated from tomographic PA images was related in part to the number of blood vessels in the tumours, measured by CD31 vessel area (r=0.45, p=0.001, **Figure 4.15A**), and is also driven by haemorrhage (r=0.71, p<0.001, **Figure 4.15B**), confirming the observations of blood pooling on the tomographic images, which gave rise to high THb^{MSOT} values. Interestingly THb^{MSOT} had a negative relationship with ASMA vessel coverage measured on IHC (r=-0.52, p<0.001, **Figure 4.15C**), reflecting the immature vessel phenotype present in tumours with a high vessel density here, which results in leaky blood vessels, poor perfusion and blood pooling.

$SO_2^{MSOT}(O_2)$ correlated positively with vessel maturity (r=0.5, p<0.001, **Figure 4.15D**) and negatively with hypoxia measured *ex vivo* by CAIX staining (r=-0.44, p=0.004, **Figure 4.15E**), similar to previous measurements in breast cell-line models[48], while the dynamic ΔSO_2^{MSOT} also correlated with vessel maturity (r=0.37, p=0.006, **Figure 4.15F**).

In mesoscopic PAI metrics, end-point blood volume and number of edges both correlate with THb^{MSOT} as expected (r=0.55 p<0.001; r=0.61 p<0.001 respectively). Blood volume and number of edges also relate to the vessel maturity (r=-0.38, p=0.003; r=-0.43, p=0.001 respectively, **Figure 4.15G**) and ultimately the hypoxic level of the whole tumour in these models (r=0.41, p=0.006; r=0.57, p<0.001 respectively, **Figure 4.15H**).
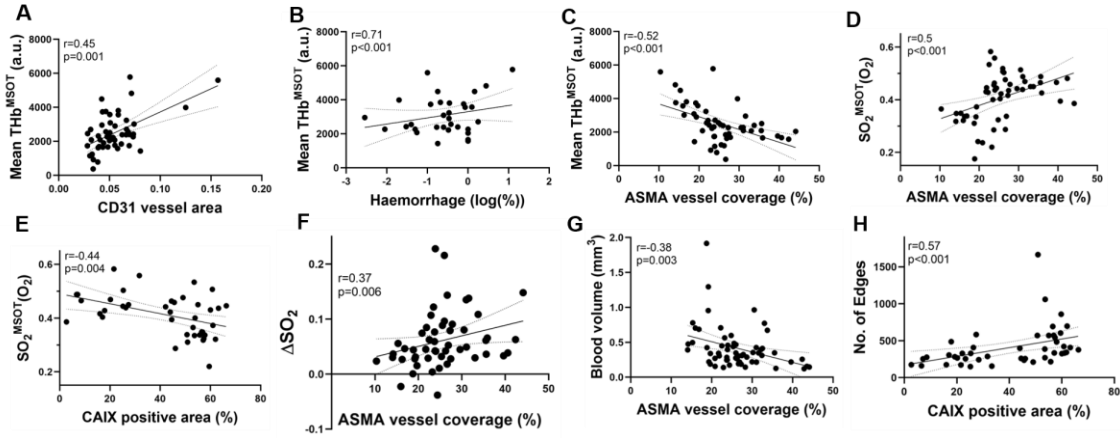
Figure 4.15. PAI vascular metrics correlate with ex vivo IHC measurements of vessel content, maturity and hypoxia. Correlations between the following metrics are shown: Mean Total Haemoglobin(THb^{MSOT}, a.u.) measured by tomographic PAI vs. (A) CD31 vessel area measured on IHC, (B) Haemorrhage (%) measured by H&E sections and (C) ASMA vessel coverage of CD31+ vessels (%) by ASMA IHC sections. SO_2^{MSOT} measured by tomographic PAI vs (D) ASMA vessel coverage by IHC and

(E) CAIX positivity measured by IHC. (F) ΔSO_2 calculated as difference between ($SO_2 (O_2)$)- ($SO_2(Air)$) measured by tomographic PAI during a gas challenge vs. ASMA vessel coverage on IHC. (G) Blood volume measured by mesoscopic PAI vs. ASMA vessel coverage by IHC. (H) Number of Edges measured by mesoscopic PAI vs. CAIX positivity measured by IHC. In all subfigures data shown as scatter plots where each data point is one tumour (biological replicate). Least square's regression line shown in black with 95% confidence intervals denoted by dotted line. All data collected from tumours at end-point (~1 cmin diameter). All IHC metrics are averaged across core and outer sections. In all subfigures, spearman's rank correlation coefficient is reported (r) along with a p-value (<0.05 considered significant). The following n numbers refer to the number of tumours represented in each sub-figure: For (A-D, F) n=52 (in B only 28 data points displayed on log scale). For (E) n=41. For (G) n=60. For (H) n=45.

4.4. Discussion

4.4.1. Multiscale PAI and IHC provide complementary information on breast PDX vascular phenotypes
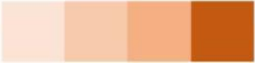
Chapter 2 introduced the 4 PDX models (2 basal: STG139 and STG321 and 2 luminal B: AB580 and STG143) and found that they displayed distinct vascular phenotypes on IHC, with differences in necrosis, hypoxia, vessel area and vessel maturity. These PDXs appear to be robust and reliable vascular models of the disease, with little inter-passage heterogeneity observed. An initial comparison to patient tissue showed some qualitative similarities between patient and PDX vasculature, but quantitative comparisons are needed. Finally, little evolution in vascular markers was seen with increasing tumour size.

In this chapter I used a combination of tomographic PAI and longitudinal mesoscopic PAI to visualise and quantify vessel phenotypes in the 4 PDXs at two different resolutions and depths. I also sought to test the mesoscopic PAI analysis pipeline described in Chapter 3 *in vivo* and generate insights into the vascular phenotypes of the 4 breast PDXs that were available. The knowledge gained from these non-invasive *in vivo* imaging techniques can be combined with and supported by the IHC presented in Chapter 2 to provide an overall picture of the vascular phenotypes in the PDXs in terms of their blood content, network maturity and hypoxia levels.

Beginning with the assessment of blood content in the PDXs (**Table 4.1**) with tomographic PAI, THb^{MSOT} was found to be highest in the basal model STG139 and lowest in the luminal B model AB580. This was complemented by blood volume and number of edges measurements taken from end-point mesoscopic PAI measurements and underpinned by CD31 vessel area measured on IHC. STG321, AB580 and STG143 all had lower blood content across all metrics compared to STG139, particularly the luminal B model AB580. Haemorrhage on IHC was also present in many STG139 tumours, which seems to drive high THb^{MSOT} measurements in this model.

Table 4.1. Blood content metrics measured across IHC, tomographic and mesoscopic PAI. Table displays mean± standard error of the mean for all metrics across all 4 PDX models (STG139, STG321, AB580 and STG143). Measurements colour-coded in orange shading to represent relatively high and low values across the 4 models. CD31 normalised area was averaged across core and outer IHC sections.
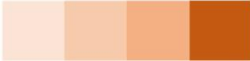
PDX model	Haemorrhage (%)	CD31 normalised area	THb (a.u.)	Blood Volume (mm³)	No. of Edges
STG139 (basal)	0.82 ± 0.39	0.066 ± 0.0039	3280.97 ± 221.84	0.59 ± 0.076	540.18 ± 60.84
STG321 (basal)	0.0094 ± 0.0052	0.050 ± 0.0016	2090.70 ± 112.30	0.29 ± 0.044	254.44 ± 28.34
AB580 (lumB)	0.00 ± 0.00	0.039 ± 0.0032	1294.51 ± 140.94	0.26 ± 0.030	245.38 ± 20.86
STG143 (lumB)	0.00 ± 0.00	0.034 ± 0.0017	2199.30 ± 146.94	0.34 ± 0.060	279.06 ± 34.89

Low ▯▯▯▮ High

Vessel network maturity was also different between the PDXs (**Table 4.2**). Here, the basal model STG321 presents with the highest vessel maturity, with a high number of connected components (subnetworks), fewer looping structures and smaller vessel diameters measured with mesoscopic PAI. A more mature vessel network will typically display elevated pericyte/smooth muscle coverage, which will result in smaller vessel diameters[251] and pruning of redundant vessels, which may lead to a reduction in looping structures and consequently an increase in vascular subnetworks (connected components). On IHC STG321 had the relatively highest ASMA vessel coverage and lowest VEGF expression, corroborating that this model has a mature vessel phenotype with less immature angiogenic vessels forming. The limited angiogenic potential of STG321 is reinforced by the lack of evolution of blood volume as tumour volume increased on mesoscopic PAI. The other basal model STG139 measures in stark contrastto STG321 and presents with an immature network with low pericyte/smooth muscle coverage. The luminal B models both have partially mature networks, with AB580 displaying slightly higher maturity on ASMA vessel coverage and mesoscopic PAI thanthe luminal B model STG143, which may be confounded by the low number of vessels in AB580.

154

Table 4.2. Vessel network maturity metrics measured across IHC, tomographic and mesoscopic PAI.
Table displays mean± standard error of the mean for all metrics across all 4 PDX models (STG139, STG321, AB580 and STG143). Measurements colour-coded in orange shading to represent relatively high and low values across the 4 models. ASMA vessel coverage was averaged across core and outer IHC sections.
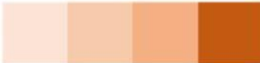
PDX model	ASMA vessel coverage (%)	VEGF (%)	Connected Components	Loops	Vessel diameter (μm)
STG139 (basal)	21.26 ± 1.01	62.45 ± 1.58	0.72 ± 0.032	0.049 ± 0.0090	125.74 ± 2.79
STG321 (basal)	35.52 ± 1.35	34.26 ± 9.08	0.84 ± 0.030	0.021 ± 0.0069	116.80 ± 2.77
AB580 (lumB)	27.36 ± 1.07	69.93 ± 1.42	0.81 ± 0.026	0.025 ± 0.0061	116.15 ± 2.43
STG143 (lumB)	23.61 ± 0.77	75.91 ± 4.63	0.74 ± 0.054	0.043 ± 0.015	123.85 ± 5.76

Low � High

Measurements of tumour hypoxia are more nuanced in the PDXs (**Table 4.3**). The basal model STG321 displayed the highest $SO_2^{MSOT}(O_2)$ measured on tomographic PAI, and had the highest responding fraction on average across the 4 PDX models. This indicates that the mature vessel network of STG321 is capable of adequately perfusing the tissue and delivering oxygen, which is corroborated by the relatively low levels of necrosis and hypoxia (CAIX) measured in this model *ex vivo*. STG139 is the most necrotic and hypoxic of all the PDXs measured on IHC, likely as a result of its immature vessel phenotype, which results in relatively low $SO_2^{MSOT}(O_2)$ and responding fraction. The two luminal B models have variable $SO_2^{MSOT}(O_2)$ measurements which on average are relatively high in AB580 and lower in STG143. This reflects the differences in vessel network maturity between the two models but doesn't reflect the differences in CAIX expression and necrosis, which are higher in AB580. Perhaps the blood is well oxygenated in AB580, but the network is too sparse to deliver oxygen sufficiently to all cancer cells. Differences in latency period between AB580 and STG143 will be explored in Chapter 5, as a possible explanation for the differences in hypoxia.

Table 4.3. Hypoxia metrics measured across IHC, tomographic and mesoscopic PAI. Table displays mean± standard error of the mean for all metrics across all 4 PDX models (STG139, STG321, AB580 and STG143). Measurements colour-coded in orange shading to represent relatively high and low values across the 4 models. Necrosis and CAIX measurements were averaged across core and outer IHC sections.

PDX model	Necrosis (%)	CAIX (%)	$SO_2(O_2)$	ΔSO_2	Responding Fraction
STG139 (basal)	24.74 ± 1.81	57.18 ± 1.35	0.38 ± 0.019	0.051 ± 0.010	0.52 ± 0.036
STG321 (basal)	14.63 ± 0.83	15.19 ± 2.74	0.45 ± 0.0090	0.075 ± 0.012	0.60 ± 0.036
AB580 (lumB)	23.69 ± 1.92	40.09 ± 2.78	0.45 ± 0.026	0.074 ± 0.021	0.55 ± 0.047
STG143 (lumB)	10.59 ± 1.14	20.10 ± 2.10	0.37 ± 0.037	0.050 ± 0.0094	0.56 ± 0.059

Low ▢▢▢▢ High

Overall, 4 distinct phenotypes have been measured in the 4 PDX models across *in vivo* tomographic and mesoscopic PAI, which were corroborated by *ex vivo* IHC. In the two basal models, one displays a dense but immature vessel network resulting in poor oxygenation and hypoxia (STG139), while the other displays a mature vessel network and relatively sufficient oxygenation (STG321). In the luminal B models, the partially mature but sparse vessel network in AB580 is able to deliver oxygen to the tumour but this does not seem sufficient to prevent hypoxia. While in STG143, the lower maturity of the network and lower blood oxygenation, still delivers sufficient oxygen to tissue to prevent hypoxia and subsequent necrosis.

Here, SO_2^{MSOT} values showed a significant difference between the basal models STG139 and STG321. Importantly these measurements were not subtype dependent. Previously, measurements taken from breast cell-line models in our laboratory showed differences in SO_2^{MSOT} between two models representing two breast cancer subtypes (ER- vs. ER+)[48]. The results from these PDXs suggest that vascular phenotypes within breast cancer subtypes are more diverse than previously reported in these cell-line models. In all 4 PDXs,

the SO_2^{MSOT} values were similar to those measured in the ER- MDA-MB-231 cell-line xenograft, possibly indicating that higher measurements taken from the ER+ MCF-7 cell line xenograft represent more extreme levels of blood oxygenation.

Evolution of THb^{MSOT} and SO_2^{MSOT} did not occur in the subset of STG139 and AB580 tumours analysed, which is corroborated by a lack of evolution of CD31 vessel area and ASMA vessel coverage relatively on IHC (Chapter 2, **Figure 2.13**). It seems that while the sub-volume monitored longitudinally over time in mesoscopic PAI undergoes evolution in blood volume, changes across the whole tumour area measured by tomographic PAI and IHC are not detectable.

In interpretation of the mesoscopic PAI findings, the penetration depth must be considered. While the system is capable of capturing high resolution tumour vessel networks, only vessel networks in the first 2 mm of the tumour are accurately captured, owing to the exponential decay of signal amplitude in depth caused by the scattering of light in tissue, the band limitation of the ultrasound detectors and the geometry of the system. Therefore, mesoscopic PAI will not necessarily inform on blood content across the whole tumour area/volume, which was instead captured in this work using tomographic PAI (although THb^{MSOT} and blood volume do correlate at end-point r=0.51). Mesoscopic PAI images are most informative when captured longitudinally, as the development of the vasculature in approximately the same sub-volume of tumour tissue can be monitored over time.

4.4.2. Dynamic measurements of oxygenation were not capable of delineating the PDX models

Measurements of SO_2^{MSOT} were taken whilst the mouse was breathing air were not significant between the models, however, when the breathing gas was changed to 100% O_2 revealed differences in SO_2^{MSOT}. This phenomenon has been reported in cell- line models by Tomaszewski et al., who validated the use of a gas challenge in PAI[125]. Perhaps the change to O_2 resulted in perfusion changes, which exaggerate the phenotypesseen on air, increasing the sensitivity of the SO_2^{MSOT}metric to different vascular phenotypes.

I hypothesised the gas challenge would provide a dynamic oxygenation read-out, which could be used as a surrogate biomarker of perfusion in these models, as has been shown previously in prostate cell-line xenografts[126]. While measurements of ΔSO_2^{MSOT} and the responding fraction were in the range of those measured in the prostate xenografts, no significant differences in these metrics were measured between the PDXs. In prostate cancer cell-line xenografts, these metrics were capable of distinguishing between a necrotic and haemorrhagic model[125], with low ΔSO_2^{MSOT} and responding fraction areas spatially correlated with areas of low perfusion and hypoxia[126]. The discrepancy between these findings may arise from spatial heterogeneity in gas challenge response, which would not be detectable in the average responses measured here. Further spatial analyses including co-registration with histology images could be conducted (as discussed in section 4.4.8. Future Work). Additionally, the previous thresholds for calculating ΔSO_2^{MSOT} and the responding fraction were optimised for the prostate-cell line xenografts, and no further optimisation was conducted here. It is also possible that the effect size in the cell-line models is higher than observed in more clinically-relevant PDX models. Nevertheless, it is important to stress that ΔSO_2^{MSOT} correlated positively with ASMA vessel coverage *ex vivo*, suggesting this measurement can provide insight into vessel maturity in these PDXs.

4.4.3. Variability of vascular phenotype in blood oxygenation could be indicative of chaotic and immature vessel network with perfusion changes

When assessing tomographic PAI metrics, SO_2^{MSOT} was highly variable across all PDXs except STG321, which presents with a mature vessel phenotype. This finding is not overly surprising considering that chaotic and immature vascular networks in the other 3 models will result in heterogeneous perfusion. Immature vessels are susceptible to changes in interstitial fluid pressure which can result in vessel collapse and blood flow alterations, which can alter perfusion on a scale of minutes to days[27,261]. When measuring SO_2^{MSOT} therefore, it is possible that the measurement is decreased by vessel collapsing at that particular moment, and had the measurement been taken an hour later, after possible reperfusion of the vessels, more oxygen could have been delivered to the tumour and a higher SO_2^{MSOT} value obtained. This assumption is supported by variability in ASMA

vessel coverage seen in STG139, suggesting variable pericyte/smooth muscle vessel coverage. This model in particular presents the most heterogeneous vessel networks across multiple IHC and PAI metrics.

The high variability in SO_2 measurements suggests that this metric may not be sensitive enough to accurately delineate different vascular phenotypes. Despite variable measurements of SO_2^{MSOT} across 3 models and particularly in STG139, there was still a relationship to ASMA vessel coverage and CAIX staining, showing that overall SO_2^{MSOT} measurements indicate the ability of the vessel network to perfuse the tumour with oxygen to prevent hypoxia. However, the relationship has significant variability, indicating that further investigation into the underlying physiological and metabolic processes that could explain SO_2^{MSOT} would be of interest to investigate in relation to the PDX models. Characterising the variability of SO_2^{MSOT} measurements in breast cancer cell-line models across longer time periods, of up to 2 hours, is currently underway in the laboratory and could be applied to measure dynamic perfusion in PDXs. Equally, a direct measure of perfusion such as dynamic contrast enhanced- MSOT using a near infra-red dye such as the clinically approved indocyaninegreen could be used[126], while measuring the oxygen consumption rate of cultured PDX cells would provide insight into the metabolic requirements of each tumour.

4.4.4. Measurements of blood content were variable across PDX passages

Inter-passage variability in PAI metrics was not expected, owing to the preservation of intra-tumoural genetic clonal architecture previously reported in these models[10] and the IHC data presented in Chapter 2, which showed minimal inter-passage heterogeneity of vascular markers *ex vivo*. Measurements of vascular function (SO_2^{MSOT}(Air), SO_2^{MSOT}(O_2), ΔSO_2^{MSOT} and responding fraction) were consistentacross 3 passages in STG139 and across 2 passages of STG321 and STG143. While CAIX staining and ASMA vessel coverage data from Chapter 2 would indicate little change in hypoxia or vessel function across passages that would be measured by these *in vivo* metrics, this finding may also reflect a lack of sensitivity in tomographic blood oxygenation metrics, which rarely significantly delineated the PDX models. Other measurements of vessel maturity taken with structural and topological analyses of the mesoscopic PA images were

also stable across STG139 and AB580 passages and passage repeats but displayed an apparent increase in vessel maturity in the other two models, particularly STG321. However with only two passages measured comments on trends are only tentative and should be assessed with further passaging in future. Additionally, these results could be confounded by a decrease in blood volume (and therefore less structures captured) between the two passages.

A drop in THb^{MSOT} was measured between P3 to P4 and P5 in STG139 was supported by CD31 vessel area data measured *ex vivo*. Additionally, THb^{MSOT} was variable across the passage repeat in AB580, and across two passages in STG321 and STG143, which may be explained by the lower initial blood volume value in the latter passages of STG321 and STG143, as measured by mesoscopic PAI. Interestingly, despite a shift in blood volume values at the initial imaging time point for the latter passages of all 4 PDX models, the evolution of the blood volume remained consistent and appears robust and inherent to the PDX. The shift is perhaps due to increased noise in the latter passages seen visually on mesoscopic PAI, and is not necessarily a biological change. Measurements in further passages would need to be taken to confirm any trends in the mesoscopic PAI data.

In the measurements taken thus far, it appears as though vascular parameters in the PDXs which relate the absolute vessel number or blood content in the PDXs are more variable than those which measure the 'function' of the vessels i.e. how mature they are and the level of hypoxia resulting. The absolute number of vessels may be influenced by the particular slice taken during tomographic imaging or histology for example, or perhaps the location of the tissue fragment on the mouse flank. The location of the PDX when implanted at surgery, will likely be consistent across the same passage (as the person conducting the surgery will implant in approximately the same place for each mouse in that cohort) but it may change from passage to passage as those are in different implantations sessions and there were no anatomical landmarks defined for implantation. The location of the tumour on the mouse flank will be more similar within a passage than between a passage. This is important, as the vascular environment surrounding the tumours upon implantation will likely be utilised by the tumour as it generates its own vascular network, so the abundance of vessels at the implantation site may influence the abundance of vessels upon measurement.

160

4.4.5. Potential for clinical translation

One of the motivations for this study was to assess the sensitivity of PAI to different vascular phenotypes present in breast PDXs, as more clinically-relevant models of breast cancer, as an advancement from previous work in breast cell-line xenografts, which likely present extreme examples that are often not clinically-relevant and representative[48,9]. Here, correlations to IHC measurements showed that measurements from tomographic and mesoscopic PAI can reveal underlying vessel area, haemorrhage, vessel maturity and hypoxia measured *ex vivo*, displaying the sensitivity of PAI measurements to vascular phenotypes in breast cancer. However, similar studies in a wider range of PDXs and patients, preferentially also representing additional breast cancer subtypes not represented by the models presented here, should be conducted to enable the sensitivity of PAI to different vascular phenotypes to be assessed on a larger scale.

Owing to its limited penetration depth, the mesoscopic PAI system described in this chapter could not be translated for clinical use and is limited to pre-clinical studies. Mesoscopic PAI captures a larger portion of the tumour than IHC, with a resolution in-between IHC and tomographic PAI. Therefore, using mesoscopic PAI in this context has allowed a useful bridge between the IHC and tomographic PAI, allowing visualisation of a sub-volume of the vascular network at high-resolution to better understand the phenotypes. Additionally, engineering advances in breast clinical PAI, using systems which cup the whole breast[144,148], have allowed tumour vascular networks of a similar resolution to be captured. Analyses pipelines and network features, such as the ones presented in this chapter, could be applied in future to provide quantitative read-outs of the networks captured with these systems.

4.4.6. Limitations

There are several limitations to this work that should be discussed. First, as noted in Chapter 3, 2D ex vivo validation of structural and topological metrics does not fully encompass the 3D topological characteristics of the vascular network and only provides a partial 2D representation of vascular phenotypes. 3D IHC, micro-CT or light sheet fluorescence microscopy may provide further ex vivo validation using exogenous labelling to identify 3D vascular structures, at end-point. Nonetheless, when applied to breast PDXs

the topology metrics do appear to capture features associated with vessel maturation measured on ex vivo IHC.

Second, values of THb^{MSOT} and SO_2^{MSOT} calculated from tomographic PAI are only relative and not absolute. This is because the data is not corrected for the effects of light fluence alterations in tissue, which results in a wavelength-dependent attenuation of the tomographic PAI data[48,125]. In PAI, absorbing structures at depth may not be detected, or detected at an artificially lower intensity, owing to the decay of light energy (fluence) as it passes through tissue. This will bias the measurements made, and is why relative not absolute measurements are reported here. I partially controlled for the light fluence problem by matching tumour size and being consistent with tumour positioning in the PAI systems, but this is not possible with patient tumours. Therefore, accurate light fluence correction is under development[158] and is needed to advance PAI in the clinic, butis not yet validated for routine use.

Finally, changing the breathing gas from air to 100% O_2 presented a physiological challenge for the NSG mice, which occasionally resulted in suffocation. Respiratory problems during the gas challenge have been reported before by the laboratory[125], although not to the same extent, with the NSG mice appearing particularly sensitive to this protocol. This adverse effect, coupled with the lack of growth in luminal B models, lead to a decrease in observations made during the gas challenge in these models, and insufficient power to monitor tomographic PAI metrics across passages in AB580.

4.4.7. Future work

First, accurate co-registration of mesoscopic and tomographic PAI with each other and with IHC should be conducted, to gain increased spatial colocalisation of *in vivo* imaging biomarkers with the underlying molecular and cellular information. Achieving such co-registration would afford further insights into the underlying tumour biology, particularly in relation to those metrics which demonstrated no significant effects over the whole tumour area such as ΔSO_2^{MSOT}. Co-registration between imaging modalities such as PAI and MRI is underway using landmarks and other methods[262], however, thereare several challenges presented by the processing of tissue *ex vivo*, such as tissue shrinkage, which makes it difficult to accurately co-register IHC with *in vivo* imaging. Here, an

approximate co-registration to tomographic PAI slices was attempted and indicated that a more accurate co-registration would likely be possible using appropriate tissue labelling and moulds in future.

The tomographic PAI analyses described in this chapter have been reported and used in the laboratory for many years[48,125,126], although this is the first report of their application in breast PDXs. Having collected such a large dataset of tomographic images in breast PDXs (~1000 images), further advancements in tomographic analyses could be optimised using this dataset. In particular, analyses of the whole tumour volume in 3D, rather than just the 2D tomographic slice, as conducted here, would provide increased spatial information of vascular parameters.

One limitation of the mesoscopic PAI system used here is that it only uses one wavelength of 532 nm. This is an isobestic point of deoxygenated and oxygenated haemoglobin, meaning that the two absorbers have the same absorption coefficient at this wavelength[106] but the two cannot be distinguished from one another in these images. As a result, only information on haemoglobin level and distribution (resulting in the blood vessel images) is captured. Multi-spectral mesoscopic PAI using at least 2 wavelengths will improve on this current system and is under commercial development. Multi-spectral mesoscopic PAI has been used recently in colon cell-line xenografts to distinguish deoxygenated and oxygenated haemoglobin and monitor oxygenation decreases upon vascular-targeted therapy[107] and could be applied to monitor oxygenation in individual vessels in breast PDXs.

Utilising PAI to monitor response to therapy non-invasively at early time-points and across many months is clinically feasible. Therefore, future work should investigate vascular responses of PDXs to traditional and novel therapies measured with PAI. PDXs have already been shown to respond to therapies in a similar manner to the patients from which they are derived[10], and so studies focusing on PAI of PDX vascular response to radiotherapy or anti-angiogenics for example, could provide clinical insight on which PAI metrics would provide biomarkers of vascular response in patients.

4.4.8. Summary

To summarise, this chapter presented data on the first combination of mesoscopic and tomographic PAI to image and quantify blood vessel networks in breast PDXs, showing distinct vascular phenotypes on longitudinal mesoscopic and tomographic PAI across the 4 models that correlated with IHC measurements. PDX vascular phenotypes displayed variability across passages in relation to blood content, whereas changes in blood oxygenation were not detected.

5 REVEALING THE UNDERLYING MECHANISMS FOR THE DEVELOPMENT OF DISTINCT VASCULAR PHENOTYPES

I extracted the RNA and worked in collaboration with Dr Ashley Sawle to analyse the sequencing data. I interpreted all results and analysed correlations between gene expression and imaging data. The Genomics Core facility at the CRUK CI conducted the library preparation and sequencing. The Histopathology Core facility at CRUK CI ran the IHC.

5.1. Introduction

5.1.1. Correlating imaging signals, immunohistochemistry and gene expression

The clinical use of molecular imaging to predict tumour behaviour and treatment response, as well as support histopathology results, is expanding. The integration of imaging and molecular biomarkers has huge potential to improve breast cancer patient diagnosis and prognosis by providing complementary information and cross validation for new biomarkers of tumour progression[263,264]. Non-invasive imaging adds spatial and temporal resolution, which complements the traditional molecular biomarkers that can be extracted from a physical tissue biopsy[265]. Imaging can also be conducted longitudinally, at multiple patient visits, meaning that validated imaging biomarkers could provide insight into tumour progression and therapy response where repeated tissue biopsy may not be possible[264].

Many clinical studies in breast cancer patients have correlated imaging biomarkers with histopathological markers of subtype and grade such as ER and Ki67 expression levels, as a way of validating imaging parameters as markers of aggressiveness[263]. Additionally, histopathological and gene expression markers can provide insight into the underlying biological processes that give rise to imaging signals. For example, HIF1α IHC and gene expression has been shown to correlate with ^{18}F-FDGPET[266] and ^{13}C- label exchange between pyruvate and lactate measured with MRI[267], respectively, providing insight into the role of hypoxia in breast tumour metabolism[267]. Applied in PAI, histopathology markers have begun to validate PAI signals as markers of vessel density, vessel maturity[48], hypoxia and perfusion[126], in breast and prostate cell-line models; here, such validation has been expanded to breast PDXs for the first time.

Integrating the use of imaging biomarkers with gene expression for clinical application is referred to as radiogenomics, an expanding field of research. Born out of radiomics, the study of textural features on medical images such as CT and MRI[265], radiogenomics investigates the use of textural features to infer gene expression[263,264]. For example, using principal component analysis to group robust radiomics features from CT scans has been shown to create a 'radiomics signature' that can predict ctDNA mutant

allele fractions in metastatic melanoma patients[265], while DCE-MRI heterogeneity features correlated with high expression of VEGF signalling pathways[268].

Integrating imaging biomarkers into the clinical setting to be complementary to histopathology and genomic profiling comes with many challenges. The studies described above and multiple others rely on correlations between imaging metrics and *ex vivo* expression markers, yet there will be many unknown confounding variables that influence these correlations which are yet to be properly understood. Standardisation between different imaging systems and protocols in different laboratories or hospitals is an active area of research across medical imaging, with new global efforts in the PAI field also[157,82]. Finally, sharing of large imaging datasets between different settings is another challenge to enable widespread-use of imaging biomarkers in clinic[264].

Despite advances in integrating medical imaging with genomics and histopathology markers, this is not routine in PAI. In fact, to the best of my knowledge tumours imaged with PAI pre-clinically or clinically have never been genomically profiled to improve understanding of the underlying biological processes that drive the PAI signals detected. In this chapter, gene expression, IHC and PAI metrics derived fromthe breast PDXs are integrated for the first time, to draw conclusions on the origins of PDX vasculature and PAI signals.

5.1.2. Unanswered questions on the origin of PDX vascular phenotypes

Throughout this thesis, *in vivo* PAI and *ex vivo* IHC metrics have shown that the 4 breast PDXs studied display distinct and repeatable vascular phenotypes, with minimal evolution or development of these phenotypes as tumours grow. All 4 PDXs create blood vessels but they are not all made equal, suggesting there is an instructive element in the implanted tumour from the cancer cells themselves, because if this were simply mouse reactions to the human tissue transplantation the vascular phenotypes would be the same.

In this chapter, I address Aim 4 of the project and gain insight into the origins of PDX vasculature by conducting RNA sequencing on a subset of the PDXs, taking samples across passages for all 4 models. The expression of a hypoxic gene signature of 52 genes[269] was evaluated, as a starting point for assessing this 'instructive element' in the

cancer cells. Correlations between hypoxic gene expression, IHC and PAI were conducted, to integrate knowledge on PDX vasculature from these complementary methods, and provide genomic validation of the PAI signals for the first time. Additionally, comparisons to corresponding patient and PDX gene expression data from the Caldas laboratory was conducted as well as an assessment of variability in hypoxic gene expression across PDX passages, to test whether the PDXs have representative and repeatable hypoxic gene expression levels. Finally, the metabolic requirements of the PDXs were briefly considered by assessing the proliferation and growth patterns, to investigate the possibility of oxygen demand as a confounding factor in the relationship between hypoxic gene expression and vascular phenotypes measured using PAI.

5.2. Methods

5.2.1. RNA sequencing and analysis

Total RNA was extracted from flash frozen tumour tissue using a Qiagen AllPrep®
DNA/RNA/Protein Mini Kit. All samples had an RIN value of >7.3 when measured on an
Agilent Bioanalyzer. Libraries for RNA-seq were prepared with an Illumina TruSeq
stranded mRNA workflow and sequencing performed on Illumina NovoSeq6000 with a
50bp paired-end run. Sequencing was conducted in 2 batches, with7 samples included in
both sequencing runs to assess batch to batch variability; 4 were from the first library
preparation with the sequencing repeated in the second run and 3 samples were re-
extracted and library preparation repeated before sequencing in the second run.

Quality of raw reads was assessed using FastQC (version 0.11.9). All samples were
of good quality with ~30 million reads each. Raw reads were trimmed using Trimmomatic
(version 0.39)[270] to remove adapter contamination. Human and mouse reads were
separated with Xenome[271] using genome references GRCm38 and GRCh38 release 102
from Ensembl[272]. Human reads were aligned to genome reference GRCh38 release 102
from Ensembl using STAR (version 2.7.6a)[273] and further quality assurance was carried
out using Picard tools (version 2.21.2), which showed over 90% alignment for all samples.
Gene expression was quantified using Salmon (version 1.4.0)[274] and the GRCh38 release
102 transcriptome from Ensembl[272].

All analyses were conducted in R. Counts were normalised using the vst function
from the Bioconductor[275,276] package DESeq2 prior to analysis. Raw counts were filtered
for genes with at least 2^5 reads in at least 1 sample to eliminate counts due to noise.
Principal component analysis (PCA) was conducted to assess variation between samples
based on PDX model, tumour subtype, PDX passage, sequencing run, or extraction batch.
PCA is a tool to reduce the dimensionality of the data. The first three principal components
were used to visualize the data and the percentage variance explained was calculated.

In order to compare the expression of the genes in a hypoxia gene signature

between samples we used a single scoring metric, which could later be easily correlated to imaging and IHC metrics by means of simple linear regression. The Bioconductor[275,276] package gene set variation analysis (GSVA) provides a means of generating such a score based on the expression of the signature genes in a similar manner to gene set enrichment analysis[277]. Expression of genes in 3 hypoxia gene signatures was assessed[269,278,279], with similar results found for each. Results from Buffa et al. are presented and interpreted in detail, as the top choice signature. This signature was chosen owing to its widely cited prognostic capabilities in breast and other solid cancers[280–284], its robustness to different pre-processing algorithms[285], and the novel use of both *a priori* gene function knowledge with analysis of *in vivo* co-expression patterns to generate the signature[269]. Hypoxia gene signature expression analysis of the corresponding patient and PDX microarray gene expression data from the Caldas lab[10] was conducted separately and qualitative comparisons to the PDX samples presented in this thesis were made.

5.2.2. Ki67 immunohistochemistry

Anti-human Ki67 IHC was conducted on sections from all PDXs as part of the QC IHC assessment as described in 2.2.2. All stained sections were qualitatively assessedby myself, with the guidance of Dr Elena Provanzano, to score the sections as high (>20% positivity) or low (<20% positivity), similarly to how the patient samples would have been scored clinically[10].

5.2.3. PDX growth curves

Tumours were measured throughout development externally using Vernier callipers and tumour volumes were calculated using the formula (A x B x B x (π/6)) being "A" the longest axis of the tumour and "B" the shortest.

5.2.4. Statistical analyses

All statistical analyses were conducted in GraphPad Prism v.9 unless otherwise stated. For STG139 and AB580, the correlation between GSVA score and tumour volume was calculated by Spearman's or Pearson's correlation coefficient respectively, depending on the distribution of the data. Mean GSVA scores for each PDX model werecompared using the R package limma to apply a linear model with Benjamini-Hochberg

multiplicity correction. To compare the means across passages in STG139 and AB580a one-way ANOVA was performed with Tukey's multiple comparison correction, unlessthe data violated the assumptions of a Gaussian distribution in which case Kruskal-Wallis

test with Dunn's multiplicity correction was conducted. To compare means between passage repeats within STG139 and AB580 an unpaired student's t-test was performed unless the data violated the assumption of a Gaussian distribution, in which case a Mann-Whitney test was conducted. Comparison of GSVA score to all *in vivo* PAI metrics and IHC vascular markers were computed using Spearman's rank correlation coefficient. All IHC metrics were averaged between the core and outer sections (described in 2.2.2). Significance was assigned to comparisons with $p < 0.05$.

5.3. Results

5.3.1. Expression of a hypoxic gene signature delineates the PDX models

Neither sequencing run nor extraction batch introduced variation in model clusters and therefore batch correction was not necessary (**Figure 5.1A, B**). Initial exploration of the RNA sequencing data using PCA showed that samples of the same model clustered together (**Figure 5.1C**). Interestingly, the largest first principal component (which explains 49.67% of the variability in the data) showed that transcriptomically the basal model STG321 sits in-between the two luminal B models (AB580 and STG143) and the basal model STG139, suggesting that transcriptomically speaking, STG321 is more similar to the luminal models than STG139. The second principal component (which explains 20.72% of the variability in the data) showed that STG321 is transcriptomically distinct from the other 3 models while the third principal component (which accounts for 12.05% of the variability in the data) separates STG143 from the other models (**Figure 5.1C**). As expected based on previous data for these PDX models[10], there was no detectable passage effect on the analysis, i.e. the clustering was not influenced by samples from different passages (**Figure 5.1D**). Overall, the 4 PDX models are transcriptomically distinct and remarkably repeatable, with differences and similarities between models reflected by the different principal components.
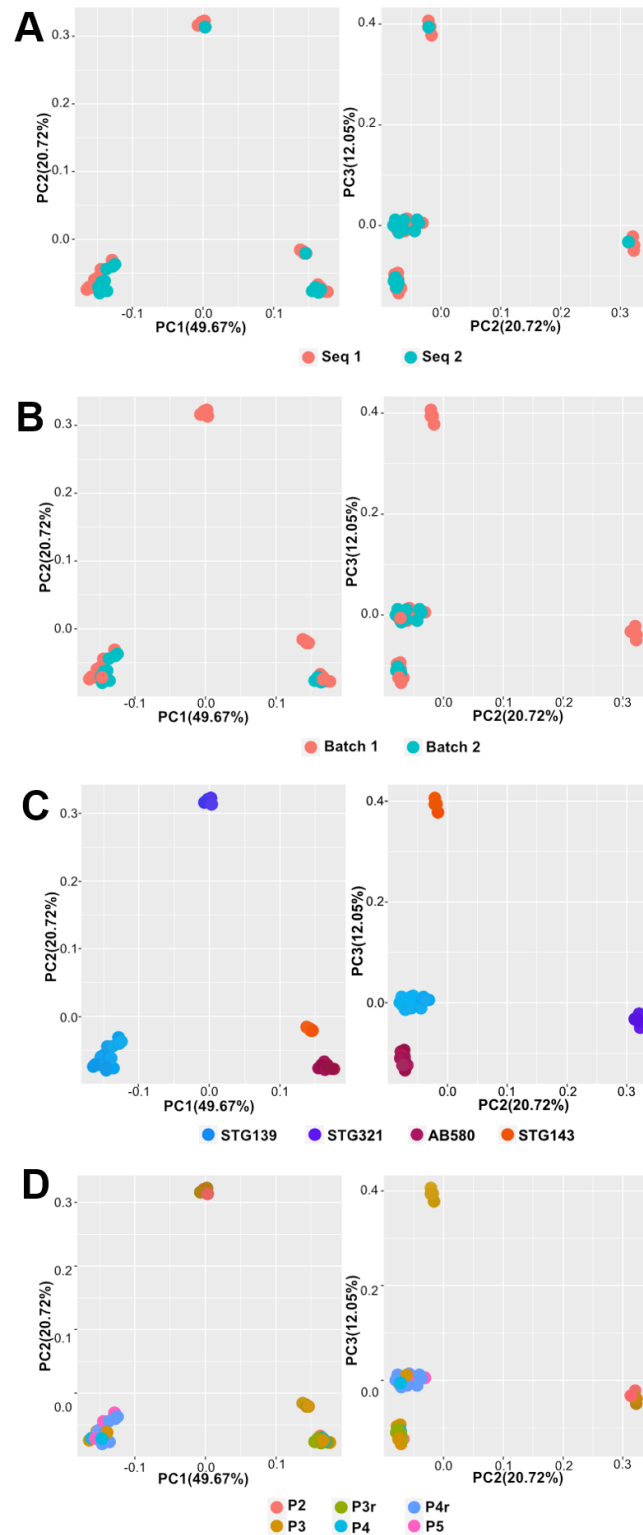
Figure 5.1. Principal component analysis demonstrates distinct transcriptomes in the 4 PDXs that are not affected by sequencing run, batch extraction or passage. In all subfigures principal components(PC) 1 vs. 2 displayed on left and PC2 vs. PC3 shown on right. (A) 4 distinct clusters seen in Sequencing (Seq) runs 1 and 2. (B) 4 distinct clusters seen in Extraction Batch 1 and 2. (C) 4 distinct clusters seen

representing models STG139, STG321, AB580 and STG143. (D) 4 distinct clusters seen across passages (P) and passage repeats (r). The following n numbers refer to the number of tumours per PDX model in all sub-figures: $n^{STG139}=19$, $n^{STG321}=7$, $n^{AB580}=13$, $n^{STG143}=4$.

Having established that distinct transcriptomes exist between the 4 PDXs, the expression of genes in a hypoxic gene signature was evaluated across the models, to investigate whether differences in expression may partially explain the 'instructive element' in the PDXs, which directs the formation of mouse host vasculature. A heatmap was generated to visualise the z-scaled (relative) expression for each gene in the hypoxia 51-gene signature[269] for all samples in both a subset of the PDX dataset presented in this thesis, as well as corresponding PDX and patient samples from the Caldas laboratory[10] (**Figure 5.2**).

STG139 tumours had the highest relative expression of the majority of genes in the signature. AB580 tumours were also relatively hypoxic in the thesis PDX samples, with high expression of genes involved in classic hypoxia signalling pathways such as angiogenesis (*vegfa, adm, hilpda*), glycolysis (*hk2, pgk1, aldoa*), collagen synthesis (*p4ha1*) and lipid accumulation (*hilpda*). These results are in agreement with CAIX positivity on IHC (**Figure 2.6**), with the gene coding for this protein (*ca9*) listed in the signature and expressed at high levels in most AB580 and STG139 samples. Interestingly, a subset of 4 STG139 tumours (labelled PEN36, PEN58, PEN35, and PEN32) and a subset of 5 AB580 tumours (PDP24, PDP11, PDP8, PDP29 and PDP28) have lower relative expression of the signature than the majority for that model. In both subsets, 3 of the samples are derived from smaller tumours (~0.1 cm^3).

In general, STG321 basal tumours had relatively low expression of the signature, although they do have high expression of genes involved in microtubule spindle formation and cytokinesis (*anln, kif20a, kif4a, tuba1c, tubb6, shcbp1*), which are essential for the completion of mitosis. These genes have been reported to be highly expressed in breast cancers and are associated with poor prognosis, independently of hypoxia[286,287]. Importantly, *vegfa* gene expression was low in all STG321 samples compared to the other models, supporting IHC data that this model has less angiogenic potential. Finally, the luminal B model STG143 had the lowest hypoxic gene expression overall.

Comparisons to corresponding patient and PDX data collected by the Caldas laboratory[10] was only possible qualitatively owing to the different methods of collecting gene expression data (the data in this thesis was collected via RNA sequencing, whereas Caldas data was collected via a DNA microarray). These data was also only available for STG139, AB580 and STG143 (**Figure 5.2**). Nevertheless, it can be concluded that hypoxic gene expression was high in the STG139 patient tumour and this has been maintained across several PDX passages collected by the Caldas lab and those presentedin this thesis. The STG143 patient tumour had relatively low hypoxic gene expression, which was maintained across 2 PDX passages collected by the Caldas lab and in the PDXsamples from this thesis. Finally, the AB580 patient tumour had little hypoxic gene expression, as did the first PDX passage (X0), collected by the Caldas lab. Later passagesanalysed for this thesis appear to have acquired higher expression of some hypoxia- related genes in the signature.
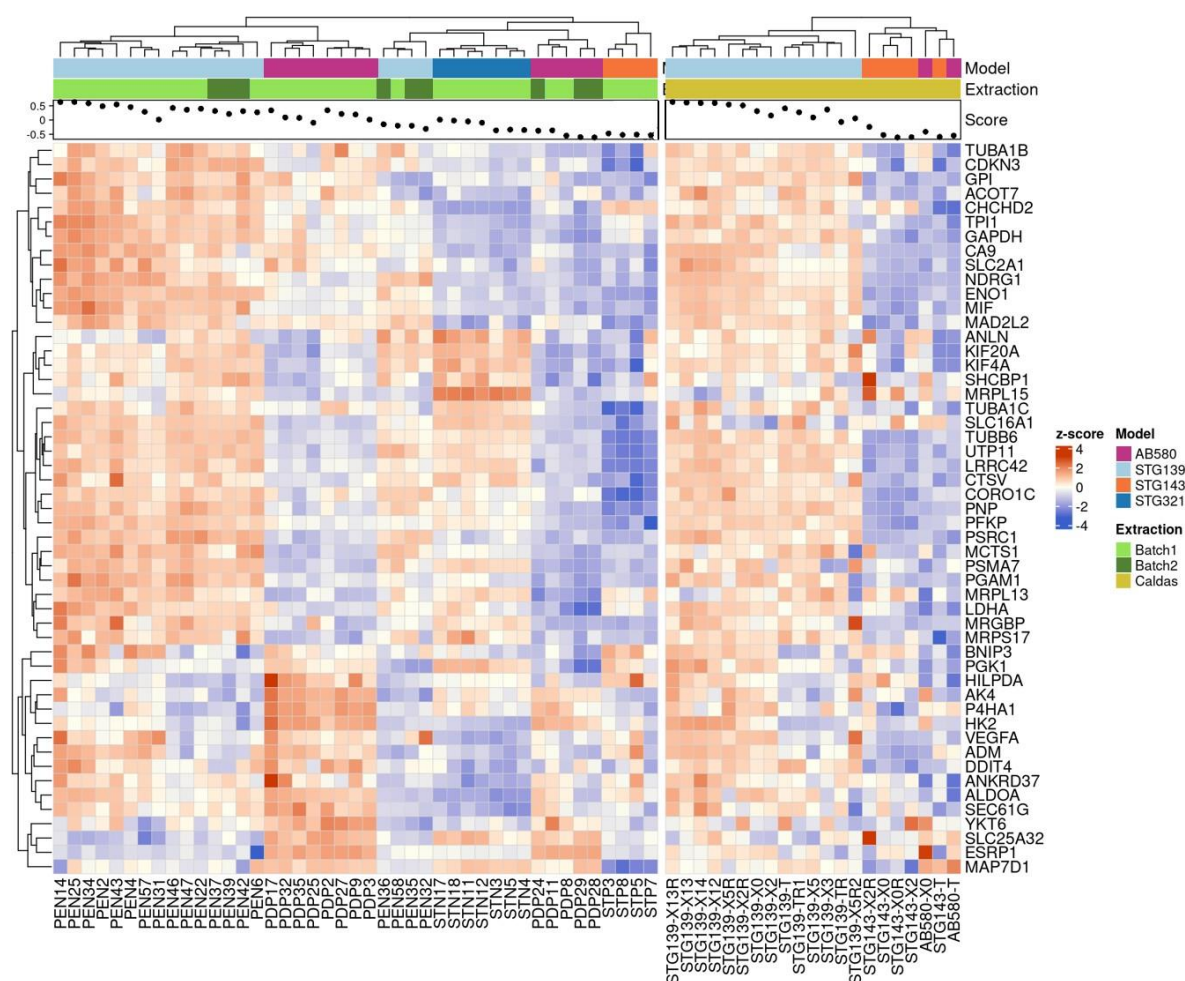
Figure 5.2. Heatmap displaying relative expression of 52 genes in a hypoxia gene signature across PDX and patient samples. The heatmap is split in two with the left-side displaying 43 PDX samples described in this thesis (data collected by RNA sequencing) and right-side displaying 21 patient and PDX samples from the Caldas lab[10] (data collected by DNA microarray). Sample IDs are listed across the bottom, with each column corresponding to one sample. Each row denotes a gene in the signature, labelled on the right-hand side. In each side of the heatmap, moving from left to right displays the samples from high to low relative z-scores (red to blue colour coding). The GSVA summary score is displayed above the heatmap as black dots ranging from -0.5 to 0.5 for each sample. The model that each sample belongs to is colour coded in the top row (Light blue = STG139, dark blue= STG321, burgundy= AB580, orange= STG143) and the extraction colour coded in the second row (Light green= batch 1, dark green= batch 2, yellow= Caldas lab). Caldas lab samples are labelled with the following abbreviations (T= patient tumour, X= passage (with corresponding number), X0= first passage from the patient tumour implanted in one mouse, R= relapse). The following n numbers refer to the number of tumours per PDX model for batch 1 and 2: n^{STG139}=19, n^{STG321}=7, n^{AB580}=13, n^{STG143}=4. The following n numbers refer to the number of tumours per PDX model for Caldas lab: n^{STG139}=13, n^{AB580}=1, n^{STG143}=4. There is 1 patient sample for STG139, AB580 and STG143 extracted by the Caldas lab represented on the heatmap.

176

Gene set variation analysis (GSVA) was used to give an overall score of signature expression. As expected, STG139 tumours were the most hypoxic with the highest GSVA score, while AB580 tumours had a significantly higher GSVA score than the other luminal B model STG143 (**Figure 5.3**). High levels of hypoxic gene expression in STG139 may explain why the blood vessel networks in this model are immature, resultingfrom high rates of angiogenesis and decreased pericyte coverage due to VEGF-A and other pro-angiogenic signalling pathways.
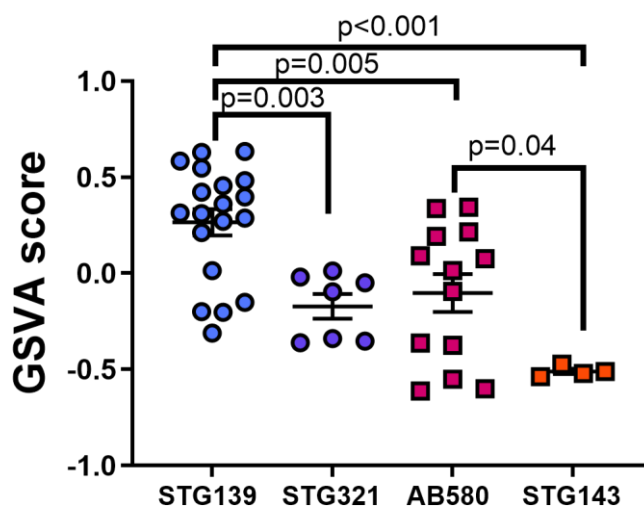
Figure 5.3. GSVA summary scores of the hypoxia gene signature show highest overall expression in STG139. Data presented as a scatter dot plot with mean ±SEM. Each data point represents data from one tumour (biological replicate). Means compared via the R package limma to apply a linear model with Benjamini-Hochberg multiplicity correction. The following n numbers refer to the number of tumours per PDX model: n^{STG139}=19, n^{STG321}=7, n^{AB580}=13, n^{STG143}=4.

### 5.3.2. Hypoxic gene expression has minimal evolution in STG139 and is not passage-dependent

Hypoxic gene expression differed between the PDX models and was highest in the basal model STG139 and the luminal B model AB580. This result may explain an instructive genetic element, which drives the formation of immature vessels. However, the question still remained as to which feature came first in tumour growth: the immature vessel networks, which poorly deliver oxygen to the tumour resulting in hypoxia, or hypoxic gene expression, which drives immature vessel network formation?

To answer this aforementioned question on the origin of PDX vascular phenotypes, the relationship between hypoxic gene expression and tumour size was assessed by correlating GSVA score to tumour volume in STG139 and AB580, two models with which different sized tumours had been preserved. In STG139, there was some evidence that GSVA score increased with tumour volume (r=0.44, **Figure 5.4A**) but this was not quite significant (p=0.06), owing to a more variable distribution of GSVA score across the volumes sampled. Perhaps this suggests a heterogeneous evolution of hypoxic gene expression as tumour volume increases, with some tumours showing stable expression, which drives the formation of immature vessel networks and others increasing expression of hypoxia-associated genes as tumours grow. On IHC, CAIX expression does not evolve with tumour growth (r= -0.0069, p=0.97) and GSVA score was relatively high across all STG139 tumours, regardless of size, suggesting a constitutive hypoxic microenvironment in this model. In AB580, GSVA score increased with tumour volume (r=0.74, p=0.004, **Figure 5.4B**), alike to CAIX protein expression on IHC, which also increased with tumour growth (r=0.53, p=0.02), suggesting evolution of the hypoxic phenotype in this model.

Finally, GSVA scores were stable across three passages and passage repeats of STG139 and AB580 (**Figure 5.4C-F**), which is in agreement with previous hypoxic and vascular IHC and PAI markers that were shown in earlier chapters to be stable in the PDXs.
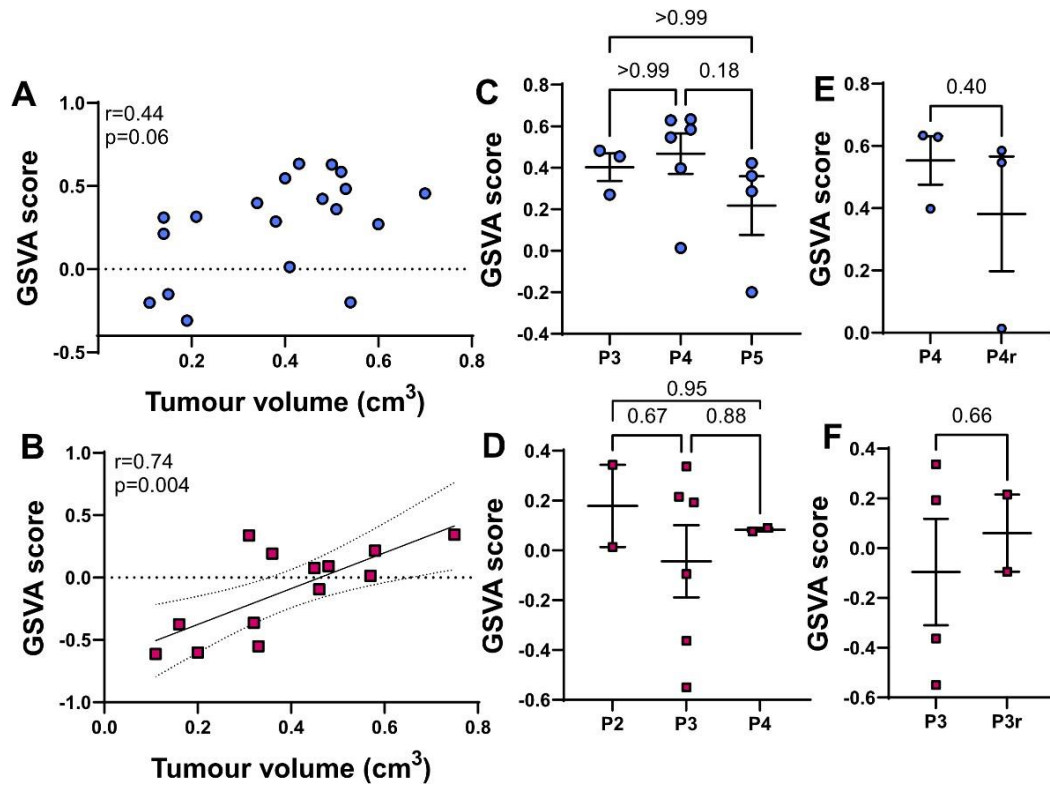
Figure 5.4. PDXs display differences in hypoxic gene expression evolution and expression is not passage-dependent. Scatter plots displaying correlation between GSVA score and tumour volume in (A) STG139 or (B) AB580, calculated by Spearman's and Pearson's correlation coefficient respectively. In (B) least square's regression line is shown in black line with 95% confidence intervals in dotted lines. GSVA score across 3 passages in (C) STG139 and (D) AB580. All p-values for pairwise comparisons are shown calculated by Kruskal-Wallis test with Dunn's multiplicity correction and One-way ANOVA with Tukey's multiplicity correction respectively. GSVA score compared between one passage and passage repeat (r) in (E) STG139 and (F) AB580. All p-values are shown calculated by Mann Whitney and Unpaired t-test respectively. In (C-F), data presented as a scatter dot plot with mean ±SEM. In all subfigures, each data point represents data from one tumour (biological replicate). In C-F mean ±SEM shown. p-values <0.05 considered significant. The following n numbers refer to the number of tumours represented in each sub-figure: for (A) n=19. For (B) n=13. The following n numbers refer to the number of tumours per PDX passage in each sub-figure: For (C) P3 n=3, P4 n=6, P5 n=4. For (D) P2 n=2, P3 n=6, P4 n=2. For (E) P4 n=3, P4r n=3. For (F) P3 n=4, P3r n=2.

5.3.3. *In vivo* PAI and *ex vivo* IHC vascular markers reflect underlying hypoxic gene expression

The final Aim 4 of the thesis also strived to determine which vascular features may be important to monitor in clinic. IHC markers or non-invasive PAI biomarkers could provide surrogate biomarkers of numerous hypoxic signalling pathways without the need for sequencing.

To this end, the GSVA summary score of the hypoxic gene signature described above was correlated to all the PAI and IHC metrics acquired on the PDX samples so far. Reassuringly, the GSVA score correlated with CAIX protein expression (r=0.62, p<0.001, **Figure 5.5A**), supporting the use of CAIX as a marker of hypoxia[207,214,288] in these models. GSVA score also correlated with necrosis (r=0.49, p=0.003, **Figure 5.5B**),which will often be a subsequent event to hypoxia in cells that do not adapt to the low oxygen conditions[126,217]. Interestingly, both SO_2 PAI measurements taken on air and O_2 correlated with GSVA (r=-0.46, p=0.017; r=-0.47, p=0.015 respectively, **Figure 5.5C, D**).

Assessment of the vasculature itself gave insight into the underlying hypoxic gene expression in these breast PDXs. Denser vessel networks, measured by CD31 vessel area, and vessels with poorer pericyte/smooth muscle coverage correlated with higher GSVA scores (r=0.49, p=0.003 and r=-0.41, p=0.017 respectively, **Figure 5.5E,F**), as didtumours with more haemorrhage detected on histology (r=0.61, p<0.001, **Figure 5.5G**) and higher THb^{MSOT} (r=0.47, p=0.014, **Figure 5.5H**) measured with tomographic PAI. These data suggest that dense and immature vascular networks, where blood pooling occurs more frequently, are associated with tumours with high hypoxic gene expression.Interestingly, none of the blood vessel network metrics quantified from mesoscopic PAIcorrelated with GSVA score, suggesting a need for broader investigation into angiogenic gene expression[289] in addition to hypoxic gene expression measured here.
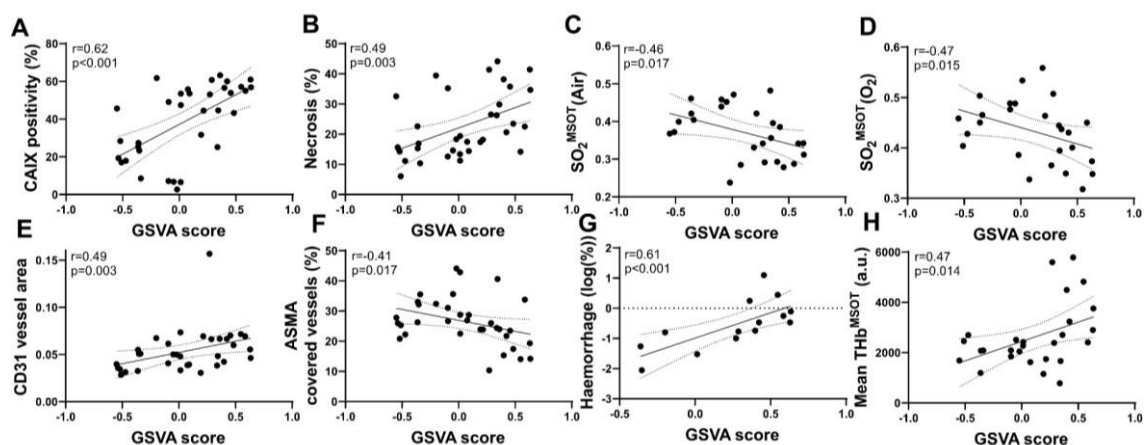
Figure 5.5. Photoacoustic imaging and vascular IHC markers correlate with the underlying hypoxic gene expression. In all subfigures data shown as scatter plots where each data point is one tumour (biological replicate). Least square's regression line shown in black with 95% confidence intervals denoted by dotted line. Correlations between GSVA score and the following metrics are shown: (A) CAIX positivity measured on IHC (B) Necrosis measured on H&E sections, (C) $SO_2^{MSOT}(Air)$ measured by tomographic PAI, (D) $SO_2^{MSOT}(O_2)$ measured by tomographic PAI, (E) CD31 vessel area measured on IHC, (F) ASMA vessel coverage of CD31+ vessels (%) on ASMA IHC sections, (G) Haemorrhage (%) measured on H&E sections, (H) Mean Total Haemoglobin (THb, a.u.) calculated from tomographic PAI. Each data point is one tumour (biological replicate). All IHC metrics are averaged across core and outer sections. For all subfigures, Spearman's correlation coefficient and p-value are shown. $p<0.05$ considered significant. The following n numbers refer to the number of tumours represented in each sub-figure: for (A, B, E-G) n=34 (in G 14 data points displayed on log scale). For (C, D, H) n=26.

5.3.4. Proliferative capacity of PDXs relates to vascular development

There are some discrepancies in the vascular phenotypes measured in the PDXs and the underlying hypoxic gene expression. For example, both luminal B models AB580 and STG143 have similar levels of vessel density and maturity measured on IHC (**Figures 2.6 and 2.7**), yet differ in hypoxic gene expression, with AB580 displaying high hypoxia (~40% CAIX positivity) and necrosis (~20-30%) levels, particularly at end-point and STG143 displaying comparatively low hypoxia (~6.5-30% depending on section location) and lower necrosis (~10%). The proliferative capacity of the PDXs may have important implications for their vascular development and the phenotypes formed, as this will impact their metabolic profile and oxygen demand. Ki67 IHC was conducted at end-point as a marker of proliferation during the QC process (described in 2.2.2) and increase in tumour

181

volume monitored, hence these markers were retrospectively considered in light of the gene expression analysis.

When looking at Ki67 protein expression of PDXs at end-point (**Figure 5.6**), the level of expression aligns with that of patient basal and luminal B tumours, with high expression in all tumours (>20%, semi-quantitative score), particularly in the basal models[290]. When monitoring the growth curves of the models, important differences can be seen longitudinally. STG139 tumours begin growth first at 6-12 weeks post-implantation and they will reach their maximum permitted volume within 20 days, sometimes even within a few days (**Figure 5.7A**). Around 75% of STG139 tumours reached exponential growth by 70 days post-implantation. In contrast, the other basal model STG321 grows relatively slowly, beginning after 3-4 months and taking normally one month to reach maximum volume (**Figure 5.7B**). Around 75% of STG321 tumours reached exponential growth by 120 days post-implantation. Both luminal B models grew slower than the basal models, which is expected, however their growth patterns are different. In AB580, the tumours grow sooner, after ~4 months, and once they begin they grow relatively quickly with many only taking one month to reach the maximum volume, similar to the basal model STG321 (**Figure 5.7C**). Around 75% of AB580 tumoursreached exponential growth by 140 days post-implantation. In contrast STG143 won't begin growth until ~6 months post-implantation and once growing, can take around 2 months or even longer to reach maximum volume (**Figure 5.7D**). Around 75% of STG143 tumours reached exponential growth by 200 days post-implantation. These different latency periods from implantation to the start of exponential growth likely contribute to differing oxygen demands in the PDXs. Oxygen serves as a key substrate in mitochondrial energy production[291], and therefore tumours with shorter latency periods will have a higher energy and oxygen demand comparedto slower growing tumours with longer latency periods. When the oxygen demand cannot be met by the supply fromthe blood vessel network (due to low vessel density or low vessel maturity and poor perfusion), this can contribute to the cells developing hypoxia. Particularly in the luminalB models, differing latency periods may explain their differing hypoxia levels. Both modelshave sparse and partially immature vessel networks, yet AB580 has a shorter latency period than STG143, meaning that oxygen demand is higher in AB580 and could explain why AB580 is more hypoxic than STG143.
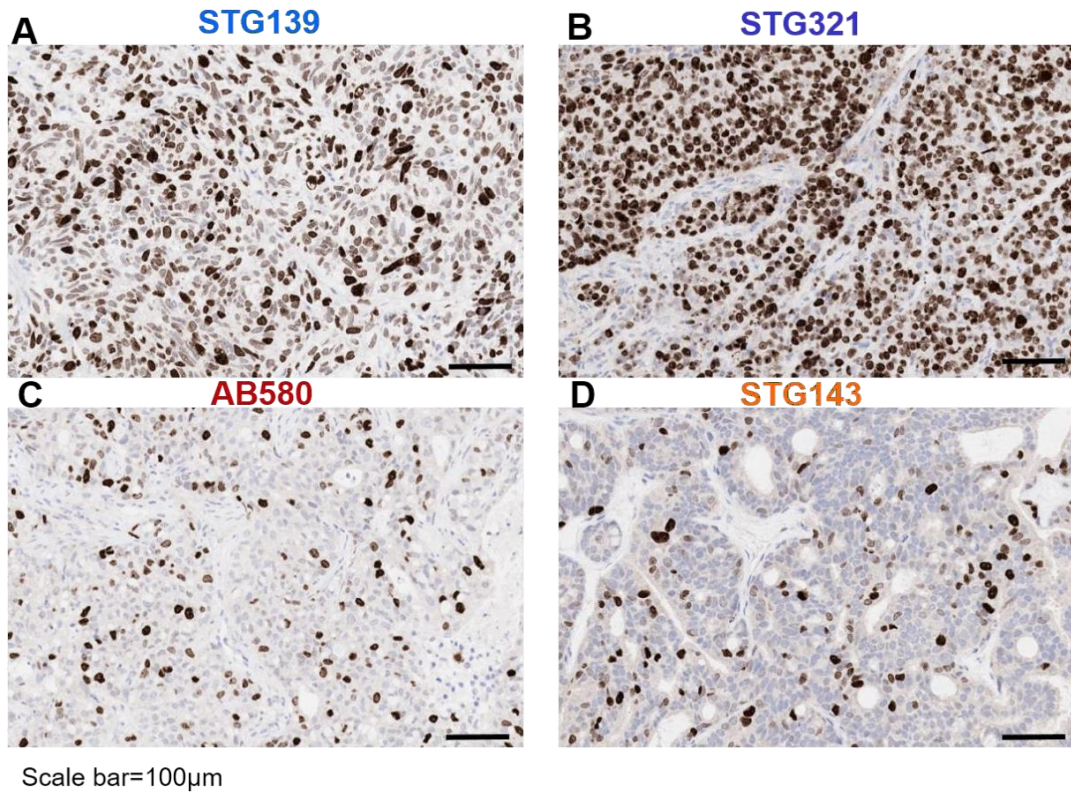
Scale bar=100μm

Figure 5.6. Ki67 expression on IHC is high in all models especially basal PDXs. (A) STG139, (B) STG321, (C) AB580, (D) STG143. Basal models shown on top row, Luminal B models shown on bottom row. Scale bar=100 μm. Expression above 20% is considered high[290].
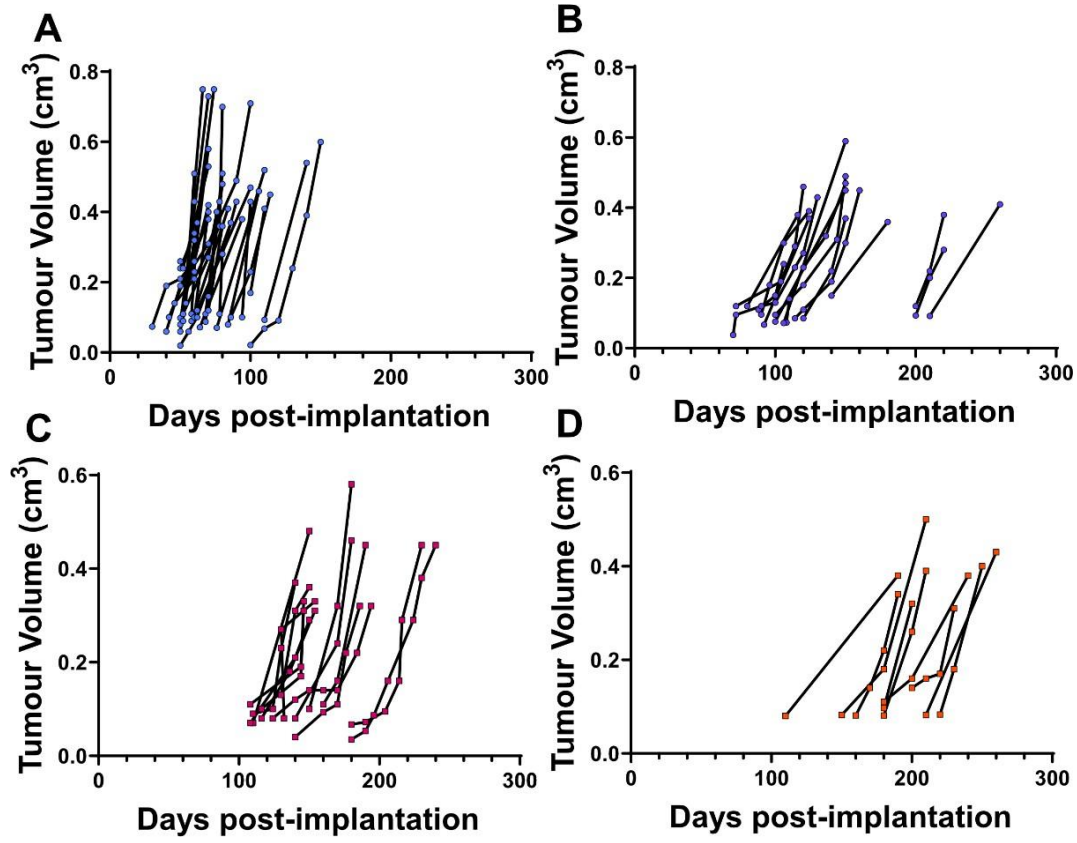
Figure 5.7. Differing latency periods of PDXs may impact metabolic demands. Tumour volume (cm^3) plotted against days post-implantation for (A) STG139, (B) STG321, (C) AB580, (D) STG143. Each line is for one tumour (biological replicate) measured at multiple time points (data points). The following n numbers refer to the number of tumours per PDX model: $n^{STG139}=31$, $n^{STG321}=17$, $n^{AB580}=15$, $n^{STG143}=9$.

5.4. Discussion

Expression of a 51-gene signature[269] comprising of genes upregulated under hypoxia was assessed in samples from the 4 breast PDXs described in this thesis thus far, as well as in corresponding patient samples and PDXs from the Caldas lab[10]. The proliferative capacity of the PDXs described in this thesis was also assessed. This was to investigate the following:

1. To correlate PAI and IHC signals to the underlying gene expression and provide genomic validation of PAI signals for the first time.
2. To assess how representative and reliable hypoxic gene expression is in breast PDXs.
3. To gain insight into the origins of PDX vascular phenotypes.

5.4.1. Hypoxic gene expression in PDXs correlates with vascular phenotypes measured by IHC and PAI

A validated hypoxic gene signature was chosen to genetically assess the level of hypoxia in the 4 breast PDXs. The relative expression of each gene in the signature displayed in a heatmap, as well as a summary GSVA score, revealed STG139 tumours to have the highest expression of the signature, corroborating CAIX IHC data and *in vivo* SO_2 PAI measurements, which showed STG139 to be less well oxygenated than the other PDXs, particularly in comparison to the other basal model STG321. Expression of the signature was also higher in the luminal B model AB580, compared to the other luminalB STG143, which corroborates differences seen in CAIX expression on IHC, despite thetwo having similar SO_2 levels in tomographic PAI measurements and similar levels of vessel density and maturity on IHC. This necessitated thought into the differing oxygen demands of the PDXs, which is discussed below.

The basal model STG321 was found to have significantly lower GSVA score than the basal model STG139, and interestingly there was low *vegfa* gene expression, supporting observations of low VEGF IHC for this model and suggesting it is less hypoxic and angiogenic. STG321 does express genes involved in microtubule spindle formation and cytokinesis, as expected for a highly proliferative model[286,287] which highlights the

185

cross-talk between proliferation and hypoxia signalling pathways and necessitates a close investigation into the roles of specific genes when using signatures, to be sure that high expression of certain genes do not confound results. STG143 had low expression of most of the genes in the signature. This corroborates previous results presented in this thesis as STG321 and STG143 had the lowest CAIX expression on IHC and STG321 had consistently high oxygenation measured by SO_2 in tomographic PAI.

Correlations between the summary GSVA score, used as a single scoring metric of hypoxic gene expression, with PAI and IHC highlighted the possible insights into underlying gene expression that can be gained by assessing the vasculature non- invasively with PAI and with the vascular IHC markers presented in this thesis. Reassuringly, the GSVA score correlated positively with CAIX and necrosis measured on IHC, indicating that the score does represent hypoxia levels and associated-cell death in the PDXs. Measurements of SO_2 taken with tomographic PAI, either whilst the mouse is breathing air or 100% O_2, both negatively correlated with GSVA score, demonstrating the potential of blood oxygenation measurements taken with PAI to provide insight into hypoxic gene expression in breast cancer. Neither of the dynamic PAI measurements (ΔSO_2 and responding fraction) correlated with GSVA, suggesting that the protocol may need to be optimised on a per model basis, as these measurements were previously shown to inversely spatially correlate with areas of hypoxia on IHC in prostate cell-line models[126].

Interestingly, denser and more immature networks measured on IHC by increased CD31 vessel area, haemorrhage and decreased ASMA vessel coverage where related to the GSVA score. Furthermore, vascular density and blood pooling from immature vascular networks can be measured using THb^{MSOT} on tomographic PAI which positively correlated with GSVA score, indicating that this measurement can provide insight not only on the density of vessels and haemorrhagic content in breast tumours but ultimately how they interplay with hypoxic gene expression. The relationship between dense vascular networks and immature vascular networks, which relate to hypoxic microenvironments in these PDXs is strong, but other more diverse phenotypes may present in clinic or in other pre-clinical models. The use of a 'PAI signature' combining measurements of multiple PAI metrics to provide robust and longitudinal insights into

186

underlying gene expression, similar to the 'radiomics signature' proposed by Gill et al. to monitor ctDNA mutations, should be investigated in future, as this may be a powerful approach to assessing underlying biological processes with PAI.

Unfortunately, GSVA score did not correlate with blood volume or topology metrics measured using mesoscopic PAI. Considering that mesoscopic PAI metrics appear to capture the angiogenic potential of PDXs by taking measurements longitudinally, as well as the maturity of these networks with topological analyses, this result is unexpected. However, discordance may arise from the different portions of tumour assessed (mesoscopic PAI captures the 2 mm tumour surface whereas hypoxic gene expression was measured in a 2 mm cube taken from a different portion of the tumour mass). Or perhaps mesoscopic measurements are most powerful when quantified longitudinally, and less insight is gained from end-point analyses such as this. Equally, this could be related to the different pathways probed by each technique. Mesoscopic PAI was used to visualise the blood vessel network architecture longitudinally, the pattern of which may be driven by a range of angiogenic factors. The hypoxic signature measures many signalling pathways, some related and some unrelated to angiogenesis and vessel formation, including processes such as microtubule organisation. Therefore, closer inspection of angiogenic gene expression[22–24,289], for example investigating endothelial and pericyte expression of focal-adhesion kinase[22,292], or angiopoietin signalling[24] in the PDXs may provide genomic validation of mesoscopic PAI. This would require optimisation of PDX tissue processing to separate the human and mouse components to get enough reads, as it will be mostly the mouse stroma expressing the angiogenesis related genes mentioned above, of which there was <5% contamination found in all samples here.

5.4.2. Gene expression is stable across passages and generally representative of patients

Aim 3 of the thesis was to assess the robustness and repeatability of vascular phenotypes in the PDXs and how well these phenotypes represented the patients from which they were derived. To this end, the stability of expression of the hypoxic gene signature across passages and passage repeats was assessed in STG139 and AB580, as

has been routine with all metrics presented in this thesis thus far. As expected given the reported stability of gene expression in the breast PDXs[10], GSVA score was stable across all passages and repeats.

Genomic profiling of the breast PDXs has also been shown to be preserved from patient to PDX and across several passages by the Caldas laboratory[10]. Here, specific expression of the hypoxic gene signature was compared between corresponding patient and PDX samples generated by the Caldas laboratory to STG139, AB580 and STG143 PDX samples generated in this thesis. Remarkable preservation of hypoxic gene expression was measured in STG139 and STG143, suggesting that these tumours were hypoxic and normoxic respectively in the patients and this is represented in the PDX samples presented in this thesis. In AB580, some changes have occurred in gene expression. In the patient and in the first (X0) passage measured by the Caldas laboratory, hypoxic gene expression was low and this has increased in subsequent passages measured in this thesis. Considering that the vessel density and maturity on IHC appeared to be maintained from patient to PDX in this model (**Figure 2.12**), and considering the vessel density and maturity is similar to that of STG143, I propose the shorter latency period and metabolicrequirements of AB580 tumours measured in this thesis may have contributed to these changes in underlying gene expression. Anecdotally the latency period of the AB580 PDXsin this thesis was shorter by a few months than those kept in the Caldas lab, suggesting that the AB580 PDXs in this thesis had a higher energy and oxygen demand compared to previously measured samples, which possibly resulted in an oxygen deficit and hypoxic gene expression in this model.

5.4.3. Evolution of hypoxic gene expression combined with PDX metabolic requirements provide insight into the origin of PDX vascular phenotypes

Studying the true evolution of gene expression longitudinally as the breast PDXs grow is not possible owing to the need to excise the tissue, yet estimates were made by comparing tumours of different sizes in STG139 and AB580. Interestingly, GSVA score increased as tumour volume increased in AB580, but the same relationship was not strong or significant in STG139 and these results are supported by CAIX IHC measurements.

Tumours of different sizes were not measured for STG321 and STG143, owing to time restraints in preparing this thesis, but the relatively low hypoxic gene expression measured in both models suggests that hypoxia does not significantly drive the vascular phenotypes seen in these two models.

STG139 presents a constitutively hypoxic model, where from patient to PDX and through several passages the hypoxic gene expression remains high. It is likely this constitutively hypoxic environment drives the formation of the dense and immature networks that are seen in STG139, which ultimately give rise to blood pooling, haemorrhage, poor perfusion and poor oxygenation in this model. Additionally, this model is the fastest growing PDX of all those measured in this thesis, suggesting that theoxygen demand of the tumour will be high but the supply of oxygen will be low owing to the immature networks described above, perpetuating this hypoxic environment.

AB580 presents a diffusion-limited hypoxia model in this thesis. Smaller AB580 tumours are not extremely hypoxic, and developing vasculature is partially mature, with some vessels lacking pericyte coverage likely owing to aberrant angiogenic pathways often seen in tumours[199]. Once growing after ~4 months post-implantation, these tumours grow relatively quickly within a month and oxygen demand will rapidly increase to meet the metabolic demands of the proliferating cells. It is at these later time-points that the sparse and only somewhat mature network in AB580 tumours cannot supply the tumour with the oxygen necessary resulting in hypoxia and the increase in hypoxic gene expression and CAIX protein expression is observed. This in turn will continue to promote vessel network formation with abnormal pericyte coverage, explaining the stability of vessel maturity measured on IHC.

STG321 is an interesting basal model as it does not appear to be angiogenic or express many genes involved in hypoxia. Despite a relatively high proliferation and short latency period, expected of a basal model, the vasculature appears mature enough to meet the oxygen demand of the tumours. There is some necrosis and hypoxia measured on IHC, in the centre of cellular islands that are surrounded by vessels covered by smooth muscle. In fact, the vessel networks in STG321 on IHC form a somewhat 'chicken-wire' appearance that has been previously noted in lung vasculature when describing lung cancer cells that 'co-opt' existing alveolar vascular networks[37]. It is

possible that STG321is presenting as a non-angiogenic vascular model, and alternative vessel forming mechanisms could be explored in this model in future.

Finally, STG143 presents as a slow-growing relatively normoxic luminal Bmodel. Taking over 6 months to begin exponential growth and taking ~2 months to reach maximal volume once growth has begun, I hypothesise that the oxygen demand of this tumour is far lower than the other PDXs. Therefore, despite a similar vessel density to the luminal B model AB580 and a fairly immature vessel network, here, the network seems sufficient to meet the low oxygen demand of the tumour and prevent hypoxia.

5.4.4. Limitations

There are some limitations to this work that should be considered. First, the smallest tumours measured here were ~0.1 cm^3 as this study was combined with *in vivo* imaging and so the tumours were left to grow to a reasonable size, taking into account the resolution and practicalities of using both the tomographic and mesoscopic PAI systems, to take at least one set of PAI measurements before excising the tissue. However, angiogenic and hypoxic signalling pathways can be activated in tumours as small as 1 mm^3 [293] and therefore more refined measurements of hypoxic gene expression evolution should be made on tumours smaller than those presented here.

Additionally, gene expression of STG143 was measured in only 4 samples from one passage. This was due to the slow growing nature of STG143 tumours meaning that these experiments were conducted before the second passage of STG143 had finished growing *in vivo*, due to time restraints for the thesis preparation. Reassuringly, there was little diversity in the gene expression between the 4 samples supporting the robust nature of PDXs, however, an increased number of samples across passages would improve confidence in the results presented.

5.4.5. Future work

In future, further gene expression studies could be conducted to validate the PAI signals presented here and gain insight into the underlying tumour biology. Here, the focus was on hypoxic gene expression to also investigate the interplay between hypoxia and vessel phenotype. However, other pathways of interest such as a focus on angiogenic

signalling[289] could be investigated and may provide further biological insights and validation for mesoscopic PAI measurements.

There is a focus in this thesis on the importance of angiogenesis in tumours and the resulting vascular phenotypes. However, one model in particular, STG321, appears to lack angiogenic potential. Therefore, alternative vessel forming mechanisms such as co-option should be investigated in this model to define exactly how its vessels are formed[37]. Growing these tumour orthotopically in the mammary fat pad could provide insight into whether this model can utilise vasculature from the original tissue, which would explain the increased vessel maturity observed in this model.

An unsupervised linear regression of all expressed genes against the imaging metrics was not investigated here, owing to the low number of PDXs used. In a laboratory with the ability to investigate several or even 100s of PDX models this could be conducted to identify new biomarkers and pathways which influence vascular phenotypes in breast cancer.

5.4.6. Summary

In summary, this chapter has presented hypoxic gene expression data, which underpins the measurements taken on IHC and non-invasively with PAI, providing genomic validation of PAI measurements for the first time. PAI measurements of blood oxygenation as well as total haemoglobin may provide insight into the underlying hypoxic gene expression in breast cancer. Hypoxic gene expression is remarkably stable across PDX passages, and is preserved from patient to PDX in two models. The latency period from implantation to the start of exponential growth likely also influences the oxygen demand and resulting hypoxia and vessel phenotypes in the PDXs with each model representing 4 different microenvironments: constitutive hypoxia, diffusion-limited hypoxia, non-angiogenic vessel formation and relative normoxia.

6 CONCLUSIONS

Cancer cells live within their environmental niche known as the tumour microenvironment (TME), where dynamic interactions between cancer and stromal cells as well as chemical and physical signals, shape tumour biology and evolution[1,2]. The vasculature is a key component of the TME and is often dysfunctional and immature leading to areas of chronic and dynamic hypoxia which further spatially fine-tune the TME[3,4].

This thesis has built on previous work which shows the powerful ability of photoacoustic imaging (PAI) to visualise tumour vasculature and oxygenation non-invasively. Using a 'light-in', 'sound-out' approach, photoacoustics presents an attractive non-invasive method for probing tumour blood vessels[95,221]. It's relatively cheap, easy- to-use, can be easily integrated into existing ultrasound systems and does not require exogenous contrast agents to image blood vessel networks. The potential of PAI to capture breast cancer blood vessels is gaining momentum, at least from an engineering perspective with many new system geometries being designed and tested[104,105,140,144,148]. However, what is lacking is the biological insight into which vascular features should bemonitored in clinic. Which features give the greatest insight into the underlying tumour biology and hypoxic signalling pathways? Is PAI sensitive enough to the vascular phenotypes present in patients? Owing to the reliance of cell-line xenograft mouse modelsin PAI to-date, these questions have not been adequately answered.

Here, I have demonstrated the use of breast cancer patient-derived xenograft (PDX) models in PAI, establishing the use of these models in PAI for the first time, as aclinically-relevant model of breast cancer[9,10]. It had already been previously shown that PDXs serve as powerful patient 'avatars', able to recapitulate and maintain the genomic architecture and heterogeneity of the original patients as well as respond to drug treatments in a similar manner to the patient tumours they are derived from[9,10].

Considering the large impact that tumour blood vessels can have on the cancer cell phenotype and genotype and ultimately treatment response, this brings into question how PDXs are such good models of the patients from which they are derived, considering that the vasculature will be derived from the mouse host[10,295-297]. Yet until this thesis, the vascular microenvironment of breast PDXs had not been studied in detail, and whether the models develop distinct vascular phenotypes that are robust, reliable and representative was not known. Therefore this thesis questioned not only the sensitivity of PAI when visualising PDX vasculature but also whether or not breast PDXs are good vascular models for cancer research.

I defined 4 aims for the thesis:

Aim 1: To characterise the vascular phenotypes in breast cancer PDXs using a combination of high-resolution and tomographic PAI and immunohistochemistry (IHC).

Aim 2: To determine whether PAI is sensitive to different vascular phenotypes in PDXs.

Aim 3: To determine whether PDXs are robust and reliable vascular models that represent the patients from which they are derived.

Aim 4: To question the origin of vascular phenotypes in PDXs and gain insight on which features may be the most significant to monitor in clinic.

Beginning with Aim 1 of the thesis, I have characterised the vascular phenotypes of 4 breast PDXs (2 basal PDXs: STG139 and STG321 and 2 luminal B PDXs: AB580 and STG143), originally derived from 4 patients and passaged in immunocompromised mice. I found STG139 to be the bloodiest of the PDXs studied, with high CD31 vessel area and haemorrhage measured on IHC. This underpinned *in vivo* PAI metrics, with high THb^{MSOT} measured using tomographic PAI and a rapid increase in blood volume measured on longitudinal mesoscopic PAI. Despite high blood content, STG139 tumours were highly necrotic and expressed high levels of CAIX *ex vivo*. Mesoscopic PAI topology indicated that STG139 vessels are immature, underpinned by low ASMA vessel coverage *ex vivo*, possibly leading to poor perfusion and oxygenation of the tissue. In stark contrast to STG139, the other basal model STG321 had relatively mature vessels with high pericyte coverage measured *ex vivo* and STG321 does not appear to be

angiogenic, with low levels of VEGF expression measured using IHC, supporting the minimal increase in blood volume over time observed with mesoscopic PAI. *In vivo* SO_2 ^{MSOT} measurements also tend to be relatively high in this model, while necrosis and CAIX expression are low, suggesting that the mature vessels are able to deliver oxygenated blood to the tumour tissue to prevent hypoxia. The two luminal B models (AB580 and STG143) had relatively low blood content, with low CD31 vessel area measured *ex vivo* and low THb^{MSOT} measured in tomographic PAI. The vessels in these models were somewhat mature, with intermediate levels of pericyte/smooth muscle coverage, in-between the two extremes denoted by the basal models. AB580 tumours had a necrotic core and although not as hypoxic as STG139, they still had high CAIX expression with ~30-50% positivity. In contrast, STG143 tumours were relatively normoxic. This may be due to the proliferation rate of the tissue, as AB580 PDXs grow quicker than STG143 and will have a higher oxygen demand that is not supplied by the sparse vascular network, resulting in the development of diffusion-limited hypoxia over time as the tumour grows. In STG143, the growth is so slow that the oxygen supply and demand appear matched. It is clear that the 4 PDXs studied display different vascular phenotypes meeting Aim 1 of the thesis.

PAI was able to distinguish different vascular phenotypes underscored by the IHC markers, meeting Aim 2. Encouragingly, despite smaller effect sizes in vascular metrics in the PDX models compared to breast and prostate CDX models measured previously[48,126], PAI was still sensitive enough to delineate the vascular phenotypes presented by more clinically-relevant models, particularly to differences in blood content. Additionally, similar studies in a wider range of PDXs and patients, preferentially also representing additional breast cancer subtypes not represented by the models presented here, would enable the sensitivity of PAI to different vascular phenotypes to be assessed on a larger scale. Considering multiple PAI measurements together as a 'PAI signature' of a tumour would provide increased insight both pre-clinically and in clinic, considering a combination of oxygenation, blood content and network structure measurements to provide surrogate biomarkers of hypoxia, vessel density and network maturity and build a greater picture of the tumour vessel phenotype non-invasively.

Aim 3 of the thesis questioned whether the breast PDXs were robust and reliable vascular models that represented the patients from which they were derived. When looking across 3 passages and passage repeats of STG139 and AB580, there is a remarkable stability in the vascular phenotypes. This was particularly true for measurements of 'vascular function' i.e. measurements of hypoxia and ASMA vessel coverage (vessel maturity) on IHC. Despite some variation in blood content, this never skewed the measurements in such a way as to create an entirely new phenotype. I found the PDXs will always produce repeatable and functionally distinct vascular phenotypes, suggesting that there is an inherent 'instruction' from the cancer cells themselves, which instructs the mouse host vasculature to form a particular phenotype.

Comparisons to patient IHC were briefly conducted on the clinical sections available and there was an indication that vessel density and maturity were preserved from patient to PDX. However, whole tissue sections of all the IHC vascular markers presented must be scored blindly by a pathologist in future. PAI was not conducted on these patients, however, it may be possible in future to examine images from another modality such as dynamic-contrast enhanced MRI, to study tumour perfusion, if these images were taken as part of the standard-of-care pathway and compare the phenotypes captured here to those captured with PAI in the PDXs.

All 4 PDXs create blood vessels but they are not all made equal, suggesting there is an instructive element in the implanted tumour, because if they were simply mouse reactions to the human tissue transplantation the vascular phenotypes would be the same. Therefore, to address Aim 4 of the project and gain insight into the origins of PDX vasculature, RNA sequencing was conducted on a subset of the PDXs, taking samples from across passages for all 4 models. Expression of a hypoxic gene signature was measured, and found to be highest in STG139, while it was relatively low in the other basal model STG321. AB580 had higher hypoxic gene expression than the other luminalB model STG143, which had the lowest expression of all 4 PDXs. Expression correlated with measurements of hypoxia on IHC, THb^{MSOT} and SO_2^{MSOT} measured with PAI, demonstrating genetic validation of *in vivo* PAI metrics for the first time to my knowledge and the potential for PAI to inform on underlying hypoxic gene expression in tumours. Interestingly, expression of the signature was constitutively high in STG139 tumours,

regardless of size. This was supported by no evolution in IHC vascular markers in STG139. In AB580 hypoxic gene expression evolved, increasing from small to large tumours, as did hypoxia measured *ex vivo*.

I only measured up to 3 early passages of PDXs during the time constraints of this thesis, so later passages may introduce further changes that were not measured here. Using early passages of the PDXs was essential for two reasons: 1. I was concerned thatlater passages may have developed changes in the vessel phenotype that would not be representative of the patients from which they were derived. 2. Many PDXs in the biobank will stop engrafting after passage 5 (except the aggressive model STG139). Therefore, one is limited to early passages of the PDXs, making them more likely to represent patienttissue but brings into question the widespread utility of the models.

Engraftment success rates were limiting throughout my thesis, particularly in the luminal B models which are less aggressive. In some AB580 and STG143 passages, engraftment was as low as 40% whereas with both basal models it was always ~90% or more. Many mice were wasted as they never grew a tumour. The Caldas lab surgery protocol is one of the fastest in the PDX field, with samples from patient to mouse implanted within 30 minutes of excision from the patient[10], and in my experience samples for passaging can be defrosted, washed and implanted within 15 minutes. Therefore, it seems this problem is inherent to PDX use, particularly with less aggressive models. Considering also the length of time taken for less aggressive tumour models to grow (in the case of STG143 this was over 6 months), this severely limits the model's utility. Despite appearing to be a more diverse and representative vascular model than CDXs, cell-line models still have a place in cancer research and in PAI, for quickly testing initial hypotheses or for pilot drug studies. Nonetheless, I would suggest a progression to a more clinically-relevant model in time.

There are other limitations to the PDXs used in this thesis. Breast PDXs were implanted subcutaneously on the flank of the mice, not orthotopically in the mammary fat pad. Anecdotally speaking, the Caldas laboratory advises that this doesn't significantly impact engraftment success or gene expression. I therefore chose to continue with their established protocol, as subcutaneous implantation was easier to perform and enabled access to the tumour for imaging in both mesoscopic and tomographic PAI systems.

However, there are numerous reports that subcutaneous vs. orthotopic implantation will impact the vascular phenotype formed in breast and other xenograft tumours[298-302]. It was recently demonstrated that a direct comparison of the two implantation sites resulted in similar breast PDX doubling times and histology[303], but these potential differences should be investigated in full, and the whole growth environment of the PDXs considered. Additionally, further advances to humanize the mouse immune system in these immunocompromised models will be vital[172] to have a more holistic approach of the vascular microenvironment, considering the influence of immune cells on the vasculature[5].

PDXs are considered 'patient avatars', with similar response to standard therapies than the patients they represent, and therefore are considered good models for preclinical testing of novel therapies[9,10]. The data presented in this thesis suggests that the diversity of vascular phenotypes observed in breast PDXs will be vital to consider when selecting and utilising PDXs in drug and imaging studies, as the vascular microenvironment, particularly blood perfusion and oxygenation, will significantly impact drug and/or contrast agent delivery and therapeutic efficacy[1].

Knowing the importance of hypoxia and blood vessel formation on tumour development and response to treatment, advances are being made to measure these features in patients and use this to stratify those who will and won't respond to particulartherapies. But currently there are no hypoxia biomarkers in routine use to aid patient management decisions[294]. This work emphasises the importance of these features and how varied they are across models (and presumably patients), supporting the non-invasivemonitoring of these features in clinic. With regards to the patients represented in this thesis, the only tumour which continually relapsed, metastasised and caused death within5 years of the initial diagnosis was the STG139 tumour. All other patients were still aliveat the time of the biobank publication[10], and were responding to therapy. Here, STG139 was consistently the bloodiest, hypoxic and most aggressive PDX model of thoseinvestigated. While the causes of relapse and metastasis in the STG139 patient tumour can only be speculated in this thesis, there may be a correlation between aggressive vascular phenotype and aggressive tumour behaviour, highlighting the vital importance of monitoring these features in clinic and finding appropriate therapeutic options for

patients that won't' respond to the current standard-of-care.

Finally, the last takeaway point outside of my aims is the importance of quantification and validation in PAI measurements and IHC. In this thesis, I have quantified all IHC vascular marker expression (Chapter 2), and created and validated a new random forest classifier to quantify mesoscopic PAI (Chapter 3) and used previously validated algorithms for tomographic PAI analysis (Chapter 4). Quantification and validation of the algorithms used for analysis of these images is not a given in the field. By doing so, I along with previous lab members[48,126], have validated PAI imaging metrics and gained a comprehensive understanding of biomarker expression across the 4 PDX models. The importance of quantification was particularly emphasised in Chapter 3, as quantification of mesoscopic PAI in the literature is ad-hoc, unstandardised and often completely lacking[106–108,113]. Of course, a lack of computational expertise and time taken to properly validate algorithms for analysis are obvious barriers to quantification. Additionally, creating ground-truths for mesoscopic PAI is difficult, owing to the noise and artefacts present and a lack of expertise and datasets in a new field. I addressed some of these issues in Chapter 3, in collaboration with others, by validating the use of a random-forest classifier to segment mesoscopic PA images with an *in silico*, phantom, *invivo* and *ex vivo* framework. Considering that the classifier is implemented in a user friendly software, now common in the life sciences[228], I hope our results and methods canbe widely used in the PAI field, and perhaps further afield with other vascular imaging modalities.

In this thesis, I have used a combination of PAI, IHC and RNA-seq to investigate the vascular phenotypes of breast PDXs across scales for the first time. I have demonstrated the power of combining PAI systems of different resolutions and penetration depths, to capture complementary information on the vascular microenvironment. I have showcased the delicate interplay between tumour vasculature and hypoxia in a new context with a clinically-relevant breast cancer model. I have shownthat PAI metrics give insight into underlying gene and protein expression, presenting a non-invasive method of probing these pathways, which could be utilised longitudinally throughout a patient's treatment regime. I have also shown that PDXs are reliable and robust vascular models, advancing not only the field of PAI, but also adding knowledge to

the utility of breast PDXs in oncology research.

Looking forward, the work conducted in my thesis has established a biobank of breast PDXs in the laboratory and over 1000 PA images of breast PDXs have been collected, along with corresponding IHC. This I hope will lead to many future works. The data collected could be used to advance image analysis pipelines beyond those I have presented in this thesis, perhaps tapping into the use of neural networks and deep-learning for advanced segmentation methods. An obvious advancement to the use of PDXs in PAI would be in treatment response studies, perhaps those targeting angiogenesis or hypoxic signalling pathways, considering that PDXs are considered very good models of patient treatment response[173]. Investigating how the vasculature evolves in response to treatment and how PAI can visualise this may provide clinically-relevant insight and could perhaps be matched to patient PAI or MRI data, to further validate the use of PDXs in PAI and learn the impact of certain vascular phenotypes on treatment response and tumour evolution.

I see a bright future ahead for the use of photoacoustic imaging in breast cancer.

7 REFERENCES

1. Quail, D. F. & Joyce, J. A. Microenvironmental regulation of tumor progression and metastasis. *Nat. Med.* **19**, 1423 (2013).

2. Gilkes, D. M., Semenza, G. L. & Wirtz, D. Hypoxia and the extracellular matrix: drivers of tumour metastasis. *Nat. Rev. Cancer* **14**, 430 (2014).

3. Lundgren, K., Holm, C. & Landberg, G. Hypoxia and breast cancer: Prognostic and therapeutic implications. *Cell. Mol. Life Sci.* **64**, 3233–3247 (2007).

4. LaGory, E. L. & Giaccia, A. J. The ever-expanding role of HIF in tumour and stromal biology. *Nat. Cell Biol.* **18**, 356 (2016).

5. De Palma, M., Biziato, D. & Petrova, T. V. Microenvironmental regulation of tumour angiogenesis. *Nat. Rev. Cancer* **17**, 457 (2017).

6. Kalluri, R. The biology and function of fibroblasts in cancer. *Nat. Rev. Cancer* **16**, 582 (2016).

7. Abadjian, M.-C. Z., Edwards, W. B. & Anderson, C. J. Imaging the Tumor Microenvironment. in *Tumor Immune Microenvironment in Cancer Progression and Cancer Therapy* (ed. Kalinski, P.) 229–257 (Springer International Publishing, 2017). doi:10.1007/978-3-319-67577-0_15

8. Weissleder, R., Schwaiger, M. C., Gambhir, S. S. & Hricak, H. Imaging approaches to optimize molecular therapies. *Sci. Transl. Med.* **8**, 355ps16 (2016).

9. Choi, S. Y. C. *et al.* Lessons from patient-derived xenografts for better in vitro modeling of human cancer. *Adv. Drug Deliv. Rev.* **79**–**80**, 222–237 (2014).

10. Bruna, A. *et al.* A Biobank of Breast Cancer Explants with Preserved Intra-tumor

Heterogeneity to Screen Anticancer Compounds. *Cell* **167**, 260-274.e22 (2016).

11.   Folkman, J. Tumor Angiogenesis: Therapeutic Implications. *N. Engl. J. Med.* **285**, 1182–1186 (1971).

12.   Hoeben, A. *et al.* Vascular endothelial growth factor and angiogenesis. *Pharmacol. Rev.* **56**, 549–580 (2004).

13.   Dewhirst, M. W., Cao, Y. & Moeller, B. Cycling hypoxia and free radicals regulate angiogenesis and radiotherapy response. *Nat. Rev. Cancer* **8**, 425–437 (2008).

14.   Ribeiro, A. L. & Okamoto, O. K. Combined effects of pericytes in the tumor microenvironment. *Stem Cells Int.* **2015**, 868475 (2015).

15.   Hanahan, D. & Weinberg, R. a. Hallmarks of cancer: the next generation. *Cell* **144**, 646–74 (2011).

16.   Krishna Priya, S. *et al.* Tumour angiogenesis—Origin of blood vessels. *Int. J. Cancer* **139**, 729–735 (2016).

17.   Nagy, J. A. & Dvorak, H. F. Heterogeneity of the tumor vasculature: the need for new tumor blood vessel type-specific targets. *Clin. Exp. Metastasis* **29**, 657–662 (2012).

18.   Nagy, J. A., Dvorak, A. M. & Dvorak, H. F. VEGF-A and the Induction of Pathological Angiogenesis. *Annu. Rev. Pathol. Mech. Dis.* **2**, 251–275 (2007).

19.   Greenberg, J. I. *et al.* A Role for VEGF as a Negative Regulator of Pericyte Function and Vessel Maturation. *Nature* **456**, 809–813 (2008).

20.   Alexopoulou, A. N. *et al.* Focal Adhesion Kinase (FAK) tyrosine 397E mutation restores the vascular leakage defect in endothelium-specific FAK-kinase dead mice. *J. Pathol.* **242**, 358–370 (2017).

21.   Chen, X. L. *et al.* VEGF-Induced Vascular Permeability Is Mediated by FAK. *Dev. Cell* **22**, 146–157 (2012).

22. Tavora, B. *et al.* Endothelial FAK is required for tumour angiogenesis. *EMBO Mol. Med.* **2**, 516–528 (2010).

23. Roy-Luzarraga, M. & Hodivala-Dilke, K. Molecular Pathways: Endothelial Cell FAK-A Target for Cancer Treatment. *Clin. Cancer Res.* **22**, 3718–3724 (2016).

24. Saharinen, P., Eklund, L. & Alitalo, K. Therapeutic targeting of the angiopoietin–TIE pathway. *Nat. Rev. Drug Discov.* **16**, 635–661 (2017).

25. Falcón, B. L. *et al.* Contrasting Actions of Selective Inhibitors of Angiopoietin-1 and Angiopoietin-2 on the Normalization of Tumor Blood Vessels. *Am. J. Pathol.* **175**, 2159–2170 (2009).

26. Nagy, J. A., Chang, S.-H., Dvorak, A. M. & Dvorak, H. F. Why are tumour blood vessels abnormal and why is it important to know? *Br. J. Cancer* **100**, 865–869 (2009).

27. Michiels, C., Tellier, C. & Feron, O. Cycling hypoxia: A key feature of the tumor microenvironment. *Biochim. Biophys. Acta - Rev. Cancer* **1866**, 76–86 (2016).

28. Trédan, O., Galmarini, C. M., Patel, K. & Tannock, I. F. Drug Resistance and the Solid Tumor Microenvironment. *JNCI J. Natl. Cancer Inst.* **99**, 1441–1454 (2007).

29. Gupta, S. C. *et al.* Upsides and downsides of reactive oxygen species for cancer: the roles of reactive oxygen species in tumorigenesis, prevention, and therapy. *Antioxid. Redox Signal.* **16**, 1295–1322 (2012).

30. Parks, S. K. & Pouysségur, J. Targeting pH regulating proteins for cancer therapy–Progress and limitations. *Semin. Cancer Biol.* **43**, 66–73 (2017).

31. Parks, S. K., Chiche, J. & Pouyssegur, J. pH control mechanisms of tumor survival and growth. *J. Cell. Physiol.* **226**, 299–308 (2010).

32. Estrella, V. *et al.* Acidity generated by the tumor microenvironment drives local invasion. *Cancer Res.* **73**, 1524–1535 (2013).

33. Rofstad, E. K., Mathiesen, B., Kindem, K. & Galappathi, K. Acidic Extracellular pH Promotes Experimental Metastasis of Human Melanoma Cells in Athymic

Nude Mice. *Cancer Res.* **66**, 6699–6707 (2006).

34. Vukovic, V. & Tannock, I. F. Influence of low pH on cytotoxicity of paclitaxel, mitoxantrone and topotecan. *Br. J. Cancer* **75**, 1167–1172 (1997).

35. Hegde, P. S. *et al.* Predictive Impact of Circulating Vascular Endothelial Growth Factor in Four Phase III Trials Evaluating Bevacizumab. *Clin. Cancer Res.* **19**, 929–937 (2013).

36. Semenza, G. L. The hypoxic tumor microenvironment: A driving force for breast cancer progression. *Biochim. Biophys. Acta - Mol. Cell Res.* **1863**, 382–391 (2016).

37. Donnem, T. *et al.* Non-angiogenic tumours and their influence on cancer biology. *Nat. Rev. Cancer* **18**, 323 (2018).

38. Qiao, L. *et al.* Advanced research on vasculogenic mimicry in cancer. *J. Cell. Mol. Med.* **19**, 315–326 (2015).

39. Maniotis, A. J. *et al.* Vascular channel formation by human melanoma cells in vivo and in vitro: vasculogenic mimicry. *Am. J. Pathol.* **155**, 739–752 (1999).

40. Williamson, S. C. *et al.* Vasculogenic mimicry in small cell lung cancer. *Nat. Commun.* **7**, 13322 (2016).

41. Angara, K. *et al.* CXCR2-Expressing Tumor Cells Drive Vascular Mimicry in Antiangiogenic Therapy-Resistant Glioblastoma. *Neoplasia* **20**, 1070–1082(2018).

42. Shirakawa, K. *et al.* Absence of Endothelial Cells, Central Necrosis, and Fibrosis Are Associated with Aggressive Inflammatory Breast Cancer. *Cancer Res.* **61**, 445 LP – 451 (2001).

43. Wagenblast, E. *et al.* A model of breast cancer heterogeneity reveals vascular mimicry as a driver of metastasis. *Nature* **520**, 358–362 (2015).

44. Delgado-Bellido, D., Serrano-Saenz, S., Fernández-Cortés, M. & Oliver, F. J. Vasculogenic mimicry signaling revisited: focus on non-vascular VE-cadherin. *Mol. Cancer* **16**, 65 (2017).

45. Sun, B., Zhang, D., Zhao, N. & Zhao, X. Epithelial-to-endothelial transition and cancer stem cells: two cornerstones of vasculogenic mimicry in malignant tumors. *Oncotarget* **8**, 30502–30510 (2017).

46. Langer, E. M. *et al.* ZEB1-repressed microRNAs inhibit autocrine signaling that promotes vascular mimicry of breast cancer cells. *Oncogene* **37**, 1005–1019(2018).

47. Cao, Z. *et al.* Tumour vasculogenic mimicry is associated with poor prognosis of human cancer patients: a systemic review and meta-analysis. *Eur. J. Cancer* **49**, 3914–3923 (2013).

48. Quiros-Gonzalez, I. *et al.* Optoacoustics delineates murine breast cancer models displaying angiogenesis and vascular mimicry. *Br. J. Cancer* **118**, 1098–1106 (2018).

49. Heldin, C.-H., Rubin, K., Pietras, K. & Östman, A. High interstitial fluid pressure — an obstacle in cancer therapy. *Nat. Rev. Cancer* **4**, 806 (2004).

50. Jain, R. K., Martin, J. D. & Stylianopoulos, T. The role of mechanical forces in tumor growth and therapy. *Annu. Rev. Biomed. Eng.* **16**, 321–346 (2014).

51. Gilkes, D. M., Bajpai, S., Chaturvedi, P., Wirtz, D. & Semenza, G. L. Hypoxia-inducible Factor 1 (HIF-1) Promotes Extracellular Matrix Remodeling under Hypoxic Conditions by Inducing P4HA1, P4HA2, and PLOD2 Expression in Fibroblasts. *J. Biol. Chem.* **288**, 10819–10829 (2013).

52. Gilkes, D. M. *et al.* Procollagen Lysyl Hydroxylase 2 Is Essential for Hypoxia-Induced Breast Cancer Metastasis. *Mol. Cancer Res.* **11**, 456–466 (2013).

53. Bordeleau, F. *et al.* Matrix stiffening promotes a tumor vasculature phenotype. *Proc. Natl. Acad. Sci.* **114**, 492–497 (2017).

54. Saupe, F. *et al.* Tenascin-C Downregulates Wnt Inhibitor Dickkopf-1, Promoting Tumorigenesis in a Neuroendocrine Tumor Model. *Cell Rep.* **5**, 482–492 (2013).

55. Colegio, O. R. *et al.* Functional polarization of tumour-associated macrophages by

tumour-derived lactic acid. *Nature* **513**, 559 (2014).

56. Britto, D. D. *et al.* Macrophages enhance Vegfa-driven angiogenesis in an embryonic zebrafish tumour xenograft model. *Dis. Model. Mech.* **11**, (2018).

57. De Palma, M., Venneri, M. A., Roca, C. & Naldini, L. Targeting exogenous genes to tumor angiogenesis by transplantation of genetically modified hematopoietic stem cells. *Nat. Med.* **9**, 789 (2003).

58. De Palma, M. *et al.* Tie2 identifies a hematopoietic lineage of proangiogenic monocytes required for tumor vessel formation and a mesenchymal population of pericyte progenitors. *Cancer Cell* **8**, 211–226 (2005).

59. Hughes, R. *et al.* Perivascular M2 Macrophages Stimulate Tumor Relapse after Chemotherapy. *Cancer Res.* **75**, 3479–3491 (2015).

60. Stockmann, C. *et al.* Deletion of vascular endothelial growth factor in myeloid cells accelerates tumorigenesis. *Nature* **456**, 814 (2008).

61. Ahmad, M., Long, J. S., Pyne, N. J. & Pyne, S. The effect of hypoxia on lipid phosphate receptor and sphingosine kinase expression and mitogen-activated protein kinase signaling in human pulmonary smooth muscle cells. *Prostaglandins Other Lipid Mediat.* **79**, 278–286 (2006).

62. Pyne, N. J. & Pyne, S. Sphingosine 1-phosphate and cancer. *Nat. Rev. Cancer* **10**, 489 (2010).

63. Baenke, F., Peck, B., Miess, H. & Schulze, A. Hooked on fat: the role of lipid synthesis in cancer metabolism and tumour development. *Dis. Model. Mech.* **6**, 1353–1363 (2013).

64. Nakajima, M., Nagahashi, M., Rashid, O. M., Takabe, K. & Wakai, T. The role of sphingosine-1-phosphate in the tumor microenvironment and its clinical implications. *Tumor Biol.* **39**, 1010428317699133 (2017).

65. Hsu, T., Nguyen-Tran, H.-H. & Trojanowska, M. Active roles of dysfunctional vascular endothelium in fibrosis and cancer. *J. Biomed. Sci.* **26**, 86 (2019).

66. Branco-Price, C. *et al.* Endothelial cell HIF-1α and HIF-2α differentially regulate metastatic success. *Cancer Cell* **21**, 52–65 (2012).

67. Calcinotto, A. *et al.* Modulation of Microenvironment Acidity Reverses Anergy in Human and Murine Tumor-Infiltrating T Lymphocytes. *Cancer Res.* **72**, 2746–2756 (2012).

68. Dickson, P. V *et al.* Bevacizumab-Induced Transient Remodeling of the Vasculature in Neuroblastoma Xenografts Results in Improved Delivery and Efficacy of Systemically Administered Chemotherapy. *Clin. Cancer Res.* **13**, 3942–3950 (2007).

69. Winkler, F. *et al.* Kinetics of vascular normalization by VEGFR2 blockade governs brain tumor response to radiation: Role of oxygenation, angiopoietin-1, and matrix metalloproteinases. *Cancer Cell* **6**, 553–563 (2004).

70. Zaha, D. C. Significance of immunohistochemistry in breast cancer. *World J. Clin. Oncol.* **5**, 382–392 (2014).

71. Rykala, J. *et al.* Angiogenesis markers quantification in breast cancer and their correlation with clinicopathological prognostic variables. *Pathol. Oncol. Res.* **17**, 809–817 (2011).

72. Giesen, C. *et al.* Highly multiplexed imaging of tumor tissues with subcellular resolution by mass cytometry. *Nat. Methods* **11**, 417–422 (2014).

73. Ali, H. R. *et al.* Imaging mass cytometry and multiplatform genomics define the phenogenomic landscape of breast cancer. *Nat. Cancer* **1**, 163–175 (2020).

74. Dravid U., A. & Mazumder, N. Types of advanced optical microscopy techniques for breast cancer research: a review. *Lasers Med. Sci.* **33**, 1849–1858 (2018).

75. Blomme, A. *et al.* Murine stroma adopts a human-like metabolic phenotype in the PDX model of colorectal cancer and liver metastases. *Oncogene* **37**, 1237–1250 (2018).

76. Alonzi, R., Padhani, A. R. & Allen, C. Dynamic contrast enhanced MRI in prostate

cancer. *Eur. J. Radiol.* **63**, 335–350 (2007).

77. Ohno, Y. *et al.* Dynamic Contrast-Enhanced CT and MRI for Pulmonary Nodule Assessment. *Am. J. Roentgenol.* **202**, 515–529 (2014).

78. Saini, R. & Hoyt, K. Recent developments in dynamic contrast-enhanced ultrasound imaging of tumor angiogenesis. *Imaging Med.* **6**, 41–52 (2014).

79. Heiken, J. P. Contrast safety in the cancer patient: preventing contrast-induced nephropathy. *Cancer Imaging* **8**, S124–S127 (2008).

80. Rogosnitzky, M. & Branch, S. Gadolinium-based contrast agent toxicity: a review of known and proposed mechanisms. *BioMetals* **29**, 365–376 (2016).

81. Hoskin, P. J. *et al.* Hypoxia in prostate cancer: correlation of BOLD-MRI with pimonidazole immunohistochemistry-initial observations. *Int. J. Radiat. Oncol. Biol. Phys.* **68**, 1065–71 (2007).

82. O'Connor, J. P. B. *et al.* Oxygen-Enhanced MRI Accurately Identifies, Quantifies, and Maps Tumor Hypoxia in Preclinical Cancer Models. *Cancer Res.* **76**, 787–795 (2016).

83. Hallac, R. R. *et al.* Correlations of noninvasive BOLD and TOLD MRI with pO2 and relevance to tumor radiation response. *Magn. Reson. Med.* **71**, 1863–1873 (2014).

84. Howe, F. A., Robinson, S. P., McIntyre, D. J. O., Stubbs, M. & Griffiths, J. R. Issues in flow and oxygenation dependent contrast (FLOOD) imaging of tumours. *NMR Biomed.* **14**, 497–506 (2001).

85. Koch, C. J. & Evans, S. M. Optimizing hypoxia detection and treatment strategies. *Semin. Nucl. Med.* **45**, 163–176 (2015).

86. Lopci, E. *et al.* PET radiopharmaceuticals for imaging of tumor hypoxia: a review of the evidence . *Am. J. Nucl. Med. Mol. Imaging* **4**, 365–384 (2014).

87. Cerussi, A. *et al.* In vivo absorption, scattering, and physiologic properties of 58

malignant breast tumors determined by broadband diffuse optical spectroscopy. *J. Biomed. Opt.* **11**, 044005 (2006).

88. Leo, G. Di, Trimboli, R. M., Sella, T. & Sardanelli, F. Optical Imaging of the Breast: Basic Principles and Clinical Applications. *Am. J. Roentgenol.* **209**, 230–238 (2017).

89. Tromberg, B. J. *et al.* Imaging in breast cancer: Diffuse optics in breast cancer: detecting tumors in pre-menopausal women and monitoring neoadjuvant chemotherapy. *Breast Cancer Res.* **7**, 279 (2005).

90. van der Veldt, A. A. M *et. al.* Quantitative parametric perfusion images using 15O-labeled water and a clinical PET/CT scanner: test–retest variability in lung cancer. *J. Nucl. Med.* **51**, 1684-1690 (2010).

91. Postema, A., Mischi, M., de la Rosette, J. and Wijkstra, H. Multiparametric ultrasound in the detection of prostate cancer: a systematic review. *World J. Urol.* **33**, 1651-1659 (2015).

92. Gee, M. S., *et al.* Doppler ultrasound imaging detects changes in tumor perfusion during antivascular therapy associated with vascular anatomic alterations. *Cancer Res.* **61**, 2974-2982 (2001).

93. Fleischer, A. C. Sonographic depiction of tumor vascularity and flow: from in vivo models to clinical applications. *J. Ultrasound Med.* **19**, 55-61 (2000).

94. Ramamonjisoa, N. and Ackerstaff, E. Characterization of the tumor microenvironment and tumor-stroma interaction by non-invasive preclinical imaging. *Front. Oncol.* **7**, 3 (2017).

95. Wang, L. V & Hu, S. Photoacoustic Tomography: In Vivo Imaging from Organelles to Organs. *Science (80-.).* **335**, 1458–1462 (2012).

96. Knieling, F. *et al.* Multispectral Optoacoustic Tomography for Assessment of Crohn's Disease Activity. *N. Engl. J. Med.* **376**, 1292–1294 (2017).

97. Steinberg, I. *et al.* Photoacoustic clinical imaging. *Photoacoustics* **14**, 77–98

(2019).

98.   Beard, P. Biomedical Photoacoustic Imaging. *Interface Focus* **1**, 602–631 (2011).

99.   Ntziachristos, V., Ripoll, J., Wang, L. V & Weissleder, R. Looking and listening to light: the evolution of whole-body photonic imaging. *Nat. Biotechnol.* **23**, 313 (2005).

100.   Wang, L. V & Yao, J. A practical guide to photoacoustic tomography in the life sciences. *Nat. Methods* **13**, 627–638 (2016).

101.   Weber, J., Beard, P. C. & Bohndiek, S. E. Contrast agents for molecular photoacoustic imaging. *Nat. Methods* **13**, 639–650 (2016).

102.   Brunker, J., Yao, J., Laufer, J. & Bohndiek, S. Photoacoustic imaging using genetically encoded reporters: A review. *J. Biomed. Opt.* **22**, 70901 (2017).

103.   Bar-Zion, A., Yin, M., Adam, D. & Foster, F. S. Functional Flow Patterns and Static Blood Pooling in Tumors Revealed by Combined Contrast-EnhancedUltrasound and Photoacoustic Imaging. *Cancer Res.* **76**, 4320–4331 (2016).

104.   Diot, G. *et al.* Multi-Spectral Optoacoustic Tomography (MSOT) of human breast cancer. *Clin. Cancer Res.* (2017). doi:10.1158/1078-0432.CCR-16-3200

105.   Neuschler, E. I. *et al.* A Pivotal Study of Optoacoustic Imaging to Diagnose Benign and Malignant Breast Masses: A New Evaluation Tool for Radiologists. *Radiology* **287**, 398–412 (2018).

106.   Laufer, J. *et al.* In vivo preclinical photoacoustic imaging of tumor vasculature development and therapy. *J. Biomed. Opt.* **17**, 056016 (2012).

107.   Haedicke, K. *et al.* High-resolution optoacoustic imaging of tissue responses to vascular-targeted therapies. *Nat. Biomed. Eng.* **4**, 286–297 (2020).

108.   Lao, Y., Xing, D., Yang, S. & Xiang, L. Noninvasive photoacoustic imaging of the developing vasculature during early tumor growth. *Phys. Med. Biol.* **53**, 4203 (2008).

109.   Omar, M., Schwarz, M., Soliman, D., Symvoulidis, P. & Ntziachristos, V. Pushing the Optical Imaging Limits of Cancer with Multi-Frequency-Band Raster-Scan Optoacoustic Mesoscopy (RSOM). *Neoplasia* **17**, 208–214 (2015).

110.   Imai, T. *et al.* Direct measurement of hypoxia in a xenograft multiple myeloma model by optical-resolution photoacoustic microscopy. *Cancer Biol. Ther.* **18**, 101–105 (2017).

111.   Omar, M., Aguirre, J. & Ntziachristos, V. Optoacoustic mesoscopy for biomedicine. *Nat. Biomed. Eng.* **3**, 354–370 (2019).

112.   Omar, M., Soliman, D., Gateau, J. & Ntziachristos, V. Ultrawideband reflection-mode optoacoustic mesoscopy. *Opt. Lett.* **39**, 3911–3914 (2014).

113.   Orlova, A. *et al.* Raster-scan optoacoustic angiography of blood vessel development in colon cancer models. *Photoacoustics* **13**, 25–32 (2018).

114.   Raumonen, P. & Tarvainen, T. Segmentation of vessel structures from photoacoustic images with reliability assessment. *Biomed. Opt. Express* **9**, 2887–2904 (2018).

115.   Soetikno, B. *et al.* Vessel segmentation analysis of ischemic stroke images acquired with photoacoustic microscopy. in *Proc.SPIE* **8223**, (2012).

116.   Meiburger, K. M. *et al.* Skeletonization algorithm-based blood vessel quantification using in vivo 3D photoacoustic imaging. *Phys. Med. Biol.* **61**, 7994–8009 (2016).

117.   Oruganti, T., Laufer, J. G. & Treeby, B. E. Vessel filtering of photoacoustic images. in *Proc.SPIE* **8581**, (2013).

118.   Zhao, H. *et al.* Multiscale Vascular Enhancement Filter Applied to In Vivo Morphologic and Functional Photoacoustic Imaging of Rat Ocular Vasculature. *IEEE Photonics J.* **11**, 1–12 (2019).

119.   Ul Haq, I., Nagaoka, R., Makino, T., Tabata, T. & Saijo, Y. *3D Gabor wavelet based vessel filtering of photoacoustic images*. *Conference proceedings: ... Annual*

International Conference of the IEEE Engineering in Medicine and BiologySociety. IEEE Engineering in Medicine and Biology Society. Conference **2016**, (2016).

120. Todorov, M. I. *et al.* Machine learning analysis of whole mouse brain vasculature. *Nat. Methods* **17**, 442–449 (2020).

121. Corliss, B. A., Mathews, C., Doty, R., Rohde, G. & Peirce, S. M. Methods to label, image, and analyze the complex structural architectures of microvascular networks. *Microcirculation* **26**, e12520–e12520 (2019).

122. Byrne, H. M. *et al.* Topological Methods for Characterising Spatial Networks: A Case Study in Tumour Vasculature. *Math. Today* (2019).

123. Chekkoury, A. *et al.* High-Resolution Multispectral Optoacoustic Tomography of the Vascularization and Constitutive Hypoxemia of Cancerous Tumors. *Neoplasia* **18**, 459–467 (2016).

124. Li, M. *et al.* Simultaneous Molecular and Hypoxia Imaging of Brain Tumors Using Spectroscopic Photoacoustic Tomography. *Proc. IEEE* **96**, 481–489 (2008).

125. Tomaszewski, M. R. *et al.* Oxygen Enhanced Optoacoustic Tomography (OE-OT) Reveals Vascular Dynamics in Murine Models of Prostate Cancer. *Theranostics* **7**, 2900–2913 (2017).

126. Tomaszewski, M. R. *et al.* Oxygen-Enhanced and Dynamic Contrast-Enhanced Optoacoustic Tomography Provide Surrogate Biomarkers of Tumor Vascular Function, Hypoxia, and Necrosis. *Cancer Res.* **78**, 5980–5991 (2018).

127. Lavaud, J., Henry, M., Coll, J. L. & Josserand, V. Exploration of melanoma metastases in mice brains using endogenous contrast photoacoustic imaging. *Int. J. Pharm.* **532**, 704–709 (2017).

128. Raes, F. *et al.* High Resolution Ultrasound and Photoacoustic Imaging of Orthotopic Lung Cancer in Mice: New Perspectives for Onco-Pharmacology. *PLoS One* **11**, e0153532 (2016).

129. Bendinger, A. L., Glowa, C., Peter, J. & Karger, C. P. Photoacoustic imaging to assess pixel-based sO_2 distributions in experimental prostate tumors. **23**, 36009–36011 (2018).

130. Gerling, M. *et al.* Real-time assessment of tissue hypoxia In Vivo with combined photoacoustics and high-frequency ultrasound. *Theranostics* **4**, 604–613 (2014).

131. Bohndiek, S. *et al.* Photoacoustic tomography detects early vessel regression and normalization during ovarian tumor response to the anti-angiogenic therapy Trebananib. *J. Nucl. Med.* jnumed.115.160002 (2015). doi:10.2967/JNUMED.115.160002

132. Zhou, H.-C. *et al.* Optical-resolution photoacoustic microscopy for monitoring vascular normalization during anti-angiogenic therapy. *Photoacoustics* **15**, 100143 (2019).

133. Rich, L. J. & Seshadri, M. Photoacoustic monitoring of tumor and normal tissue response to radiation. *Sci. Rep.* **6**, 21237 (2016).

134. Costa, M. *et al. Photoacoustic imaging for the prediction and assessment of response to radiotherapy in vivo*. (2018). doi:10.1101/329516

135. Becker, A. *et al.* Multispectral optoacoustic tomography of the human breast: characterisation of healthy tissue and malignant lesions using a hybrid ultrasound-optoacoustic approach. *Eur. Radiol.* **28**, 602–609 (2018).

136. Dogan, B. E. *et al.* Optoacoustic imaging and gray-scale us features of breast cancers: Correlation with molecular subtypes. *Radiology* **292**, 564–572 (2019).

137. Menezes, G. L. G. *et al.* Optoacoustic imaging of the breast: correlation with histopathology and histopathologic biomarkers. *Eur. Radiol.* **29**, 6728–6740 (2019).

138. Mann, R. M. Do we need optoacoustic assessment of hypoxia to differentiate molecular subtypes of breast cancer? *Radiology* **292**, 573–574 (2019).

139. Manohar, S., Kharine, A., van Hespen, J. C. G., Steenbergen, W. & van Leeuwen,

T. G. The Twente Photoacoustic Mammoscope: system overview and performance. *Phys. Med. Biol.* **50**, 2543 (2005).

140. Heijblom, M. *et al.* The state of the art in breast imaging using the Twente Photoacoustic Mammoscope: results from 31 measurements on malignancies. *Eur. Radiol.* **26**, 3874–3887 (2016).

141. Nyayapathi, N. *et al.* Dual Scan Mammoscope (DSM)—A New Portable Photoacoustic Breast Imaging System With Scanning in Craniocaudal Plane. *IEEE Trans. Biomed. Eng.* **67**, 1321–1327 (2020).

142. Nyayapathi, N. *et al.* A new photoacoustic breast cancer tomography system that images the patient in standing pose. in (eds. A.A., O. & L.V., W.) **11240**, (SPIE, 2020).

143. Kruger, R. A. *et al.* Dedicated 3D photoacoustic breast imaging. *Med. Phys.* **40**, 113301 (2016).

144. Toi, M. *et al.* Visualization of tumor-related blood vessels in human breast by photoacoustic imaging system with a hemispherical detector array. *Sci. Rep.* **7**, 41970 (2017).

145. Yamaga, I. *et al.* Vascular branching point counts using photoacoustic imaging in the superficial layer of the breast: A potential biomarker for breast cancer. *Photoacoustics* **11**, 6–13 (2018).

146. Oraevsky, A. *et al.* Full-view 3D imaging system for functional and anatomical screening of the breast. in *Photons Plus Ultrasound: Imaging and Sensing 2018* (eds. Oraevsky, A. A. & Wang, L. V) **10494**, 217–226 (SPIE, 2018).

147. Li, X., Heldermon, C. D., Yao, L., Xi, L. & Jiang, H. High resolution functional photoacoustic tomography of breast cancer. *Med. Phys.* **42**, 5321–5328 (2015).

148. Lin, L. *et al.* Single-breath-hold photoacoustic computed tomography of the breast. *Nat. Commun.* **9**, 2352 (2018).

149. Waterhouse, D. J., Fitzpatrick, C. R. M., Pogue, B. W., O'Connor, J. P. B. & Bohndiek, S. E. A roadmap for the clinical implementation of optical-imaging biomarkers. *Nat. Biomed. Eng.* **3**, 339–353 (2019).

150. Abeyakoon, O. *et al.* Optoacoustic Imaging Detects Hormone-Related Physiological Changes of Breast Parenchyma TT - Optoakustische Bildgebung detektiert physiologische Veränderungen des Brustparenchyms in Abhängigkeit von Zyklusphasen. *Ultraschall Med* (2018). doi:10.1055/a-0628-6248

151. Bohndiek, S. E., Bodapati, S., Van De Sompel, D., Kothapalli, S.-R. & Gambhir, S. S. Development and application of stable phantoms for the evaluation of photoacoustic imaging instruments. *PLoS One* **8**, e75533–e75533 (2013).

152. Joseph, J. *et al.* Evaluation of Precision in Optoacoustic Tomography for Preclinical Imaging in Living Subjects. *J. Nucl. Med.* **58**, 807–814 (2017).

153. Martinho Costa, M. *et al.* Quantitative photoacoustic imaging study of tumours in vivo: Baseline variations in quantitative measurements. *Photoacoustics* **13**, 53–65 (2018).

154. Neuschmelting, V. *et al.* Performance of a Multispectral Optoacoustic Tomography (MSOT) System equipped with 2D vs. 3D Handheld Probes for Potential Clinical Translation. *Photoacoustics* **4**, 1–10 (2015).

155. Helfen, A. *et al.* Multispectral Optoacoustic Tomography: Intra- and Interobserver Variability Using a Clinical Hybrid Approach. *J. Clin. Med.* **8**, 63 (2019).

156. O'Connor, J. P. B. *et al.* Imaging biomarker roadmap for cancer studies. *Nat. Rev. Clin. Oncol.* **14**, 169–186 (2017).

157. Bohndiek, S. Addressing photoacoustics standards. *Nat. Photonics* **13**, 298 (2019).

158. Brochu, F. M. *et al.* Towards Quantitative Evaluation of Tissue Absorption Coefficients Using Light Fluence Correction in Optoacoustic Tomography. *IEEE Trans. Med. Imaging* **36**, 322–331 (2017).

159. Cox, B., Laufer, J. G., Arridge, S. R. & Beard, P. C. Quantitative spectroscopic

photoacoustic imaging: a review. *J. Biomed. Opt.* **17**, 061202 (2012).

160. Li, X. *et al.* Optoacoustic mesoscopy analysis and quantitative estimation of specific imaging metrics in Fitzpatrick skin phototypes II to V. *J. Biophotonics* **12**, e201800442 (2019).

161. Heijblom, M. *et al.* Photoacoustic image patterns of breast carcinoma and comparisons with Magnetic Resonance Imaging and vascular stained histopathology. *Sci Rep* **5**, 11778 (2015).

162. Menezes, G. L. G. *et al.* Downgrading of Breast Masses Suspicious for Cancer by Using Optoacoustic Breast Imaging. *Radiology* **288**, 355–365 (2018).

163. Nyayapathi, N. & Xia, J. Photoacoustic imaging of breast cancer: a mini review of system design and image features. *J. Biomed. Opt.* **24**, 1–13 (2019).

164. Hindelang, B. *et al.* Non-invasive imaging in dermatology and the unique potential of raster-scan optoacoustic mesoscopy. *J. Eur. Acad. Dermatology Venereol.* **33**, 1051–1061 (2019).

165. Li, Y. *et al.* In vivo photoacoustic/ultrasonic dual-modality endoscopy with a miniaturized full field-of-view catheter. *J. Biophotonics* **11**, e201800034 (2018).

166. Qu, Y. *et al.* Transvaginal fast-scanning optical-resolution photoacoustic endoscopy. *J. Biomed. Opt.* **23**, 1–4 (2018).

167. Yoon, T.-J. & Cho, Y.-S. Recent advances in photoacoustic endoscopy. *World J. Gastrointest. Endosc.* **5**, 534–539 (2013).

168. Amidi, E. *et al.* Classification of human ovarian cancer using functional, spectral, and imaging features obtained from in vivo photoacoustic imaging. *Biomed. Opt. Express* **10**, 2303–2317 (2019).

169. Holen, I., Speirs, V., Morrissey, B. & Blyth, K. In vivo models in breast cancer research: Progress, challenges and future directions. *DMM Dis. Model. Mech.* **10**, 359–371 (2017).

170. Curtis, C. *et al.* The genomic and transcriptomic architecture of 2,000 breast tumours reveals novel subgroups. *Nature* **486**, 346–352 (2012).

171. Dawson, S.-J., Rueda, O. M., Aparicio, S. & Caldas, C. A new genome-driven integrated classification of breast cancer and its implications. *EMBO J.* **32**, 617–628 (2013).

172. Byrne, A. T. *et al.* Interrogating open issues in cancer precision medicine with patient-derived xenografts. *Nat. Rev. Cancer* **17**, 254–268 (2017).

173. Cassidy, J. W., Batra, A. S., Greenwood, W. & Bruna, A. Patient-derived tumour xenografts for breast cancer drug discovery. *Endocr. Relat. Cancer* **23**, T259–T270 (2016).

174. Oshi, M. *et al.* Novel breast cancer brain metastasis patient-derived orthotopic xenograft model for preclinical studies. *Cancers (Basel).* **12**, (2020).

175. Turner, T. H., Alzubi, M. A. & Harrell, J. C. Identification of synergistic drug combinations using breast cancer patient-derived xenografts. *Sci. Rep.* **10**, (2020).

176. Coussy, F. *et al.* BRCAness, SLFN11, and RB1 loss predict response to topoisomerase I inhibitors in triple-negative breast cancers. *Sci. Transl. Med.* **12**, (2020).

177. Gris-Oliver, A. *et al.* Genetic alterations in the PI3K/AKT pathway and baseline AKT activity define AKT inhibitor sensitivity in breast cancer patient-derived xenografts. *Clin. Cancer Res.* (2020). doi:10.1158/1078-0432.CCR-19-3324

178. Guo, S. *et al.* GLL398, an oral selective estrogen receptor degrader (SERD), blocks tumor growth in xenograft breast cancer models. *Breast Cancer Res. Treat.* **180**, 359–368 (2020).

179. Andreano, K. J. *et al.* G1T48, an oral selective estrogen receptor degrader, and the CDK4/6 inhibitor lerociclib inhibit tumor growth in animal models of endocrine-resistant breast cancer. *Breast Cancer Res. Treat.* **180**, 635–646 (2020).

180. Coussy, F. *et al.* Combination of PI3K and MEK inhibitors yields durable

remission in PDX models of PIK3CA-mutated metaplastic breast cancers. *J. Hematol. Oncol.* **13**, (2020).

181. Newell, M., Goruk, S., Mazurak, V., Postovit, L. & Field, C. J. Role of docosahexaenoic acid in enhancement of docetaxel action in patient-derived breast cancer xenografts. *Breast Cancer Res. Treat.* **177**, 357–367 (2019).

182. Syed, A. K., Woodall, R., Whisenant, J. G., Yankeelov, T. E. & Sorace, A. G. Characterizing Trastuzumab-Induced Alterations in Intratumoral Heterogeneity with Quantitative Imaging and Immunohistochemistry in HER2+ Breast Cancer. *Neoplasia* **21**, 17–29 (2019).

183. Gómez-Miragaya, J. *et al.* The altered transcriptome and DNA methylation profiles of docetaxel resistance in breast cancer PDX models. *Mol. Cancer Res.* **17**, 2063–2076 (2019).

184. McKnight, B. N., Kim, S., Boerner, J. L. & Viola, N. T. Cetuximab PET delineated changes in cellular distribution of EGFR upon dasatinib treatment in triple negative breast cancer. *Breast Cancer Res.* **22**, (2020).

185. Sand, A. *et al.* WEE1 inhibitor, AZD1775, overcomes trastuzumab resistance by targeting cancer stem-like properties in HER2-positive breast cancer. *Cancer Lett.* **472**, 119–131 (2020).

186. Shi, J., Li, Y., Jia, R. & Fan, X. The fidelity of cancer cells in PDX models: Characteristics, mechanism and clinical significance. *Int. J. Cancer* **146**, 2078–2088 (2020).

187. Mignion, L. *et al.* Metabolic Imaging Using Hyperpolarized Pyruvate–Lactate Exchange Assesses Response or Resistance to the EGFR Inhibitor Cetuximab in Patient-Derived HNSCC Xenografts. *Clin. Cancer Res.* **26**, 1932–1943 (2020).

188. Dutta, P. *et al.* Combining Hyperpolarized Real-Time Metabolic Imaging and NMR Spectroscopy to Identify Metabolic Biomarkers in Pancreatic Cancer. *J. Proteome Res.* **18**, 2826–2834 (2019).

189. Dong, Y. *et al.* Hyperpolarized MRI visualizes Warburg effects and predicts treatment response to mTOR inhibitors in patient-derived CCRCC xenograft models. *Cancer Res.* **79**, 242–250 (2019).

190. Randall, E. C. *et al.* Localized metabolomic gradients in patient-derived xenograft models of glioblastoma. *Cancer Res.* **80**, 1258–1267 (2020).

191. Taylor, E. *et al.* Quantifying Reoxygenation in Pancreatic Cancer During Stereotactic Body Radiotherapy. *Sci. Rep.* **10**, (2020).

192. Hauge, A. *et al.* DCE-MRI and Quantitative Histology Reveal Enhanced Vessel Maturation but Impaired Perfusion and Increased Hypoxia in Bevacizumab-Treated Cervical Carcinoma. *Int. J. Radiat. Oncol. Biol. Phys.* **104**, 666–676 (2019).

193. Scott, A. J. *et al.* Cabozantinib exhibits potent antitumor activity in colorectal cancer patient-derived tumor xenograft models via autophagy and signaling mechanisms. *Mol. Cancer Ther.* **17**, 2112–2122 (2018).

194. Folaron, M., Merzianu, M., Duvvuri, U., Ferris, R. L. & Seshadri, M. Profiling the stromal and vascular heterogeneity in patient-derived xenograft models of head and neck cancer: Impact on therapeutic response. *Cancers (Basel).* **11**, (2019).

195. Boult, J. K. R. *et al.* Preclinical transgenic and patient-derived xenograft models recapitulate the radiological features of human adamantinomatous craniopharyngioma. *Brain Pathol.* **28**, 475–483 (2018).

196. Xue, W. *et al.* Patient–derived orthotopic xenograft glioma models fail to replicate the magnetic resonance imaging features of the original patient tumor. *Oncol. Rep.* **43**, 1619–1629 (2020).

197. Meehan, T. F. *et al.* PDX-MI: Minimal Information for Patient-Derived Tumor Xenograft Models. *Cancer Res.* **77**, e62–e66 (2017).

198. Ben-David, U. *et al.* Patient-derived xenografts undergo mouse-specific tumor evolution. *Nat. Genet.* **49**, 1567–1575 (2017).

199. Morikawa, S. *et al.* Abnormalities in Pericytes on Blood Vessels and Endothelial Sprouts in Tumors. *Am. J. Pathol.* **160**, 985–1000 (2002).

200. Lloyd, M. C. *et al.* Vascular measurements correlate with estrogen receptor status. *BMC Cancer* **14**, 279 (2014).

201. Santagostino, S. F., Arbona, R. J. R., Nashat, M. A., White, J. R. & Monette, S. Pathology of Aging in NOD scid gamma Female Mice. *Vet. Pathol.* **54**, 855–869 (2017).

202. van Mourik, J. A., Leeksma, O. C., Reinders, J. H., de Groot, P. G. & Zandbergen-Spaargaren, J. Vascular endothelial cells synthesize a plasma membrane protein indistinguishable from the platelet membrane glycoprotein IIa. *J. Biol. Chem.* **260**, 11300–11306 (1985).

203. Goncharov, N. V, Nadeev, A. D., Jenkins, R. O. & Avdonin, P. V. Markers and Biomarkers of Endothelium: When Something Is Rotten in the State. *Oxid. Med. Cell. Longev.* **2017**, 9759735 (2017).

204. Choi, W. W. L. *et al.* Angiogenic and lymphangiogenic microvessel density in breast carcinoma: correlation with clinicopathologic parameters and VEGF-family gene expression. *Mod. Pathol.* **18**, 143–152 (2005).

205. Qian, H., Yang, L., Zhao, W., Chen, H. & He, S. A comparison of CD105 and CD31 expression in tumor vessels of hepatocellular carcinoma by tissue microarray and flow cytometry. *Exp. Ther. Med.* **16**, 2881–2888 (2018).

206. Owens, G. K., Kumar, M. S. & Wamhoff, B. R. Molecular regulation of vascular smooth muscle cell differentiation in development and disease. *Physiol. Rev.* **84**, 767–801 (2004).

207. Tan, E. Y. *et al.* The key hypoxia regulated gene CAIX is upregulated in basal-like breast tumours and is associated with resistance to chemotherapy. *Br. J. Cancer* **100**, 405–411 (2009).

208. Kaluz, S., Kaluzová, M., Liao, S.-Y., Lerman, M. & Stanbridge, E. J. Transcriptional control of the tumor- and hypoxia-marker carbonic anhydrase 9: A

one transcription factor (HIF-1) show? *Biochim. Biophys. Acta - Rev. Cancer* **1795**, 162–172 (2009).

209. Woo, X. Y. *et al.* Conservation of copy number profiles during engraftment and passaging of patient-derived cancer xenografts. *Nat. Genet.* **53**, 86–99 (2021).

210. Bhadury, J. *et al.* Hypoxia-regulated gene expression explains differences between melanoma cell line-derived xenografts and patient-derived xenografts. *Oncotarget* **7**, 23801–23811 (2016).

211. Gillet, J.-P. *et al.* Redefining the relevance of established cancer cell lines to the study of mechanisms of clinical anti-cancer drug resistance. *Proc. Natl. Acad. Sci. U. S. A.* **108**, 18708–18713 (2011).

212. Liu, Z.-G. & Jiao, D. Necroptosis, tumor necrosis and tumorigenesis. *Cell Stress* **4**, 1–8 (2019).

213. Roberts, N. *et al.* Toward Routine Use of 3D Histopathology as a Research Tool. *Am. J. Pathol.* **180**, 1835–1842 (2012).

214. Choi, J., Jung, W.-H. & Koo, J. S. Metabolism-Related Proteins Are Differentially Expressed according to the Molecular Subtype of Invasive Breast Cancer Defined by Surrogate Immunohistochemistry. *Pathobiology* **80**, 41–52 (2013).

215. Yehia, L. *et al.* Expression of HIF-1α and Markers of Angiogenesis Are Not Significantly Different in Triple Negative Breast Cancer Compared to Other Breast Cancer Molecular Subtypes: Implications for Future Therapy. *PLoS One* **10**, e0129356 (2015).

216. Liu, Y. *et al.* The association between vascular endothelial growth factor expression in invasive breast cancer and survival varies with intrinsic subtypes and use of adjuvant systemic therapy: results from the Nurses' Health Study. *Breast Cancer Res. Treat.* **129**, 175–184 (2011).

217. Brown, E., Brunker, J. & Bohndiek, S. E. Photoacoustic imaging as a tool to probe the tumour microenvironment. *Dis. Model. &amp; Mech.* **12**, dmm039636 (2019).

218. Jährling, N., Becker, K. & Dodt, H.-U. 3D-reconstruction of blood vessels by ultramicroscopy. *Organogenesis* **5**, 227–230 (2009).

219. Keller, P. J. & Dodt, H. U. Light sheet microscopy of living or cleared specimens. *Current Opinion in Neurobiology* **22**, 138–143 (2012).

220. Kelch, I. D. *et al.* Organ-wide 3D-imaging and topological analysis of the continuous microvascular network in a murine lymph node. *Sci. Rep.* **5**, 16534 (2015).

221. Ntziachristos, V. Going deeper than microscopy: the optical imaging frontier in biology. *Nat. Methods* **7**, 603–614 (2010).

222. Aguirre, J. *et al.* Precision assessment of label-free psoriasis biomarkers with ultra-broadband optoacoustic mesoscopy. *Nat. Biomed. Eng.* **1**, 68 (2017).

223. Regensburger, A. P., Brown, E., Krönke, G., Waldner, M. J. & Knieling, F. Optoacoustic Imaging in Inflammation. *Biomedicines* **9**, (2021).

224. Rebling, J., Greenwald, M. B.-Y., Wietecha, M., Werner, S. & Razansky, D. Long-Term Imaging of Wound Angiogenesis with Large Scale Optoacoustic Microscopy. *Adv. Sci.* **8**, 2004226 (2021).

225. Krig, S. Ground Truth Data, Content, Metrics, and Analysis. in *Computer Vision Metrics* 283–311 (Apress, Berkeley, CA, 2014). doi:10.1007/978-1-4302-5930-5_7

226. Zhao, F., Chen, Y., Hou, Y. & He, X. Segmentation of blood vessels using rule-based and machine-learning-based methods: a review. *Multimed. Syst.* **25**, 109– 118 (2019).

227. Moccia, S., De Momi, E., El Hadji, S. & Mattos, L. S. Blood vessel segmentation algorithms — Review of methods, datasets and evaluation metrics. *Comput. Methods Programs Biomed.* **158**, 71–91 (2018).

228. Sommer, C., Straehle, C., Kothe, U. & Hamprecht, F. A. Ilastik: Interactive learning and segmentation toolkit. in *Eighth IEEE International Symposium on*

Biomedical Imaging 230–233 (2011). doi:10.1109/ISBI.2011.5872394

229. Berg, S. *et al.* ilastik: interactive machine learning for (bio)image analysis. *Nat. Methods* **16**, 1226–1232 (2019).

230. Omar, M., Gateau, J. & Ntziachristos, V. Raster-scan optoacoustic mesoscopy in the 25-125 MHz range. *Opt. Lett.* **38**, 2472–2474 (2013).

231. Lindenmayer, A. Mathematical models for cellular interactions in development I. Filaments with one-sided inputs. *J. Theor. Biol.* **18**, 280–299 (1968).

232. *Lindenmayer Systems: Impacts on theoretical computer science, computer graphics, and development biology.* (Springer-Verlag Berlin Heidelberg, 1992). doi:10.1007/978-3-642-58117-5

233. Galarreta-Valverde, M. A., Macedo, M. M. G., Mekkaoui, C. & Jackowski, M. P. Three-dimensional synthetic blood vessel generation using stochastic L-systems. in *Medical Imaging 2013: Image Processing* 86691I (2013). doi:10.1117/12.2007532

234. Galarreta-Valverde, M. A. Geração de redes vasculares sintéticas tridimensionais utilizando sistemas de Lindenmayer estocásticos e parametrizados. (Instituto de Matemática e Estatística, 2012). doi:10.11606/D.45.2012.tde-30112012-172822

235. Bresenham, J. E. Algorithm for computer control of a digital plotter. *IBM Syst. J.* **4**, (1965).

236. Janek Gröhl, Kris K. Dreher, Melanie Schellenberg, Alexander Seitel, L. M.-H. SIMPA: an open source toolkit for simulation and processing of photoacoustic images. *Photons Plus Ultrasound Imaging Sens. 2021* (2021).

237. Treeby, B. E. & Cox, B. T. k-Wave: MATLAB toolbox for the simulation and reconstruction of photoacoustic wave fields. *J. Biomed. Opt.* **15**, 1–12 (2010).

238. Sternberg. Biomedical Image Processing. *Computer (Long. Beach. Calif).* **16**, 22–34 (1983).

239. Tsai, W.-H. Moment-preserving thresolding: A new approach. *Comput. Vision,*

Graph. Image Process. **29**, 377–393 (1985).

240. Sato, Y. *et al.* Three-dimensional multi-scale line filter for segmentation and visualization of curvilinear structures in medical images. *Med. Image Anal.* **2**, 143–168 (1998).

241. Frangi, A. F., Niessen, W. J., Vincken, K. L. & Viergever, M. A. Multiscale vessel enhancement filtering. in *Medical Image Computing and Computer-Assisted Intervention --- MICCAI'98* (eds. Wells, W. M., Colchester, A. & Delp, S.) 130–137 (Springer Berlin Heidelberg, 1998).

242. Ronneberger, O., Fischer, P. & Brox, T. U-Net: Convolutional Networks for Biomedical Image Segmentation. in *Medical Image Computing and Computer-Assisted Intervention – MICCAI 2015. MICCAI 2015. Lecture Notes in Computer Science* **9351**, 234–241 (Springer, 2015).

243. Çiçek, Ö., Abdulkadir, A., Lienkamp, S. S., Brox, T. & Ronneberger, O. 3D U- net: Learning dense volumetric segmentation from sparse annotation. in *Medical Image Computing and Computer-Assisted Intervention – MICCAI 2016. MICCAI2016. Lecture Notes in Computer Science* **9901**, (Springer, 2016).

244. Belchi, F. *et al.* Lung Topology Characteristics in patients with Chronic Obstructive Pulmonary Disease. *Sci. Rep.* **8**, 5341 (2018).

245. Stolz, B. J. *et al.* Multiscale topology characterises dynamic tumour vascular networks. *arXiv* (2020). doi:2008.08667

246. Bates, R. Russ-learn: set of tools for application and training of deep learning methods for image segmentation and vessel analysis. (2018).

247. Bates, R. Learning to Extract Tumour Vasculature: Techniques in Machine Learning for Medical Image Analysis. (University of Oxford, 2017).

248. Harrell, F. E. *Regression modeling strategies*. (Springer International Publishing, 2016).

249. Dice, L. R. Measures of the Amount of Ecologic Association Between Species.

Ecology **26**, 297–302 (1945).

250. Bretz, F., Hothorn, T. & Westfall, P. *Multiple comparisons Using R*. (Chapman and Hall/CRC., 2010).

251. Barlow, K. D., Sanders, A. M., Soker, S., Ergun, S. & Metheny-Barlow, L. J. Pericytes on the tumor vasculature: jekyll or hyde? *Cancer Microenviron. Off. J. Int. Cancer Microenviron. Soc.* **6**, 1–17 (2013).

252. Dantuma, M., van Dommelen, R. & Manohar, S. Semi-anthropomorphic photoacoustic breast phantom. *Biomed. Opt. Express* **10**, 5921–5939 (2019).

253. Epah, J. *et al.* 3D imaging and quantitative analysis of vascular networks: A comparison of ultramicroscopy and micro-computed tomography. *Theranostics* **8**, 2117–2133 (2018).

254. Hlushchuk, R., Haberthür, D. & Djonov, V. Ex vivo microangioCT: Advances in microvascular imaging. *Vascul. Pharmacol.* **112**, 2–7 (2019).

255. Jia, D. & Zhuang, X. Learning-based algorithms for vessel tracking: A review. *Comput. Med. Imaging Graph.* **89**, 101840 (2021).

256. Morscher, S., Driessen, W. H. P., Claussen, J. & Burton, N. C. Semi-quantitative Multispectral Optoacoustic Tomography (MSOT) for volumetric PK imaging of gastric emptying. *Photoacoustics* **2**, 103–110 (2014).

257. Virtanen, P. *et al.* SciPy 1.0: fundamental algorithms for scientific computing in Python. *Nat. Methods* **17**, 261–272 (2020).

258. Clark, M. Mixed models with R. Available at: https://github.com/m-clark/mixed-models-with-R. (Accessed: 13th September 2021)

259. Pinheiro, J. C. & Bates, D. M. *Mixed-Effects Models in S and S-PLUS*. (Springer, New York, NY, 2000). doi: 10.1007/b98882

260. Pillinger, R. Random slope models. Available at: http://www.bristol.ac.uk/cmm/learning/videos/random-slopes.html. (Accessed:

17th August 2021)

261.   Gillies, R. J., Schornack, P. A., Secomb, T. W. & Raghunand, N. Causes and Effects of Heterogeneous Perfusion in Tumors. *Neoplasia* **1**, 197–207 (1999).

262.   Gehrung, M., Tomaszewski, M., McIntyre, D., Disselhorst, J. & Bohndiek, S. Co-registration of optoacoustic tomography and magnetic resonance imaging data from murine tumour models. *Photoacoustics* **18**, 100147 (2020).

263.   Incoronato, M., Mirabelli, P., Grimaldi, A. M., Soricelli, A. & Salvatore, M. Correlating imaging parameters with molecular data: An integrated approach to improve the management of breast cancer patients. *Int. J. Biol. Markers* **35**, 47–50 (2020).

264.   Gillies, R. J., Kinahan, P. E. & Hricak, H. Radiomics: Images Are More than Pictures, They Are Data. *Radiology* **278**, 563–577 (2016).

265.   Gill, A. B. *et al.* Correlating Radiomic Features of Heterogeneity on CT with Circulating Tumor DNA in Metastatic Melanoma. *Cancers (Basel).* **12**, (2020).

266.   Jeong, Y.-J. *et al.* Correlation of hypoxia inducible transcription factor in breast cancer and SUVmax of F-18 FDG PET/CT. *Nucl. Med. Rev. Cent. East. Eur.* **20**, 32–38 (2017).

267.   Gallagher, F. A. *et al.* Imaging breast cancer using hyperpolarized carbon-13 MRI. *Proc. Natl. Acad. Sci.* **117**, 2092–2098 (2020).

268.   Yeh, A. C. *et al.* Radiogenomics of breast cancer using dynamic contrast enhanced MRI and gene expression profiling. *Cancer Imaging* **19**, 48 (2019).

269.   Buffa, F. M., Harris, A. L., West, C. M. & Miller, C. J. Large meta-analysis of multiple cancers reveals a common, compact and highly prognostic hypoxia metagene. *Br. J. Cancer* **102**, 428–435 (2010).

270.   Bolger, A. M., Lohse, M. & Usadel, B. Trimmomatic: a flexible trimmer for Illumina sequence data. *Bioinformatics* **30**, 2114–2120 (2014).

271. Conway, T. *et al.* Xenome—a tool for classifying reads from xenograft samples. *Bioinformatics* **28**, i172–i178 (2012).

272. Howe, K. L. *et al.* Ensembl 2021. *Nucleic Acids Res.* **49**, D884–D891 (2021).

273. Dobin, A. *et al.* STAR: ultrafast universal RNA-seq aligner. *Bioinformatics* **29**, 15–21 (2013).

274. Patro, R., Duggal, G., Love, M. I., Irizarry, R. A. & Kingsford, C. Salmon provides fast and bias-aware quantification of transcript expression. *Nat. Methods* **14**, 417–419 (2017).

275. Gentleman, R. C. *et al.* Bioconductor: open software development for computational biology and bioinformatics. *Genome Biol.* **5**, R80 (2004).

276. Huber, W. *et al.* Orchestrating high-throughput genomic analysis with Bioconductor. *Nat. Methods* **12**, 115–121 (2015).

277. Hänzelmann, S., Castelo, R. & Guinney, J. GSVA: gene set variation analysis for microarray and RNA-Seq data. *BMC Bioinformatics* **14**, 7 (2013).

278. Ye, I. C. *et al.* Molecular Portrait of Hypoxia in Breast Cancer: A Prognostic Signature and Novel HIF-Regulated Genes. *Mol. Cancer Res.* **16**, 1889–1901 (2018).

279. Hu, Z. *et al.* A compact VEGF signature associated with distant metastases and poor outcomes. *BMC Med.* **7**, 9 (2009).

280. Bhandari, V. *et al.* Molecular landmarks of tumor hypoxia across cancer types. *Nat. Genet.* **51**, 308–318 (2019).

281. Harris, B. H. L., Barberis, A., West, C. M. L. & Buffa, F. M. Gene Expression Signatures as Biomarkers of Tumour Hypoxia. *Clin. Oncol. (R. Coll. Radiol).* **27**, 547–560 (2015).

282. Favaro, E., Lord, S., Harris, A. L. & Buffa, F. M. Gene expression and hypoxia in breast cancer. *Genome Med.* **3**, 55 (2011).

283. Abou Khouzam, R. *et al.* Integrating tumor hypoxic stress in novel and more adaptable strategies for cancer immunotherapy. *Semin. Cancer Biol.* **65**, 140–154 (2020).

284. Eustace, A. *et al.* A 26-gene hypoxia signature predicts benefit from hypoxia-modifying therapy in laryngeal cancer but not bladder cancer. *Clin. cancer Res. an Off. J. Am. Assoc. Cancer Res.* **19**, 4879–4888 (2013).

285. Fox, N. S., Starmans, M. H. W., Haider, S., Lambin, P. & Boutros, P. C. Ensemble analyses improve signatures of tumour hypoxia and reveal inter-platform differences. *BMC Bioinformatics* **15**, 170 (2014).

286. Nakamura, M. *et al.* Characterization of KIF20A as a prognostic biomarker and herapeutic target for different subtypes of breast cancer. *Int J Oncol* **57**, 277–288 (2020).

287. Nami, B. & Wang, Z. Genetics and Expression Profile of the Tubulin Gene Superfamily in Breast Cancer Subtypes and Its Relation to Taxane Resistance. *Cancers (Basel).* **10**, (2018).

288. van Kuijk, S. J. A. *et al.* Prognostic Significance of Carbonic Anhydrase IX Expression in Cancer Patients: A Meta-Analysis. *Front. Oncol.* **6**, 69 (2016).

289. Langlois, B. *et al.* AngioMatrix, a signature of the tumor angiogenic switch-specific matrisome, correlates with poor prognosis for glioma and colorectal cancer patients. *Oncotarget* **5**, 10529–10545 (2014).

290. Hashmi, A. A. *et al.* Ki67 index in intrinsic breast cancer subtypes and its association with prognostic parameters. *BMC Res. Notes* **12**, 605 (2019).

291. Nakazawa, M. S., Keith, B. & Simon, M. C. Oxygen availability and metabolic adaptations. *Nat. Rev. Cancer* **16**, 663–673 (2016).

292. Lechertier, T. *et al.* Pericyte FAK negatively regulates Gas6/Axl signalling to suppress tumour angiogenesis and tumour growth. *Nat. Commun.* **11**, 2810 (2020).

293. Hillen, F. & Griffioen, A. W. Tumour vascularization: sprouting angiogenesis and

beyond. *Cancer Metastasis Rev.* **26**, 489–502 (2007).

294. Thiruthaneeswaran, N. *et al.* Lost in application: Measuring hypoxia for radiotherapy optimisation. *Eur. J. Cancer* **148**, 260–276 (2021).

295. Hylander, B. L. et al. Origin of the vasculature supporting growth of primary patient tumor xenografts. *J. Transl. Med.* **11**, 110 (2013).

296. DeRose, Y. S. et al. Tumor grafts derived from women with breast cancer authentically reflect tumor pathology, growth, metastasis and disease outcomes. *Nat. Med.* **17**, 1514–1520 (2011).

297. Sanz, L. et al. Differential transplantability of human endothelial cells in colorectal cancer and renal cell carcinoma primary xenografts. *Lab. Invest.* **89**, 91–97 (2009).

298. Fung, A. S., Lee, C., Yu, M. & Tannock, I. F. The effect of chemotherapeutic agents on tumor vasculature in subcutaneous and orthotopic human tumor xenografts. *BMC Cancer* **15**, 112 (2015).

299. Invrea, F. et al. Patient-derived xenografts (PDXs) as model systems for human cancer. *Curr. Opin. Biotechnol.* **63**, 151–156 (2020).

300. Fleming, J. M., Miller, T. C., Meyer, M. J., Ginsburg, E. & Vonderhaar, B. K. Local regulation of human breast xenograft models. *J. Cell. Physiol.* **224**, 795–806(2010).

301. Zhang, Y. et al. Establishment of a murine breast tumor model by subcutaneous or orthotopic implantation. *Oncol. Lett.* **15**, 6233–6240 (2018).

302. Ho, K. S., Poon, P. C., Owen, S. C. & Shoichet, M. S. Blood vessel hyperpermeability and pathophysiology in human tumour xenograft models of breast cancer: a comparison of ectopic and orthotopic tumours. *BMC Cancer* **12**, 579 (2012).

303. Draheim, K. M., Banzon, R. R., Tewodros, M. M., VanBuskirk, D. & Cheng, M. Abstract 1672: Comparing subcutaneous to mammary fat pad implantation on the growth kinetics, histology and drug response of PDX breast cancer models. *Cancer Res.* **80**, 1672 (2020).

8 APPENDICES

APPENDIX 1: 3D CONVOLUTIONAL NEURAL NETWORK FOR ROI DELINEATION

APPENDIX 2: NETWORK ANALYSES OF AT+VF SEGMENTATION MASKS COMPARING STG139 AND AB580 TUMOURS

APPENDIX 1: 3D CONVOLUTIONAL NEURAL NETWORK FOR ROI DELINEATION

Preparation of training data for CNN

Image volumes consist of a series of 8-bit grayscale Tiffs (no compression) of 600 x 600 pixels in the XY-plane and a stack of 700 images in Z, with anisotropic voxels of size 20x 20 x 4 μm^3. Our dataset has a total of 166 PAI volumes, each paired with a corresponding binary semi-manually-annotated volume, where a voxel value of 0 and 255indicates the background or tumour ROIs, respectively. The annotated volumes were generated by an experienced user (ELB), who first identified the top and bottom image containing the tumour in Z. Within these upper and lower bounds, ROIs were manually drawn in the XY plane on approximately 4 image slices. Bound by these data, a convex hull was extrapolated to approximate the ROI in the remaining image slices.

Prior to training, image volumes and binary masks were downsampled to an isotropic volume of 128 x 128 x 128 voxels to fit into computer memory. Data were normalised toa pixel range between 0 and 1 and the volumes randomly partitioned into training, validation, and testing subsets. Here, ~5% of images were allocated for testing, with the remaining portion split 80:20 for training and validation respectively (8 / 126 / 32 image volumes, respectively).

Neural Network Architecture for ROI delineation

The 3D convolutional neural network (CNN) is based on the U-Net architecture[242] extended for volumetric delineation[243] (**Figure 8.1**). The structure consists of an encoder, which extracts spatial features from a 3D image volume, and a decoder, which constructsa segmentation map from these features (**Figure 8.1**). The network architecture consists of five convolutional layers. The encoder path contains two 3 x 3 x 3 convolutions, eachof which passed through a rectified linear unit (ReLU) activation for faster convergence and accuracy[243]. Each ReLU activation is followed by 2 x 2 x 2 max pooling with strides

of two in each dimension. For the 3rd, 4th and 5th layers, dropout is applied to reduce segmentation bias and ensure segmentation is performed utilising high-level features that may have not been considered in our semi-manual ROI annotations.

The decoder path consists of two 3 x 3 x 3 deconvolutions of strides of 2 in each dimension, followed by 3 x 3 x 3 convolutions, batch normalisation and ReLU activation. High-resolution features were provided via shortcut connections from the same layer in the encoder path. The final layer applied an additional 1 x 1 x 1 convolution followed by sigmoid activation to ensure the correct number of output channels and range of pixel values [0, 1]. The input layer is designed to take n grayscale (one channel) tumour volumes as input with a pre-defined volume (128 x 128 x 128 voxels in X, Y, Z-directionused here). The U-Net binary mask prediction contains an equal number of voxels as theinput. The CNN was implemented in Keras (https://keras.io) with the Tensorflow framework. The model was trained and tested on a Dell Precision 7920 with a Dual IntelXeon Gold 5120 CPU with 128 GB RAM and a NVIDIA Quadro GV100 32 GB GPU.
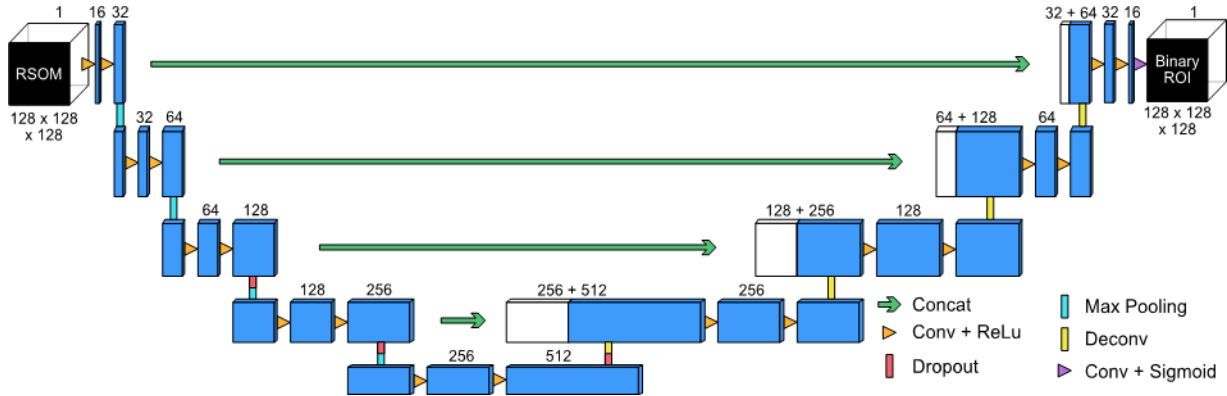
Figure 8.1. 3D U-Net architecture. The blue boxes indicate feature maps with the number of channels denoted above. The input and output image volumes consist of 128 x 128 x 128 voxels.

## Hyperparameter Optimisation

Hyperparameters were optimised and evaluated using Talos (https://github.com/autonomio/talos) , a fully-automated hyperparameter tuner for Keras.

A random search optimisation strategy was deployed using the quantum random method.

Here, a probabilistic reduction scheme was used to reduce the number of parameter permutations by removing poorly performing hyperparameter configurations from the remaining search space after a predefined interval. The number of filters used ranged from 16 in the 1st layer to 512 in the 5th. Dropout at a rate of 0.2 was applied in the 3rd,4th and 5th layers. A Glorot uniform initialiser was used for all convolution anddeconvolution layers. The model was trained using an Adam optimiser with learning anddecay rates of 10-5 and 10-8, respectively, and the dice coefficient (F1)[249] used as the lossfunction.

U-net training and predictions

Training was performed with a batch size of 3 image volumes for a total of 120 epochs (**Figure 8.2A**). The fully-trained network achieved an accuracy of 88.3% and 87.3% on the training and validation sets respectively (**Figure 8.2B**). Following training and test, we applied the CNN to the entire set of volumes to compare predictions of ROI volume to the ground truth (**Figure 8.2C**). Blood volumes were then calculated within the predicted ROIs using the AT method and compared against the user annotations (**Figure8.2D**). We found a significant correlation between user annotated and predicted data for both ROI volume (Spearman's rank correlation: $r = 0.821$, $p < 0.0001$) and blood volume($r = 0.958$, $p < 0.0001$), indicating our CNN achieves sufficient performance against the experienced user to be applied for extracting tumours prior to testing the segmentation pipeline.
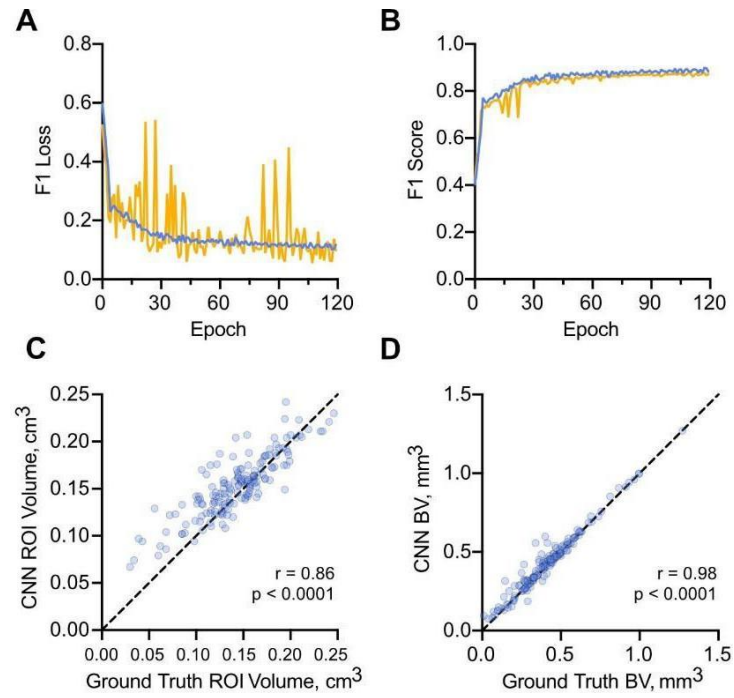
Figure 8.2. U-Net training metrics and predictions from the fully-trained architecture. Training metrics: (A) F1 loss and (B) F1 score for the training (blue) and validation (orange) datasets. (C) Region-of-interest volumes calculated from the ground truth (GT) versus the U-Net mask. (D) Computed blood volumes using the ground truth and U-Net ROI estimations from (C). Note, the lines in (C) and (D) indicate a 1-to-1 relationship, and blood volumes in (B) were calculated using our auto-thresholding segmentation method.

APPENDIX 2: NETWORK ANALYSES OF AT+VF SEGMENTATION MASKS COMPARING STG139 AND AB580 TUMOURS
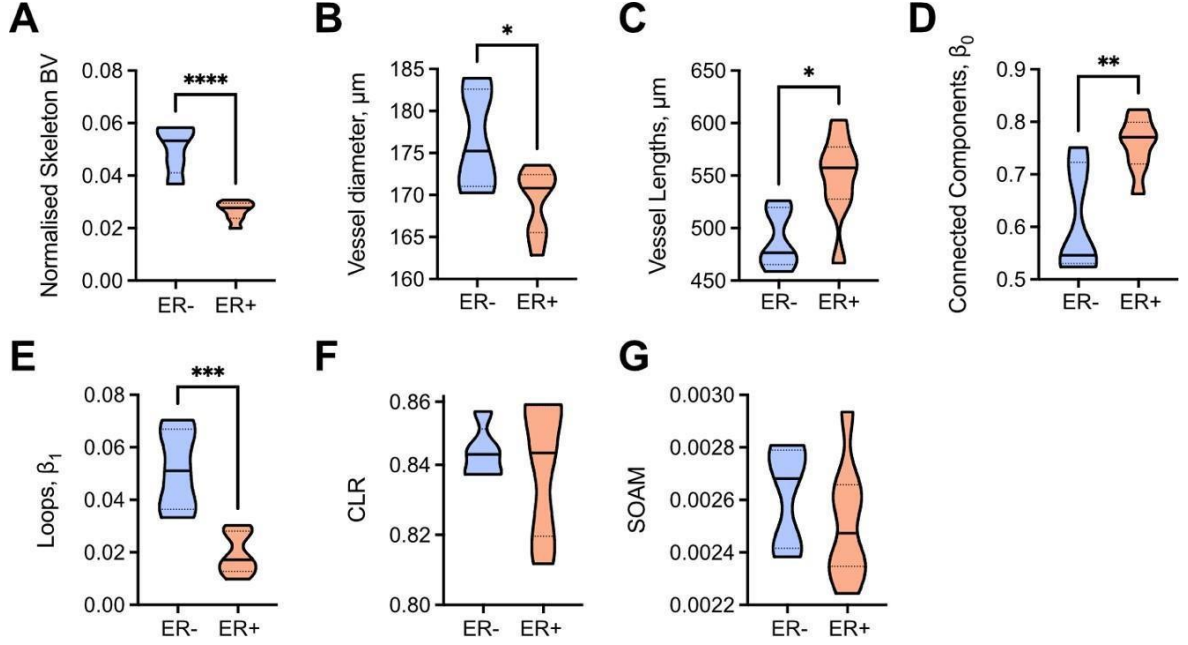
Data are represented by truncated violin plots with interquartile range (dotted black) and median (solid black). Comparisons between STG139 (ER-) and AB580 (ER+) tumours made with unpaired t-test. For (A) STG139 n=6, AB580 n=8. For (B-G) STG139 n=5, AB580 n=8, one STG139 image is excluded with artefact that would impact network structure/topology. p<0.05 considered significant.

*=p<0.05, **=p<0.01, ***=p<0.001, ****=p<0.0001.